UNIVERSITY OF SOUTHAMPTON

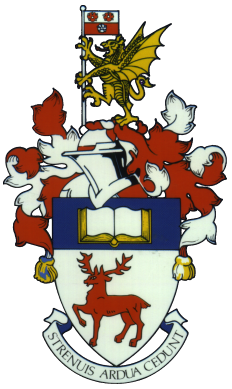

Cones of Silence, Complex Rays, & Catastrophes: Novel Sources of High-Frequency Noise in Jets

by

Jonathan T. Stone

A thesis submitted in partial fulfillment for the
degree of Doctor of Philosophy

in the
Faculty of Engineering and the Environment
Institute of Sound and Vibration Research

March 2016

Declaration of Authorship

I, JONATHAN T. STONE, declare that this thesis titled, 'Cones of Silence, Complex Rays, & Catastrophes: Novel Sources of High-Frequency Noise in Jets' and the work presented in it are my own. I confirm that:

- This work was done wholly or mainly while in candidature for a research degree at this University.
- Where any part of this thesis has previously been submitted for a degree or any other qualification at this University or any other institution, this has been clearly stated.
- Where I have consulted the published work of others, this is always clearly attributed.
- Where I have quoted from the work of others, the source is always given. With the exception of such quotations, this thesis is entirely my own work.
- I have acknowledged all main sources of help.
- Where the thesis is based on work done by myself jointly with others, I have made clear exactly what was done by others and what I have contributed myself.

Signed: _____

Date: _____

"Arithmetic is being able to count up to twenty without taking off your shoes."

Mickey Mouse

UNIVERSITY OF SOUTHAMPTON

Abstract

Faculty of Engineering and the Environment
Institute of Sound and Vibration Research

Doctor of Philosophy

Cones of Silence, Complex Rays, & Catastrophes: Novel Sources of High-Frequency Noise in Jets

by Jonathan T. Stone

As industrial design continues to look at less conventional jet engine nozzles that produce typically asymmetric mean flows, there is now a need for completely 3D noise prediction schemes. To date, most prediction schemes have been based on extensions of the acoustic analogy given by Lighthill. The most popular, due to Lilley for a parallel shear flow, proves too restrictive when considering the flows from complicated nozzle geometries. However, a generalised acoustic analogy based on an arbitrary mean flow with prescribed nonlinear source terms remains a viable method for industrial computations.

Since any source can be decomposed into a sum of point sources, a critical step in acoustic analogies is the construction of the mean field Green's function. In general the numerical determination of the Green's function still remains a major undertaking, and so much attention has been focused on the simplifications afforded to high-frequency ray approximations. Typically ray theory suffers from three main deficiencies: multiplicity of solutions, singularities at caustics, and the determining of complex solutions. The latter lying beyond-all-orders of the divergent ray expansion in the wavenumber parameter, but proving critical when computing the acoustic field in shadow zones such as the cone of silence.

The purpose of this thesis is to generalise, combine and apply existing methods of tackling these deficiencies to moving media scenarios for the first time. Multiplicities are dealt with using an equivalent two-point boundary-value problem, whilst non-uniformities at caustics are corrected using diffraction catastrophes. Complex rays are found using a combination of imaginary perturbations, an assumption of caustic stability, and analytic continuation of the receiver curve.

As a demonstration of the solver two problems are studied with increasing utility to jet noise. The most important is the application to Lilley's equation for an off-axis point source. This solution is representative of high-frequency source positions in real jets and is rich in caustic structures. Full utilisation of the ray solver is shown to provide excellent results.

Acknowledgements

Firstly, I would like to thank my academic supervisors Dr. Rod Self and Prof. Chris Howls for their advice and support whilst allowing me the room to work in my own way. I have enjoyed discussing all aspects of my PhD with them and I am grateful for their patience and knowledge.

Secondly, I would like to thank Feargus Kewin for his help getting started with the Lilley solver right back at the beginning of this project, and W. Garrett Mitchener for his help redeveloping a Stokes solver. I am also grateful to all those colleagues who have offered advice and support...and the odd chatz along the way.

Last, but by no means least, I would like to thank my family for their love and support, and my dog (RIP, boy) who probably got me into jet noise in the first place.

Contents

List of Figures

Abbreviations

AA	**A**coustic **A**nalogy
AC	**A**nti-**C**austic
(**A**)**S**	(**A**nti-)**S**tokes
B/I VP	**B**oundary/**I**nitial **V**alue **P**roblem
CDP	**C**austic **D**isappearance **P**oint
CoS(**B**)	**C**one of **S**ilence (**B**oundary)
CRT	**C**omplex **R**ay **T**racing
DRE	**D**erived **R**ay **E**quations
EPNL	**E**ffective **P**erceived **N**oise **L**evel
GA	**G**enetic **A**lgorithm
GF	**G**reen's **F**unction
LEE	**L**inearised **E**uler **E**quations
LLP	**L**inear-**L**ayer **P**roblem
LRT	**L**ighthill **R**ay **T**racing
LS	**L**iapunov-**S**chmidt
P2C	**P**oint to **C**urve
WK	**W**undrow & **K**havaran
RANS	**R**eynolds **A**veraged **N**avier **S**tokes
SIPQ	**S**tatistically **I**sotropic **P**oint **Q**uadrupole
WKB	**W**entzel-**K**ramers-**B**rillouin
WNM	**W**inding **N**umber **M**ethod
WM	**W**eiestrass-**M**algrange

Symbols

Fluid dynamical variables

p	Pressure
ρ	Density
u_i	Fluid velocity
s	Entropy
f_i, q	Nonlinear volume sources
c	Speed of sound
ω	Radian frequency
k_0	Characteristic wavenumber
St	Strouhal number
n_D	Real space dimension
$\delta(\cdot)$	Delta function
δ_{ij}	Kronecker delta
$g_{\nu\eta}$	LEE vector Green's function
Γ	Autocorrelation function
I_ω	Spectral density function
H	Source cross-spectral density function
$\mathscr{D}_\omega$	Ring source directivity function
$\mathbb{G}_\omega$	Reduced Green's function
$\mathscr{G}_\omega^{(n_D)}$	n_D-dim. Helmholtz Green's func.

Coordinate systems

$\boldsymbol{x} = \{x_1, x_2, \ldots, x_{n_D}\}$	Cartesian receiver position
$\boldsymbol{x}_s$	Source position
$\boldsymbol{\eta}$	Source separation vector
Polar system based on source	
r	Cylindrical polar radius
R	Spherical polar radius
θ	Polar angle
φ	Azimuthal angle

Operators

$\mathscr{A}_i$	Vector ray operator
$E[\cdot]$	Expected value operator
$\mathscr{F}_a(f), \mathscr{F}_b^{-1}(\hat{f})$	Fourier transform pair of f; b to a
$\mathscr{L}, \mathscr{L}_\omega$	Lilley operator: time dep., frequency dom.
L_{uv}	LEE propagator
$\langle\cdot\rangle_\varphi$	Azimuthal average
$\langle\,\cdot\,,\cdot\,\rangle$	Inner product
$\wedge$	Wedge product

Ray variables & Continuation

$\boldsymbol{\varsigma}$	Ray firing variables
$\boldsymbol{p}$	Ray slowness
S	Ray phase
r_n, m_{i_n}, s_n, P_n	Ray amplitudes
α	Control parameter
$\Gamma_\varsigma^B(\alpha)$	Set of bifurcation curves
D, D_Z	Ray Jacobian operators
$\mathbf{F}$	Ray BVP function
$\mathbf{Z}$	Tangent variables
$\mathscr{J}$	LS reduced function
ϕ^{LS}	LS projected function
Λ	LS control parameters

Uniform functions

ℓ	Corank
K	Codimension
s, t	State variables
$\boldsymbol{\xi}$	Control variables
$\Phi_K, \Phi^{(E,H,P)}$	Catastrophe functions
$\Psi_K, \Phi^{(E,H,P)}$	Canonical functions
$\{A_0, A_1, \ldots, A_K\}$	Path formulation coefficients
$\{\Lambda_{\text{ctl}}, \Lambda_1, \ldots, \Lambda_k\}$	LS path formulation parameters
n_K	No. of contributing coalescing rays
$c_{n,m}$	WM uniform coefficients
$\boldsymbol{V}$	Van der Monde matrix
S_{nm}	Dingle's singulant

Parallel shear flow

$\text{Ai}(z)$	Airy function

$J_n(z)$	Bessel function of the first kind
$H_n^{(1,2)}(z)$	Hankel function
$\Gamma(z)$	Gamma function
$\mathscr{R}_\omega$	Flow-factor
$\nu_\star$	Saddle-point
ψ_{WK}	WK phase function
$\Phi_K^{\mathscr{E}}$	Eucatastrophe potential
$\mathscr{E}_K$	Eucatastrophe

To my parents

Chapter 1

Introduction

1.1 Jet Noise

In the past 50-60 years there have been rapid developments in the understanding and prediction of jet noise. Jet noise is a significant contributor to an aircraft's noise signature, and consequently there has a been a considerable desire to control and mitigate this contribution. Despite a flurry of activity and over four-fold reductions in jet noise alone since the 1960s, aviation noise is still a serious and growing problem. In small developed countries such as those in the UK it is also one of controversy, particularly aggravated by the drive to cater - via large transport hubs - for expanding markets in the global economy. In an addition to this, there is also an urgency to design and validate new engines that provide noise benefits as increasingly stringent noise requirements, such as those found in ICAO's annex 16 [1, 2], come into force.

In the modern day, jet flows are predominantly produced by coaxial turbofan powerplants, whereby a large cold flow that bypasses the engine core mixes with a hot core flow in the jet exhaust. A typical example of the jet flows that result from this configuration is shown in Fig. 1.1(a). As the flow exits the nozzle(s) the turbulent mixing of the flow with the ambient medium creates, as a byproduct, a component of pressure that propagates acoustically to an observer, resulting in jet noise. It is the wide range of energy bearing scales within the subsonic flow that provides the characteristic broadband structure to the pressure spectrum. Figure 1.1(b) is a good illustration of both the fine-scale turbulence and the large coherent structures present in a single stream jet. While coaxial flows are more complicated than those of single stream jets, these fine-scale and large structures are present in both. It is the identification of this latter noise mechanism that led to the use of enhanced mixing devices, such as tabs and

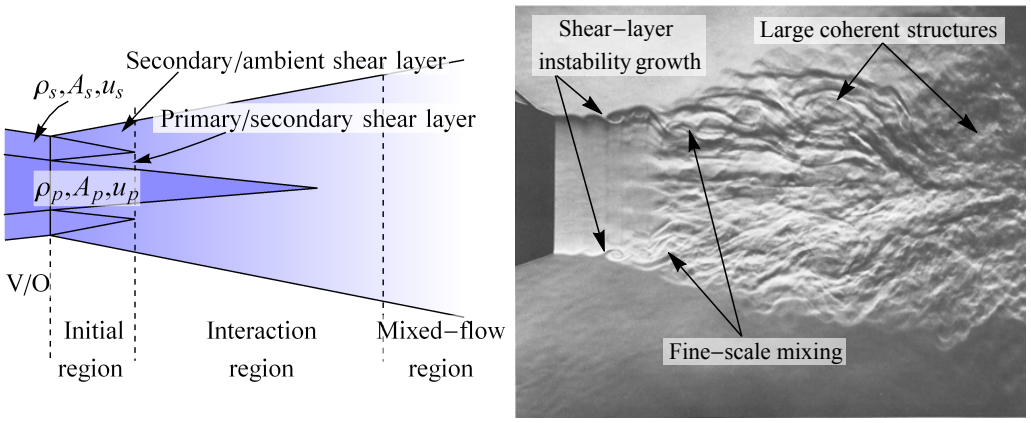

(a) Coaxial jet (b) Single stream jet

FIGURE 1.1: Flow regimes of a coaxial and single stream jet. (a) Coaxial jet with primary and secondary flows; jet is broken up into initial, interaction and mixed-flow regions; ρ, A, u are the operating density, area and velocity of each flow. (b) Schlieren of a single stream jet in transition to turbulence showing fine-scale and large scale mixing. Reproduced from Van Dyke [3].

chevrons, which aim to break up the large-scale structures at the expense of creating more fine-scale turbulence.

Perhaps the most important parameter from the coaxial turbofan jet in the context of jet noise is the bypass-ratio (bpr). The bypass-ratio is the ratio of the secondary and primary mass flows and is proportional to the velocity, density, and area ratios of the two nozzles. As will be shown in subsequent sections, it is the increase of the bypass-ratio that has overseen the decrease in jet noise since their first development. For constant thrust engines, increasing bpr increases the area ratio leading to trade-offs with other aircraft/engine design parameters such as drag, fuel consumption, weight, and ground clearance. Additionally, the engine's large size also sees it move into closer proximity of the wing thus leading to interaction between the wings trailing edge and the jet exhaust generating and enhancing existing noise mechanisms.

While current bprs, typically in excess of 10, can be increased, there is a need to look at less conventional nozzle geometries that typically produce asymmetric mean fields for noise benefits. However, many of the current methods are limited to assumptions of symmetry or through computational demand. Therefore, an accurate and robust solver is required that can be used in the design of more efficient noise-suppression devices.

The first steps can be made by noting that the wavelengths at which most noise is produced are shorter than the characteristic length scale of the mean flow. In this situation the noise is considered high-frequency and asymptotic approximations can

be used to provide gross simplifications in the governing equations. The use of high-frequency solutions is also consistent with the use of enhanced mixing devices that increase the high-frequency producing fine-scale content of the turbulence as opposed to the low frequency large coherent structures. For general flows, high-frequency solutions are best described by ray theory, and while the use of these solutions is not new, a consistent framework for the application of rays - perhaps surprisingly - is yet to exist in aeroacoustics.

It is the aim of this thesis to construct a ray solver that deals with arbitrary flows in the free-field and accounts for well known ray deficiencies such as: multiplicities due to the arrival of rays taking alternative, but distinct paths, to an observer; singularities at caustics where regions of high intensity are erroneously predicted as unphysical divergences; and the determination of complex rays - evanescent waves - in shadow zones. Accounting for these deficiencies allows for high accuracy to be achieved as not only are nearly all ray contributions tracked down, but the field is also bounded in a neighbourhood containing the caustic, meaning overestimates due to singularities are not made. The use of complex rays is critical for calculations when the observer is located in the cone of silence - a shadow zone based on the downstream axis. Hitherto, there is no general method for their calculation.

Though ray theory is an extremely powerful tool and can be applied to both linear and nonlinear equations, it is not necessarily obvious as to whether this should be applied to the full Navier-Stokes equations or an appropriate linearisation for best effect. One resolution is to look at the source of noise being dealt with: the fine scale structures. These sound sources may be modelled as compact acoustic sources and are best served by an acoustic analogy; therefore it is expedient to start with a review of the acoustic analogy and its derivatives as a starting point for the ray solver in this thesis.

The following review has been split up into three sections in order to help the reader navigate through the large amount of material covered. The first review, §1.2, as mentioned above concerns the acoustic analogy, and we use this to support our use of the vector Green's function/source decomposition in Chapter 3. The second, §1.3, and third, §1.4, reviews cover ray theory in aeroacoustics and ray deficiencies respectively. The former supports the development of the ray framework used in Chapter 3, while the latter covers the background material for the work overcoming ray deficiencies in Chapters: 4, continuation; 3, 4, complex rays; 5, caustics/uniform asymptotics.

1.2 Acoustic Analogies

Even though the field of aeroacoustics is relatively new, a large number of jet noise prediction techniques already exist, each with a differing degree of computational complexity. These methods are not necessarily in direct competition, but may be constructed *ad hoc* for investigative work. For instance, one might be interested in the Kelvin-Helmholtz instability at high-Reynolds numbers, or a fast database-driven prediction method valid in the far-field. In the case of the former, a case may take days, whereas the latter may only take seconds. Many of these methods are based on, or have taken inspiration from, the acoustic analogy (AA). In particular, some of the fundamental results that will be discussed below can be applied to a family of jets using the similarity properties of jets, i.e., the congruence of the characteristic jet regions (i.e., mixing, transition, developed regions) under simple scalings that lead to universal spectra. Despite advances in other branches of aeroacoustic prediction, the AA still remains eligible as complete simulations of jet turbulence and noise generation are too computationally expensive for high Reynolds number flows.

The first acoustic analogy was given by Lighthill [4, 5] in the 1950s and for several decades remained the dominant jet noise theory. Lighthill theory provides a systematic basis for predicting jet noise which starts by rearranging the Navier-Stokes equations into the form of a linear wave equation (hence the analogy with acoustic propagation) in density for a quiescent medium with a non-linear source term,

$$\left(\frac{1}{c_\infty^2}\frac{\partial^2}{\partial t^2} - \frac{\partial^2}{\partial x_i \partial x_i}\right)(\rho - \rho_\infty) = \frac{\partial^2 T_{ij}}{\partial x_i \partial x_j}, \tag{1.1}$$

where T_{ij} is the so-called Lighthill tensor,

$$T_{ij} = \underbrace{\rho u_i u_j}_{\text{Turbulent stresses}} + \underbrace{\left((p - p_\infty) - c_\infty^2(\rho - \rho_\infty)\right)\delta_{ij}}_{\text{Non-linearity coefficient}} - \underbrace{\sigma_{ij}}_{\text{Viscous stresses}}. \tag{1.2}$$

The crucial step in the acoustic analogy is that the source term is either known *a priori*, say through experiment, or by statistical modelling. Thus the problem appears to be just a matter of determining the Green's function, which in the absence of boundaries is trivially equal to $\delta(t - \tau - |\boldsymbol{x} - \boldsymbol{x_s}|/c_\infty)/4\pi|\boldsymbol{x} - \boldsymbol{x}_s|$. The acoustic field is then given in principle by,

$$p(\boldsymbol{x}, t) = \frac{1}{4\pi}\frac{\partial^2}{\partial x_i \partial x_j}\int_V \frac{T_{ij}(t - |\boldsymbol{x} - \boldsymbol{x}_s|/c_\infty)}{|\boldsymbol{x} - \boldsymbol{x}_s|}\,\mathrm{d}^3\boldsymbol{x}_s. \tag{1.3}$$

This rearrangement results in an equivalent set of sources that remain non-negligible in a limited region of space. At this point the arrangement is exact but some deduction must

be made to the form of the source distribution. This is often based on the expression (1.2), but other heuristic expositions also exist (see for e.g., Morris & Farassat [6], Tam & Auriault [7]).

Lighthill argued that for unheated, high-Reynolds number jets, the dominant sources of jet noise are the turbulent stresses and their double divergence leads to an acoustic field with quadrupole characteristics. As a precursor to the wealth of experimental data currently available, Lighthill used (1.3) to deduce his celebrated 8^{th} power scaling law. Assuming the turbulent eddies to be compact so that $\lambda = c_\infty/f = 2\pi c_\infty/\omega \gg l$, where l is a characteristic lengthscale (e.g., the jet nozzle diameter, D), λ is the acoustic wavelength and $M = u/c_\infty$ is a Mach number based on a characteristic velocity (e.g., the jet mean exit velocity, U_J), Lighthill scaled the far-field acoustic power as,

$$W \sim \rho_\infty \frac{u^8}{c_\infty^5} l^2. \tag{1.4}$$

In what is one of the few genuine scientific predictions, the significance of this scaling is ubiquitous and is the main motivation for increasing the nozzle diameter and bypass ratio, while maintaining constant thrust. This result has been generalised more than once for example, for convecting sources, and in 1/3 octave bands by Lush [8] for large observer radii $R \to \infty$,

$$I(f,R,\theta) \sim \underbrace{\frac{\rho_s^2 u^8 D^2}{\rho_\infty c_\infty^5 R^2}}_{u^8\text{law}} \underbrace{(1-M_c\cos\theta)^{-5}}_{\text{Source Convection}} \underbrace{F\left[\frac{\omega D}{U_J}(1-M_c\cos\theta)\right]}_{\text{Universal spectrum}}. \tag{1.5}$$

Returning to the integral result in (1.3), it should be noted that what is really of interest is the normalised pressure autocorrelation function[1] of this integral in the far-field. There are two reasons for this: first, when jet noise is measured, it is measured using averaging techniques and that autocorrelation is an averaging procedure; secondly, for modelling purposes it is easier to model the statistics and correlations of the source field than it is the sources directly. The normalised pressure correlation is given by (see Goldstein [9]),

$$\Gamma(\boldsymbol{x},\tau) \equiv \frac{\overline{[p(\boldsymbol{x},t+\tau)-p_\infty]\,[p(\boldsymbol{x},t)-p_\infty]}}{\rho_\infty c_\infty}, \tag{1.6}$$

which can be written, in the far-field,

$$\Gamma(\boldsymbol{x},\tau) = \frac{\rho_\infty x_i x_j x_k x_l}{16\pi^2 c_\infty^5 x^6} \frac{\partial^4}{\partial\tau^4} \int\int \mathscr{R}_{ijkl}\left(\boldsymbol{x}_s', \boldsymbol{\eta}, \tau + \frac{\boldsymbol{\eta}}{c_\infty}\cdot\frac{\boldsymbol{x}}{x}\right) \mathrm{d}\boldsymbol{x}_s' \mathrm{d}\boldsymbol{\eta}, \tag{1.7}$$

[1] In acoustics this has the form of acoustic intensity.

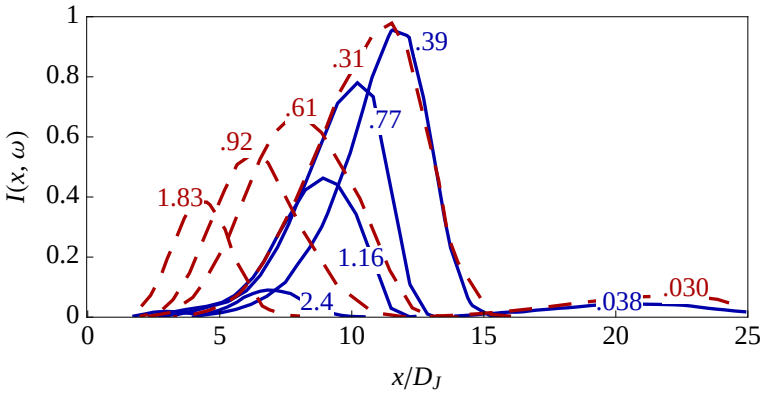

FIGURE 1.2: Axial source distributions per effective Strouhal number for coaxial jets, reproduced from Ilário [11]. bpr=1.25, solid blue line; bpr = 2, red dashed line. End of primary potential core $10D_J$ approx.

where,

$$\mathscr{R}_{ijkl}(\boldsymbol{x}'_s,\boldsymbol{\eta},\tau)=\frac{\overline{T_{ij}(\boldsymbol{x}'_s,t)T_{kl}(\boldsymbol{x}'_s+\boldsymbol{\eta},t+\tau)}-\varphi_{ijkl}(\boldsymbol{x}'_s,\boldsymbol{\eta})}{\rho_\infty^2}, \tag{1.8}$$

is the source correlation tensor. Here φ_{ijkl} is an arbitrary tensor that is chosen to simplify the source modelling.

For stationary random functions of time then the Wiener-Khinchin (see for e.g., Engelberg [10]) theorem can be used to relate the autocorrelation with power spectral density function via Fourier transforms; this allows one to analyse jet noise at a particular frequency.

$$I(\boldsymbol{x},\omega)=\frac{\omega^4\rho_\infty}{32\pi^3c_\infty^5}\frac{x_ix_jx_kx_l}{x^6}\int_{-\infty}^{\infty}\int\int \mathrm{e}^{\mathrm{i}\omega(\tau-(\boldsymbol{x}/x)\cdot\boldsymbol{\eta}/c_\infty)}\mathscr{R}_{ijkl}(\boldsymbol{x}'_s,\boldsymbol{\eta},\tau)\mathrm{d}\boldsymbol{x}'_s\mathrm{d}\boldsymbol{\eta}\,\mathrm{d}\tau. \tag{1.9}$$

It is the source correlation $\mathscr{R}_{ijkl}$ that has to be modelled and there are various ways of doing this. Typically this is done by assuming the source correlations have a Gaussian form which can then be fixed by matching with experimential data at 90° (where convection effects are negligible) in the far-field. As an example of the source distributions that can result from using Lighthill's acoustic analogy, Fig. 1.2 shows the axial distribution of sources at various effective Strouhal numbers for two coaxial jets of different bypass ratio. It can be seen that the Gaussian assumption of the correlations is physically consistent: the centroid of each Strouhal distribution moves closer to the jet nozzle with increasing Strouhal number, i.e., high-frequency noise is generated near the nozzle where there is predominantly fine-scale mixing.

Lighthill's theory, however, does contain ambiguity and its application is limited since the analogy with a quiescent medium sees it restricted in its description of flow-acoustic interaction. Part of the problem is that this analogy does not completely separate

the sources from the propagation as is apparent if one examines the correlation tensor $\mathscr{R}_{ijkl}$. This, from (1.2), is clearly a function of velocity correlations $\overline{u_i u_j u_k u_l}$. A flow decomposition into mean and fluctuating parts would show that the mean field is an integral part of these correlations. It can be shown that φ_{ijkl} is useful in reducing the complexity of $\mathscr{R}_{ijkl}$, but its arbitrariness does not detail how it should be applied to general cases, and it does not completely eliminate the mean field from the source.

Since Lighthill there have been several efforts to improve the acoustic analogy, notably, Phillips [12], Lilley [13, 14], Ffowcs-Williams [15], Ribner [16], Goldstein & Rosenbaum [17]. These formulations differ only in the model decomposition into acoustic sources and propagation. Both Phillips [12] and Lilley [13, 14] sought to generalise the analogy by rearranging the Navier-Stokes equations into the form of an inhomogeneous convective equation where the mean flow profiles are a function of the transverse coordinates only. In the case of Phillips the propagation was governed by a second order convective wave equation, with nonlinear source terms. Lilley argued that Phillips' equation did not completely separate the propagation from the source term, he then proceeded to further manipulate Phillips' equation until the propagation obeyed a third order convective wave equation. Although the mean flow gradients are explicitly represented in the propagation and not lumped with the source term, as is required for consistent use of the acoustic analogy, the non-linear source terms do not have an explicit quadrupole & dipole nature as in Lighthill theory.

The difference in source nature between the Lighthill and Lilley analogies wasn't rectified until 2001 when Goldstein [18] reworked Lilley's equation using non-linear "generalised" dependent variables. Goldstein was able to show that Lilley's analogy did have the quadrupole-dipole nature, while the reduction of the generalised variables to standard acoustic variables in the far-field meant the formulation remained useful for computations. With this success Goldstein developed the generalised acoustic analogy again using nonlinear dependent variables. This formulation linearises the Navier-Stokes about a general mean flow with a source term that includes Reynolds stresses. While the propagation is governed by the linearised Euler equations, and for a particular flow regime may be reduced to more familiar propagators, the generalised dependent variables mean that more propagation effects have been sifted out of the source term. This has led the generalised analogy to compare favourably with other analogies, Samanta et al. [19].

The generalised acoustic analogy, however, only provides the most unambiguous analogy to-date; the problem of source and propagation modelling still persists. Progress can be made by noting that any source distribution can be decomposed into a sum of point sources, and, since the propagation is linear, it is expedient to separate the source and propagation effects by employing a Green's function. Once a source model is specified

a convolution integral can be specified just as in (1.3). Due to separation of source and propagation, the Green's function can be reused for various source models.

Green's functions allow the solution to written down in theory, but their determination still remains non-trivial for all but a few soluble cases. The analogies of Phillips and Lilley remain the most complicated base-flows that allow for a scalar wave equation to be formed without recourse to perturbation methods. Even then, perturbation techniques typically yield a result that is difficult to extend beyond leading order, and thus remain limited.

It appears that an accurate noise prediction scheme that is valid for fully 3D flows - i.e., an acoustic analogy about a generic mean flow - requires a fast, accurate and reliable method for computing generic mean flow Green's functions. If the problem is considered high-frequency as discussed before then one can apply a ray ansatz to the equations for the Green's function. Given the success of Goldstein's generalised analogy, a suitable framework for the ray theory are the full linearised Euler equations (Goldstein [9]) with a vector of point sources, instead of a full source distribution. This will be used as the basis for the ray solutions in this thesis.

1.3 Ray theory

The argument for ray theory is that the acoustic wavelengths are much smaller than the typical scales of the propagating medium. For an acoustic analogy this medium is time-independent, not turbulent, and most likely supplied by RANS, so this assumption is satisfactory. Ray theory has been applied with success to time-variant media (see for e.g., Freund et al. [20]), but ray propagation is expensive computationally in this case and thus lies outside the scope of the AA considered here.

Assuming that the acoustic field behaves locally like a plane wave, the wavefront moves according to a simple vector sum of the wavefront normal and local fluid velocity. This motivates an asymptotic ray ansatz that has a controlling factor equal to a generalised plane wave multiplied by an infinite series in decreasing powers of k_0, the characteristic wavenumber of the field, i.e.,

$$p' \sim \mathrm{e}^{\mathrm{i}k_0 S} \sum_{n=0}^{\infty} \frac{\alpha_n}{k_0^{n+\gamma_{bl}}}, \tag{1.10}$$

so that explicit representation of k_0 allows it to play the role of a book-keeping parameter, and γ_{bl} allows the ansatz to tackle problems more involved than those found in this thesis. Formal introduction of the ray ansatz (1.10) into any aeroacoustic field equations, linear

or nonlinear, results in a system of nonlinear equations ordered by the wavenumber k_0. At leading order is the eikonal equation that governs the phase S, while the remaining infinite number of equations couple together the phase and the amplitude terms α_n. Notably, the eikonal is not soluble in closed form and must be tackled using ray tracing techniques.

Aside from computing the terms in a ray expansion, there is a more pertinent question and that pertains to the inherent divergent nature of the series (1.10). If each ray series diverges then is (1.10) meaningful? The answer to this - as pointed out by Dingle [21] - is that asymptotic series initially converge before diverging as the number of terms included in the sum (1.10) are increased. Consequently, by truncating the ray series at a finite number of terms and ignoring the remainder, an approximation to the acoustic field can be made. In this thesis, the leading order approximation made by taking the first term, $p' \sim \alpha_0 \mathrm{e}^{\mathrm{i}k_0 S}/k_0^{\gamma_{bl}}$, will be used.

The use of the ray ansatz (1.10) and its various guises within aeroacoustics is not new - in fact far from it. There have been notable contributions from several authors, for example in free space problems: Goldstein [22], Candel [23], Durbin [24], and Colonius et al. [25]; and in boundary problems: Abrahams et al. [26–28]. The use of ray theory here is not academic: it really does present a viable computational method. Of course this begs the question as to how low-frequency noise generation is propagated, at what frequency does ray theory "work", and how is this accounted for in the aforementioned references?

The main issue with a high-frequency ansatz is that the source distributions pertaining to jet noise provide energy across a broad range of frequencies. It seems likely that some frequencies will be poorly provided for when ray theory is employed. The argument in this case is provided by Figs. 1.2 and 1.3. The latter of these, showing typical jet broadband structures, shows a peak Strouhal number St_{PC} which contains frequencies that dominate the sound field and $St_{1/2} = 1/2$ which is a nominal lower bound taken from the above references (more detail on the lower bound in chapter 2).[2]

Firstly, it is important for the peak Strouhal number to be propagated accurately, as this is the most important Strouhal for prediction purposes; this is captured by the nominal lower bound $St_{1/2}$ in Fig. 1.3(b). Secondly, low frequencies for which $St < St_{PC}$ (St_{PC} scales with the potential core Tester & Morfey [29]), occur at axial positions greater than the potential core length where the shear layer is weaker. In this scenario the ray solution tends to that of the convected Helmholtz equation, which it solves exactly. Thus, there is a crossover between the source frequency lowering and the Green's function tending to the exact convected Helmholtz result. The resulting accuracy, then, is not

[2]Strouhal number being defined in terms of characteristic quantities: $St = fD_{ch}/U_{ch}$.

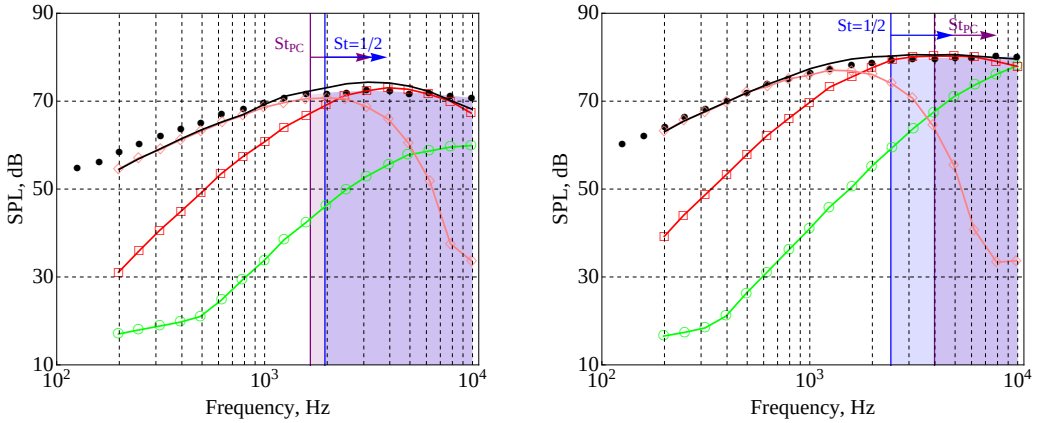

(a) bpr = 1.26 (b) bpr = 2

FIGURE 1.3: Coaxial jet source distributions reproduced from Ilário [11]. Mixed-flow region, pink diamond; interaction region, red square; initial region, green circle; total, black line; experiment, black filled circle. Purple region $St > St_{PC}$; blue region $St > St_{1/2}$.

expected to diminish dramatically. The success ray theory has already encountered within aeroacoustics is testament to this remarkable theory, especially as the expansion of the ray ansatz is about the "wavenumber at infinity".

1.4 Ray theory deficiencies

Despite the success that ray theory has had and the gross simplifications it provides, it is not a free lunch. There are several fundamental deficiencies suffered by the ansatz (1.10). Though aeroacoustics provides the most testing cases for ray theory, it has been used extensively across many disciplines, for example in subjects as diverse as, quantum mechanics (Berry [30]), water/ship wave theory (Kelvin [31, 32], Ursell [33, 34]), seismic prospecting (Červenỳ [35, 36], Thomson [37]), and optics (Berry [38], Egorchenkov & Kravtsov [39]), but to name a few. In some of these cases ray theory not only offers a computational advantage but also physical insight into the workings of complicated systems. Fortunately, this wide use of ray theory means there is a wealth of material that can be extended to tackle problems in the complex flow problems of aeroacoustics.

The deficiencies discussed here do not form an exhaustive list. Other deficiencies, such as those at boundaries can be treated by Keller's Geometrical Theory of Diffraction (GTD) [40]. This treatment is not necessary in the free space problems of the AA. In fact we will only deal with three here and these directly related to the form and functions found in (1.10). In order of appearance below, these are: the multiplicity problem, involving the determination of as many ray solutions or branches of the eikonal equation governing

S; the continuation of rays into the complex plane to allow for $S \in \mathbb{C}$; and finally the correction to the divergence of α_n experienced in the neighbourhood of a caustic using diffraction catastrophes.

In this thesis a key step is to identify from a theoretical and computational point of view, that each of the three deficiencies is inherently linked to the other. In some cases it is necessary to highlight these links, as treatment and computation of one deficiency need not be handled completely separately from the others.

1.4.1 Multiplicities

The multiplicity problem is simply the matter of determining all solutions to the eikonal equation that propagate to the desired receiver. In generic moving media problems the eikonal equation has no closed-form solutions and must be solved numerically using the method of characteristics (see for e.g., Sneddon [41]). This method, known as ray tracing, is naturally in the form of an initial value problem (IVP). It computes the normal to the high-frequency wavefront given a set of ray parameters equal to the union of firing parameters - to launch the ray, and an integration time. The relation between the ray parameters and the receiver position in general is non-trivial.

The first attempt to overcome this in a stationary heterogeneous medium was made by Sambridge & Kennett [42]. This was a generalisation of work by Wesson [43, 44], Julian and Gubbins [45], Pereyra et al. [46]. They recast the IVP as a boundary value problem (BVP), or two-point problem (in analogy with numerical ode methods), by explicitly representing the receiver position in a cost function as the difference with ray trajectory endpoint. This almost trivial step is the natural generalisation of the root finding required when using saddle-points or stationary phase techniques to evaluate integrals asymptotically. The roots of the cost function equal the desired rays, and so a whole host of optimisation techniques can be applied. The simplest and fastest is the multi-dimensional Newton method used by several authors, notably Sambridge & Kennett [42], Hanyga and Helle [47], Keller and Perozzi [48], and Farra [49]. This work was then extended by Haynga [50] who went to great extent to incorporate bifurcation theory within ray tracing. This was based on the continuation of receiver points into receiver curves thus generating bifurcation curves in all ray parameters. Hanyga sped up the calculation by employing a predictor-corrector method based on the pseudo-arclength continuation of Keller [51], homotopy or continuation methods were then used to track rays across caustics.

Continuation methods draw heavily upon numerical methods to determine solutions. Not all the apparatus introduced by Haynga is necessary. The more layers one uses the

higher the computational burden. The majority of methods used by Hanyga can be found in works by Keller [52, 53], Doedel et al. [54], Allgower and Georg [55]. In the context of seismic propagation a good text is the compendium edited by Doornbos [56].

1.4.2 Complex rays

Complex rays are simply extensions of the familiar real rays to the scenario $S \in \mathbb{C}$. In engineering parlance, complex rays are evanescent waves, though their unphysical counterparts necessarily exist too. The determination of complex rays is not really a flaw in the ray method, rather it is the difficulty of calculating solutions when no closed-form field integral exists. When the latter does exist, it is a simple matter of analytic continuation of the integral's saddle points to provide a complex ray expansion: formally there is no difference in the method of expansion.

In terms of the ray ansatz (1.10) the exponentially small solution can be explicitly added as,

$$p' \sim \mathrm{e}^{\mathrm{i}k_0 S_1} \sum_{n=0}^{\infty} \frac{\alpha_n}{k_0^{n+\gamma_{bl}}} + \mathrm{e}^{-k_0 \mathrm{Im}(S_2)} \mathrm{e}^{\mathrm{i}k_0 \mathrm{Re}(S_2)} \sum_{n=0}^{\infty} \frac{\beta_n}{k_0^{n+\gamma_{bl}}}. \tag{1.11}$$

The most peculiar aspect of (1.11) is that the exponentially small term lies beyond all orders of $k_0^{n+\gamma_{bl}}$, but the leading order approximation is $p' \sim \alpha_0 \mathrm{e}^{\mathrm{i}k_0 S_1}/k_0^{\gamma_{bl}} + \ldots + \beta_0 \mathrm{e}^{-k_0 \mathrm{Im}(S_2)} \mathrm{e}^{\mathrm{i}k_0 \mathrm{Re}(S_2)}/k_0^{\gamma_{bl}}$. This is easily resolved by distinguishing between an asymptotic expansion as in (1.11) and the summation of its component asymptotic series (see Dingle [21] for an extended discussion). By summing the component series in this way the solution permits the appearance of the exponential term even though there may be exponential error in the first asymptotic series. The argument now is then, Why would be the exponentially small term be retained?

A physical complex ray, one that decays, is exponentially small in the limit $k_0 \to \infty$ and so that there is a good argument for the neglect of such contributions, especially if their only contribution serves to embellish the field in the presence of real, purely oscillatory rays. Of course an engineering approximation might well do this: however, the dangers of doing this lie in the existence of regions, called shadow zones, in jets where the field is exclusively complex, i.e., $\alpha_n = 0, \forall n$.

Despite the possibility of shadow zones there is no framework for generic complex ray computation, where the best provision for complex rays has been through Lilley's equation and perturbed variants - these cases now being too specific. This contrasts significantly with other disciplines where the appreciation, significance and computation

of complex rays is far greater. Though this is not an exhaustive list, some notable uses/contributions are as follows. In quantum mechanics complex rays are significant in bridging the gap between the classical (particle) and quantum (wave) descriptions of matter, for example in quantum tunnelling problems (Morse & Feshbach [57], Bender & Orszag [58], Heading [59]). In water wave theory complex rays are necessary for the smoothing of Kelvin ship waves (Keller [60], Kelvin [31, 32], Ursell [33, 34]) and the engendering of ripples as flows pass over discontinuous surfaces, Lustri [61]. From a computational perspective complex rays are important for the calculation of seismograms in seismic prospecting (Thomson [37], Hanyga & Seredyńska [62], Hanyga & Helle [47]). This use of complex rays differs slightly from the first two examples which are more theoretical devices whereas seismology requires a more computationally intensive programme that involves the tracing of complex ray trajectories. In all seismology cases cited, complex rays are solutions to a complexified two-point problem as discussed in the previous section. Similar numerical computations of ray trajectories have also been made by Kravtsov [63] and Egorchenkov & Kravtsov [39] who focus on problems in quantum mechanics and optics. The former also discusses the existence of complex rays as a generalization of Fermat's principle (Pierce [64]). Other useful works on complex ray theory (CRT) are by Chapman et al. [65] which serves as a useful compendium on constant coefficient Helmholtz problems - though the ray trajectories are solved analytically, Deschamps [66], Felsen [67], Arnaud [68] and Norris [69] who consider the Gaussian beam (a useful tool in itself, e.g., in photonics) as being composed of complex rays from complex sources thus showing the equivalence of complex sources with a real one, and from an historical perspective the papers by Seckler & Keller [70, 71] which utilise complex rays in inhomogeneous media.

In all of the above there is some underlying need for complex rays either from a computational or theoretical perspective. This is why we should return to the question of whether or not CRT is really useful in aeroacoustics. The answer is yes and the reason pertains to the aforementioned shadow zones. It is well known that point sources in jets suffer from a reduced intensity in a region about the jet axis as high-frequency waves are refracted away from the jet axis (Durbin [72], Goldstein [22]). High-frequency analysis shows that this engenders a shadow zone about the axis that is typically asymmetric in angular observer coordinates and its existence a function of radial distance (Hubbard [73]). This region is known as the Cone of Silence (CoS), or sometimes cone of relative silence, though this is somewhat a misnomer as the region is generally not conic. Indeed, if it were a matter of considering just the field of a Green's function then it would be tempting to neglect the CoS. However, as previous sections show, the Green's function is convolved with a source term, and if the source term is large in the downstream direction the multiplication of these two quantities often results in a non-negligle amount.

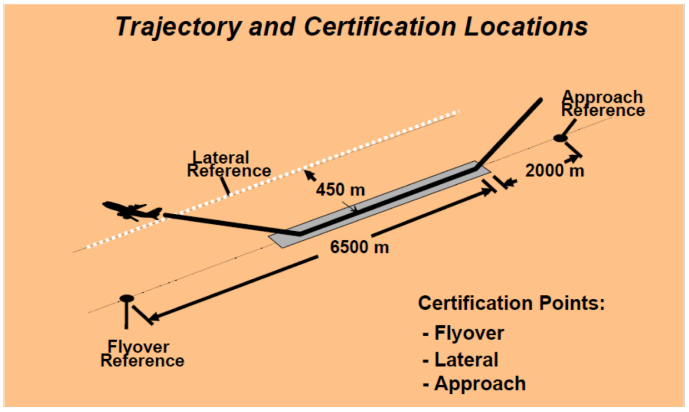

(a) Aircraft certification route showing positions of approach, lateral and flyover microphones.

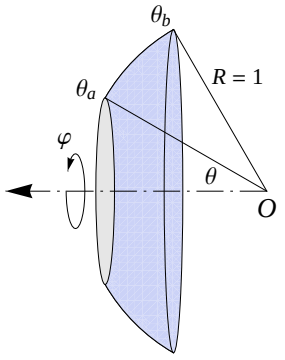

(b) Example of angular region

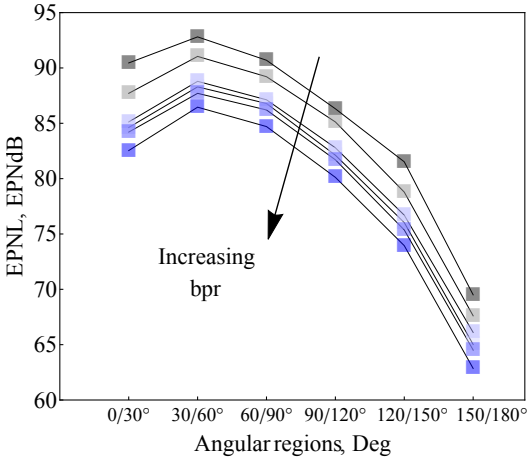

(c) EPNL at the flyover mic as a function of angular region θ_a/θ_b and bypass-ratio, bpr.

FIGURE 1.4: Bypass-ratio study for a certification problem. Angular regions such that $\theta = 0$ lies along jet axis.

In order to provide some heuristic argument for the CoS's importance, the following figures show the angular breakdown Fig. 1.4(b) of a database (empirical data) coaxial jet flown along a certification flight path Fig. 1.4(a) and the resulting Effective Perceived Noise Levels (EPNL) recorded at the flyover mic (the reference where jet noise is the dominant noise source on an aircraft), Fig. 1.4(c).[3] The angular breakdown supplies a directivity function $H(\theta - \theta_a)H(\theta_b - \theta)$ to the SPL spectra, where $H(\cdot)$ is a Heaviside function.

It can be seen that low angles are just as important if not more so than high angles in terms of EPNL. This is true for all bpr shown. This observation is mainly down to the high exposure times of mics. in the line of sight of the jet axis at take-off. As the CoS previously explained is for a point source, it is important to understand the difference between that and the one used by experimentalists to define an aggregate or bulk CoS. This is roughly defined as the conic angle $\theta_{CoS} = \cos^{-1}(1/1 + 0.71M_p)$, which evaluates

[3]The EPNL is an aircraft specific metric that is penalizes high-frequencies, see [1, 2] for details

to $\theta_{CoS} = 48.7°$ for $M_p = 0.72$ considered. This information shows that the CoS is very much important to evaluating jet noise annoyance.

This argument serves as motivation for the use of complex rays especially from an aircraft annoyance point of view. There is, however, more to be said about using CRT that is often emitted from the majority of the literature already cited. This pertains to the more subtler aspects of CRT to do with ray contributions rather than ray existence. This is because the latter is necessary but not sufficient for a ray to be employed in a field calculation. The object that determines the contribution of a complex ray is known as a Stokes multiplier after Stokes (Berry [74–76], Heading [59, 77, 78]). This quantity can turn exponentially small rays "on" or "off" according to its value: this value can change discontinuously (in a topological sense) as a receiver crosses Stokes lines (lines of evanescence) that may exist in the field. Stokes multipliers are readily available for odes and saddle point expansions, the work done by (Berry [79], Berry & Howls [80, 81]) confirms this.

As far as ray tracing is concerned the Stokes phenomenon has been discussed in papers by Chapman et al. [65], [82] for Helmholtz problems with an aim to extend Keller's GTD, and by Lustri et al. [61] & Lustri [83], for the calculation of so-called second generation Stokes lines in surface flow problems. In more complex ray tracing problems where the trajectories are not soluble in closed form, for instance in the seismological and aeroacoustic communities where these cases arise, the Stokes phenomenon is explicitly absent - though the properties of complex continuation are occasionally discussed, for e.g., Thomson [37]. A review of this phenomenon is not gratuitous as these constants will impact engineering calculations. Additionally, Stokes structures exist due to singularities in the field, so the presence of singularities discussed in the next section necessarily involve this phenomenon.

1.4.3 Caustics

The last ray deficiency is the correction of unphysical divergences of the ray field from the true field in the vicinity of caustics. These singularities, if not corrected, will result in a poor approximations to the field, and erroneous conclusions about a flow's interaction effects would be reached. The singularities pertain to the amplitude terms α_n of the ray ansatz (1.10), with each term (in n) progressively better at blowing up. The ray solution is thus degenerate, implying that a caustic doesn't have a locally plane wave structure. The logical step is to look for another local form that remains bounded at the caustic, whilst still exploiting the $k_0 \to \infty$ limit of the field. Such forms are necessarily more complicated than the ray expansion and in the words of some authors (e.g., Berry [84], Felsen [85], Mazar & Felsen [86]) this is akin to attaching diffraction flesh to the bare bones (the rays) of the field.

The caustic problem is well documented and there are several different methods of providing uniformity. These range from Gaussian beams (see for e.g., Babich et al. [87], Cerveny et al. [88]) as they can be constructed as bundles of complex rays that *do not* suffer from singularities when considered as a bundle, coherent states (Klauder [89], Thomson [90]) based on windowed Fourier transforms, to Maslov's canonical operators (for theory: Maslov [91, 92], Maslov & Fedoriuk [93]; for applications: Thomson & Chapman [94], Kendall & Thomson [95], Ziolkowski & Deschamps [96]). It is the latter method that is of interest here as the extension of Maslov's method by Arnol'd [97] leads to his version of elementary catastrophe theory and the use of oscillatory local forms/integrals valid in the neighbourhood containing the caustic.

Catastrophe theory is the tool that will be used in this thesis to provide uniformity along with elements of the closely related Maslov/Arnol'd theory. The full catastrophe theory classification was introduced by René Thom [98, 99] in the 1970s, and then developed further by Arnol'd [100], Zeeman [101]. It is a far-reaching theoretical tool that deals with the unexpectedness of discontinuous effects when they are produced by continuous causes, such as the caustic discontinuity in a ray field under smooth changes in observer position. The use of catastrophe theory to provide uniform asymptotics in high-frequency regimes is but an application of the theory. The catastrophe functions are multivariate polynomials whose behaviour is used to mimic the local behaviour of the phase function in Arnol'd's oscillatory integral. As $k_0 \to \infty$ this leads to the diffraction catastrophes that are integrals of exponentials raised to the power of k_0 times a catastrophe function. The diffraction catastrophes being the desired local forms at the caustic mentioned above.

There are seven elementary catastrophes introduced by Thom, and therefore seven diffraction catastrophes to deal with discontinuous phenomena in this thesis. These catastrophes are split into two groups: the cuspoids and the umbillics. There are more than seven catastrophes in general, however, seven turns out to be the smallest number required to model problems in physics that contain at most 3-space + 1-temporal dimensions. In fact these limits draw from the first applications of the theory in optics. Consequently, this is also where most of the development in catastrophe theory arose with appreciable work in this context by Arnol'd [102, 103], Duistermaat [104], and in terms of diffraction catastrophes Berry [38, 105], Berry et al. [106], Nye [107, 108], Wright [109, 110].

The application of catastrophe theory is wide, but its use here is not founded on (relative) popularity. The most favourable aspect of catastrophe theory is its inherent and logical taxonomic structure making it ideal for computation, Gilmore [111]. Furthermore, its connection to ray theory is straightforward: one expands the diffraction catastrophes with $k_0 \to \infty$ using the saddle point method to give the ray field. Perhaps the downside of catastrophe theory is that the diffraction catastrophes are not well known in comparison with the special functions of analysis. So much so that even though catastrophes were known about by mathematicians in the 1960s they were not by physicists, hence their omission from classic texts such as Abramowitz & Stegun [112] (first published 1964). However, in the last 16 years there has been an attempt to incorporate the diffraction catastrophes (as well as others) into the common and recognizable patterns that the special functions (e.g., Bessel, Laguerre funcs.) enjoy (see for e.g., DLMF [113]).

There are two cases of diffraction catastrophe that are more common than others, particularly in acoustics and aeroacoustics, and are pertinent to the applications in this thesis. The first governs the so-called fold or simple caustic and is therefore called the fold catastrophe. This problem was tackled by Ludwig [114] (the American school) and Kravtsov [115] (the Russian school) for point source Helmholtz problems in which fold caustics appear. Both of these authors express their solutions in terms of the Airy function as the fold can be expressed globally in terms of this special function. In aeroacoustics the fold catastrophe has appeared in shear flow problems with a boundary (Abrahams et al. [26–28]) and in free flows (Wundrow & Khavaran [116]), where the latter models part of the CoS boundary (CoSB). This serves as a starting point in this thesis. The second diffraction catastrophe is the Pearcey function (Pearcey [117]) which governs the cusp caustic. In acoustics the Pearcey function is most prevalent in the modelling of weak shock wave focusing (Coulouvrat [118], Hayes [119], Hunter & Keller [120]), though it does occur in linear flow problems as a result of reflections from boundaries (see Abrahams et al. above).

The incorporation of cuspoid diffraction catastrophes into the two-point ray tracing method was made by Hanyga [50, 121] which was used most recently by Amodei et al. [122]. Only in the cases of the fold and cusp caustics can one determine the coefficients of a catastrophe polynomial in closed form, so the generic calculation is determined numerically, with the most efficient implementation an iterative procedure introduced by Connor & Curtis [123]. This highlights what is perhaps another issue applying catastrophes: determining the catastrophe arguments may be as problematic as calculating the catastrophe itself. As far as this latter point is concerned diffraction catastrophes tend not to be included in standard software packages and computing the elementary catastrophes is undertaken *ab initio*. Computing the increasingly complex diffraction catastrophes is no trivial matter although uniform methods tend to only require these functions in a limited range. The main difficulty is dealing with the oscillatory integrand which requires high precision integration techniques if the integration domain is left unaltered as the real line. There are two alternative techniques that are popular in literature: the first is a simple contour deformation; the second is the solution of an equivalent set of pdes introduced by Connor & Curtis [123]. The former is much preferred due to ease of use and has been used by several authors to compute catastrophes in their work: the Pearcey function, Stamnes & Spjelkavik [124]; the swallowtail catastrophe, Connor et al. [125]; generic cuspoids, Kirk et al. [126], Stamnes [127]; the elliptic umbilic, Berry et al. [106]; the hyperbolic umbilic, Nye [128]. Other methods of diffraction catastrophe calculation involve Taylor expansion (based on expansions found in [113]), which are slow and offer poor accuracy away from the expansion point, and programmes that involve exotic transformation and polynomial methods (Borghi [129, 130]).

To cap off this section, we recall the connection between singularity and Stokes structures. Each diffraction catastrophe has a Stokes structure that increases in complexity as the diffraction catastrophe hierarchy is traversed. In any generic flow system we must allow for the possibility of any of the catastrophes and their Stokes structures to be present. If Stokes structures lie in real space then they definitely cannot be ignored as the neglect of Stokes switching will disrupt the accuracy of the field. Currently, there is no framework for computing Stokes multipliers & structures using two-point ray tracing in the same manner as integral methods. The most likely solution to this is by reference to the known Stokes structures of the diffraction catastrophes and an argument based on the Stokes multipliers embedded in the catastrophes. In the former we have both Wright [131] (cuspoids) and Berry & Howls [132] (umbilics) to thank. In the latter the switching mechanism that controls the Stokes multipliers is found to be embedded in the coefficients of a uniform expansion involving diffraction catastrophes. This is particularly enlightening as the contribution of complex rays locally can then be determined by the diffraction catastrophe (Berry & Howls [76, 81]).

1.5 Conclusion

It is clear from the review in this chapter that the desired ray solver draws from a broad range of elements. The three ray deficiencies must be tackled almost simultaneously if there is to be any chance of a realisable ray solver for AA calculations. This thesis seeks to develop the relevant mathematical framework to undertake this problem before unifying each element to provide a proof of principle of the CRT framework. Where necessary, and occasionally where possible, we will delve further into theory than the bare bones reviewed here.

1.6 Novel contributions and supporting work

The main novel contributions of this thesis are listed below:

1. A general framework for computing vector Green's functions to the linearised Euler equations in the high-frequency limit using ray theory. This work generalises the solutions of Durbin [24] to vector cases. Application of ray theory to correlation integrals using far-field simplifications applied to the multiple ray solutions. See Chapter 3.

2. The development of a unified complex ray tracing tool accouting for multiplicities, uniformity and complex rays. This uses continuation methods (Chap. 4), catastrophe theory (Chap. 5) and complex integration (Chap. 4) to create a programme capable of computing high-frequency effects in complicated flows. A simple continuation method is also proposed that bypasses the need for bifurcation analysis.

3. Winding number theory applied to the ray BVP. Both single variable and multiple variable theories are considered. See Chapter 4.

4. Application of the ray tool to a parallel shear flow and a demonstration of accuracy against a high-frequency modal solutions including the discovery of the Pearcey function in a parallel shear flow. See Chapter 6.

5. Near to far-field computations of parallel shear flow Green's functions, thus demonstrating the smooth nature of the near field and eliciting properties of the cone of silence. See Chapter 6.

6. Novel use of singulants in ray-tracing to appraise the accuracy of the ray solver. Singulants are also used for the calculation of crossover between uniform solutions and the ray field. See Chapter 5.

7. Analysis of perturbed ring source models in a parallel shear flow in light of the caustics found in Chap. 8. See Chapter 7.

8. First description and analysis of the anti-caustic and use of eucatastrophes for the analysis of such degenerate cases. See Chapter 6.

Some of the work in this thesis has been presented by the author and the supervisory team at international conferences. By the author: American Institute of Aeronautics and Astronautics (AIAA), Atlanta 2014. By C. J. Howls: Modern Applications of Complex Variables, Banff International Research Station (BIRS) 2015; joint British Mathematical Colloquium (BMC) & British Applied Mathematics Colloquium (BAMC), Cambridge 2015.

1.7 Thesis structure

Chapter 2 presents a review of acoustic analogies based on Lilley's equation. Starting with the analogy due to Tester & Morfey [29], a flow factor is calculated using a statistically isotropic point quadrupole (SIPQ). The aim is to determine approximately a lower frequency bound for ray solutions in order to appraise the applicability of ray solutions whilst also introducing the concept of a ring source. The second part of the chapter is devoted to a 3D Green's function calculation of Lilley's equation in the high-frequency limit using the WKB method to calculate the modes (Wundrow & Khavaran [116]).

Chapter 3 derives the 3D vector Green's function to the LEE that forms the basis of this thesis. Complex ray theory is introduce as a means of providing high-frequency asymptotic solutions to the LEE. In addition to obvious simplifications by the ray ansatz, other advantages of the ray solution are highlighted in the context of two-point pressure correlations.

Chapter 4 presents the solution to the multiplicity problem inherent in the nonlinear eikonal equation via an equivalent BVP. Three techniques are demonstrated whereby a derivative-based (Newtonian) and a derivative-free (GA) distinguish the two most efficient. Methods of continuation across caustics are also provided using either a LS-reduction method or a complex continuation. The latter proves a suitable replacement of the former, which often results in unwieldy analysis. The third technique, though not suitable for large scale engineering calculations, provides an elegant connection between winding number theory and ray theory.

Chapter 5 applies catastrophe theory to the caustic problem. Diffraction catastrophes are discussed and a computational method for mapping the ray field to the uniform field is proposed. These maps, based on work by Berry [38] and Hanyga [121], use codim. and corank detection supplied by the continuation methods of Chapter 4. Use of Dingle's [21] singulants to appraise the application of the uniform solutions is also shown.

Chapter 6 sees the ray solver applied to a parallel shear flow whose benchmark is provided by the modal solution developed in Chapter 2. The off-axis asymmetric solution provides a suitable demonstration of all the methods found in this thesis, with a variety of caustic and non-caustic structures present. To conclude we examine the novel feature of an anti-caustic using eucatastrophes. The simplest example is controlled by the Pearcey function on its line of symmetry: critically this is a Maxwell set of non-local bifurcations unlike local-bifurcations at caustics.

Chapter 7 determines the effect of caustics in the scenario of multiple points sources in parallel shear flow. Discrete sums and perturbed ring source models are considered.

Chapter 2

Lilley's acoustic analogy

This chapter focuses on derivatives of Lilley's acoustic analogy, namely those due to Tester & Morfey [29] and Wundrow & Khavaran [116]. The former is used to back-up the proposed high-frequency solutions providing an estimation of the high-frequency lower bound. It also serves to introduce the ring source model that has proved extremely popular in aeroacoustics due to both the analytic simplifications it engenders and the turbulence physics it reflects. The latter analogy provides the benchmark for the ray method derived in the remainder of this thesis. This analogy gives a first taste of high-frequency approximations and can be used to initiate considerations of the more subtle features of these approximations: the Stokes phenomenon.

2.1 Tester & Morfey Acoustic Analogy

The Tester & Morfey [29] acoustic analogy is used here as additional motivation for the use of high-frequency solutions. Their work is based on Lilley's shear flow analogy [13, 14] and was developed to explain two features that appeared in detailed noise measurements. These were an additional source term for hot jets at high speeds, and the effect of mean flow interaction on sound radiation from turbulence. Clearly, the latter is of most interest here and although there is some source coupling involved - which is not completely in accordance with the desired Green's function approach outlined in the previous chapter - this provides some background to the use of ring source models in jet noise as well as the first encounter with a flow factor in aeroacoustics.

The governing equation for pressure fluctuations, p', in a shear flow is Lilley's equation,

$$\mathscr{L}\, p' = \bar{c}^2 \bar{\rho}\, Q \tag{2.1}$$

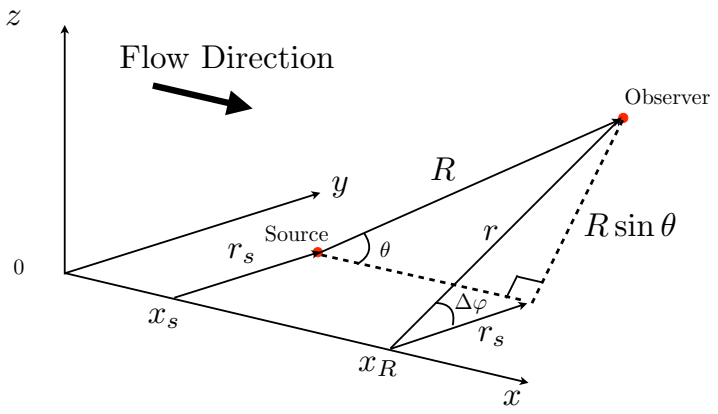

FIGURE 2.1: Cylindrical and spherical coordinate system for an observer/receiver position $\boldsymbol{x}_R$ based on the source position $\boldsymbol{x}_s$. The x-coordinate measures along the jet downstream axis.

where $\mathscr{L}$ is the time domain Lilley operator defined as,

$$\mathscr{L} \equiv \frac{\overline{D}}{Dt}\left(\frac{\overline{D}^2}{Dt^2} - \frac{\partial}{\partial x_j}\bar{c}^2\frac{\partial}{\partial x_j}\right) + 2\bar{c}^2\frac{\partial}{\partial x_j}\bar{u}_1\frac{\partial}{\partial x_j}\frac{\partial}{\partial x}, \quad j = 1, 2. \tag{2.2}$$

Here we have used a cylindrical polar coordinate system, defined by the triple $\{x, r, \Delta\varphi\}$ (with shorthand $x_2 = y$, $x_3 = z$) as shown in Fig. 2.1, to express the mean axial velocity and sound speed profiles as functions of $r = \sqrt{y^2 + z^2}$, i.e., $\bar{u}_1(r)$ and $\bar{c}(r)$. The normalised coordinate $\Delta\varphi = \varphi - \varphi_s$ allows the coordinate system to measure in the plane of the point source. In this section we can set $\varphi_s = 0$. The mean convective derivative is defined as $\overline{D}/Dt \equiv \partial/\partial t + \bar{u}_1\partial/\partial x$, while it is assumed that the medium behaves as a perfect gas, so that the mean pressure $\bar{p}$ (assumed as constant in this model) is related to the mean sound speed, density and static temperature profiles through $\bar{c}^2 = \gamma_a\bar{p}/\bar{\rho}$ and $\bar{p} = \bar{\rho}R_H\overline{T}$, where γ_a and R_H are the adiabatic and individual gas constants, respectively. The ambient values of these variable will always be denoted by subscript ∞, while source values are denoted by subscript s.

Before moving onto the source term Q, it is worthwhile making the coordinate system and its asymptotic properties concrete. Essentially there are two coordinate systems used in this thesis, both of which are spherical polar and represent the receiver $\boldsymbol{x}_R$: however, they differ in that one is based on the origin, while the other is based on the source point. In the far-field where the computations in this section will be made it can be shown that the two systems are asymptotically equivalent. Denoting the coordinate

system based at the origin by O, and letting $R \to \infty$,

$$\begin{aligned} \varphi &\sim \varphi_O + \frac{r_s}{R_O}\cos\theta_O \sin\Delta\varphi_O + \ldots, \\ \theta &\sim \theta_O + \frac{r_s}{R_O}\cos\theta_O(1-\cos\Delta\varphi_O) + \ldots, \\ R &\sim R_O + r_s \sin\theta_O(1-\cos\Delta\varphi_O) + \ldots \end{aligned} \tag{2.3}$$

The theoretical difference between the coordinate systems is also reflected in the numerical computations, i.e., that it is really immaterial to which is used at this stage. The main reason for highlighting these coordinate systems is for future work on ray theory, where it is expedient to base the coordinate system on the source for the purposes of near-to-farfield studies.

Returning to the Tester & Morfey model we use displacement source defined in [29] to model Q as,

$$Q = \frac{\overline{D}^3}{Dt^3}\left(\frac{1}{2}\frac{\partial^2 \xi_i' \xi_j'}{\partial x_i \partial x_j}\right), \quad i,j = 1,2,3. \tag{2.4}$$

where the quantities ξ_i' are the fluctuating displacements of a fluid particle relative to the basic flow. They are defined by,

$$\frac{\overline{D}}{Dt}\xi_i' - \frac{\partial \bar{u}_1}{\partial x_k}\xi_k' = u_i', \tag{2.5}$$

where u_i' is the fluctuating particle velocity.

In the above it is convenient to use the following notation for the quadrupole operator $M_{ij} = \partial^2/\partial x_i \partial x_j$, so that we may use the general result in Appendix A to write M_{ij} in cylindrical polar coordinates as,

$$M_{ij} = \begin{pmatrix} \frac{\partial^2}{\partial x^2} & \frac{1}{r}\frac{\partial^2}{\partial x \partial r}r & \frac{1}{r}\frac{\partial^2}{\partial x \partial \varphi} \\ \frac{1}{r}\frac{\partial^2}{\partial x \partial r}r & \frac{1}{r}\frac{\partial^2}{\partial r^2}r & \frac{1}{r^2}\frac{\partial^2}{\partial r \partial \varphi}r \\ \frac{1}{r}\frac{\partial^2}{\partial x \partial \varphi} & \frac{1}{r^2}\frac{\partial^2}{\partial r \partial \varphi}r & \frac{1}{r^2}\frac{\partial^2}{\partial \varphi^2} - \frac{1}{r}\frac{\partial}{\partial r} \end{pmatrix}, \tag{2.6}$$

giving,

$$Q = \overline{D}^3 S_{TM}/Dt^3, \quad S_{TM} = \frac{1}{2}M_{\alpha\beta}\xi_\alpha'\xi_\beta'. \tag{2.7}$$

2.1.1 Method of solution

The first step of the solution is to consider a time-harmonic field so the time dependence is proportional to $\mathrm{e}^{-\mathrm{i}\omega t}$, where ω is the frequency, and $k_0 = \omega/\bar{c}_\infty$ the characteristic wavenumber of the field. Here we shall drop the dash to denote a time-harmonic component. Furthermore, as is well known with the Lilley operator, a Fourier-transform

pair (denoted by $\tilde{}$) can be introduced in the axial coordinate x with wavenumber k_1,

$$\tilde{p} = \mathscr{F}_{k_1}\{p\} = \int_{-\infty}^{\infty} p\, \mathrm{e}^{\mathrm{i}k_1 x}\, \mathrm{d}x, \quad p = \mathscr{F}_x^{-1}\{\tilde{p}\} = \frac{1}{2\pi}\int_{-\infty}^{\infty} \tilde{p}\, \mathrm{e}^{-\mathrm{i}k_1 x}\, \mathrm{d}k_1. \tag{2.8}$$

This is then coupled with an azimuthal modal decomposition,

$$\tilde{p} = \frac{1}{2\pi}\sum_{n=-\infty}^{+\infty} \tilde{p}_n \mathrm{e}^{\mathrm{i}n\varphi}, \tag{2.9}$$

which exploits the periodicity of the φ coordinate.

Under this transformation the Lilley equation reduces to an ordinary differential equation in r that has the general form for function $\tilde{p}_n$,

$$\mathscr{Q}_{(r;k_0,n,\kappa,\Phi)}\tilde{p}_n = \mathscr{Z}, \tag{2.10}$$

where the operator,

$$\mathscr{Q}_{(r;k_0,n,\kappa,\Phi)} \equiv \frac{\Phi^2}{r}\frac{\mathrm{d}}{\mathrm{d}r}\left(\frac{r}{\Phi^2}\frac{\mathrm{d}}{\mathrm{d}r}\right) + \left[k_0^2(\Phi^2-\kappa^2) - \frac{n^2}{r^2}\right], \tag{2.11}$$

with,

$$\kappa \equiv k_1/k_0, \quad \Phi \equiv (1+\kappa M(r))/a(r), \quad M(r) = \bar{u}_1(r)/\bar{c}_\infty, \quad a(r) = \bar{c}(r)/\bar{c}_\infty. \tag{2.12}$$

The Fourier-transformed source term $\widetilde{S}_{TM}$ is given by,

$$\widetilde{S}_{TM} = \widetilde{M}_{\alpha\beta}\widetilde{B}_{\alpha\beta}, \quad \alpha,\beta = 1,2,3. \tag{2.13}$$

where,

$$\widetilde{M}_{ij} = \begin{pmatrix} -k_1^2 & -\frac{\mathrm{i}k_1}{r}\frac{\mathrm{d}}{\mathrm{d}r}r & k_1\frac{n}{r} \\ -\frac{\mathrm{i}k_1}{r}\frac{\mathrm{d}}{\mathrm{d}r}r & \frac{1}{r}\frac{\mathrm{d}^2}{\mathrm{d}r^2}r & \frac{\mathrm{i}n}{r^2}\frac{\mathrm{d}}{\mathrm{d}r}r \\ k_1\frac{n}{r} & \frac{\mathrm{i}n}{r^2}\frac{\mathrm{d}}{\mathrm{d}r}r & -\frac{n^2}{r^2} - \frac{1}{r}\frac{\mathrm{d}}{\mathrm{d}r} \end{pmatrix}, \quad k_0^{-2}\widetilde{M}_{ij}^\dagger = \begin{pmatrix} -\kappa^2 & \mathrm{i}\kappa\frac{\mathrm{d}}{\mathrm{d}\bar{r}} & \kappa\frac{n}{\bar{r}} \\ \mathrm{i}\kappa\frac{\mathrm{d}}{\mathrm{d}\bar{r}} & \frac{\mathrm{d}^2}{\mathrm{d}\bar{r}^2} & -\mathrm{i}n\frac{\mathrm{d}}{\mathrm{d}\bar{r}}\frac{1}{\bar{r}} \\ \kappa\frac{n}{\bar{r}} & -\mathrm{i}n\frac{\mathrm{d}}{\mathrm{d}\bar{r}}\frac{1}{\bar{r}} & -\frac{n^2}{\bar{r}^2} + \frac{1}{\bar{r}}\frac{\mathrm{d}}{\mathrm{d}\bar{r}} \end{pmatrix} \tag{2.14}$$

so that $\tilde{p}$ can be solved as,

$$\tilde{p}_n(\bar{r}) = k_0^{-2}\int_0^\infty \widetilde{B}_{\alpha\beta}(\bar{r}_s)\widetilde{M}^\dagger_{\alpha\beta}(\bar{r}_s)\widetilde{G}_n(\bar{r}|\bar{r}_s)\,\bar{r}_s\,\mathrm{d}\bar{r}_s, \tag{2.15}$$

where $\widetilde{M}_{ij}^\dagger$ is the adjoint of $\widetilde{M}_{ij}$, and a radial Green's function $\widetilde{G}_n$ which satisfies,

$$k_0^{-2}\mathscr{Q}_{(\bar{r};k_0,n,\kappa,\Phi)}\widetilde{G}_n = -\bar{\rho}_s a_s^2\omega^2\Phi_s^2\frac{\delta(\bar{r}-\bar{r}_s)}{\bar{r}_s}. \tag{2.16}$$

The radial Green's function can be written down in theory (see for e.g., Duffy [133]) as

$$\tilde{G}_n(\bar{r}|\bar{r}_s) = \begin{cases} \bar{\rho}_s a_s^2 \omega^2 \Phi_s^2 \frac{\overline{w}_1(\bar{r})\overline{w}_2(\bar{r}_s)}{\bar{r}_s \overline{\mathscr{W}}(\bar{r}_s|\kappa)}, & \bar{r} > \bar{r}_s, \\ \bar{\rho}_s a_s^2 \omega^2 \Phi_s^2 \frac{\overline{w}_1(\bar{r}_s)\overline{w}_2(\bar{r})}{\bar{r}_s \overline{\mathscr{W}}(\bar{r}_s|\kappa)}, & \bar{r} < \bar{r}_s, \end{cases} \tag{2.17}$$

where $\overline{w}_i$ are homogeneous solutions satisfying,

$$k_0^{-2} \mathscr{Q}_{(\bar{r};k_0,n,\kappa,\Phi)} \overline{w}_i = 0, \quad i = 1, 2., \tag{2.18}$$

and $\overline{\mathscr{W}}(\bar{r}_s|\kappa)$ is the Wronskian of these two solutions (which is independent of both $\bar{r}$ and $\bar{r}_s$, see [29]). Given that solutions will be obtained in the far-field, we need only consider the $\bar{r} > \bar{r}_s$ solution of (2.18).

In general there is no closed form solution to (2.18) so a numerical scheme is typically employed which is valid for all wavenumbers. This can be posed as a boundary value problem if one takes the limits $\bar{r} \to 0$ and ∞ as the boundaries of the differential equation. The determination of the values of the ode at the boundary are determined by applying the bounded condition at the origin, and outward propagation condition at infinity.

The most convenient form for numerical integration is a system of first order equations,

$$\frac{\mathrm{d}}{\mathrm{d}\bar{r}} \overline{w}_{i,1} = -\frac{\bar{r}}{\bar{\rho} a^2 \omega^2 \Phi^2} \overline{w}_{i,0}, \tag{2.19}$$

$$\frac{\mathrm{d}}{\mathrm{d}\bar{r}} \overline{w}_{i,0} = \frac{\bar{\rho} a^2 \omega^2 \Phi^2}{\bar{r}} \overline{w}_{i,1}, \tag{2.20}$$

with initial conditions (subs. J denotes jet centerline values),

$$\overline{w}_{1,0} = H_n^{(1)}(\sqrt{1-\kappa^2}\bar{r}), \quad \overline{w}_{1,1} = -(\bar{r}/\bar{\rho} a^2 \omega^2 \Phi^2) \mathrm{d}H_n^{(1)}(\sqrt{1-\kappa^2}\bar{r})/\mathrm{d}\bar{r}, \quad \bar{r} \gg 1, \tag{2.21}$$

$$\overline{w}_{2,0} = J_n(\sqrt{\Phi_J^2 - \kappa^2}\bar{r}), \quad \overline{w}_{2,1} = (\bar{r}/\bar{\rho} a^2 \omega^2 \Phi^2) \mathrm{d}J_n(\sqrt{\Phi_J^2 - \kappa^2}\bar{r})/\mathrm{d}\bar{r}, \quad \bar{r} \ll 1, \tag{2.22}$$

The desired solutions can then be found from $\overline{w}_1 = \overline{w}_{1,0}$ and $\overline{w}_2 = \overline{w}_{2,0}$. In the far-field it is acceptable for $\overline{w}_1$ to be replaced by $H_n^{(1)}$, however for the purposes of the Wronksian $\overline{w}_1$ must still be evaluated at $\bar{r}_s$ using the numerical scheme.

The solution to (2.18) can be written in principle as,

$$\widetilde{G}_n(\bar{r}|\bar{r}_s) = -\frac{1}{2} \mathrm{i}\pi \omega^2 \bar{\rho}_\infty C_n(\bar{r}_s) H_n^{(1)}(\sqrt{1-\kappa^2}\bar{r}), \tag{2.23}$$

where,

$$C_n(\bar{r}) = \mathrm{i}\overline{w}_2(\bar{r}) \left(2\bar{\rho} a^2 \Phi^2 / \bar{\rho}_\infty\right) / \pi \bar{r} \overline{\mathscr{W}}. \tag{2.24}$$

The far-field nature of the solution allows the Fourier transform in k_1 to be inverted asymptotically using the method of stationary-phase (see for e.g., Bleistein [134] and Erdélyi [135]) as $R \to \infty$. This is facilitate by large argument asymptotics of the Hankel function,

$$H_n^{(1)}(\sqrt{1-\kappa^2}\bar{r}) \sim (2/\pi\sqrt{1-\kappa^2}\bar{r})^{1/2}\mathrm{e}^{\mathrm{i}(\sqrt{1-\kappa^2}\bar{r}-0.5n\pi-0.25\pi)}, \tag{2.25}$$

giving,

$$p = \mathscr{F}_x^{-1}\{\tilde{p}\} = \frac{1}{2\pi}\sqrt{\frac{2\pi k_0 \sin^3\theta}{R}}\mathrm{e}^{\mathrm{i}k_0 R\cos^2\theta}\tilde{p}(\kappa_\star), \tag{2.26}$$

where $\kappa_\star = -\cos\theta$ (see for e.g., Kewin [136]) is the stationary point found once spherical polar coordinates (see Fig. 2.1) are introduced. The time-harmonic pressure is now given by,

$$\frac{p(R,\theta,\varphi)}{\bar{\rho}_\infty \bar{c}_\infty^2} \sim -k_0^2\frac{\mathrm{e}^{\mathrm{i}k_0 R}}{4\pi R}\sum_{n=-\infty}^{\infty}\mathrm{e}^{\mathrm{i}n(\varphi-\frac{\pi}{2})}\int_0^\infty \widetilde{B}_{\alpha\beta}(\bar{r}_s)\widetilde{M}^\dagger_{\alpha\beta}(\bar{r}_s)C_{n\alpha\beta}(\bar{r}_s)\bar{r}_s\,\mathrm{d}\bar{r}_s, \tag{2.27}$$

using the stationary point $\kappa_\star = -\cos\theta$ and leaving the Hankel function in its large argument form. The coefficients $C_{n\alpha\beta}$ are in terms of C_n,

$$C_{nxx} = -\cos^2\theta\, C_n, \tag{2.28}$$

$$C_{nxr} = -\mathrm{i}\cos\theta\,\mathrm{d}C_n/\mathrm{d}\bar{r}, \tag{2.29}$$

$$C_{nrr} = \mathrm{d}^2C_n/\mathrm{d}\bar{r}^2, \tag{2.30}$$

$$C_{nx\varphi} = -\cos\theta(n/\bar{r})C_n, \tag{2.31}$$

$$C_{nr\varphi} = -\mathrm{i}n\left[(1/\bar{r})\mathrm{d}C_n/\mathrm{d}\bar{r} - C_n/\bar{r}^2\right], \tag{2.32}$$

$$C_{n\varphi\varphi} = \left[(1/\bar{r})\mathrm{d}C_n/\mathrm{d}\bar{r} - (n^2/\bar{r}^2)C_n\right], \tag{2.33}$$

where it can be shown that the radial derivatives can be evaluated using,

$$\mathrm{d}C_n/\mathrm{d}\bar{r} = (1/\bar{w}_2)(\mathrm{d}\bar{w}_2/\mathrm{d}\bar{r})C_n, \tag{2.34}$$

$$\mathrm{d}^2C_n/\mathrm{d}\bar{r}^2 = -\left(\kappa^2 - n^2/\bar{r}^2\right)C_n + (\bar{r}/\bar{\rho}a^2\Phi^2)\left[\mathrm{d}(\bar{\rho}a^2\Phi^2/\bar{r})/\mathrm{d}\bar{r}\right](\mathrm{d}C_n/\mathrm{d}\bar{r}). \tag{2.35}$$

The stationary phase evaluation introduces two subtleties that have physical implications. Firstly, (2.27) is independent of x, and secondly $\kappa_\star = -\cos\theta$ is the dispersion relation of monopole source in a quiescent medium. The first is to be expected since the medium is invariant along the x-axis. The second means that the source and propagation have become highly localised at the origin when viewed by the observer in the far-field. Asymptotically, this sifts out the dominant wavenumbers as those propagating with a wavefront normal parallel to the line between source and observer.

2.1.2 Source model

For the purposes of investigating flow effects it is expedient to use a simplified model to simulate the jet turbulence. In order to do this a statistically isotropic quadrupole (SIPQ) model is introduced that has an omnidirectional directivity in the absence of flow. The first aspect of the model is that the source distribution is concentrated at a radial point (a ring source), i.e.,

$$\widetilde{B}_{\alpha\beta}(k_1, n, \omega; r) \rightarrow \widetilde{B}_{\alpha\beta}(k_1, n, \omega)\delta(r - r_s)/r_s, \tag{2.36}$$

It can be seen from (2.36) that the term point quadrupole refers to the source being concentrated at a radial point, i.e., a ring and not a 3D point. At this point developing a flow-factor is difficult because of the necessity of modelling $\widetilde{B}_{\alpha\beta}(k_1, n, \omega)$. Motivated by the fact that one can make modelling assumptions about the statistics of 4^{th}-order correlation tensors (see Chap. 1 & Goldstein [9] for details), the mean square pressure in the frequency domain is formed:

$$\begin{aligned}\frac{16\pi^2 R^2}{k_0^8}\frac{p(R,\varphi;\omega)p^*(R,\varphi;\omega)}{\bar{\rho}_\infty^2\bar{c}_\infty^4} = \sum_{n=-\infty}^{\infty}\sum_{m=-\infty}^{\infty} p_n p_m^* \exp(\mathrm{i}(n-m)\varphi) = \\ \sum_{n=-\infty}^{\infty}\sum_{m=-\infty}^{\infty} \widetilde{B}_{\alpha\beta}(r_s; k_1, n, \omega)\widetilde{B}^*_{\alpha\beta}(r_s; k_1, m, \omega)C_{n\alpha\beta}(r_s)C^*_{m\delta\gamma}(r_s)\exp(\mathrm{i}(n-m)\varphi),\end{aligned} \tag{2.37}$$

The double sum decouples if the coherence between the azimuthal modes is negligible, i.e.,

$$\widetilde{B}_{\alpha\beta}(\ldots, n)\widetilde{B}^*_{\alpha\beta}(\ldots, m) = \widetilde{B}_{\alpha\beta}(\ldots, n)\widetilde{B}^*_{\alpha\beta}(\ldots, n)\delta_{nm}. \tag{2.38}$$

The spectral density can then be found by using the expected value operator E and allowing the sample time T_s to tend to infinity,

$$\frac{16\pi^2 R^2}{k_0^8\bar{\rho}_\infty^2\bar{c}_\infty^4}\lim_{T_s\rightarrow\infty} E\left[p(R,\varphi;\omega)p^*(R,\varphi;\omega)\right] = \sum_{n=-\infty}^{\infty}\lim_{T_s\rightarrow\infty} E\left[\widetilde{B}_{\alpha\beta}\widetilde{B}_{\delta\gamma}/2T_s\right] C_{n\alpha\beta}(\bar{r}_s)C^*_{n\delta\gamma}(\bar{r}_s). \tag{2.39}$$

Now if the source excitation is assumed to be statistically isotropic so that it can presented as an isotropic tensor then,

$$\lim_{T\rightarrow\infty} E\left[\widetilde{B}_{\alpha\beta}\widetilde{B}_{\delta\gamma}/2T\right] = \left(b_1\delta_{\alpha\beta}\delta_{\delta\gamma} + b_2\delta_{\alpha\delta}\delta_{\beta\gamma} + b_3\delta_{\alpha\gamma}\delta_{\beta\delta}\right). \tag{2.40}$$

The coefficients b_i can be evaluated using the assumption that $\lim_{T\rightarrow\infty} E\left[\widetilde{B}_{\alpha\beta}\widetilde{B}_{\delta\gamma}/2T\right]$ is the same for all pairings of $\alpha\beta$ and $\delta\gamma$ that contain the same numbers and that

coherence between different quadrupole sources is zero, i.e.,

$$\lim_{T\to\infty} E\left[\widetilde{B}_{ab}\tilde{B}_{ab}/2T\right] = \lim_{T\to\infty} E\left[\widetilde{B}_{ab}\widetilde{B}_{ba}/2T\right] = H(k_1, n; \omega), \tag{2.41}$$

and

$$\lim_{T\to\infty} E\left[\tilde{B}_{aa}\tilde{B}_{bb}/2T\right] = 0, \tag{2.42}$$

where $H(k_1, n; \omega)$ is the squared magnitude of the cross-power spectral density of each and every quadrupole strength integrated over the source volume. Using (2.41) and (2.42) the coefficients b_i are determined to be,

$$b_2 + b_3 = H(k_1, n; \omega), \tag{2.43}$$

$$b_1 = 0. \tag{2.44}$$

which arbitrarily choosing $b_2 = b_3 = H(k_1, n; \omega)/2$ leads to the following,

$$\frac{16\pi^2 R^2}{k_0^8 \bar{\rho}_\infty^2 \bar{c}_\infty^4} |p(R, \varphi; \omega)|^2 = \sum_{n=-\infty}^{\infty} H(k_1, n; \omega) C_{n\alpha\beta}(\bar{r}_s) C^*_{n\alpha\beta}(\bar{r}_s). \tag{2.45}$$

Any computation of (2.45) still requires some modelling of $H(k_1, n; \omega)$. However, if one assumes that $H(k_1, n; \omega) \to H(k_1; \omega)$ is the same for all modes the following source independent fraction can be formed,

$$\frac{16\pi^2 R^2}{k_0^8 \bar{\rho}_\infty^2 \bar{c}_\infty^4} \frac{|p(R, \varphi; \omega)|^2}{H(k_1; \omega)} = \sum_{n=-\infty}^{\infty} C_{n\alpha\beta}(\bar{r}_s) C^*_{n\alpha\beta}(\bar{r}_s) = F_{ff}(\omega). \tag{2.46}$$

Equation (2.46) thus defines a flow-factor measuring the changes in the radiated pressure spectrum due to the presence of a flow. It can be shown that in a homogeneous medium the flow-factor is trivially $F_{ff}(\omega) = 1$.

2.1.3 High and low-frequency asymptotes

The high-frequency solution developed by [29] is based on the Blokhintsev conservation principle (see for e.g., Pierce [64]). In terms of high-frequency propagation the Blokhintsev invariant is a well-known device for calculating the amplitude of ray solutions. The high-frequency solution derived here is notable for the simple reason that it approximates the shear flow by a plug flow, i.e., a constant flow with velocity M_s joined in a piecewise manner with the ambient quescient medium. This leads to the aggregate CoS definition mentioned in Chap. (1).

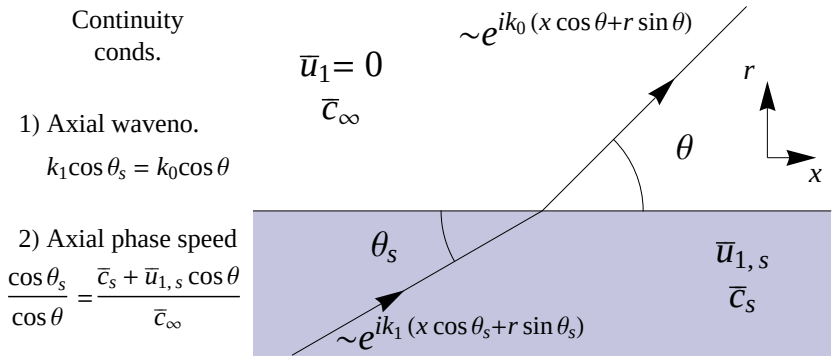

FIGURE 2.2: Snell's law for a plug flow with velocity $M(r_s) = \bar{u}_{1,s}/\bar{c}_\infty$. Continuity conditions between the ingoing wave $\mathrm{e}^{\mathrm{i}k_1(x\cos\theta_s + r\sin\theta_s)}$. and the outgoing wave $\mathrm{e}^{\mathrm{i}k_0(x\cos\theta_\infty + r\sin\theta_\infty)}$, lead to the relations in the main text.

The derivation begins from a zero-flow result relating the power spectrum $|\tilde{p}(R,\varphi;\omega)|^2$ to the quadrupole cross-spectrum in the far-field for a stationary medium,

$$R^2|\tilde{p}(R,\varphi;\omega)|^2 \propto \bar{\rho}_s^2 H(k_1;\omega), \tag{2.47}$$

which can be generalised to cover a uniform flow in the axial direction by using a Doppler shift Φ_s,

$$R^2|\tilde{p}(R,\varphi;\omega)|^2 \propto \bar{\rho}_s^2 a_s^6 \Phi_s^6 H(k_1;\omega), \tag{2.48}$$

where the R^2 factor normalises the spherical spreading and Doppler factors are arrived at from a change of coordinate system in the definition of $H(k_1;\omega)$. In order to form the flow-factor some modelling assumptions must be made about the form of the quadrupole spectrum. We use the same approximation made in [29] that the cross-power spectrum scales according to the following,

$$H(k_1;\omega) \propto |\mathbf{k}|^4. \tag{2.49}$$

Then near the source the following scaling holds,

$$R^2|\tilde{p}(R,\varphi;\omega)|^2 \propto \bar{\rho}_s^2 \bar{c}_s^{-4} a_s^{10} \Phi_s^{10}. \tag{2.50}$$

The azimuthal averages, denoted by $<>_\varphi$, of the power spectrum at the source and in the far-field are related by Blokhintsev's energy conservation law. The energy propagating into the conic sector $(\theta_s, \theta_s + \mathrm{d}\theta_s)$ near the source is conserved and propagates into the conic sector $(\theta, \theta + \mathrm{d}\theta)$ where the angles are related via,

$$\cos\theta = \Phi_s \cos\theta_s, \tag{2.51}$$

which is Snell's law for propagation between a stationary medium and one in uniform motion (Morse & Ingard [137]), and is a simple transposition of the phase speed match shown in Fig. 2.2. The reader should note that it is both the plug flow nature and high-frequency regime that allows us to utilise Snell's law - which then admits plane wave solutions.

The Snell's law solution can then be used in tandem with the power radiated through the differential element of the conic sector,

$$< R^2|\tilde{p}(R,\varphi;\omega)|^2 >_\varphi (1/\bar{\rho}_\infty \bar{c}_\infty)\mathrm{d}(\cos\theta) =< R^2|\tilde{p}(R,\varphi;\omega)|^2 >_{\varphi,s} (1/\bar{\rho}_s \bar{c}_\infty)\bar{a}_s^{-3}\Phi_s^{-2}\mathrm{d}(\cos\theta_s). \tag{2.52}$$

to give a relation between the sound power inside and outside of the flow,

$$< R^2|\tilde{p}(R,\varphi;\omega)|^2 >_\varphi / < R^2|\tilde{p}(R,\varphi;\omega)|^2 >_{\varphi,s} = \bar{\rho}_\infty/(\bar{\rho}_s a_s^4 \Phi_s^4). \tag{2.53}$$

Finally it can be deduced that the flow-factor is given by,

$$F_{ff} = (\bar{\rho}_s/\bar{\rho}_\infty)(\bar{c}_s/\bar{c}_\infty)a_s^6\Phi_s^6, \tag{2.54}$$

which is independent of k_0 in the $k_0 \to \infty$ limit. Equation (2.54) is strictly only true for angles outside the cone of silence. This way the average power spectrum only needs to normalised by the spherical spreading term R^2. Inside the cone of silence an exponential decay would need to computed. The cone of silence here *is* defined as a conic angle for which,

$$\kappa^2 = \Phi^2 - \cos^2\theta, \tag{2.55}$$

which can be solved for $\cos\theta$ as the root of a polynomial to give,

$$-1/(a_s - M_s) < \cos\theta_{CoS} < 1/(a_s + M_s). \tag{2.56}$$

The larger of these two roots then gives the CoS angle as $\cos\theta_{CoS} = 1/(a_s + M_s)$. This is similar to the definition of θ_{CoS} in Chap. 1, though that particular condition takes into account an eddy convection speed equal to 0.71 of the primary jet velocity.

The reason the cone of silence here is delimited by a constant θ, i.e., not a function of φ, is because of the ring-source's symmetrical properties. Additionally, it may not be apparent why (2.55) determines the cone of silence for a ring-source, but it turns out this is a simple turning-point criterion for an azimuthal mode. At this stage we have only solved the modes using quadrature and therefore not encountered turning-points.

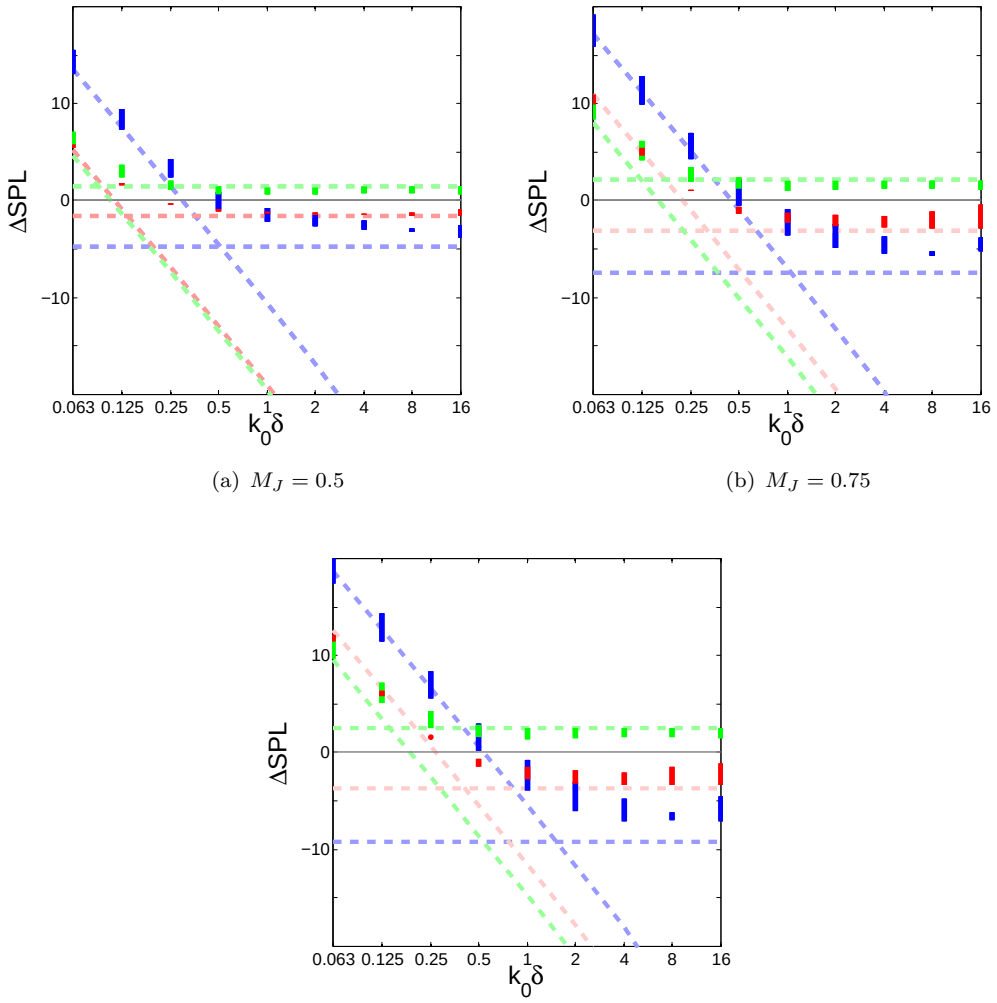

(a) $M_J = 0.5$

(b) $M_J = 0.75$

(c) $M_J = 0.9$

FIGURE 2.3: Isothermal Flow Factors $TR = 1.0$, for $M_J = 0.5, 0.75$ and 0.9. Solid lines, exact SIPQ; diagonal dashed, low frequency asymptote; horizontal dashed, high frequency asymptote. Blue, $\theta = 65°$; red, $\theta = 80°$; green $\theta = 100°$. Values of $k_0 r_s$ specified in main text.

2.1.3.1 Low frequency asymptote

The low frequency asymptote is given as,

$$F_{ff}(\omega) = 2\left(\frac{\sin 2\theta(1 - M_s\cos\theta)}{1 + (1 - M_J\cos\theta)^2}\frac{1}{k_0\delta}\left.\frac{\mathrm{d}M}{d\chi}\right|_s\right)^2. \tag{2.57}$$

The notable difference between this asymptote and that given by (2.54) is that (2.57) is an explicit function of frequency. The high-frequency solution makes an explicit statement about the form in which the frequency appears: this will be evident in the next chapter.

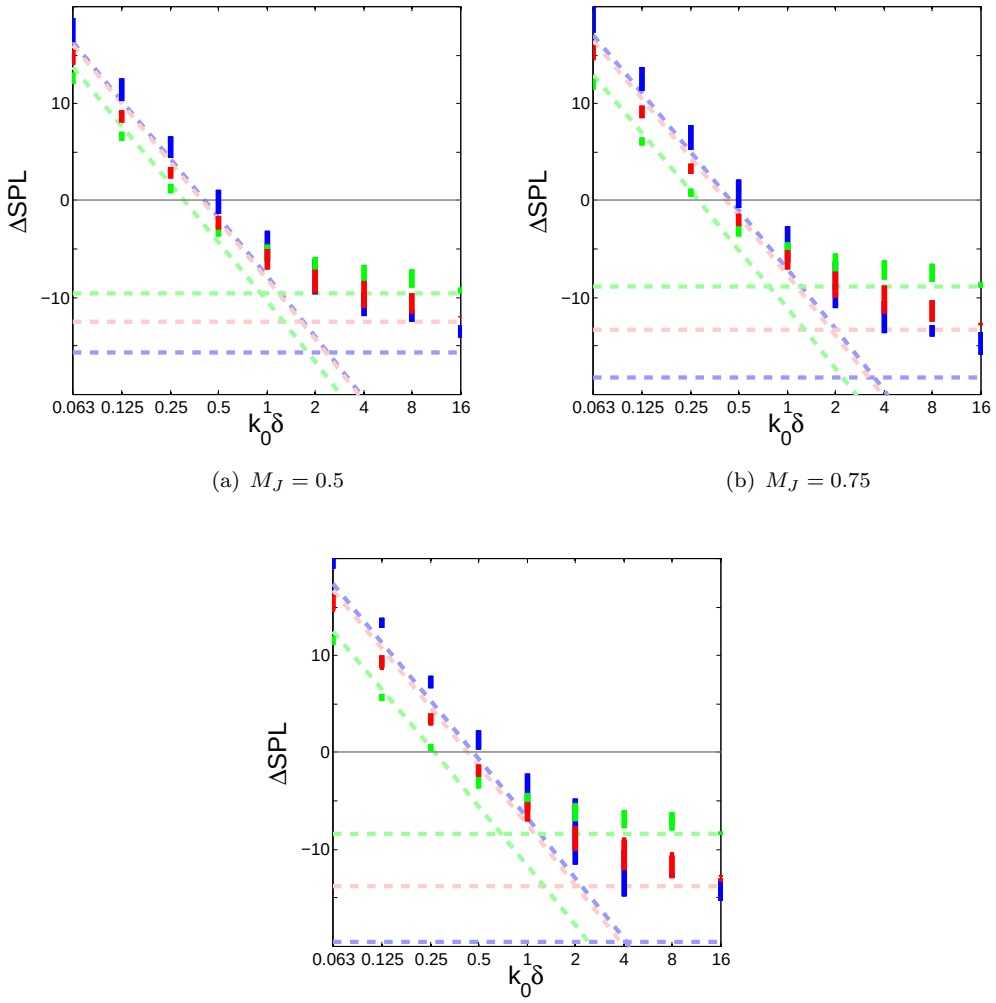

(a) $M_J = 0.5$

(b) $M_J = 0.75$

(c) $M_J = 0.9$

FIGURE 2.4: Heated flow factors $TR = 3$, for $M_J = 0.5, 0.75$ and 0.9. Key the same as Fig. 2.3.

2.1.4 Numerical results

Numerical calculations of the flow-factor using (2.46) are compared with the low and high-frequency asymptotes using (2.57) and (2.54), respectively. The flow and temperature profiles are given by,

$$\begin{aligned} \overline{u}_1(r)/\overline{u}_{1,J} &= \frac{1}{2}\left(1 - \mathrm{erf}(\sqrt{\pi}\chi)\right), \\ \overline{T}(r)/T_s &= 1 + (\overline{T}_J/\overline{T}_s - 1)\overline{u}_1(r)/\overline{u}_{1,J}, \\ \chi &= (r - r_s)/\delta_{\mathrm{sh}} - 0.168, \end{aligned} \tag{2.58}$$

where for parallel shear flows the temperature profile can always be deduced from the velocity profile according to the Crocco-Busemann relation (Schlichting & Gersten [138]),

$$\frac{\overline{T}_{tot}(r) - \overline{T}_\infty}{\overline{T}_{tot,J} - \overline{T}_\infty} = \frac{\overline{u}_1(r)}{\overline{u}_{1,J}} \tag{2.59}$$

where $\overline{T}_{tot}$ is the mean field total temperature defined by $\overline{T}_{tot} = \overline{T}\left(1 + \frac{\gamma_a - 1}{2} M^2\right)$.

The isothermal case $TR = 1.0$ where $TR = \overline{T}/\overline{T}_\infty$ is shown in Fig. 2.3 for centerline Mach numbers of $M_J = 0.5$, 0.75 and 0.9, with $\theta = 65°$, 80° and 100° for each Mach number. The heated case $TR = 3.0$ is shown in Fig. 2.4 with the same M_J and θ. It should be noted that the values of θ mean that $\theta > \theta_C$ for all flow configurations used. The flow-factor is calculated as a function of $k_0\delta_{\text{sh}}$ and $k_0 r_s$, i.e., the Helmholtz numbers for the shear layer and source position, respectively. For each shear layer width the algorithm will calculate the following $k_0 r_s$ values: $k_0 r_s \in \{0.125, 0.25, 0.5, 1, 2, 4, 8, 16\}$.

It is clear from Figs. 2.3 and 2.4 that together the low and high-frequency asymptotes capture the shape of the analytic flow-factor well. It is also clear that the high-frequency limit is approached rapidly and this is best for angles furthest away from the cone of silence. The main reason for this disparity is the divergence of the ray solution away from the true field near the cone of silence caustic. The values of $k_0\delta$ for which the high-frequency asymptote matches well depends on the Mach number and temperature, meaning a constant value of Strouhal number St_{sh}, based on the shear layer thickness, cannot be reached. However, the agreement of the high-frequency asymptote at low $k_0\delta$ is encouraging and an estimate of St_δ are $St_\delta = \pi^{-1}$ for the heated case and $S_\delta = 0.25\pi^{-1}$ for the isothermal case, indicate the possible success of future ray calculations. This success should be carried over to more general flows since the shear layer scales with jet diameter, D_s, implying that a Strouhal number based on this lengthscale is $St_{D_s} = O(S_\delta)$ if $D_s/\delta_{\text{sh}} = O(1)$, and that flow-factors as a function of St_{D_s} would be similarly matched well with a high-frequency asymptotic solution.

To conclude these results it is worth pointing out a subtle feature, shown by the majority of the figures, that is easy to miss. This pertains to the variation of the exact result with $k_0 r_s$. It can be seen that in general there is little variation, but when there is, it is mostly concentrated toward larger $k_0 r_s$. One plausible explanation to this is that as the source Helmholtz number increases, the scale on a wavelength is slower and there is more time in propagation terms for waves to be diffracted; in other words, lower frequencies see the flow as less of a diffracting object than high-frequency rays.

2.1.5 Critique of the Tester & Morfey analogy

The inclusion of Tester & Morfey's work, though not the current state of the art, has been for several reasons. The first is for reasons of continuity: it is a natural place to start for investigating solutions of Lilley's equation taking into account the theory briefly touched upon in Chap. 1. Secondly, this work reinforces some of the conclusions reached in Chap. 1 concerning the requirements of a 3D ray solver. The most notable being that the utility of a ray solver is greatly enhanced if any source modelling is absent or readily generalisable. The use of a ring source is evidence of this: great simplifications were necessary to reach a solution whose calculation was bearable.

The final note on this work again concerns the ring source. It is readily seen that this model engenders great simplifications: however, these are not without justification. The ring source reflects a simplified understanding of turbulence physics in round jets. This makes it ideal for generalisations and a platform for work in the final technical chapter of this thesis.

2.2 Wundrow & Khavaran's Modal Solution

The Tester and Morfey acoustic analogy as a basis for further work in this thesis remains unsatisfactory for two reasons: the Green's function is coupled with a source term; and the Green's function is not fully three-dimensional. In this section a 3D Green's function is calculated using the same Lilley propagator. This is in-keeping with the aims of this thesis set out in chapter 1 and serves as a benchmark for the 3D ray solver developed in subsequent chapters.

The equation to be solved is simpler in principle than (2.1) as it requires no source modelling, it does however require more apparatus to solve given its 3D nature. Two Green's functions are defined for reasons that will become apparent in later chapters. The first is defined as,

$$\mathscr{L}_\omega G_\omega = \overline{D}_\omega \overline{c}_\infty^2 \delta(\boldsymbol{x} - \boldsymbol{x}_s), \tag{2.60}$$

and the second defined by,

$$\mathscr{L}_\omega \mathbb{G}_\omega = \overline{c}_\infty^2 \delta(\boldsymbol{x} - \boldsymbol{x}_s), \tag{2.61}$$

where $\mathscr{L}_\omega$ is the frequency domain Lilley operator with $\overline{D}/Dt \to \overline{D}_\omega \equiv (-\mathrm{i}\omega + \bar{u}_1 \partial/\partial x)$.

The difference in definition between (2.60) and (2.61) does not present any additional difficulties as the two are related via,

$$G_\omega(\boldsymbol{x}|\boldsymbol{x}_s) = -\left(\mathrm{i}\omega + \overline{u}_s\frac{\partial}{\partial x_s}\right)\mathbb{G}_\omega. \tag{2.62}$$

The method of solution to this equation is very similar to that used in the previous section, whilst it is virtually the same as that shown in Goldstein [9] differing in the solution of the Fourier coefficients. In light of previous results the Green's function is expressed in terms of a Fourier series and Fourier transform:

$$G_\omega(\boldsymbol{x}|\boldsymbol{x}_s) = \frac{1}{4\pi^2}\sum_{n=-\infty}^{\infty}\mathrm{e}^{\mathrm{i}n\Delta\varphi}\int_{-\infty}^{\infty}G_n(r|r_s;\omega,k_1)\mathrm{e}^{-\mathrm{i}k_1(x-x_s)}\,\mathrm{d}k_1. \tag{2.63}$$

where $\Delta\varphi = \varphi - \varphi_s$ is measure of the asymmetry of the field w.r.t. the source azimuthal source position. In terms of (2.10) the Fourier coefficients satisfy,

$$\mathscr{Q}_{(r;k_0,n,\kappa,\Phi)}G_n = -\frac{\delta(r-r_s)}{r_s a_s^2}, \tag{2.64}$$

and are related to the Green's function $\widetilde{G}_n$ of (2.16) via $\widetilde{G}_n(\bar{r}|\bar{r}_s) = \bar{\rho}_s a_s^4\omega^2\Phi_s^2k_0^2G(r|r_s)$. Again the solution can be written down as,

$$G_n(r|r_s;\omega,k_1) = \begin{cases}\frac{w_1(r|\kappa)w_2(r_s|\kappa)}{r_s a_s^2\mathscr{W}(r_s|\kappa)}, & r > r_s,\\ \frac{w_1(r_s|\kappa)w_2(r|\kappa)}{r_s a_s^2\mathscr{W}(r_s|\kappa)}, & r < r_s,\end{cases} \tag{2.65}$$

where $\mathscr{Q}_{(r;k_0,n,\kappa,\Phi)}w_j = 0$, with boundary conditions,

$$w_1 \sim r^{-1/2}\mathrm{e}^{\mathrm{i}k_0\sqrt{1-\kappa^2}r}, \quad r\to\infty, \tag{2.66}$$

$$w_2 \sim r^{|n|} \quad r\to 0. \tag{2.67}$$

In the last section the propagation conditions given were the same, but required little thought process once they had been applied. In this section, although the same conditions apply, it should be noted that propagation and extinction conditions are applied at infinity thus allowing for multiple reflections to occur *before* propagation to the far-field and changes from exponentially growing to exponentially decaying behaviour as waves propagate. We highlight this fact now since this is pertinent to any solutions that have a ray-type ansatz.

The inverse Fourier transform (2.63) can be evaluated following the stationary phase method as in (2.25) and (2.26). The stationary point is exactly the same up to $O(R^{-1})$,

i.e., $\kappa^\star = -\cos\theta$. Thus we have the following expression for G_ω:

$$G_\omega(\boldsymbol{x}|\boldsymbol{x}_s) = \frac{1}{4\pi^2}\sum_{-\infty}^{+\infty} \mathrm{e}^{\mathrm{i}n\Delta\varphi} \int_{-\infty}^{\infty} G_n(r|r_s;\omega,k_1)\mathrm{e}^{-\mathrm{i}k_1(x-x_s)}\,\mathrm{d}k_1$$
$$\sim \left(\frac{2\pi k_0 \sin^2\theta}{\mathrm{i}R}\right)^{1/2} \frac{w_1(r|-\cos\theta)w_2(r_s|-\cos\theta)}{r_s a_s^2 \mathscr{W}(r_s|-\cos\theta)} \mathrm{e}^{\mathrm{i}k_0 R\cos^2\theta}. \tag{2.68}$$

2.2.1 WKB solution

In general (2.64) must be solved numerically as was the case with Eq. (2.18). However, the high-frequency regime can be exploited by seeking WKB solutions to (2.64) (see for e.g., Olver [139], Bender & Orszag [58], Heading [59]). This is best facilitated by recasting the homogeneous version of (2.64) into a standard form containing no first derivative. This is achieved using the transformation,

$$w_j(r|-\cos\theta) = \frac{\Phi(r)}{\sqrt{r}} v_j(r), \quad \text{for } j = 1, 2, \tag{2.69}$$

so that in "Q-form" v_j each satisfy,

$$\frac{\mathrm{d}^2 v_j}{\mathrm{d}r^2} + \left(k_0^2 Q_n^2 + \mathscr{I}\right) v_j = 0, \tag{2.70}$$

where $\mathscr{I} \equiv \Phi(r\Phi'/\Phi^2)'/r + (1/2r)^2$ which is neglected as $k_0 \to \infty$, (see for e.g., Heading [59]), and

$$rQ_n(r) \equiv \sqrt{r^2q^2 - (n/k_0)^2}, \quad q(r) \equiv \sqrt{\Phi^2 - \cos^2\theta}, \quad n = O(k_0). \tag{2.71}$$

The standard WKB solutions of (2.70) are of the form,

$$v_j(\mathrm{r}) \sim \sum_{i=1}^{2} \gamma_{ij}\, Q_n(\mathrm{r})^{-1/2} \exp\left((-)^i \mathrm{i}k_0 \int_{r_\delta}^{\mathrm{r}} Q_n(r')\,\mathrm{d}r'\right), \quad \mathrm{r} = \begin{cases} r & \text{if} \quad j = 1 \\ r_s & \text{if} \quad j = 2 \end{cases} \tag{2.72}$$

where r_δ are turning-points (also called phase references) such that $Q_n(r_\delta) = 0$, and γ_{ij} are constants to be determined. The final solution is composed so that $v_1(r)v_2(r_s)$ contains a phase that is integrated from r_s to r. However proceedings are not straightforward even in the simplest cases. The occurrence of turning-points leads to failure of the WKB solutions when either r or r_s lies in a k_0 dependent domain containing r_δ. Whenever r and r_s are separated by at least one turning-point then connection formulae must be used to link solutions either side of (and away from) the r_δ's. This potentially leads

to multiple reflections/scatterings between turning-points before the integration reaches the observer, hence the relaxation of propagation/extinction conditions to infinity and not in the near-field (r to r_s).

In the vicinity of any r_δ's the WKB solutions fail and must be replaced by uniform solutions dependent upon the order of the zero in $Q_n(r_\delta) = 0$. Therefore it is not simply a matter of integrating across the turning point to find the solution on the other side. One must either rescale the equations and find an appropriate local form or bypass the turning-point by detouring into complex space. This latter method is more elegant but one must take account of Stokes phenomenon to obtain the correct solution. Stokes phenomenon (see for e.g., Olver [139], Bender & Orszag [58]) is a topologically discontinuous but numerically smooth (Berry [74, 75]) switching that turns on exponentially small or subdominant solutions when crossing Stokes lines emanating from turning-points/singularities. These subdominant solutions resurge from the divergent tail of the dominant solutions. It was shown by Berry that this switching - at leading order - is controlled by the error function. For a second order equation such as (2.70) with two solutions (setting $\gamma_1 = 1$ for simplicity),

$$v(\mathrm{r}) \sim Q_n^{-1/2}(\mathrm{r})\exp\left(+\mathrm{i}k_0\int_{r_\delta}^{\mathrm{r}} Q_n(r')\,\mathrm{d}r'\right) + \mathrm{i}\,S(\mathrm{r};k_0)Q_n^{-1/2}(\mathrm{r})\exp\left(-\mathrm{i}k_0\int_{r_\delta}^{\mathrm{r}} Q_n(r')\,\mathrm{d}r'\right). \tag{2.73}$$

The positive branch has been chosen to be the dominant one in this example given appropriate cuts. The *Stokes multiplier* γ_2 is expressed in terms of the error function $\gamma_2 = \mathrm{i}\,S(\mathrm{r};k_0)$ where,

$$S(\sigma_{\mathrm{Stokes}}) = \frac{1}{\sqrt{\pi}}\int_{-\infty}^{\sigma_{\mathrm{Stokes}}} \exp\left(-t^2\right)\,\mathrm{d}t, \tag{2.74}$$

and σ_{Stokes} is the Stokes variable,

$$\sigma_{\mathrm{Stokes}} \equiv k_0^{1/2}\Im(F)/(2\Re(F))^{1/2}, \tag{2.75}$$

where $F \equiv 2\mathrm{i}k_0\int_{r_\delta}^{\mathrm{r}} Q_n(r')\,\mathrm{d}r'$ is Dingle's singulant [21]: the difference between the dominant and subdominant phases. So that the singulant controls the switching through the Stokes variable. The appearance of the singulant means that the region about the Stokes line in which the switching occurs (numerically) has a width that increases with distance from the turning-point. This property along with the singulant as a measure of resurgence will be used in later chapters (though the definition is equal to $-\mathrm{i}F$ of that above) in order to resolve what would an arbitrary choice.

Applying connection formulae to the Green's function solutions (2.72) must take into account all possible reflections/scatterings from turning points that eventually travel to

the far-field. This does not violate the outward propagation condition as the radiation condition applies to sources at infinity. A point source emits energy in all directions, so this must be taken into account when deriving the modal solutions.

For large distance observers $r \gg \max(r_\delta)$ or $r \to \infty$, then the "r" WKB solution is straight forward. The difficulty of the problem pertains to the r_s solutions and various connection and uniform formulae must be derived. For each turning-point problem (one exists for each mode) then not only should the number of turning-points be considered but also the positions of the source with respect to them. Here we shall only consider two cases of a single real turning-point. For generic parallel shear flows, particularly at high θ angles, multiple turning-points do exist on the real line. One also has to be careful of the influence of complex turning points near the real axis when root finding numerically; derivative based solvers may return a local minimum between such points.

Though we will only consider two specific cases, it is expedient to introduce the general notation for a hypothetical list of N_δ real and positive turning-points: $r_{\delta_N} > r_{\delta_{N-1}} > \ldots > r_{\delta_1} \geq 0$. In the $N_\delta + 1$ regions delimited by turning-points a solution of the form (2.72) may exist, so that in order to differentiate between these solutions we now use $\gamma_{ij}^{(n)}$ where (n) denotes the solution to the left of the r_{δ_n}-th turning-point.

The Stokes structure sprouting from each turning-point depends on the order of the zero of Q_n^2, $m_{r_{\delta_n}}$. Then there are $m_{r_{\delta_n}} + 1$ Stokes lines (lines of pure decay), with each pair separated by one of $m_{r_{\delta_n}} + 1$ anti-Stokes lines (lines of pure oscillation). In the locality of the turning-point the Stokes and anti-Stokes lines are straight and separated by an angle of $2\pi/(m_{r_\delta} + 2)$, respectively.

Returning to the case of one turning-point we can immediately write down $v_1(r)$ as $r \to \infty$; it is simply

$$v_1(r) \sim \gamma_{21}^{(2)} Q_n^{-1/2}(r) \exp\left(+\mathrm{i}k_0 \int_{r_{\delta_1}=r_\delta}^{r} Q_n(r')\,\mathrm{d}r' \right). \tag{2.76}$$

The $v_2(r_s)$ solutions are more complicated. In the following the case of a single isolated turning-point and a coalesced singles turning-point are studied. Both appear in the parallel shear flow case and are classic problems of WKB theory. The branch cuts from $\pm r_\delta$ are chosen to be locally at an angle $-\pi/2$ (the same as [116]). Due to the complicated form of Q other turning-points will influence the numerical determination of these branch cuts.

2.2.1.1 Single first-order turning-point

This problem treats the case when Q_n^2 disappears linearly at $r_\delta > 0$, i.e.,

$$Q_n^2(r_s) = (r_s - r_\delta)Q_{n,1}^2(r_s) + O(r_s - r_\delta)^2, \tag{2.77}$$

so that $Q_n \gtrless 0$ for $(r_s - r_\delta) \gtrless 0$. According to theory this engenders 3 Stokes lines as $m_{r_\delta} = 1$. The primary[1] turning-point structure is shown in Fig. 2.5(a) along with the negative image of r_δ. The problem appears to depict the well-known quantum-well problem, [58], except integration in the negative half-plane is not considered. The presence of the pole at the origin doesn't affect the Stokes structure for this configuration.

The solution either side of the turning-point is well known and given by,

$$v_2(r_s) \sim \begin{cases} \gamma_{12}^{(2)} \left(Q_n^{-1/2}(r_s) \exp\left(-\mathrm{i}k_0 \int_{r_\delta}^{r_s} Q_n(r')\,\mathrm{d}r' \right) - \mathrm{i}\, Q_n^{-1/2}(r_s) \exp\left(+\mathrm{i}k_0 \int_{r_\delta}^{r_s} Q_n(r')\,\mathrm{d}r' \right) \right), & r_s > r_\delta \\ \gamma_{12}^{(1)} Q_n^{-1/2}(r_s) \exp\left(-k_0 \int_{r_s}^{r_\delta} |Q_n(r')|\,\mathrm{d}r' \right), \quad r_s < r_\delta, \end{cases} \tag{2.78}$$

with the connection between the two constants either side of r_δ is well known to be $\gamma_{12}^{(1)} = \mathrm{e}^{-\mathrm{i}\pi/4}\gamma_{12}^{(2)}$. In this problem the Stokes constant is given by $-\mathrm{i}$. The solution this term premultiplies (in $r_s > r_\delta$) can be thought of as the reflected branch.

Whenever, $|r_s - r_\delta| = O(k_0^{-2/3})$ the solution (2.78) fails and must be replaced by a uniform solution. This is well known to be in the form of an Airy function (see for e.g., [116] and [58]):

$$v_2(r_s) \sim \gamma_{12}^{(1)} \left(\frac{4\pi\sqrt{-\eta_n(r_s)}}{Q_n(r_s)} \right)^{1/2} \mathrm{Ai}\left(\eta_n(r_s)\right), \tag{2.79}$$

where,

$$\eta_n(\mathrm{r}) \equiv -\left(\frac{3}{2} k_0 \zeta_n(\mathrm{r}) \right)^{2/3}, \quad \zeta_n(\mathrm{r}) \equiv \int_{r_\delta}^{\mathrm{r}} Q_n(r')\,\mathrm{d}r', \tag{2.80}$$

which matches up with the WKB solutions when expanded for large argument.

2.2.1.2 Single second-order turning-point

The single second-order turning-point occurs when the turning-point and its negative image coalesce. At this point we don't consider the implications of $-r_\delta$ except that it exists. However, when $r_\delta \to 0$, $\pm r_\delta$ coalesce. If $r_s \gg k_0^{-1/2}$ then one can still apply the $r_s > r_\delta$ solution from (2.78): we just let $r_\delta \to 0$ in those solutions and discard the $r_s < r_\delta$

[1] We have neglected the infinite number of Stokes structures due to complex turning-points.

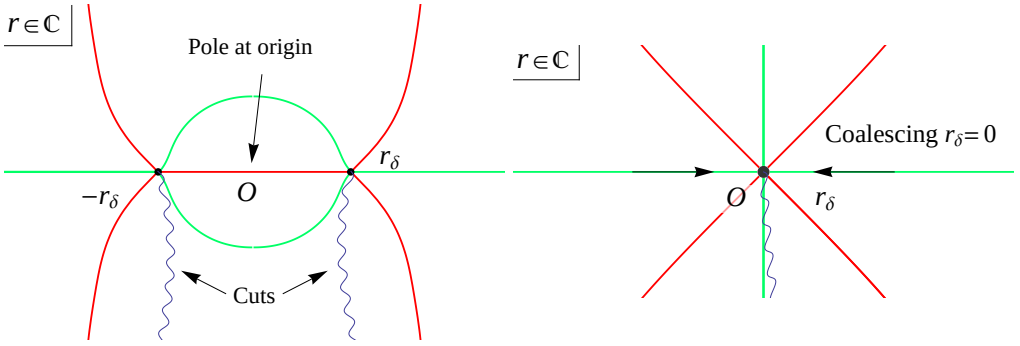

(a) Single first order turning-point structure (b) Single second order turning-point structure

FIGURE 2.5: Two single turning-point structures found in the WKB solution. (anti-)Stokes lines are in (green)red, while cuts are shown as wavy lines.

solution. When $r_s = O(k_0^{-1/2})$ we must look for another uniform solution. However, the turning-points $\pm r_\delta$ are not separated and,

$$Q_n^2(r_s) = (r_s - r_\delta)^2 Q_{n,2}^2(r_s) + O(r_s - r_\delta)^3, \tag{2.81}$$

so a new local form must be introduced. The appropriate local form is well known to be in terms of parabolic cylinder functions or Bessel functions (see [58] and [59]). Here the outgoing wave must contain two branches of the WKB solution rather than just one as in the cited works, though we will revisit this solution again in Chap. 6 where the case is just one branch. It can be shown that the uniform solution is,

$$v_2(r_s) \sim \sqrt{\frac{\eta_n^{(2)}(r_s)}{k_0 Q_n(r_s)}} \left(\gamma_1^J J_{1/4}\left(\eta_n^{(2)}(r_s)/2\right) + \gamma_2^J J_{-1/4}\left(\eta_n^{(2)}(r_s)/2\right)\right), \tag{2.82}$$

or

$$v_2(r_s) \sim \left(\frac{\sqrt{\eta_n^{(2)}(r_s)}}{k_0 Q_n(r_s)}\right)^{1/2} \left(\gamma_1^P D_{-1/2}\left(\sqrt{2}\mathrm{e}^{\pi \mathrm{i}/4}\sqrt{\eta_n^{(2)}(r_s)}\right) + \gamma_2^P D_{-1/2}\left(\sqrt{2}\mathrm{e}^{3\pi \mathrm{i}/4}\sqrt{\eta_n^{(2)}(r_s)}\right)\right), \tag{2.83}$$

where,

$$\eta_n^{(2)}(\mathrm{r}) \equiv 2k_0 \int_{r_\delta}^{\mathrm{r}} Q_n(r')\,\mathrm{d}r'. \tag{2.84}$$

At this stage it is preferable to use the parabolic cylinder form. This is due to the difficulty in matching up the Bessel solutions with (2.78) and the requirement that the uniform function must be bounded for zero argument (thus necessitating $\gamma_2^J = 0$).

Using large argument asymptotics the constants are determined via,

$$\begin{aligned} \gamma_2^P \mathrm{e}^{7\pi\mathrm{i}/8}/k_0^{1/2}2^{3/4} &= -\mathrm{e}^{\pi\mathrm{i}/2}\gamma_{12}^{(2)}, \\ \gamma_2^P \mathrm{e}^{\pi\mathrm{i}/8}/k_0^{1/2}2^{3/4} + \gamma_2^P \mathrm{e}^{3\pi\mathrm{i}/8}/k_0^{1/2}2^{1/4} &= \gamma_{12}^{(2)}. \end{aligned} \tag{2.85}$$

Having provided two local forms to cover the expected cases of degenerate WKB solutions, we return to the computation of the Green's function. The next step is the Wronskian.

The Wronskian can be computed by observing that it is constant (in Q-form Eq. (2.70)) via Abel's identity,

$$\frac{\mathrm{d}\mathscr{V}}{\mathrm{d}r} = 0 \quad \Longrightarrow \quad \mathscr{V} = \text{const.}, \tag{2.86}$$

where $\mathscr{W}(r_s) = \Phi^2(r_s)\mathscr{V}(r_s)/r_s$. For each modal problem in n, $\mathscr{V}$ can be evaluated at large r using (2.76), and a solution in r_s for any turning-point scenario. For the single turning-point problems the Wronskian is given by [116] as,

$$\mathscr{V} \sim -\mathrm{i}2k_0\gamma_{21}^{(2)}\gamma_{12}^{(1)}\mathrm{e}^{\mathrm{i}\pi/4}. \tag{2.87}$$

It can be seen that connection formulae relate the constant of each solution from one side of the turning-point to that of the solution on the other-side. Thus the Wronskian will contain these constants in a multiplicative form (e.g., (2.87)) leading to their elimination from the final Green's function.

The most convenient final final form the Green's function $\mathbb{G}_\omega$ - given the predominance of one turning-point problems - is given by,

$$\mathbb{G}_\omega \sim \frac{\mathrm{i}\mathscr{G}_\omega^{(3)}\mathscr{R}_\omega}{\overline{c}_\infty k_0 a_s(1 - M_s\cos\theta)^2}, \tag{2.88}$$

where $\mathscr{R}_\omega$ is,

$$\mathscr{R}_\omega \sim \sum_{n=-\infty}^{\infty}\left(\frac{2}{k_0}\frac{\sqrt{-\eta_n(r_s)}}{r_s Q_n(r_s)}\right)^{1/2}\mathrm{Ai}\left(\eta_n(r_s)\right)\mathrm{e}^{\mathrm{i}n\Delta\varphi + \mathrm{i}k_0(\zeta_n(r) - R\sin^2\theta)}, \tag{2.89}$$

and $\mathscr{G}_\omega^{(3)} \equiv \mathrm{e}^{\mathrm{i}k_0 R}/4\pi R$.

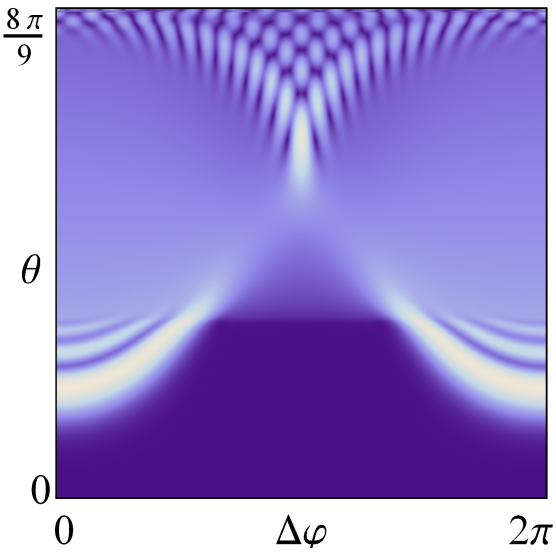

FIGURE 2.6: $|\mathbb{G}_\omega/\mathscr{G}_\omega^{(3)}|$ for $r_s = 0.75$, $M_J = 0.9$, $St = 5$ or $k_0 = 28.7$.

2.2.2 Computation of the Green's function.

The following computations of $\mathbb{G}_\omega/\mathscr{G}_\omega^{(3)}$ analysis will be restricted to isothermal flows such that $a = 1$. The parallel shear flow used will be the same as [116] and is equal to $\overline{u}_1(r) = M_J \text{sech}^2(2r)$ with $M_J = 0.9$. The results are best calculated as a function of Strouhal number,

$$St \equiv \frac{k_0}{\pi} \frac{r_J}{a(0)M_J}, \tag{2.90}$$

which is inverted to find the wavenumber once St is fixed (r_J the effective jet radius is determined by equal to 1/2 by [116]).

An example of $|\mathbb{G}_\omega/\mathscr{G}_\omega^{(3)}|$ is shown for source position 0.75 (source positions in the jet are shown in Fig. 2.7(a)) in Fig. 2.6. Off-axis sources such as this are realistic of noise source positions in real jets where the dominant sources are located in the shear layer where the turbulent intensities are the highest [9]. We will only consider off-axis point sources in this thesis, though on-axis source solutions do exist having been derived in [116] and computed in Stone et al. [140].

The solution shown in Fig. 2.6 has a diffraction pattern characteristic of all off-axis sources with a field of significantly reduced magnitude in an asymmetric region of low-θ (forward arc) values predominantly delimited by an interference pattern. This is the cone of silence (CoS) for a point source and in later chapters a study is conducted to calculate its exact shape and properties. Clearly, though, this region is asymmetric which differs from the ring source and experimentalist definitions.

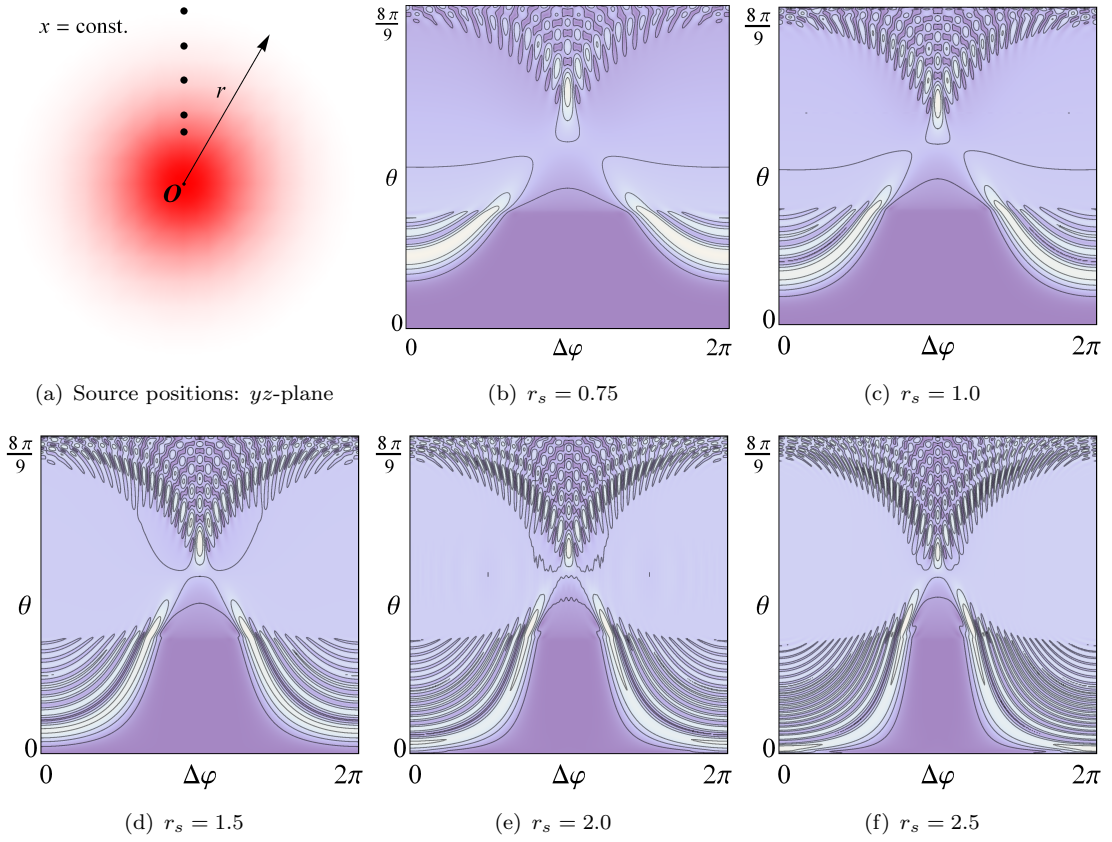

(a) Source positions: yz-plane (b) $r_s = 0.75$ (c) $r_s = 1.0$

(d) $r_s = 1.5$ (e) $r_s = 2.0$ (f) $r_s = 2.5$

FIGURE 2.7: Source position parametric study for the same flow regime as Fig. 2.6.

Towards high angles (rear arc) of θ there is a cusp shaped interference pattern with a peak in magnitude on the symmetry line $\Delta\varphi = \pi$. The peak values due to the cusp pattern and region surrounding the cone of silence can be explained in terms of ray singularities (see Chap. 6), but for the mean time it is sufficient to recognise their importance due to the increased magnitude in their vicinity.

2.2.2.1 Source position studies.

An interesting parametric study that can be achieved using (2.89) is the effect of source position on the point source field. Figure 2.7 shows the magnitude of the Green's function $|\mathbb{G}/\mathscr{G}_\omega^{(3)}|$ for various radial source positions. For each source position the cone of silence changes smoothly. As the source radius increases the cone of silence reduces in size being engulfed by the interference pattern until only a small region remains in the vicinity of the line $\Delta\varphi = \pi$. The interference patterns in both the forward and rear arcs increase in size and contain a finer scale of oscillation. In all cases the field is considerable amplified around the boundary of the cone of silence (for the most part) and the boundary of the cusp diffraction pattern. In reality sound fields are made up of more than one source

and many source models use a continuum of sources. This begs the question of whether in the presence of other sources these intense regions still persist? We will look into this question in more depth in Chapter 6.

A key property mentioned above is the smoothness and persistence of the interference patterns as the source position changes. This may seem obvious but it is an important property that is exhibited by the agents engendering these patterns. However, all is not smooth if one considers the on-axis source: this does not contain the diffraction varieties present in the off-axis solution (sol. shown in [140]). This is the reason off-axis source positions are studied: they contain are larger number of ray deficiencies that can be used to test our ray solver.

2.2.3 Notes on the continuity and analytic continuation of r_δ

During the derivation of the modal solution to the Green's function, (2.89), there are several conventions that need to be adhered to. They are adhered to because the modal solution has been shown by [116] to provide an excellent match to a numerical solution of Lilley's equation.

The first convention is that all the turning-points must be real. This means that scattering from complex turning-points are neglected. When a real turning-point doesn't exist on the real line, then a WKB integration can be applied as usual. When a real turning-point leaves the real line, this turning-point is not continued into the complex plane. The convention that there is no turning-point is adhered to.

The final convention is that we don't consider Langer's $1/4r^2$ correction term (see Langer [141]), due to a pole term in $\mathscr{I}$ that is singular at the origin. This is an important correction for quantum-mechanical solutions in radial coordinates: however, all turning-point structures disappear with Q having no roots under this correction. It is for this reason we neglect this correction.

2.3 Conclusion

In this chapter two acoustic analogies based on Lilley's equation have been reviewed. The first is Tester & Morfey's adaptation of the Lilley analogy that uses a statistical isotropic point quadrupole to develop a ring source model. This was reviewed to demonstrate the applicability of ray theory for a range of observer polar angles. It was shown for both isothermal and heated jets that outside the CoS, a ray theory solution makes a good approximation down to low Strouhal numbers. This agrees with conclusions by other

authors (notably [116]) that good approximations can be made below $St = O(1)$. This is the beauty of asymptotic solutions: they work well outside their region of validity, i.e., $k_0 \to \infty$ in this case. The main disagreement of the ray theory near the CoS angle is likely due to a caustic deficiency. We expect a complex ray theory solution inside the CoS to show good agreement as well, as there is no reason to suspect that real rays work better than their complex counterparts.

The second model is the Lilley equation's Green's function for a 3D point source, this will provide a benchmark for the ray calculations in Chapter 6. These solutions have two interesting diffraction patterns which persist for off-axis source locations. The exact causes of these diffractions are also discussed in Chapter 6.

This chapter has also set the template - from a physical point-of-view - for the ring source solution. In later chapters we will extend the ring source solution to study the effects of certain singular structures. Though the main aim of this thesis is to compute point source ray solutions, it is useful to be able to assess the impact of multiple point source on the total field.

Chapter 3

Flow Factor and Vector Green's Functions

3.1 Introduction

In the previous chapter work focused on Green's function solutions to Lilley's equation in either two or three dimensions. The latter proved in keeping with the aims of this thesis: a Green's function completely decoupled from the source model valid in the high-frequency limit. In light of this, the first part of this chapter pursues a vector Green's function solution to the linearised Euler equations. This is more general than Lilley's Green's function as it applies to arbitrary mean flows and can be used within a generalised acoustic analogy framework. Motivated by prior success of high-frequency solutions a ray ansatz is applied to the vector Green's function and a flow-factor formed. Solutions to the leading order term are kept general bearing in mind the necessity of complex trajectories to compute complex rays. In the second part of this chapter the ray solutions are used to provide large simplifications to the algebra of correlation and spectral integrals thus showing their further utility in acoustic calculations.

3.2 Linearised acoustic equations and flow-factor definition

In the spirit of the acoustic analogy the derivation of the flow factor starts from the inviscid linearised acoustic equations of continuity, momentum, energy, and state. These are commonly known as the linearised Euler equations and form the basis of linear aeroacoustic theory. The Euler equations are derived from the full nonlinear fluid-dynamic equations by decomposing the dependent variables into mean $O(1)$, and fluctuating

$O(\epsilon)$, $\epsilon \ll 1$, parts. Retaining the terms linear in these perturbations and leaving the nonlinear sources unaffected gives (Goldstein [9]),

$$\bar{\rho}\left(\frac{\overline{D}u_i'}{Dt} + u_j'\frac{\partial \bar{u}_i}{\partial x_j}\right) + \rho'\bar{u}_j\frac{\partial \bar{u}_i}{\partial x_j} + \frac{\partial p'}{\partial x_i} = f_i, \tag{3.1}$$

$$\frac{\overline{D}\rho'}{Dt} + \rho'\frac{\partial \bar{u}_j}{\partial x_j} + \frac{\partial}{\partial x_j}\bar{\rho}u_j' = \bar{\rho}q, \tag{3.2}$$

$$\frac{\overline{D}s'}{Dt} + u_j'\frac{\partial \bar{s}}{\partial x_j} = 0, \tag{3.3}$$

$$p' - \bar{c}^2\rho' - \left(\frac{\overline{\partial \mathcal{K}}}{\partial s}\right)s' = 0, \tag{3.4}$$

where p',ρ', u_i', and s' are the fluctuating pressure, density, particle velocity and entropy, respectively. The nonlinear volume sources f_i and q are assumed to be of the same order as the fluctuating variables. The barred variables denote an average so that $\bar{\rho}$, $\bar{u}_i$, and $\bar{s}$ are the mean or "base" flow for density, velocity and entropy, respectively. The barred operator $\overline{D}/Dt \equiv \partial_t + \bar{u}_j\partial_{x_j}$ is the mean convective derivative. Equation (3.4) makes use of the equation of state relating the pressure, density and entropy together, i.e., $p = \mathcal{K}(\rho, s)$. The mean sound speed is then defined $\bar{c}^2 = \overline{\partial \mathcal{K}}/\partial\rho$.

The mean variables satisfy the following,

$$\bar{\rho}\bar{u}_j\frac{\partial \bar{u}_i}{\partial x_j} = -\frac{\partial \bar{\rho}}{\partial x_i}, \tag{3.5}$$

$$\frac{\partial}{\partial x_j}\bar{\rho}\bar{u}_j = 0, \tag{3.6}$$

$$\bar{u}_j\frac{\partial \bar{s}}{\partial x_j} = 0, \tag{3.7}$$

$$\bar{u}_j\frac{\partial \bar{p}}{\partial x_j} = \bar{c}^2\bar{u}_j\frac{\partial \bar{\rho}}{\partial x_j}. \tag{3.8}$$

No assumption has been made on the mean pressure gradient. It makes no appearance in the linearised equations (3.1) to (3.4) because linearisation eliminates it to leading order.

The equation of state $p = \mathcal{K}(\rho, s)$ can be used to define relations:

$$\begin{Bmatrix} \partial/\partial x_i \\ \overline{D}/Dt \end{Bmatrix}\bar{p} = \bar{c}^2\begin{Bmatrix} \partial/\partial x_i \\ \overline{D}/Dt \end{Bmatrix}\bar{\rho} + \left(\frac{\overline{\partial \mathcal{K}}}{\partial s}\right)\begin{Bmatrix} \partial/\partial x_i \\ \overline{D}/Dt \end{Bmatrix}\bar{s}, \tag{3.9}$$

$$\begin{Bmatrix} \partial/\partial x_i \\ \overline{D}/Dt \end{Bmatrix}p' = \bar{c}^2\begin{Bmatrix} \partial/\partial x_i \\ \overline{D}/Dt \end{Bmatrix}\rho' + \left(\frac{\overline{\partial \mathcal{K}}}{\partial s}\right)\begin{Bmatrix} \partial/\partial x_i \\ \overline{D}/Dt \end{Bmatrix}s', \tag{3.10}$$

since thermodynamic formulae allow differential operators other than just total derivatives to be applied.

The linear properties of the propagating LHS of Eqs. (**??**)-(**??**) mean that the sources can be separated from the propagation using the Green's function technique. However, the Green's function for dependent variable must be a vector since this is a vector system. This becomes clear if we restate the linear acoustic equations in the compact notation,

$$L_{\kappa v}\tilde{v}_v = \tilde{s}_\kappa, \tag{3.11}$$

where

$$\{\tilde{v}_v\} = \{u_i', \rho', p', s'\}, \quad \text{and} \quad \{\tilde{s}_\kappa\} = \{f_i, q, 0, 0\}. \tag{3.12}$$

The vector Green's function $g_{v\eta}(\boldsymbol{x}, t|\boldsymbol{x}_s, t_s)$ for (3.11) can be written in dyadic form (Morse & Feshbach [57]) as,

$$L_{\kappa v}g_{v\eta} = \delta_{\kappa\eta}\delta(\boldsymbol{x} - \boldsymbol{x}_s)\delta(t - t_s). \tag{3.13}$$

or explicitly as,

$$\bar{\rho}\left(\frac{\overline{D}g_{i\eta}}{Dt} + g_{j\eta}\frac{\partial \bar{u}_i}{\partial x_j}\right) + g_{4\eta}\bar{u}_j\frac{\partial \bar{u}_i}{\partial x_j} + \frac{\partial g_{5\eta}}{\partial x_i} = \delta_{i\eta}\delta(\boldsymbol{x} - \boldsymbol{x}_s)\delta(t - t_s), \tag{3.14}$$

$$\frac{\overline{D}g_{4\eta}}{Dt} + g_{4\eta}\frac{\partial \bar{u}_j}{\partial x_j} + \frac{\partial}{\partial x_j}\bar{\rho}g_{j\eta} = \delta_{4\eta}\delta(\boldsymbol{x} - \boldsymbol{x}_s)\delta(t - t_s), \tag{3.15}$$

$$\frac{\overline{D}g_{6\eta}}{Dt} + g_{j\eta}\frac{\partial \bar{s}}{\partial x_j} = 0, \tag{3.16}$$

$$g_{5\eta} - \bar{c}^2 g_{4\eta} - \left(\frac{\overline{\partial \mathcal{K}}}{\partial s}\right) g_{6\eta} = 0. \tag{3.17}$$

Each column of the Green's function $g_{v\eta}$ is ordered according to (3.12), so for example the pressure components are $g_{5\eta}$. Additionally each component obeys the causality condition in the time domain:

$$g_{v\eta}(\boldsymbol{x}, t|\boldsymbol{x}_s, t_s) = 0 \quad \text{for} \quad t < t_s. \tag{3.18}$$

In this thesis we are only concerned with the frequency domain behaviour so a Fourier transform pair (denoted by $\hat{}$) is introduced,

$$\hat{g}_{v\eta} = \mathscr{F}_\omega\{g_{v\eta}\} = \int_{-\infty}^{\infty} g_{v\eta}\mathrm{e}^{\mathrm{i}\omega(t-t_s)}\,\mathrm{d}t, \quad g_{v\eta} = \mathscr{F}^{-1}_{t-t_s}\{\hat{g}_{v\eta}\} = \frac{1}{2\pi}\int_{-\infty}^{\infty} \hat{g}_{v\eta}\mathrm{e}^{-\mathrm{i}\omega(t-t_s)}\,\mathrm{d}\omega, \tag{3.19}$$

and applied to the linear equations (3.13). This results in the time-harmonic Green's function which solves,

$$\hat{L}_{\kappa v}\hat{g}_{v\eta} = \delta_{\kappa\eta}\delta(\boldsymbol{x} - \boldsymbol{x}_s), \tag{3.20}$$

where $\hat{L}_{\kappa v}$ is the Fourier transform of the operator $L_{\kappa v}$ and can be found by replacing $\overline{D}/Dt$ by $\overline{D}_\omega \equiv -\mathrm{i}\omega + \bar{u}_j\partial_{x_j}$ in (3.14)-(3.17).

The physical frequency domain variables such as pressure $\hat{p'}$ are then computed using,

$$\hat{v}_v = \int_V \hat{g}_{v\kappa}(\boldsymbol{x}|\boldsymbol{x}_s)\hat{s}_\kappa \,\mathrm{d}\boldsymbol{x}_s, \tag{3.21}$$

where V is the source volume.

So far, the introduction of a vector Green's function is consistent with the flow-factors considered in previous chapters. However, whereas before the flow-factor was a point force response to a scalar equation we now require 24 components to calculate all $\hat{v}_v$ with just 4 for the pressure. Thus any one of these could be a flow-factor. The maximum number of components required also appears to suggest that the Green's function method is expensive computationally. In the next section we make some considerable simplification if we assume that the problem is explicitly one of high-frequency propagation.

3.3 High-frequency approximation

In this section a matched ray solution is derived for the time-harmonic vector Green's function. One of the most important tenets of ray theory is that the transmitting medium varies slowly on the order of a wavelength, in other words the acoustic field is locally plane. In the vicinity of a point source the acoustic field oscillates rapidly so that ray theory is not applicable. Fortunately the method of matched asymptotic expansions can exploit the highly localised nature of the delta function allowing the construction of an "inner" solution valid in the vicinity of the source that can be matched asymptotically with an "outer" solution which solves the homogeneous linear equations. The technique employed here is due to Durbin [24], and a discussion of determining ray data for Helmholtz equations can be found in Bleistein [142]. This matching procedure is consistent with Keller's Geometrical Theory of Diffraction (see e.g., [40], [71]) where an inner canonical problem is matched with an outer ray solution.

3.3.1 Inner equation

In the vicinity of the source the mean field takes on "at source" constant values and the gradients of these quantities disappear allowing a wave equation in pressure to be

formed. The time harmonic versions of equations (3.14)-(3.17) reduce to,

$$\bar{\rho}_s \overline{D}_\omega \hat{g}_{i\eta} + \frac{\partial \hat{g}_{5\eta}}{\partial x_i} = \delta_{i\eta}\delta(\boldsymbol{x} - \boldsymbol{x}_s), \tag{3.22}$$

$$\overline{D}_\omega \hat{g}_{4\eta} + \bar{\rho}_s \frac{\partial \hat{g}_{j\eta}}{\partial x_j} = \delta_{4\eta}\delta(\boldsymbol{x} - \boldsymbol{x}_s), \tag{3.23}$$

$$\overline{D}_\omega \hat{g}_{6\eta} = 0, \tag{3.24}$$

so using (3.24) and (3.10) for the Green's functions' components gives,

$$\overline{D}_\omega \hat{g}_{4\eta} = \frac{1}{\bar{c}^2} \overline{D}_\omega \hat{g}_{5\eta}, \tag{3.25}$$

thus by standard techniques,

$$\frac{1}{\bar{c}_s^2} \overline{D}_\omega^2 \hat{g}_{5\eta} - \frac{\partial^2 \hat{g}_{5\eta}}{\partial x_i^2} = \overline{D}_\omega \delta_{4\eta}\delta(\boldsymbol{x} - \boldsymbol{x}_s) - \frac{\partial}{\partial x_i}\delta_{i\eta}\delta(\boldsymbol{x} - \boldsymbol{x}_s). \tag{3.26}$$

The source term on the right of this equation suggest we look for an inner equation of the form,

$$\frac{1}{\bar{c}_s^2} \overline{D}_\omega^2 g_{\text{in}} - \frac{\partial^2 g_{\text{in}}}{\partial x_i^2} = \delta(\boldsymbol{x} - \boldsymbol{x}_s), \tag{3.27}$$

which, upon expanding the convective derivative, can be written as (as in Durbin [24]),

$$\frac{1}{\bar{c}_s^2}\left(-\omega^2 - 2\mathrm{i}\omega \bar{u}_j(\boldsymbol{x}_s)\frac{\partial}{\partial x_j} + \bar{u}_j(\boldsymbol{x}_s)\bar{u}_k(\boldsymbol{x}_s)\frac{\partial^2}{\partial x_j \partial x_k}\right) g_{\text{in}} - \frac{\partial^2 g_{\text{in}}}{\partial x_i^2} = \delta(\boldsymbol{x} - \boldsymbol{x}_s) \tag{3.28}$$

where the following dimensionless quantities have been introduced: Mach number $M_i = \bar{u}_i/c_r$, sound speed ratio $a = \bar{c}/c_r$, matrix $T_{ij} = \delta_{ij} - M_i M_j/a^2$ (with inverse $T_{ij}^{-1} = \delta_{ij} + M_i M_j/\beta^2 a^2$; $\beta^2 = 1 - M_k M_k/a^2$), and reference sound speed c_r. Furthermore with inner variable $\boldsymbol{y} = k_0(\boldsymbol{x} - \boldsymbol{x}_s)$, this can be written as,

$$\frac{1}{a_s^2}\left(1 + 2\mathrm{i}M_{s_j}\frac{\partial}{\partial y_j}\right) g_{\text{in}} + \frac{\partial}{\partial y_i} T_{s_{ij}} \frac{\partial}{\partial y_j} g_{\text{in}} = -k_0^{n-2}\delta(\boldsymbol{y}). \tag{3.29}$$

It is convenient to introduce a solution of the form,

$$g_{\text{in}} = \mathrm{e}^{-\mathrm{i}\boldsymbol{y}\cdot\boldsymbol{M}_s/\beta_s^2 a_s^2} \Psi_{\text{in}}(\boldsymbol{y}), \tag{3.30}$$

so that $\Psi_{\text{in}}(\boldsymbol{y})$ satisfies,

$$\frac{\partial}{\partial y_i} T_{s_{ij}} \frac{\partial}{\partial y_j} \Psi_{\text{in}} + \Psi_{\text{in}}/a_s^2\beta_s^2 = -\delta(\boldsymbol{y}) k_0^{n_D - 2}. \tag{3.31}$$

Because T_{ij} is symmetric, the operator $\partial_{y_i} T_{ij} \partial_{y_j}$ can be diagonalized. In fact if the variable ζ defined by,

$$\zeta^2 = y_i T^{-1}_{s_{ij}} y_j = y_i y_i + (y_i M_{s_i})^2 / a_s^2 \beta_s^2, \tag{3.32}$$

the equation in Ψ_{in} can be expressed as an ode,

$$\frac{1}{\zeta^{n_D-1}} \frac{\mathrm{d}}{\mathrm{d}\zeta} \zeta^{n_D-1} \frac{\mathrm{d}\Psi_{\text{in}}}{\mathrm{d}\zeta} + \Psi_{\text{in}} / a_s^2 \beta_s^2 = -\frac{\delta(\zeta) k_0^{n_D-2}}{\det(T_{s_{ij}})^{1/2}} = -\frac{\delta(\zeta) k_0^{n_D-2}}{\beta_s}, \tag{3.33}$$

where n_D is the dimension of the problem: here $n_D = 2, 3$. Equation (3.33) has solution in terms of Hankel functions,

$$\Psi_{\text{in}} = \mathrm{i} H^{(1)}_{(n_D-2)/2} \left(\zeta / \beta_s a_s\right) k_0^{n_D-2} / 4\beta_s (2\pi\zeta a_s \beta_s)^{(n_D-2)/2}, \tag{3.34}$$

which as $|\boldsymbol{y}| \to \infty$ gives outer solution for g_{in},

$$g_{\text{in}} \sim \left[\mathrm{e}^{\mathrm{i}(3-n_D)\pi/4} a_s k_0^{(n_D-3)/2} / 2(2\pi\xi a_s \beta_s)^{(n_D-1)/2} \right] \mathrm{e}^{\mathrm{i}k_0 S_s}, \tag{3.35}$$

where, $\xi^2 = (x_i - x_{s_i}) T^{-1}_{s_{ij}} (x_j - x_{j_s})$ and $S_s = \xi / a_s \beta_s - (x_i - x_{s_i}) M_{s_i} / a_s^2 \beta_s^2$.

3.3.2 Outer equation

The solution in the outer region is to be obtained through a ray acoustics approximation. It is important to note that in the outer region the solution is far enough away from the (highly localised) delta functions so that only the homogeneous acoustic equations are dealt with. Away from the delta functions we drop any reference to η in $\hat{g}_{i\eta}$ for clarity (these are brought back in the matching process). It is also convenient to eliminate the pressure variable in these equations using the state equation (3.17) so only $\hat{g}_i (i = 1, 2, 3), \hat{g}_5$, and $\hat{g}_6$ are used. It will then be shown that $\hat{g}_4$ can be determined in terms of $\hat{g}_5$ to leading order algebraically.

As a generalisation of the one-dimensional case, $\hat{g}_4$, $\hat{g}_i$ and $\hat{g}_6$ are expanded in inverse powers of $\mathrm{i}k_0$,

$$\hat{g}_4 \sim \mathrm{e}^{\mathrm{i}k_0 S} \sum_{n=0}^{\infty} \frac{r_n}{(\mathrm{i}k_0)^n}, \quad \hat{g}_i \sim c_r \mathrm{e}^{\mathrm{i}k_0 S} \sum_{n=0}^{\infty} \frac{m_{i_n}}{(\mathrm{i}k_0)^n}, \quad \hat{g}_6 \sim \mathrm{e}^{\mathrm{i}k_0 S} \sum_{n=0}^{\infty} \frac{s_n}{(\mathrm{i}k_0)^n}, \tag{3.36}$$

and substituted into the frequency domain linearised equations,

$$\begin{aligned}-\mathrm{i}\omega\bar{\rho}\hat{g}_i + \bar{\rho}\bar{u}_j\frac{\partial\hat{g}_i}{\partial x_j} + \bar{\rho}\hat{g}_j\frac{\partial\bar{u}_i}{\partial x_j} + \hat{g}_4\bar{u}_j\frac{\partial\bar{u}_i}{\partial x_j} + \bar{c}^2\frac{\partial\hat{g}_4}{\partial x_i} + h\frac{\partial\hat{g}_6}{\partial x_i} = \\ -\hat{g}_4\left(\overline{\frac{\partial^2\mathcal{K}}{\partial\rho^2}}\frac{\partial\bar{\rho}}{\partial x_i} + \overline{\frac{\partial^2\mathcal{K}}{\partial\rho\partial s}}\frac{\partial\bar{s}}{\partial x_i}\right) - \hat{g}_6\left(\overline{\frac{\partial^2\mathcal{K}}{\partial\rho\partial s}}\frac{\partial\bar{\rho}}{\partial x_i} + \overline{\frac{\partial^2\mathcal{K}}{\partial s^2}}\frac{\partial\bar{s}}{\partial x_i}\right),\end{aligned} \tag{3.37}$$

$$-\mathrm{i}\omega\hat{g}_4 + \bar{u}_j\frac{\partial\hat{g}_4}{\partial x_j} + \hat{g}_4\frac{\partial\bar{u}_j}{\partial x_j} + \hat{g}_j\frac{\partial\bar{\rho}}{\partial x_j} + \bar{\rho}\frac{\partial\hat{g}_j}{\partial x_j} = 0, \tag{3.38}$$

$$-\mathrm{i}\omega\hat{g}_6 + \bar{u}_j\frac{\partial\hat{g}_6}{\partial x_j} + \hat{g}_j\frac{\partial\bar{s}}{\partial x_j} = 0, \tag{3.39}$$

Equating terms at $O(k_0)$ leads to,

$$O(k_0)\begin{cases}\left(1 - M_j\frac{\partial S}{\partial x_j}\right)r_0 - \bar{\rho}\frac{\partial S}{\partial x_j}m_{j_0} = 0, \\ \left(1 - M_j\frac{\partial S}{\partial x_j}\right)\bar{\rho}m_{i_0} - \left(a^2 r_0 + \overline{\frac{\partial\mathcal{K}}{\partial s}}\frac{s_0}{\bar{c}^2}\right)\frac{\partial S}{\partial x_i} = 0, \\ \left(1 - M_j\frac{\partial S}{\partial x_j}\right)s_0 = 0,\end{cases} \tag{3.40}$$

These equations are in the form $\boldsymbol{A}\boldsymbol{x} = \boldsymbol{0}$, so in order for a non-trivial solution to exist (i.e., not all $r_0 = m_{i_0} = s_0 = 0$), the determinant of these equations must be non-trivial (i.e. $\det(\boldsymbol{A}) = 0$). It is straightforward to show that this condition leads to,

$$\bar{\rho}^3\left(1 - M_j p_j\right)^3\left[\left(1 - M_j p_j\right)^2 - a^2 p_j p_j\right] = 0, \tag{3.41}$$

where the wavefront normal $p_i = \partial S/\partial x_i$ has been introduced.

Therefore there are two possibilities for (3.41) to be satisfied: first, $(1 - M_j p_j) = 0$ which then implies that $r_0 = m_{i_0} = s_0 = 0$ in (3.40). It is well known that this solution represents a convective incompressible disturbance. In other words, an observer moving with at local mean flow velocity would not observe a sound wave fluctuating in time. As noted in Durbin [24] the high-frequency convective disturbance has been studied in relation to the rapid distortion theory of turbulence.

The second solution from (3.41) is,

$$\left(1 - M_j p_j\right)^2 - a^2 p_j p_j = 0, \tag{3.42}$$

and corresponds to the propagation of acoustic waves. Equation (3.42) is commonly known as the eikonal equation. Given that $(1 - M_j p_j) \neq 0$, then the following are true for the acoustic disturbance,

$$\bar{\rho}m_{i_0} = \frac{a^2 r_0 p_i}{1 - M_j p_j}, \tag{3.43}$$

$$\bar{\rho}^2 m_{j_0} m_{j_0} = a^2 r_0^2, \tag{3.44}$$

$$s_0 = 0, \tag{3.45}$$

The first of these implies that r_0 and m_{i_0} can be written algebraically in terms of one (currently unknown) scalar function Φ_{pot},

$$r_0 = \frac{\bar{\rho}}{a^2}\left(1 - M_j p_j\right)\Phi_{\text{pot}}(\boldsymbol{x}), \quad m_{i_0} = -p_i \Phi_{\text{pot}}. \tag{3.46}$$

To leading order r_0 and m_{i_0} are the only quantities required to compute the field as (3.47) shows that to leading order the ray solution is isentropic. From the state equation (3.17) and the ray ansatz (3.36),

$$A_n = \bar{c}^2 r_n + \left(\frac{\overline{\partial \kappa}}{\partial s}\right) s_n \implies A_0 = \bar{c}^2 r_0, \tag{3.47}$$

where A_n are the coefficients of the pressure ray ansatz: $\hat{g}_5 \sim \mathrm{e}^{\mathrm{i}k_0 S}\sum A_n/(\mathrm{i}k_0)^n$.

3.3.2.1 Solving the eikonal equation using rays

The eikonal equation can be solved using the method of characteristics (see for e.g., Sneddon [41]). The phase of the field may be determined by propagating rays $\boldsymbol{x}(\tau)$ from the source according to the initial value problem (IVP),

$$\frac{\mathrm{d}x_i}{\mathrm{d}\tau} = T_{ij}(\boldsymbol{x})p_j + \frac{M_i(\boldsymbol{x})}{a(\boldsymbol{x})^2}, \tag{3.48}$$

$$\frac{\mathrm{d}p_i}{\mathrm{d}\tau} = -\frac{1}{2}p_j \frac{\partial T_{j\ell}}{\partial x_i}p_\ell - p_j \frac{\partial}{\partial x_i}\left(\frac{M_j(\boldsymbol{x})}{a(\boldsymbol{x})^2}\right) + \frac{1}{2}\frac{\partial a^{-2}}{\partial x_i}(\boldsymbol{x}), \tag{3.49}$$

$$\frac{\mathrm{d}S}{\mathrm{d}\tau} = p_j \frac{\mathrm{d}x_j}{\mathrm{d}\tau}. \tag{3.50}$$

Only in the simplest cases (e.g., homogeneous media) can equations (3.48)-(3.50) be solved analytically, so the standard procedure is to integrate, or "fire off", $\boldsymbol{x}(\tau)$ numerically. Firing off a ray from a point source in 3D requires two angular parameters $\tilde{\mu} = \{\mu, \lambda\}$ along with final integration time τ_R. The initial firing normal $\tilde{\nu}_s = \{\cos\mu, \sin\mu\cos\lambda, \sin\mu\sin\lambda\}$ is chosen to be proportional to the ray group velocity $\dot{x}_i = \sigma_s \tilde{\nu}_s$, where the constant of proportionality is the ray speed defined as $\sigma = \sqrt{\dot{x}_j \dot{x}_j}$. Thus the IVP has initial conditions,

$$x_i(0) = x_{s_i}, \quad p_i(0) = T^{-1}_{s_{ij}}\left(\sigma_s \tilde{\nu}_{s_j} - M_{s_j}/a_s^2\right), \quad \sigma_s^{-2} = \left(\tilde{\nu}_{s_i} T^{-1}_{s_{ij}} \tilde{\nu}_{s_j}\right) a_s^2 \beta_s^2, \quad S(0) = 0. \tag{3.51}$$

3.3.2.2 Amplitude equations

$$
\begin{array}{c} O(k_0^{-n}) \\ n \geq 0 \end{array}
\begin{cases}
-\left(1 - M_j \frac{\partial S}{\partial x_j}\right) r_{n+1} + \bar{\rho} m_{j_{n+1}} \frac{\partial S}{\partial x_j} + M_j \frac{\partial r_n}{\partial x_j} + m_{j_n} \frac{\partial \bar{\rho}}{\partial x_j} + \bar{\rho} \frac{\partial m_{j_n}}{\partial x_j} + r_n \frac{\partial M_j}{\partial x_j} = 0, \\
-\left(1 - M_j \frac{\partial S}{\partial x_j}\right) \bar{\rho} m_{i_{n+1}} + a^2 r_{n+1} \frac{\partial S}{\partial x_i} + \frac{h}{c_r^2} s_{n+1} \frac{\partial S}{\partial x_i} + \bar{\rho} M_j \frac{\partial m_{i_n}}{\partial x_j} + \ldots \\
\qquad \ldots + r_n M_j \frac{\partial M_i}{\partial x_i} + a^2 \frac{\partial r_n}{\partial x_i} + \frac{r_n}{c_r^2} \left(\overline{\frac{\partial^2 \mathcal{k}}{\partial \rho^2}} \frac{\partial \bar{\rho}}{\partial x_i} + \overline{\frac{\partial^2 \mathcal{k}}{\partial \rho \partial s}} \frac{\partial \bar{s}}{\partial x_i} \right) = 0, \\
-\left(1 - M_j \frac{\partial S}{\partial x_j}\right) s_{n+1} + \frac{\partial \bar{s}}{\partial x_j} m_{j_n} = 0,
\end{cases}
\tag{3.52}
$$

It can be shown (see for e.g., Jones [143]) that for $n = 0$ these equations can be manipulated into the following equation in terms of the first order amplitude terms r_0 and m_{0_i};

$$
(1 - M_j p_j) \left[\frac{\partial}{\partial x_i} r_0 M_i + \bar{\rho} \frac{\partial m_{j_0}}{\partial x_j} \right] + p_j \left[\bar{\rho} M_k \frac{\partial m_{j_0}}{\partial x_k} + \bar{\rho} m_{k_0} \frac{\partial M_j}{\partial x_k} + \frac{\partial}{\partial x_j} r_0 a^2 \right] = 0, \tag{3.53}
$$

to which further manipulation leads to the familiar divergence,

$$
\frac{\partial}{\partial x_j} \left[\frac{a^4 r_0^2 \dot{x}_j}{\bar{\rho}(1 - M_k p_k)^2} \right] = 0, \tag{3.54}
$$

and conservation along a ray tube (using Eq. (3.46)),

$$
\bar{\rho} \sigma \Phi_{\text{pot}}^2 J = \text{constant}, \tag{3.55}
$$

where J is the Jacobian of the rays, and equals the determinant of the Jacobian matrix,

$$
J_{\text{mat}} = \begin{pmatrix} \partial x_1/\partial \mu & \partial x_2/\partial \mu & \partial x_3/\partial \mu \\ \partial x_1/\partial \lambda & \partial x_2/\partial \lambda & \partial x_3/\partial \lambda \\ \partial x_1/\partial \tau & \partial x_2/\partial \tau & \partial x_3/\partial \tau \end{pmatrix}. \tag{3.56}
$$

So the expression for $\hat{g}_5$ using (3.47) is,

$$
\hat{g}_5 \sim \frac{\bar{c}^2 \bar{\rho}}{a^2} (1 - M_k p_k) \left(\frac{\text{constant}}{\sigma \bar{\rho} J} \right)^{1/2} \mathrm{e}^{\mathrm{i} k_0 S}. \tag{3.57}
$$

The constant can be found by taking the limit as $\boldsymbol{x} \to \boldsymbol{x}_s$ and then matching with the outer expansion $|\boldsymbol{y}| \to \infty$ of the inner solution (3.35). Using the initial condition for ray speed (see Eqs. (3.51)) to express ξ in terms of ray arclength s_{ray} and ray speed so $\xi = s_{\text{ray}}/\sigma_s a_s \beta_s$, and that near the source $J \sim s_{\text{ray}}^{n_D - 1} \sin^{n_D - 2} \mu$, the constant is

determined to be,

$$\text{constant} = \frac{a_s^6 \mathrm{e}^{\mathrm{i}(n_D-3)\pi/2} k_0^{(n_D-3)} \sigma_s^{n_D} \sin^{n_D-2}\mu}{4(2\pi)^{(n_D-1)} \bar{c}_s^4 \bar{\rho}_s (1 - M_{s_j} p_{s_j})^2}. \tag{3.58}$$

so the expression for the field along a generic ray is,

$$\hat{g}_5 \sim a_s \frac{(1 - M_k p_k)}{(1 - M_{s_k} p_{s_k})} \left(\frac{\bar{\rho} \sigma_s^{n_D} \sin^{n_D-2}\mu}{\bar{\rho}_s \sigma J} \right)^{1/2} \frac{\mathrm{e}^{\mathrm{i}(3-n_D)\pi/4} k_0^{(n_D-3)/2} \mathrm{e}^{\mathrm{i}k_0 S}}{2(2\pi)^{(n_D-1)/2}}. \tag{3.59}$$

3.3.2.3 Solving the amplitude transport using rays

The amplitude transport equation can be solved along rays in the same way as the phase. Noting that the only quantity that varies along the ray in (3.59) is the Jacobian J, and that this in turn can be calculated using the elements of J_{mat}. The equations governing these elements are known as the derived ray equations (DRE) and were first postulated by Hayes [144]. They form an extended system of coupled equations that are integrated in addition to the standard ray IVP. The odes for the elements are found by differentiating the ray equations for position and slowness w.r.t. the ray firing parameters $\tilde{\mu}$, using,

$$\frac{\partial}{\partial \tilde{\mu}_k} \frac{\mathrm{d}x_i}{\mathrm{d}\tau} = \frac{\mathrm{d}}{\mathrm{d}\tau} \frac{\partial x_i}{\partial \tilde{\mu}_k}, \quad \frac{\partial}{\partial \tilde{\mu}_k} \frac{\mathrm{d}p_i}{\mathrm{d}\tau} = \frac{\mathrm{d}}{\mathrm{d}\tau} \frac{\partial p_i}{\partial \tilde{\mu}_k}, \tag{3.60}$$

where $\tilde{\mu}_k,\ k = 1, 2$ refers to the elements of $\tilde{\mu}$. There is no need to calculate the elements $\partial x_i / \partial \tau$ as these become ordinary derivatives along the ray and are given by (3.48). The derived ray equations are as follows:

$$\frac{\mathrm{d}y_{ik}}{\mathrm{d}\tau} = \left[(\partial_n T_{ij} p_j) + \partial_n (M_i(\boldsymbol{x})/a(\boldsymbol{x})^2) \right] y_{nk} + T_{ij} z_{jk}, \tag{3.61}$$

$$\begin{aligned} \frac{\mathrm{d}z_{ik}}{\mathrm{d}\tau} = \left[-\frac{1}{2} p_j \left(\partial_n \partial_i T_{j\ell} \right) p_\ell - p_j \partial_n \partial_i (M_j(\boldsymbol{x})/a(\boldsymbol{x})^2) + \frac{1}{2} \partial_n \partial_i (a(\boldsymbol{x})^{-2}) \right] y_{nk} + \dots \\ \dots + \left[-(\partial_i T_{j\ell}) p_\ell - \partial_i (M(\boldsymbol{x})_j / a(\boldsymbol{x})^2) \right] z_{jk}, \end{aligned} \tag{3.62}$$

In order to distinguish between the derived elements, $y_{ik} = \partial x_i / \partial \tilde{\mu}_k$ are known as the geodesic elements and $z_{ik} = \partial p_i / \partial \tilde{\mu}_k$ are the conjugate elements. The initial conditions are found in the same way as the DRE: derivatives are taken w.r.t. the initial conditions (3.51),

$$y_{ik}(0) = 0 \quad \forall i, k. \tag{3.63}$$

$$\begin{aligned} z_{ik}(0) &= \frac{\partial \sigma_s}{\partial \tilde{\mu}_k} T^{-1}_{s_{ij}} \tilde{\nu}_{s_j} + \sigma_s T^{-1}_{s_{ij}} \frac{\partial \tilde{\nu}_{s_j}}{\partial \tilde{\mu}_k} \\ &= \sigma_s^3 \left(M_{s_j} \frac{\partial \tilde{\nu}_{s_j}}{\partial \tilde{\mu}_k} \right) \left[M_{s_i} - (\tilde{\nu}_{s_k} M_{s_k}) \tilde{\nu}_{s_i} \right] + \sigma_s \frac{\partial \tilde{\nu}_{s_i}}{\partial \tilde{\mu}_k}, \end{aligned} \tag{3.64}$$

where,

$$\frac{\partial \sigma_s}{\partial \tilde{\mu}_k} = -\sigma_s^3 \left(\tilde{\nu}_{s_i} M_{s_i}\right) \left(M_{s_j} \frac{\partial \tilde{\nu}_{s_j}}{\partial \tilde{\mu}_k}\right), \tag{3.65}$$

has been used.

3.4 Complex ray tracing

When dealing with complex rays every quantity in the ray tracing routine must be allowed to go complex. Complex ray tracing may proceed by directly integrating equations (3.48)-(3.50) and (3.60)-(3.61) using a complex step as in Egorchenkov & Kravtsov [39], however it is not so straightforward to generalise this method to arbitrary complex paths in practice. Additionally, many in-built ode solvers will not be able to cope with the extension to complex numbers, particularly as many step-size and error conditions will be violated. Instead it is preferable to split the equations into their real and imaginary parts using a real parameterisation of the complex path. This results in a system double the size of the original.

According to equations (3.48), (3.61) et seq., a generic ray quantity χ_i is propagated along a ray via the first order ode,

$$\frac{\mathrm{d}\chi_i}{\mathrm{d}\tau} = h(\chi_i, \boldsymbol{\chi}, \tau), \quad \text{with initial condition,} \quad \chi_i(0) = \chi_{i_s}, \tag{3.66}$$

where $\boldsymbol{\chi}$ represents all other dependent ray quantities that may appear in the LHS of (3.48)-(3.50) and (3.60)-(3.61). The parameterisation is effected by recognising that whenever $\tau \in \mathbb{C}$ a real monotonically increasing variable $s_\tau = [0, 1]$ may used to represent the path as,

$$\tau = f_1(s_\tau) + \mathrm{i} f_2(s_\tau), \tag{3.67}$$

where $f_1, f_2 \in \mathbb{R}$. Thus, $\mathrm{Re}(\tau_R) = f_1(1)$ and $\mathrm{Im}(\tau_R) = f_2(1)$. Then we can think of τ_R as the vector $[\mathrm{Re}(\tau_R), \mathrm{Im}(\tau_R)]$. The variable χ_i is then split into real and imaginary parts, i.e., $\chi_i = \chi_{i_{\mathrm{Re}}} + \mathrm{i}\chi_{i_{\mathrm{Im}}}$ so that coupled with (3.67), (3.66) may be expressed as the real o.d.e system,

$$\begin{aligned}
\frac{\mathrm{d}\chi_{i_{\mathrm{Re}}}}{\mathrm{d}s_\tau} &= f_1'(s_\tau)\mathrm{Re}(h(\chi_i, \boldsymbol{\chi}, s_\tau)) - f_2'(s_\tau)\mathrm{Im}(h(\chi_i, \boldsymbol{\chi}, s_\tau)), \quad \chi_{i_{\mathrm{Re}}}(0) = \mathrm{Re}(\chi_{i_s}), \\
\frac{\mathrm{d}\chi_{i_{\mathrm{Im}}}}{\mathrm{d}s_\tau} &= f_2'(s_\tau)\mathrm{Re}(h(\chi_i, \boldsymbol{\chi}, s_\tau)) + f_1'(s_\tau)\mathrm{Im}(h(\chi_i, \boldsymbol{\chi}, s_\tau)), \quad \chi_{i_{\mathrm{Im}}}(0) = \mathrm{Im}(\chi_{i_s}),
\end{aligned} \tag{3.68}$$

where a prime denotes differentiation w.r.t s_τ. The only equation that does not have this form is the complex phase S, since the $\mathrm{d}\tau/\mathrm{d}s_\tau$ term cancels out in (3.50). The

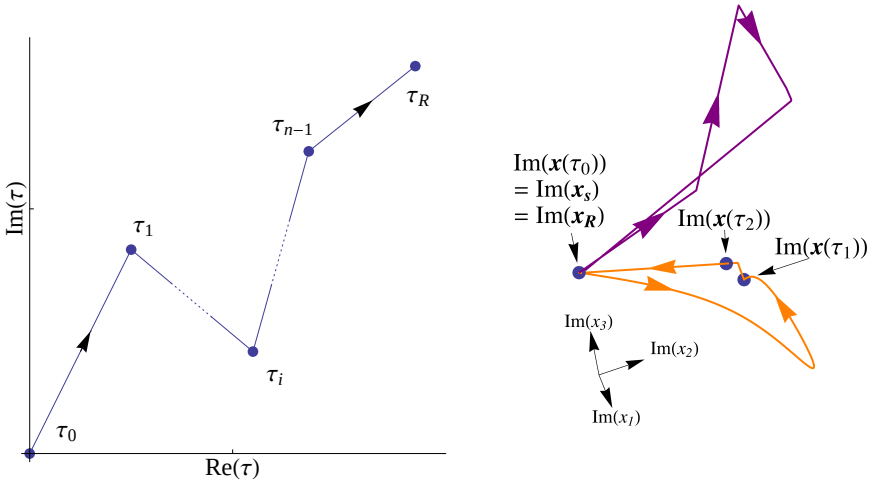

(a) Piecewise τ-integration path.

(b) Example of standard (purple) and piecewise (piecewise) ray paths. Images of additional nodes shown on the latter.

FIGURE 3.1: Piecewise τ integration path and its image $\mathrm{Im}(\boldsymbol{x}(\tau))$. (a) The τ-integration path composed of n contiguous sections and joined at nodes τ_i and τ_{i-1}. (b) $\mathrm{Im}(\boldsymbol{x}(\tau))$ for a standard (purple) and piecewise (orange) path, showing the images of the τ nodes delimiting segments of the paths.

complex phase equation can be expressed as,

$$\begin{aligned}\frac{\mathrm{d}S_{\mathrm{Re}}}{\mathrm{d}s_\tau} &= \mathrm{Re}(h(S,\boldsymbol{\chi},s_\tau)), \quad S_{\mathrm{Re}}(0)=0,\\ \frac{\mathrm{d}S_{\mathrm{Im}}}{\mathrm{d}s_\tau} &= \mathrm{Im}(h(S,\boldsymbol{\chi},s_\tau)), \quad S_{\mathrm{Im}}(0)=0.\end{aligned} \tag{3.69}$$

Here the simplest parameterisation possible is used, i.e., a straight line between $\tau = 0$ and $\tau = \tau_R$, and is known henceforth as the standard path. Explicitly the standard path is parameterised so $\tau = [\mathrm{Re}(\tau_0), \mathrm{Im}(\tau_0)] + s[\mathrm{Re}(\tau_R) - \mathrm{Re}(\tau_0), \mathrm{Im}(\tau_R) - \mathrm{Im}(\tau_0)]$, and $f'_{1,2}$ are constant. It is, however, possible to integrate along any piecewise smooth path joining the integration endpoints given that there no singularities obstructing path deformation. For example a piecewise path with straight lines (i.e., a 1-chain, Hatcher [145]) is constructed by partitioning the ray path into n contiguous segments delimited by nodes $\tau_i = [\mathrm{Re}(\tau_i), \mathrm{Im}(\tau_i)]$ and $\tau_{i+1} = [\mathrm{Re}(\tau_{i+1}), \mathrm{Im}(\tau_{i+1})]$ as shown in Fig. 3.1(a), so the ray path can be expressed as $\tau = [\tau_0, \tau_1] + \ldots + [\tau_i, \tau_{i+1}] + \ldots + [\tau_{n-1}, \tau_R]$. Then the parameterised path between each node is (in vector form) $\tau = \tau_i + s\partial[\tau_i, \tau_{i+1}] = \tau_i + s(\tau_{i+1} - \tau_i)$.[1] The initial conditions for each segment are trivially those at the end of the last segment.

An example of partitioning the integration path into segments for a real observer is shown in Fig. 3.1(b) depicting only the imaginary part of the trajectory. For a real observer the

[1] ∂ here finds the boundary of the chain.

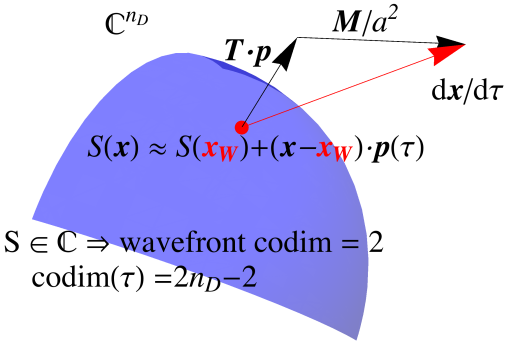

FIGURE 3.2: Complex wavefront as a codimension object.

imaginary parts of the ray will form loops starting and ending at the origin. These loops may appear to be discontinuous (even in the standard path case), but this is a matter of resolution as the ray undergoes rapid changes in its imaginary part.[2] The piecewise path shows the position of two nodes $|\tau_1| = O(1)$ and $|\tau_2| = O(10)$ along the integration path to $|\tau_R| = O(100)$. An interesting observation is that the majority of the imaginary loop has been completed by τ_2. Another observation is that nodes lying just off of the standard path can produce distinctly different results to that of the standard path, and these paths are in no way predictable from the standard path.

While the above deals with an algorithm for calculate a complex ray between two points in τ it doesn't explain why only τ is necessary to explore the field. To do this we need to introduce the concept of codimension. Codimension is a relative concept defined for one object inside another, and one central to this thesis. Simply, the codimension is defined as the difference between the dimension of the object and the dimension of the space it lies in. This means that the codimension is equal to the number of equations required to describe the object within the space it is embedded in, e.g., a codim $= 1$ object in $\mathbb{R}^3$ is a 2-surface with one equation $f(\boldsymbol{x}) = c$. This applies to rays in the following manner in $\mathbb{C}^{n_D}$ as shown in Fig. 3.2. Given that a wavefront is a surface of constant phase $S(\boldsymbol{x}) = c$, then this defines two equations for the real and imaginary parts of S, and thus gives codim $= 2$. A codim $= 2$ surface is a $(2n_D - 2)$-dimensional hypersurface which leaves two free dimensions. It is these extra two dimensions that are spanned by the complex τ allowing the wavefront to move.

[2]Rapid changes are not limited to just the imaginary part of $\boldsymbol{x}(\tau)$.

3.5 Efficiency of ray mathematics and normalisation

3.5.1 Relating $\hat{g}_5$ to $\hat{g}_{5\eta}$ and other components

The generic ray contribution given by (3.59) solves the inner equation with source given by (3.27) and not (3.26). Using the delta function properties and their application to the ray theory solution found in Appendix C this is straightforward. The components $\hat{g}_{5\eta},\ \eta = 1, \ldots, 4$, are related to $\hat{g}_{\text{in}}$ using the vector,

$$\hat{g}_{5\eta} = \mathscr{A}_\eta \hat{g}_5 = \{\partial/\partial x_{s_1}, \partial/\partial x_{s_2}, \partial/\partial x_{s_3}, -\mathrm{i}\omega - \bar{u}_j(\boldsymbol{x}_s)\partial/\partial x_{s_j}\}\hat{g}_5, \tag{3.70}$$

which using ray theory leads to,

$$\hat{g}_{5\eta} = \mathscr{A}_\eta \hat{g}_5 = \{-\mathrm{i}k_0 p_{s_1}, -\mathrm{i}k_0 p_{s_2}, -\mathrm{i}k_0 p_{s_3}, -\mathrm{i}\omega + \mathrm{i}k_0 \bar{u}_j(\boldsymbol{x}_s)p_{s_j}\}\hat{g}_5. \tag{3.71}$$

The velocity components $g_{i\eta}$ can be found using (3.43) and (3.47), i.e.,

$$\hat{g}_{i\eta} = \frac{p_i a^2}{\bar{\rho}\bar{c}^2(1 - M_j p_j)}\hat{g}_{5\eta}. \tag{3.72}$$

3.5.2 Normalising the Flow Factor

So far in this chapter we have shown that using ray theory we need only consider one component of the vector Green's function, and that all other components can be calculate according to formulae shown in previous sections. Considering only the pressure components, then depending on the problem at hand the simplest component will be chosen. The Flow Factor is calculated by normalising the Green's function (from now on we refer to the chosen component as the Green's function) w.r.t. a solution of the Helmholtz equation in the appropriate dimension (e.g., $n_D = 2, 3$),

$$\left(\nabla^2 + k_0^2\right)\mathscr{G}_\omega^{(n_D)} = \delta(\boldsymbol{x} - \boldsymbol{x}_s), \tag{3.73}$$

with solutions and large $k_0|\boldsymbol{x} - \boldsymbol{x}_s| \gg 1$ asymptotics,

$$\mathscr{G}_\omega^{(2)} = \begin{cases} \frac{1}{4\mathrm{i}}\mathrm{H}_0^{(1)}(k_0|\boldsymbol{x} - \boldsymbol{x}_s|), \\ \sim \frac{\mathrm{e}^{\mathrm{i}k_0|\boldsymbol{x}-\boldsymbol{x}_s|}}{4\mathrm{i}k_0^{1/2}|\boldsymbol{x}-\boldsymbol{x}_s|^{1/2}} \end{cases} \qquad \mathscr{G}_\omega^{(3)} = \begin{cases} -\frac{\mathrm{e}^{\mathrm{i}k_0|\boldsymbol{x}-\boldsymbol{x}_s|}}{4\pi|\boldsymbol{x}-\boldsymbol{x}_s|}, \\ \sim -\frac{\mathrm{e}^{\mathrm{i}k_0|\boldsymbol{x}-\boldsymbol{x}_s|}}{4\pi|\boldsymbol{x}-\boldsymbol{x}_s|} \end{cases} \tag{3.74}$$

Where an analytical solution exists in the far-field use will be made of the large argument Green's functions. For numerical computations using ray theory the same large argument solution will be used. This is allowed because the ray solution is valid at distances

greater than $O(k_0^{-1})$, the same region of validity as the asymptotics in (3.74). Choosing the normalisation is arbitrary up to a constant and meant purely to eliminate spherical spreading.

3.5.3 Two-point correlations

The simplifications that may be gained using the ray method are best demonstrated using the two-point correlations. It is these correlations that are of physical interest and are used for comparison with experiment.

The pressure $p'(\boldsymbol{x},t)$ at any point may be found using (3.21),

$$p'(\boldsymbol{x},t) = \frac{1}{2\pi}\int_{-\infty}^{\infty}\int_{V'} \hat{g}_{5i}(\boldsymbol{x}|\boldsymbol{x}'_s,\omega')\hat{s}_i(\boldsymbol{x}'_s,\omega')\mathrm{e}^{-\mathrm{i}\omega' t}\,\mathrm{d}^3\boldsymbol{x}'_s\mathrm{d}\omega', \tag{3.75}$$

where i ranges from 1 to 4. However, in order to shift the correlation of p' onto the source only, it is expedient to proceed from,

$$p'(\boldsymbol{x},t) = \int_{t''=-\infty}^{\infty}\int_{V''} g_{5i}(\boldsymbol{x},t|\boldsymbol{x}''_s,t''_s)s_i(\boldsymbol{x}''_s,t''_s)\,\mathrm{d}^3\boldsymbol{x}''_s\mathrm{d}t''_s. \tag{3.76}$$

Forming a pressure correlation (Goldstein [9]) noting as in Goldstein & Leib [146] that temporal variables occur as differences (e.g., $t-t''_s$) in the argument of the Green's function,

$$\begin{aligned}&\Gamma(\boldsymbol{x},\tau) = \overline{p'(\boldsymbol{x},t)p'(\boldsymbol{x},t+\tau)} = \\ &\frac{1}{2T}\int_{-T}^{T}\int_{t'=-\infty}^{\infty}\int_{t''=-\infty}^{\infty}\int_{V'}\int_{V''} g_{5i}(\boldsymbol{x},t-t''_s|\boldsymbol{x}''_s)g_{5j}(\boldsymbol{x},t+\tau-t'_s|\boldsymbol{x}'_s) \\ &\qquad\qquad \times s_i(\boldsymbol{x}''_s,t''_s)s_j(\boldsymbol{x}'_s,t'_s)\,\mathrm{d}^3\boldsymbol{x}''_s\mathrm{d}^3\boldsymbol{x}'_s\mathrm{d}t''\mathrm{d}t'\mathrm{d}t.\end{aligned} \tag{3.77}$$

Then making the change of variables $t_a = t - t''_s$ and $t_b = t''_s - t'_s$ leads to,

$$\begin{aligned}&\Gamma(\boldsymbol{x},\tau) = \\ &\int_{t_b=-\infty}^{\infty}\int_{t_a=-\infty}^{\infty}\int_{V'}\int_{V''} g_{5i}(\boldsymbol{x},t_a|\boldsymbol{x}''_s)g_{5j}(\boldsymbol{x},t_a+t_b+\tau|\boldsymbol{x}'_s)\overline{s_i(\boldsymbol{x}''_s,t'_s+t_b)s_j(\boldsymbol{x}'_s,t'_s)}\,\mathrm{d}^3\boldsymbol{x}''_s\mathrm{d}^3\boldsymbol{x}'_s\mathrm{d}t_a\mathrm{d}t_b,\end{aligned} \tag{3.78}$$

where,

$$\overline{s_i(\boldsymbol{x}''_s,t'_s+t_b)s_j(\boldsymbol{x}'_s,t'_s)} = \frac{1}{2T}\int_{-T}^{T} s_i(\boldsymbol{x}''_s,t'_s+t_b)s_j(\boldsymbol{x}'_s,t'_s)\,\mathrm{d}t'_s, \tag{3.79}$$

The Fourier transform (giving a Fourier pair of $\mathscr{F}_\omega$ and $\mathscr{F}_\tau^{-1}$) of (3.78) is proportional to the spectral density function $I_\omega(\boldsymbol{x})$,

$$\begin{aligned} I_\omega(\boldsymbol{x}) &= \mathscr{F}_\omega\left\{\Gamma(\boldsymbol{x},\tau)\right\} = \\ &\frac{1}{\bar{\rho}_\infty \bar{c}_\infty}\int_{t_b=-\infty}^{\infty}\int_{V'}\int_{V''}\mathscr{F}_\omega\left\{\int_{t_a=-\infty}^{\infty} g_{5i}(\boldsymbol{x},t_a|\boldsymbol{x}_s'')g_{5j}(\boldsymbol{x},t_a+t_b+\tau|\boldsymbol{x}_s')\,\mathrm{d}t_a\right\} \\ &\qquad\times \mathrm{e}^{-\mathrm{i}\omega t_b}\overline{s_i(\boldsymbol{x}_s'',t_s'+t_b)s_j(\boldsymbol{x}_s',t_s')}\,\mathrm{d}^3\boldsymbol{x}_s''\mathrm{d}^3\boldsymbol{x}_s'\mathrm{d}t_b, \end{aligned} \tag{3.80}$$

where the Fourier pair inside the integral above corresponds to $\mathscr{F}_\omega$ and $\mathscr{F}_{t_b+\tau}^{-1}$. Given that the Fourier transform of a correlation integral, say $\int_{-\infty}^{\infty} f(t+\tau)g(t)\,\mathrm{d}t$, is just $\mathscr{F}_\omega(f(t))\mathscr{F}_\omega^*(g(t))$, $\omega\in\mathbb{R}$; we have,

$$\begin{aligned} I_\omega(\boldsymbol{x}) = &\\ &\frac{1}{\bar{\rho}_\infty \bar{c}_\infty}\int_{V'}\int_{V''}\hat{g}_{5i}^*(\boldsymbol{x}|\boldsymbol{x}_s'',\omega)\hat{g}_{5j}(\boldsymbol{x}|\boldsymbol{x}_s',\omega) \\ &\int_{t_b=-\infty}^{\infty}\mathrm{e}^{-\mathrm{i}\omega t_b}\overline{s_i(\boldsymbol{x}_s'',t_s'+t_b)s_j(\boldsymbol{x}_s',t_s')}\,\mathrm{d}t_b\,\mathrm{d}^3\boldsymbol{x}_s''\mathrm{d}^3\boldsymbol{x}_s' \end{aligned} \tag{3.81}$$

which could be written as,

$$\begin{aligned} I_\omega(\boldsymbol{x}) = &\\ &\frac{1}{\bar{\rho}_\infty \bar{c}_\infty}\int_{V'}\int_{V''}\hat{g}_{5i}^*(\boldsymbol{x}|\boldsymbol{x}_s'',\omega)\hat{g}_{5j}(\boldsymbol{x}|\boldsymbol{x}_s',\omega)\hat{s}_i^*(\boldsymbol{x}_s'',\omega)\hat{s}_j(\boldsymbol{x}_s',\omega)\,\mathrm{d}^3\boldsymbol{x}_s''\mathrm{d}^3\boldsymbol{x}_s', \end{aligned} \tag{3.82}$$

if we proceeded to Fourier transform the source correlation since,[3]

$$\int_{t_b=-\infty}^{\infty}\mathrm{e}^{-\mathrm{i}\omega t_b}\overline{s_i(\boldsymbol{x}_s'',t_s'+t_b)s_j(\boldsymbol{x}_s',t_s')}\,\mathrm{d}t_b = (\hat{s}_i(\boldsymbol{x}_s'',\omega)\hat{s}_j^*(\boldsymbol{x}_s',\omega))^* = \hat{s}_i^*(\boldsymbol{x}_s'',\omega)\hat{s}_j(\boldsymbol{x}_s',\omega). \tag{3.83}$$

As an aside, we can use (3.82) to derive a directivity factor $\mathscr{D}_\omega^{(c)}$ that will be used in later chapters to enforce the relevance of the ring source model as used in Chap. 2. First the separation vector $\boldsymbol{\eta}$ is introduced via $\boldsymbol{\eta}=\boldsymbol{x}_s''-\boldsymbol{x}_s'$ so that the first spatial integral of (3.82) looks like,

$$\begin{aligned} \mathscr{D}_\omega^{(c)}(\boldsymbol{\eta}) = &\\ &\int_{V'}\mathscr{A}_i^*\hat{g}_5^*(\boldsymbol{x}|\boldsymbol{x}_s',\omega'')\mathscr{A}_j\hat{g}_5(\boldsymbol{x}|\boldsymbol{x}_s'+\boldsymbol{\eta},\omega'')\hat{s}_i^*(\boldsymbol{x}_s',\omega'')\hat{s}_j(\boldsymbol{x}_s'+\boldsymbol{\eta},,\omega'')\,\mathrm{d}^3\boldsymbol{x}_s'. \end{aligned} \tag{3.84}$$

Physically, the new variable $\boldsymbol{\eta}$ measures the distance between two points of the correlation. A key point to note for the future use of (3.84) is that it is the combination

[3]Note the use of a standard Fourier transform for s_i where $\int_{-\infty}^{\infty}|s_i(t)|^2\,\mathrm{d}t<\infty$. Previously we used a truncated integral with $T\to\infty$ to allow the statistics of the correlation to converge.

of Green's functions, i.e., Green's function with complex conjugate, that is important. Asymmetries and diffraction patterns that appear in this combination have implications for I_ω as well as $\mathscr{D}_\omega^{(c)}$. Furthermore, the evaluation of (3.84) at $\boldsymbol{\eta} = \mathbf{0}$ is even more significant as the integrand can be treated as the product of a slow function (the propagator) and fast function (the source), as will be shown below.

Returning to the acoustic spectra we can show via (3.71) the large simplifications that can be made to the computation of I_ω when rays are employed.

$$\begin{aligned} I_\omega(\boldsymbol{x}) = & \\ & \frac{1}{\bar{\rho}_\infty \bar{c}_\infty} \int_{V'} \int_{V''} \underbrace{\mathscr{A}_i^* \hat{g}_5^*(\boldsymbol{x}|\boldsymbol{x}'_s, \omega'') \mathscr{A}_j \hat{g}_5(\boldsymbol{x}|\boldsymbol{x}''_s, \omega'')}_{\text{Only } \hat{g}_5 \text{ required}} \\ & \int_{t_b=-\infty}^{\infty} \mathrm{e}^{-\mathrm{i}\omega t_b} \overline{s_i(\boldsymbol{x}''_s, t'_s + t_b) s_j(\boldsymbol{x}'_s, t'_s)} \, \mathrm{d}t_b \, \mathrm{d}^3\boldsymbol{x}''_s \mathrm{d}^3\boldsymbol{x}'_s. \end{aligned} \tag{3.85}$$

Clearly, once ray $\hat{g}_5$ is computed then $\hat{g}_5^*$ is readily computed. Thus the 8 components required just to compute the pressure correlation have been replaced by one. In the next section we make further simplifications to (3.85), consider two source models, and justify our interest in complex rays.

3.5.3.1 Source models for correlation integrals and propagator simplifications

The first simplifications can be motivated by introducing a source correlation model into (3.81) once it is rewritten using the separation vector $\boldsymbol{\eta}$, i.e.,[4]

$$\begin{aligned} & I_\omega(\boldsymbol{x}) = \\ & \frac{1}{\bar{\rho}_\infty \bar{c}_\infty} \int_{V'} \int_{V''} \int_{t_b=-\infty}^{\infty} \hat{g}_{5i}^*(\boldsymbol{x}|\boldsymbol{x}'_s + \boldsymbol{\eta}, \omega) \hat{g}_{5j}(\boldsymbol{x}|\boldsymbol{x}'_s, \omega) \mathrm{e}^{-\mathrm{i}\omega t_b} \overline{s_i(\boldsymbol{x}'_s + \boldsymbol{\eta}, t'_s + t_b) s_j(\boldsymbol{x}'_s, t'_s)} \, \mathrm{d}t_b \, \mathrm{d}^3\boldsymbol{\eta} \mathrm{d}^3\boldsymbol{x}'_s. \end{aligned} \tag{3.86}$$

Before introducing explicit forms for the source correlations, we know qualitatively that a good approximation is given by a Gaussian (Batchelor [147], Lilley [13]) in the separation coordinates $\boldsymbol{\eta}$ and correlation time t_b, even though the true behaviour is not Gaussian. Regardless, this model means that the integral (3.86) w.r.t. $\boldsymbol{\eta}$ contains both a slow factor given by the propagators, and a fast factor given by the source correlation. The integrand can therefore be approximated to some extent by appropriate manipulation of $\hat{g}_{5i}^*(\boldsymbol{x}|\boldsymbol{x}'_s + \boldsymbol{\eta}, \omega) \hat{g}_{5j}(\boldsymbol{x}|\boldsymbol{x}'_s, \omega)$. To do this we consider the source position $\boldsymbol{x}'_s$ to be perturbed by a small vector parameter $\boldsymbol{\epsilon}$ for generality.

[4] V'' now denotes the domain for $\boldsymbol{\eta}$.

For two sources near each other separated by a small distance $\boldsymbol{\epsilon}$, $|\boldsymbol{\epsilon}| \ll 1$ say, we are interested in the change of phase for an observer $\boldsymbol{x}$ in the far-field due to the separation. The reason we focus purely on phase is that it pertains to the controlling factor (the exponential) of the ray solution; whereas amplitude does not. Expressing the source position $\boldsymbol{x}_s^{(2)}$ in terms of the nearby source position and separation vector as $\boldsymbol{x}_s^{(1)} + \boldsymbol{\epsilon}$, the phase is Taylor expanded as,

$$\begin{aligned} S(\boldsymbol{x}|\boldsymbol{x}_s^{(2)}) = S(\boldsymbol{x}|\boldsymbol{x}_s^{(1)} + \boldsymbol{\epsilon}) &= S(\boldsymbol{x}|\boldsymbol{x}_s^{(1)}) + \epsilon_i \partial_{x_{s_i}} S(\boldsymbol{x}|\boldsymbol{x}_s^{(1)}) + O(|\boldsymbol{\epsilon}|^2), \\ &= S(\boldsymbol{x}|\boldsymbol{x}_s^{(1)}) - \epsilon_i \partial_{x_i} S(\boldsymbol{x}|\boldsymbol{x}_s^{(1)}) + O(|\boldsymbol{\epsilon}|^2), \end{aligned} \tag{3.87}$$

which for a small source separation vector $\boldsymbol{\epsilon}$ leads to,

$$S(\boldsymbol{x}|\boldsymbol{x}_s^{(2)}) \approx S(\boldsymbol{x}|\boldsymbol{x}_s^{(1)}) - \boldsymbol{\epsilon} \cdot \boldsymbol{p}, \tag{3.88}$$

where $\boldsymbol{p}$ is the wavefront normal evaluated at the observer position. Of course, if the ray is complex then $\boldsymbol{p}$ may also be complex, even if the observer is real. This may lead to the Taylor expansion changing the dominancy of a ray if $\boldsymbol{\epsilon}$ is too large. If an anti-Stokes line is crossed then this is unacceptable: however, we make the assumption that the small parameter is small enough to make no changes in a rays dominancy and neglect the imaginary part of $\boldsymbol{p}$. Even so, $\boldsymbol{p}$ pertains to a particular ray and we will deal with sums of rays (see next chapter) when constructing a Green's function; hence this factor cannot be pulled out of a ray sum. If the observer is in the far-field then one might assume that $\boldsymbol{p} \sim \boldsymbol{x}_R/R$. This factor can be pulled out. Considering this approximation to $\boldsymbol{p}$ then the Green's function can be approximated by,

$$\hat{g}(\boldsymbol{x}|\boldsymbol{x}_s^{(2)}) = \hat{g}(\boldsymbol{x}|\boldsymbol{x}_s^{(1)}+\boldsymbol{\epsilon}) = \sum_{n=1}^{N} A_n(\boldsymbol{x}|\boldsymbol{x}^{(1)}+\epsilon)\mathrm{e}^{\mathrm{i}k_0 S_n(\boldsymbol{x}|\boldsymbol{x}^{(1)}+\epsilon)} \approx \mathrm{e}^{-\mathrm{i}k_0 \boldsymbol{\epsilon}\cdot\mathrm{Re}(\boldsymbol{p})} \sum_{n=1}^{N} A_n(\boldsymbol{x}|\boldsymbol{x}^{(1)})\mathrm{e}^{\mathrm{i}k_0 S_n(\boldsymbol{x}|\boldsymbol{x}^{(1)})}, \tag{3.89}$$

where reference to $\mathrm{Re}(\boldsymbol{p})$ is dropped for just $\boldsymbol{p}$ in future correlation integrals.

In the following we consider two correlation models to illustrate the possible use of the above approximation. The first (Case A) is similar to the acoustic analogies proposed by Lighthill [4, 5] and Goldstein [9] and employs a moving observer that travels with alongside a convected disturbance with velocity U_c; the second (Case B) is similar to that of Tam & Auriault [7] and Morris & Farassat [6], employing a fixed frame correlation.

Case A

For Case A, we switch to a reference frame travelling at the convection velocity U_c, i.e., $\boldsymbol{\xi} \equiv \boldsymbol{\eta} - \hat{\boldsymbol{\imath}} U_c t_b$ gives,

$$I_\omega(\boldsymbol{x}) = \frac{1}{\bar{\rho}_\infty \bar{c}_\infty} \int_{V'} \int_{V''} \int_{t_b=-\infty}^{\infty} \hat{g}^*_{5i}(\boldsymbol{x}|\boldsymbol{x}'_s + \boldsymbol{\xi} + \hat{\boldsymbol{\imath}} U_c t_b, \omega) \hat{g}_{5j}(\boldsymbol{x}|\boldsymbol{x}'_s, \omega) \\ \mathrm{e}^{-\mathrm{i}\omega t_b} \overline{s_i(\boldsymbol{x}'_s + \boldsymbol{\xi} + \hat{\boldsymbol{\imath}} U_c t_b, t'_s + t_b) s_j(\boldsymbol{x}'_s, t'_s)} \, \mathrm{d}t_b \, \mathrm{d}^3\boldsymbol{\xi} \mathrm{d}^3\boldsymbol{x}'_s, \tag{3.90}$$

which we can start approximating for small correlation times $t_b \ll 1$ by applying the Taylor expansion above with $\boldsymbol{\epsilon} = \hat{\boldsymbol{\imath}} U_c t_b$. Then (3.90) becomes,

$$I_\omega(\boldsymbol{x}) = \frac{1}{\bar{\rho}_\infty \bar{c}_\infty} \int_{V'} \int_{V''} \int_{t_b=-\infty}^{\infty} \hat{g}^*_{5i}(\boldsymbol{x}|\boldsymbol{x}'_s + \boldsymbol{\xi}, \omega) \hat{g}_{5j}(\boldsymbol{x}|\boldsymbol{x}'_s, \omega) \\ \mathrm{e}^{-\mathrm{i}\omega(1 - M_c \cos\theta) t_b} \overline{s_i(\boldsymbol{x}'_s + \boldsymbol{\xi} + \hat{\boldsymbol{\imath}} U_c t_b, t'_s + t_b) s_j(\boldsymbol{x}'_s, t'_s)} \, \mathrm{d}t_b \, \mathrm{d}^3\boldsymbol{\xi} \mathrm{d}^3\boldsymbol{x}'_s. \tag{3.91}$$

where $M_c = U_c/\bar{c}_\infty$, and θ remains the observer coordinate. As is well known, the $\mathrm{e}^{\mathrm{i}\omega M_c \cos\theta t_b}$ factor leads to Doppler in the Fourier transform, as can be seen below.

$$I_\omega(\boldsymbol{x}) = \frac{1}{\bar{\rho}_\infty \bar{c}_\infty} \int_{V'} \int_{V''} \hat{g}^*_{5i}(\boldsymbol{x}|\boldsymbol{x}'_s + \boldsymbol{\xi}, \omega) \hat{g}_{5j}(\boldsymbol{x}|\boldsymbol{x}'_s, \omega) H^*_{ij}(\boldsymbol{x}'_s|\boldsymbol{\xi}, \omega(1 - M_c \cos\theta)) \, \mathrm{d}^3\boldsymbol{\xi} \mathrm{d}^3\boldsymbol{x}'_s. \tag{3.92}$$

where H_{ij} is defined by,

$$H_{ij}(\boldsymbol{x}'_s|\boldsymbol{\xi}, \omega) = \int_{-\infty}^{\infty} \overline{s_i(\boldsymbol{x}'_s + \boldsymbol{\xi} + \hat{\boldsymbol{\imath}} U_c t_b, t'_s + t_b) s_j(\boldsymbol{x}'_s, t'_s)} \mathrm{e}^{\mathrm{i}\omega t_b} \, \mathrm{d}t_b. \tag{3.93}$$

If H_{ij} varies much faster with $\boldsymbol{\xi}$ than the propagator $\hat{g}_{5i}$ then it is safe to make the approximation $\hat{g}_{5i}(\boldsymbol{x}|\boldsymbol{x}'_s + \boldsymbol{\xi}, \omega) \approx \hat{g}_{5i}(\boldsymbol{x}|\boldsymbol{x}'_s \omega)$, so that,

$$I_\omega(\boldsymbol{x}) \approx \frac{1}{\bar{\rho}_\infty \bar{c}_\infty} \int_{V'} \hat{g}^*_{5i}(\boldsymbol{x}|\boldsymbol{x}'_s, \omega) \hat{g}_{5j}(\boldsymbol{x}|\boldsymbol{x}'_s, \omega) \Psi^*_{ij}(\boldsymbol{x}'_s|\omega(1 - M_c \cos\theta)) \, \mathrm{d}^3\boldsymbol{x}'_s, \tag{3.94}$$

where,

$$\Psi_{ij}(\boldsymbol{x}'_s|\omega) = \int_{V''} H_{ij}(\boldsymbol{x}'_s|\boldsymbol{\xi}, \omega) \, \mathrm{d}^3\boldsymbol{\xi}. \tag{3.95}$$

Then defining the intensity $I_\omega(\boldsymbol{x}|\boldsymbol{x}'_s)$ at $\boldsymbol{x}$ due to a point source $\boldsymbol{x}'_s$ gives,

$$I_\omega(\boldsymbol{x}|\boldsymbol{x}'_s) = \hat{g}^*_{5i}(\boldsymbol{x}|\boldsymbol{x}'_s, \omega) \hat{g}_{5j}(\boldsymbol{x}|\boldsymbol{x}'_s, \omega) \Psi^*_{ij}(\boldsymbol{x}'_s|\omega(1 - M_c \cos\theta)). \tag{3.96}$$

The total intensity is then given by,

$$I_\omega(\boldsymbol{x}) = \int_{V'} I_\omega(\boldsymbol{x}|\boldsymbol{x}'_s)\,\mathrm{d}^3\boldsymbol{x}'_s. \tag{3.97}$$

If the source term s_i is such that it has the form of a gradient or divergence then these operators ($\mathscr{A}_i^s$, say) can be switched to the Green's function by integrating (3.76) by parts:

$$I_\omega(\boldsymbol{x}|\boldsymbol{x}'_s) = \begin{cases} \mathscr{A}_i^{s*}\hat{g}^*_{5i}(\boldsymbol{x}|\boldsymbol{x}'_s,\omega)\mathscr{A}_j^s\hat{g}_{5j}(\boldsymbol{x}|\boldsymbol{x}'_s,\omega)\Psi^*(\boldsymbol{x}'_s|\omega(1-M_c\cos\theta)), & s_i = \frac{\partial}{\partial x'_{s_i}}s,\ \mathscr{A}_i^s = \frac{\partial}{\partial x'_{s_i}} \\ \mathscr{A}_k^{s*}\hat{g}^*_{5i}(\boldsymbol{x}|\boldsymbol{x}'_s,\omega)\mathscr{A}_l^s\hat{g}_{5j}(\boldsymbol{x}|\boldsymbol{x}'_s,\omega)\Psi^*_{ijkl}(\boldsymbol{x}'_s|\omega(1-M_c\cos\theta)), & s_i = \frac{\partial}{\partial x'_{s_k}}s_{ik},\ \mathscr{A}_k^s = \frac{\partial}{\partial x'_{s_k}} \end{cases}, \tag{3.98}$$

In the case of a divergence operator (first case above) the (cross)-spectral density function, $H_{ij} \to H$ can be given as (Self [148]),

$$H(\boldsymbol{x}'_s|\boldsymbol{\xi},\omega) = \sqrt{\pi}\tau_s u_s^4 \exp\left(-\frac{1}{4}\tau_s^2\omega^2\right)\exp\left(-\frac{\eta_1^2}{l_1^2}-\frac{\eta_2^2}{l_2^2}-\frac{\eta_3^2}{l_3^2}\right), \tag{3.99}$$

so that,

$$\Psi(\boldsymbol{x}'_s|\omega) = \pi^2 u_s^4\tau_s l_1 l_2 l_3 \exp\left(-\frac{1}{4}\tau_s^2\omega^2\right), \tag{3.100}$$

where τ_s measures the eddy's lifetime (not to be confused with the ray tracing parameter), l_1, l_2, l_3 are three lengthscales characterising the size of the eddies, and u_s is a velocity characteristic of the turbulence. In the use of u_s it should be noted that we make an assumption about the source we are modelling. It should be clear that by including a velocity scaling, it is implied that the source is a function of fluctuating velocity. Each of these scales is a function of source position $\boldsymbol{x}'_s$.

Case B

There are two subcases to Case B: the first neglects $\boldsymbol{\eta}$ inside the Green's function as above; the second Taylor expands the Green's function for small separation distances $|\boldsymbol{\eta}| \ll 1$. In both cases the source correlation is of the form:

$$\overline{s_i(\boldsymbol{x}'_s+\boldsymbol{\eta},t'_s+t_b)s_j(\boldsymbol{x}'_s,t'_s)} = \frac{q_s^2}{\bar{c}^2}\exp\left(-\frac{|\eta_1|}{\overline{u}_1\tau_s}-\frac{1}{l_s^2}\left[(\eta_1-\overline{u}_1 t_b)^2+\eta_2^2+\eta_3^2\right]\right), \tag{3.101}$$

which subtlety different from that in Case A, which is Gaussian in all correlation variables. Here, τ_s is as before, l_s is an eddy lengthscale, q_s^2 is a measure of rms fluctuating kinetic energy, and $\bar{c}$ the mean sound speed. Note that the above correlation is given by Morris & Farassat [6] and is similar to that of Tam & Auriault [7]. In both subcases

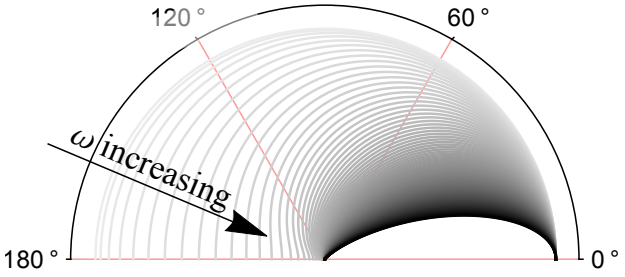

FIGURE 3.3: Gaussian source spectra directivity, $\exp\left(-\frac{1}{4}\tau_s^2\omega^2(1-M_c\cos\theta)^2\right)$, as function of ω and θ; nominally set $\tau_s = 1$, $M_c = 0.9$. As the source frequency ω increases (darker lines) the source begins to beam strongly in the downstream θ-small direction.

the relevant version of (3.86) is,

$$\sqrt{\pi}\int_{V'}\int_{V''}\frac{l_s}{\overline{u}_1}\frac{q_s^2}{\overline{c}^2}\mathscr{A}_i^{s*}\hat{g}_{5i}^*(\boldsymbol{x}|\boldsymbol{x}'_s+\boldsymbol{\eta},\omega)\mathscr{A}_j^s\hat{g}_{5j}(\boldsymbol{x}|\boldsymbol{x}'_s,\omega)\mathrm{e}^{-\mathrm{i}\omega\eta_1/\overline{u}_1}\mathrm{e}^{-l_s^2\omega^2/4\pi^2}\mathrm{e}^{-|\eta_1|/\overline{u}\tau_s}\mathrm{e}^{-\eta_2^2/l_s^2-\eta_3^2/l_s^2}\mathrm{d}^3\boldsymbol{\eta}\mathrm{d}^3\boldsymbol{x}'_s, \tag{3.102}$$

then when $\boldsymbol{\eta}$ is neglected in $\hat{g}_{5i}^*(\boldsymbol{x}|\boldsymbol{x}'_s+\boldsymbol{\eta},\omega)$, the integral (3.102) can be reduced to,

$$\int_{V'}\frac{2\pi^{3/2}l_s^3\tau_s}{1+\omega^2\tau_s^2}\frac{q_s^2}{\overline{c}^2}\mathscr{A}_i^{s*}\hat{g}_{5i}^*(\boldsymbol{x}|\boldsymbol{x}'_s,\omega)\mathscr{A}_j^s\hat{g}_{5j}(\boldsymbol{x}|\boldsymbol{x}'_s,\omega)\mathrm{e}^{-l_s^2\omega^2/4\pi^2}\,\mathrm{d}^3\boldsymbol{x}'_s, \tag{3.103}$$

when we don't neglect $\boldsymbol{\eta}$, but use a Taylor expansion (as above) then we have,

$$\int_{V'}\frac{2\pi^{3/2}l_s^3\tau_s}{1+\omega^2\tau_s^2(1-\overline{u}_1p_1/\overline{c}_\infty)^2}\frac{q_s^2}{\overline{c}^2}\mathscr{A}_i^{s*}\hat{g}_{5i}(\boldsymbol{x}|\boldsymbol{x}'_s,\omega)\mathscr{A}_j^s\hat{g}_{5j}(\boldsymbol{x}|\boldsymbol{x}'_s,\omega)\mathrm{e}^{-l_s^2\omega^2/4\pi^2}\mathrm{e}^{-(\omega^2/\overline{c}_\infty^2)l_s^2(p_2^2+p_3^2)}\,\mathrm{d}^3\boldsymbol{x}'_s, \tag{3.104}$$

where the inclusion of the perturbed term $\mathrm{e}^{\mathrm{i}k_0\boldsymbol{\eta}\cdot\boldsymbol{p}}$ acts to Fourier transform the separation coordinates $\boldsymbol{\eta}$, notably engendering Gaussian terms (functions of observer variable) that are not present in (3.102). It is worthwhile pointing out that the Taylor expansion w.r.t. $\boldsymbol{\eta}$ could also be applied to the moving frame correlation integral.

The appearance of the observer coordinates in the source model leads to some interesting consequences. The most important is that the polar angle θ (amongst other parameters) controls the strength of the source spectra, while φ does not enter the source spectra for the models we have considered. However, there is a sharp distinction between the two models we have considered. In the Lighthill-esque model (Case A), the moving frame resulted in a Doppler shift leading to a Gaussian term $\exp\left(-\frac{1}{4}\tau_s^2\omega^2(1-M_c\cos\theta)^2\right)$ that beams in the downstream direction (see Fig. 3.3). In the first subcase of Case B, the source correlation is a weak function of polar angle, appearing only in $1/(1+\omega^2\tau_s^2(1-\overline{u}_1p_1\overline{c}_\infty)^2)$, as $\boldsymbol{\eta}$ is neglected in the propagator. However, making the Taylor expansion in $\boldsymbol{\eta}$ sees θ return to the Gaussian through $p_2^2+p_3^2=\sin^2\theta$, again leading to a beaming effect.

3.6 Conclusions

In this chapter a matched ray solution to a vector Green's function has been developed. This vector Green's function governs the acoustic propagation of the linearised Euler equations. Whilst in-keeping with the concept of a generalised acoustic analogy, the large number of components (24 in all) meant that computing it on a wavenumber basis was not tangible for large scale applications. The introduction of the ray ansatz allowed all 24 components to be expressed in terms of just one component, thus bypassing this problem. The perfect demonstration of this reduction in complexity was through the development of correlation and spectral integrals upon which engineering calculations are based. The introduction of the directivity factor, which is nested inside the aforementioned integrals, will prove a useful tool for demonstrating the impact of ray singularities upon the aggregate acoustic field.

Chapter 4

Complex Rays and Continuation Methods

4.1 Introduction

This chapter looks at the ray multiplicity problem generated by the nonlinearity of the eikonal equation and presents the solution in the context of Chapter 3. Generic flow problems typically allow for the arrival of multiple solutions at a receiver point and consequently decent estimates of the field require that almost the complete solution set are found. The first part of this chapter addresses this issue by recasting the IVP as a nonlinear or two-point boundary value problem (BVP) whose roots are the desired rays. Three methods of calculation are discussed: a derivative-free Genetic Algorithm, an equivalent functional iteration effected by Newton's method, and a winding number method. The second part of this chapter focuses on the continuation techniques employed to carry ray solutions from point-to-point. Two of the most popular techniques are applied: natural parameter continuation, and predictor-corrector continuation, and these are judged upon there computational efficiency and their ability to tackle natural boundaries such as those that arise at caustics. The resolution of this latter scenario stems from bifurcation theory and complex continuation.

4.2 Conversion to a boundary value problem (BVP)

As it remains the initial value ray problem of Chap. 3 is a function of the ray parameters $\boldsymbol{\varsigma} = \{\tilde{\boldsymbol{\mu}}, \tau_R\}$ and not of the receiver coordinates $\boldsymbol{x}_R$. This is somewhat contrary to what we expect from Green's functions whose argument consists of both $\boldsymbol{x}_s$ and $\boldsymbol{x}_R$. In

general the relationship between these two is nontrivial and only in a few cases (e.g., constant flow and linear gradients) can the problem be inverted analytically. In order to represent the receiver explicitly the following, rather innocuous, function is defined as in Sambridge & Kennett [42] (see also Pereyra et al. [46] and Wesson [43]),

$$\mathbf{F}(\boldsymbol{\varsigma}; \boldsymbol{x}_R) \equiv \boldsymbol{x}(\boldsymbol{\varsigma}) - \boldsymbol{x}_R, \tag{4.1}$$

so that rays arriving at the receiver point satisfy $\mathbf{F} = \mathbf{0}$. It can be readily seen that this is the natural extension of saddle-point methods or moreover, the saddle-point condition. Equation (4.1) mirrors the saddle-point method[1] in that it provides a necessary but not sufficient condition for a ray contribution. We must also factor in growth conditions, for physical reasons, and Stokes (multiplier) conditions due to resurgence. For the time being (4.1) is in the form of an optimisation problem and so there are various methods of attack that can be used. Here, we start by examining two methods distinct in that one is derivative based, i.e., a Newton method; while the other, a genetic algorithm approach, isn't.

4.2.1 Genetic Algorithms

The genetic algorithm is a stochastic search heuristic that mimics the process of natural selection. Genetic algorithms have been applied to a wide range of problems (see for e.g., Davis et al. [149]), but the application to ray two-point problems is novel. In brief, a genetic algorithm requires: a genetic representation of the solution domain (typically an array of bits, i.e., its chromosomes); and a fitness function to evaluate the solution domain. Clearly, (4.1) is consistent with these requirements in that the ray firing parameters once split into real and imaginary parts (the problem is then in $2n_D$ dimensions) can be encoded in bits since they are just numbers, and the equation itself can provide a scalar fitness function. In fact any norm formed from the vector $\mathbf{F}$ is sufficient. For instance when considering complex rays,

$$\mathrm{F}_{fitness} \equiv \sum_{i=1}^{N} (\mathrm{Re}(\mathrm{F}_i)^2 + \mathrm{Im}(\mathrm{F}_i)^2), \tag{4.2}$$

is zero whenever $\mathbf{F} = \mathbf{0}$. Once a solution domain has been defined[2] in terms of the ray parameters, for example $0 \leq \mathrm{Re}(\mu) < 2\pi$, the genetic algorithm generates a population of randomly generated individuals, known as the first generation, measuring the fitness of each individual via (4.2). The fitter individuals (unfit candidates are discarded) are then modified by a process of recombination (splicing together the bit string with other

[1] The property known as equivalence is discussed in later sections.

[2] This is not always necessary but it speeds up computation.

fit members of the population) or mutation (random changes to the bit string) to form a new generation. The new generation is then used in the next iteration of the algorithm. Depending on the algorithm elitism is also used. This preserves the fittest individual from each iteration into the next in an attempt to speed up convergence. The algorithm stops when either a fixed number of generations is reached or some tolerance has been reached on the fitness function. Here the former is preferred as decent tolerances are unlikely to be reached in acceptable times for generic flow problems.

From a ray perspective all that is required to compute (4.2) are the ray trajectories $\boldsymbol{x}(\tau)$. Since we do not require derivatives, no more ray equations need be added, and therefore the size of ray system in Eqs. (3.48)-(3.50), which has already doubled, stays the same. Thus it becomes a matter of choice as to whether the amplitude A_0 is computed exactly (using Eqs. (3.60) and (3.61)) using the DRE or approximately by equating it with the Helmholtz spherical spreading term $1/4\pi R$ and therefore eliminate the dependence on the DRE completely. Such an approximation may be appropriate for complex rays as the overall amplitude is dominated by the exponential decay of the phase.

From a computational point of view, the pros and cons are well balanced. In the positive, the number of ray equations stays the same and the method is straight forward to implement. It is not derivative based and so divergence is not experienced if trial solutions are poor. However, the method is remarkably slow in generic 6D problems ($n_D = 3$ being of most interest) especially if one chooses a large search domain. Additionally, there is also some variability in the answer as the method does not converge in the same way as a deterministic method. When seeking a fast ray solver, it is perhaps this criterion that renders any benefits obsolete. For this reason we prefer the iterative approach, though a hybrid method where a GA seeds the Newton method is plausible.

4.2.2 Iterative approach

The iterative approach described in this section is markedly different from the genetic algorithm. The main difference is that it is deterministic and not stochastic. It relies on stability to converge to a solution, and the repeatability of the solution makes it preferable for finding ray solutions. Furthermore, iterative methods such as Newton's method exhibit superlinear convergence, making the algorithm very fast.

To solve (4.1) in terms of ray parameters $\boldsymbol{\varsigma}$, an iterative system of equations is formed that is equivalent to it (see for e.g., Keller[53]). The most effective procedure is a multidimensional Newton method applied to Eq. (4.1),

$$\boldsymbol{\varsigma}^{(k+1)} = \boldsymbol{\varsigma}^{(k)} - D\mathbf{F}^{-1}(\boldsymbol{\varsigma}^{(k)}; \boldsymbol{x}_R)\mathbf{F}(\boldsymbol{\varsigma}^{(k)}; \boldsymbol{x}_R), \tag{4.3}$$

where $D\mathbf{F}$ is the transpose of the Jacobian matrix Eq. (3.56), and k is an iteration counter.

The Newton method is at best a local search method that should not really be employed globally. Fortunately, it does work well when global searches are undertaken for real rays where the initial estimates, or seeds, are $\tau^{(0)} = O(R)$, $0 \leq \mu^{(0)} \leq \pi$, and $0 \leq \lambda^{(0)} \leq 2\pi$. In the far-field, good initial estimates of the firing parameters are the observer angles themselves. In shadow zones real solutions will not converge to anything meaningful, they will likely oscillate wildly before tending to a final, spurious, solution. In this circumstance if tolerances are placed on $\mathbf{F} \approx \mathbf{0}$, then the iteration could go on indefinitely. It is recommended that the overall algorithm starts real ray finding in a region likely to be populated by real rays. One suggestion is $\theta = 90^\circ$ with $\Delta\varphi = 0$.

The determination of complex rays is slightly more involved, particularly as they may exist in real ray illuminated regions. This is further complicated by highly localised domains of convergence that lead to overflow if divergence is promoted by a poor initial guess. Complex rays are determined in a local manner according to the next section.

Considering real rays, the basic procedure for their determination at one point using (4.3) is:

1. A distribution of real test rays $\boldsymbol{\varsigma}^{(0)}$ are fired for a particular receiver point.
2. The Newton system is iterated until either the maximum iterations are reached or convergence is detected.
3. All non-unique $\boldsymbol{\varsigma}$'s are discarded (to within a fine tolerance).

This last step is the criterion for unique rays, i.e., through the ray parameters and not through the phase or amplitude/Jacobian as in Amodei et al. [122]. Unique rays can (see Chap. 6 for example) arrive at the same point with the same amplitude and phase even though their firing parameters are distinct.

When applying (4.3) from a numerical point of view it should be noted that the inverse matrix $D\mathbf{F}^{-1}$ is calculated using a Moore-Penrose pseudoinverse denoted by superscript $+$ (see Allgower & George [55], Kincaid & Cheney [150]). The pseudoinverse is defined for all matrices whose entries are real or complex numbers, and is calculated using a singular-value-decomposition (SVD) of $D\mathbf{F}^{-1}$, i.e.,

$$D\mathbf{F}^{-1} = PDQ, \tag{4.4}$$

where $D\mathbf{F}^{-1}$ is of size $m \times n$, P and Q are square unitary matrices of size $m \times m$ and $n \times n$ respectively, and D is an $m \times n$ containing the eigenvalues of the matrix $(D\mathbf{F}^{-1})^* D\mathbf{F}$,

where $*$ denotes the conjugate transpose. The pseudoinverse is then given by,

$$D\mathbf{F}^{+} = Q^{*} D^{+} P^{*}, \tag{4.5}$$

where D^{+} is defined as a diagonal matrix with elements reciprocal of those in D. The pseudoinverse defined by (4.5) exists and is unique when the matrix is of full rank. When the rank is not maximum the pseudoinverse does exist[3] but it is not unique. This is a major benefit as $D\mathbf{F}^{+}$ exists for non-square matrices, and at caustics where the rank of $D\mathbf{F}$ and its inverse are not maximum.

The actual elements of $D\mathbf{F}$ are computed using the ray group velocity (3.48) and the geodesic elements (updated every iteration) given by (3.61). This can be seen explicitly by taking derivatives of (4.1) with respect to the ray parameters $\boldsymbol{\varsigma}$,

$$D\mathbf{F} = \partial_{\boldsymbol{\varsigma}}(\boldsymbol{x}(\boldsymbol{\varsigma}) - \boldsymbol{x}_R) = \partial_{\boldsymbol{\varsigma}}\boldsymbol{x}(\boldsymbol{\varsigma}). \tag{4.6}$$

This procedure is worth highlighting because iterative mechanisms are not limited by expansions based on $\boldsymbol{\varsigma}$. Equation (4.6) also serves to illustrate the dual purpose of the geodesic elements: calculating amplitude and roots of (4.1). Additionally, there is no loss of generality with the consideration of only real rays in this section; the pseudoinverse iteration is readily extendable to the complex rays determined in the next section.

4.3 Continuation techniques and caustics

For most calculations interest is not focused at just a point, but a long a curve generated by some monotonic scalar parameter within $\mathbf{F}$, α say. Typically, α will be located in $\boldsymbol{x}_R$ so that solutions at $\boldsymbol{x}_R(\alpha)$ can be used to find solutions at a nearby point $\boldsymbol{x}_R(\alpha + \delta\alpha) = \boldsymbol{x}_R + \delta\boldsymbol{x}_R$. In this case α generates a receiver curve. As α is varied, bifurcation curves $\Gamma^{B}_{\boldsymbol{\varsigma}}(\alpha)$ in all the ray parameters are generated as guaranteed by the implicit function theorem [111]. In fact all parameters - including α- can be written as functions of arclength s_{arc} along each curve, though α is still the controlling variable. In the following sections two methods are discussed for the continuation of rays along receiver curves: one is a simple natural parameter continuation, the other a more involved predictor-corrector method.

[3]The solution minimizes the quantity $||D\mathbf{F}(\boldsymbol{\varsigma}^{(k)} - \boldsymbol{\varsigma}^{(k+1)}) - \mathbf{F}||$ in the least squares sense.

4.3.1 Natural parameter continuation

Natural parameter continuation is the simplest continuation possible as solutions from one point (completed after k iterations say) are used as inputs for the first iteration of a nearby point, i.e., $\boldsymbol{\varsigma}^{(k)}(\alpha) \to \boldsymbol{\varsigma}^{(0)}(\alpha+\delta\alpha)$. Convergence is likely so long as the bifurcation path itself is not experiencing rapid deviations: such behaviour may be expected at a bifurcation. If $\delta\alpha$ is too large then there is also the possibility of the algorithm switching to other branches, which can be a considerable nuisance.

4.3.2 Predictor-corrector (PC) method

The predictor-corrector (PC) method uses the tangent of the bifurcation branch corresponding to α, to predict the point at the nearby point $\alpha + \delta\alpha$. The predicted point is then corrected using the system (4.3) to iterate until convergence. This procedure is analogous to that used in numerical methods for computing odes: however, the convergence of the corrector is of course superlinear and thus much faster than the odes' analogy. The predictor-corrector method forms the basis of Hanyga's [50] Point-to-Curve (P2C) for homogenous no-flow problems. The BVP has already been expressed in (4.1) but for future use it is stated again as,

$$\mathbf{F}(\boldsymbol{\varsigma}, \mathbf{q}(\alpha)) = \mathbf{0}, \tag{4.7}$$

where the vector $\mathbf{q} = \{\boldsymbol{x}_s, \boldsymbol{x}_R, \ldots\}$ contains the fixed input data (into one particular iteration), which can later be used to generalise the receiver curve, i.e., α can parameterise any element(s) of $\mathbf{q}$. We also introduce the vector $\mathbf{Z} = \{\boldsymbol{\varsigma}, \alpha\}$ for tangent calculation.

To calculate the tangent vector one needs to find the vector $\mathbf{t} \in \mathbb{C}^{n_D+1}$ that satisfies,

$$D_Z\mathbf{F} \cdot \dot{\mathbf{Z}} = D_Z\mathbf{F} \cdot \mathbf{t} = 0, \quad \text{orthogonality}, \tag{4.8}$$

$$||\mathbf{t}|| = 1, \quad \text{unit norm}, \tag{4.9}$$

$$\det\left(D_Z\mathbf{F}^*, \mathbf{t}\right) > 0, \quad \text{orientation}, \tag{4.10}$$

which is simply the definition of the tangent space with normed tangent along the bifurcation curves at the point α. The Frechet derivative denoted by D_Z now denotes taking derivatives with respect to the variables in $\mathbf{Z}$ and $\cdot$ denotes differentiation w.r.t. s_{arc}. In this instance s_{arc} is used purely to illicit the tangent vector. The only addition work required here is the calculation of $\partial_\alpha \boldsymbol{x}_R(\alpha)$ in $D_Z\mathbf{F}$. When α corresponds to an observer variable (as in this thesis), this differentiation can be achieved analytically.

At regular points, e.g., away from caustics the next point on the curve is predicted by taking an Euler step,

$$\mathbf{Z}_{i+1} = \mathbf{Z}_i + h_{\text{step}}\mathbf{t}, \tag{4.11}$$

where h_{step} is the step size. Because $\mathbf{Z}$ contains α this means that (4.11) will predict a new α. If the user wants to control α_{i+1} then the step size can be chosen using $h_{\text{step}} = (\alpha_{i+1} - \alpha_i)/t_{N+1}$.

Non-trivial solutions to Eqs. (4.8)-(4.10) can be found using a QR decomposition that is outlined in Appendix C. Other methods of calculating the tangent based on a matrix decomposition are available, see for e.g., Keller [52]. Tangent based prediction is clearly more computationally intensive than the natural parameter continuation discussed in the previous section, but it has two benefits. First, a larger step size can be taken along the bifurcation branch, second rapid changes in the branch that are not due to caustics can be predicted.

4.3.3 Continuation at caustics: bifurcation formulae

At caustics two or more bifurcation paths coalesce and the implicit function theorem cannot be called upon to continue solutions through the caustics: the caustic is a natural boundary for our algorithm. Numerically the Newton method can be continued but the jumps in ray parameters often leads to failure. In this section standard bifurcation methods are examined and the algorithm for the simplest cases of continuation are presented.

It so happens that many problems in applied mathematics involving multiple solutions can be reduced to a simpler systems of equations of the form,

$$\mathscr{J}_i(\varrho, \Lambda) = 0, \quad i = 1, \ldots, n, \tag{4.12}$$

where $\varrho = \{\varrho_1, \ldots, \varrho_n\}$, $\varrho \in \mathbb{C}^n$ are unknowns and $\Lambda = \{\Lambda_1, \ldots, \Lambda_k\}$, $\Lambda \in \mathbb{R}^k$ the bifurcation parameters. Study of these equation's multiple solutions in ϱ as Λ varies and the bifurcation of these branches at certain critical Λ's are well known (Golubitsky & Schaeffer [151]). The concept behind the reduction above is the concept of equivalence[4], where two local forms j_1, j_2 have the same structure and are therefore expressible via diffeomorphism by the same *canonical form* at the singularity $\Lambda = \mathbf{0}$. The equivalence relation required here is *contact equivalence*,

$$j_1(\varrho, \mathbf{0}) = h(\varrho, \mathbf{0}) j_2(\mathscr{T}(\varrho, \mathbf{0}), \mathbf{0}), \tag{4.13}$$

[4]Equivalence and its particular relations are key to the local procedures used in this thesis.

where the two mappings $j_1, j_2 : \mathbb{R}^m \to \mathbb{R}^m$, and $\mathscr{T}$ is a diffeormorphic function, and h a smooth nonsingular matrix. Then the reduced function can be expressed as,

$$\mathscr{J}_i(\varrho, \Lambda) = \mathscr{H}(\varrho, \Lambda)\mathscr{U}(\mathscr{T}(\varrho, \Lambda), \mathscr{S}(\Lambda)), \tag{4.14}$$

where $\mathscr{U}$ is normal form, $\mathscr{H}$ is a smooth matrix, and $\mathscr{T}$ and $\mathscr{S}$ are diffeomorphic mappings.

Finding the appropriate normal and its unfolding is known as a recognition problem, first, though, we need to be able to reduce the two-point problem (4.1) to the simpler system (4.12). This can be acheived using the Liapunov-Schmidt reduction [151]. To do this we need to introduce the four fundamental subspaces of a matrix L.

If L is an $m \times n$ matrix, with column vectors $\mathbf{v}_1, \mathbf{v}_2, \ldots, \mathbf{v_n}$ and row vectors $\mathbf{r}_1, \mathbf{r}_2, \ldots, \mathbf{r_m}$, then the *four fundamental subspaces* of L are the following:

Subspaces of $\mathbb{C}^n$

1. The *nullspace/kernel* of L is $\mathcal{N}(L) = \{v \in \mathbb{C}^n : Lv = 0\}$.
2. The *rowspace* of L is $\mathcal{R}(L^*) = \text{span}\{\mathbf{r}_1, \mathbf{r}_2, \ldots, \mathbf{r_m}\}$.

Subspaces of $\mathbb{C}^m$

1. The *left nullspace/cokernel* of L is $\mathcal{N}(L^*) = \{w \in \mathbb{C}^m : L^*w = 0\}$, or $\{w \in \mathbb{C}^m : w^*L = 0\}$.
2. The *column space/range* of L is $\mathcal{R} = \text{span}\{\mathbf{v}_1, \mathbf{v}_2, \ldots, \mathbf{v_n}\}$.

In the above we can always make $n = m$ by appending the tangent vector $\mathbf{t}$ of the bifurcation branch being traversed up to the caustic so that $D_Z\mathbf{F}^A = (D_Z\mathbf{F}, \mathbf{t}^*)$, which has dimensions $n_D + 1 \times n_D + 1$. This can be achieved by appending scalar normalisation (or pseudo-arclength constraint) to $\mathbf{F}$ to give $\mathbf{F}^A$ (see for e.g., Keller [51]). Alternatively, we can consider L as $D\mathbf{F}$ which has dimensions $n_D \times n_D$.

In order for the nullspace to be non-trivial or dimension greater than one for square and non-square matrices ($m \times n$) respectively, L cannot have maximum rank. The extent to which $r \neq m$, is characterised by the dimension of each of the spaces. For a square matrix the determinant must be zero, otherwise the inverse of L exists and $\mathcal{N}(L) = \mathbf{0}$. The most important relationship between the subspaces is the *rank-nullity* theorem and the equivalent for left-nullspace ($m \times n$ matrix);

$$r + \dim \mathcal{N}(L) = n, \tag{4.15}$$

$$r + \dim \mathcal{N}(L^T) = m. \tag{4.16}$$

The basis found for the subspaces are linearly independent but not necessarily orthogonal. An orthonormal basis can be created using a process such as Gram-Schmidt [150].

At a caustic the matrix $D_Z\mathbf{F}$ is degenerate and so has a null space of dimension greater than one (the tangent at a regular point is the only element otherwise). The dimension of these spaces depends on the corank ℓ of the singularity. The corank is related to the rank, r, of the matrix via $\ell + r = n_D$ where the size of the matrix $D_Z\mathbf{F}$ is $n_D \times n_D + 1$. If the rank of the matrix is $\text{Rank}(D_Z\mathbf{F}) = n_D - \ell$ then the rank-nullity theorem gives (with $L = D_Z\mathbf{F}(\mathbf{Z}_C)$,

$$n_D - \ell + \dim\mathcal{N}(D_Z\mathbf{F}(\mathbf{Z}_C)) = n_D + 1 \Rightarrow \dim\mathcal{N}(D_Z\mathbf{F}(\mathbf{Z}_C)) = 1 + \ell, \tag{4.17}$$

$$n_D - \ell + \dim\mathcal{N}(D_Z\mathbf{F}^T(\mathbf{Z}_C)) = n_D \Rightarrow \dim\mathcal{N}(D_Z\mathbf{F}^T(\mathbf{Z}_C)) = \ell, \tag{4.18}$$

where C denotes the value for which the caustic occurs. If either $D_Z\mathbf{F}^A$ or $D\mathbf{F}$ is used, then both (4.17) and (4.18) yield $\dim\mathcal{N}(L) = \dim\mathcal{N}(L^*) = \ell$.

Using $L = D\mathbf{F}$ and its associated spaces,[5] the Liapunov-Schmidt reduction theorem then allows us to write the reduced functions $\mathscr{J}_i$ in terms of $\mathbf{F}$ as,

$$\mathscr{J}_i(\varrho, \Lambda) = \langle w_i^*, \phi^{LS}(\boldsymbol{\varsigma}_C + \varrho_1 v_1 + \ldots + \varrho_\ell v_\ell, \Lambda)\rangle, \quad i = 1, \ldots, \ell, \tag{4.19}$$

$$\phi^{LS}(v, \Lambda) = (I - E)\mathbf{F}(v + W(v, \Lambda), \Lambda), \tag{4.20}$$

where I is the identity matrix, and $E = (I - w_1 w_1^*)$ is the projection operator onto the range space, and $\langle \cdot, \cdot \rangle$ denotes an inner product.[6] W is a vector that must be solved for in order to determine all branches; derivatives of W must also be solved for.[7]

Now that a method for computing $\mathscr{J}_i$ has been found, we claim that in order to study the bifurcation we can Taylor expand (which leads to an approximation rather than exactness) $\mathscr{J}_i$ in ϱ into an equivalent polynomial that mimics the normal form, given that $\mathscr{J}_i$ obeys constraints of a recognition problem. This polynomial is intricately linked to catastrophe theory (the subject of Chap. 5) and the stable canonical polynomials found therein. Here we shall concentrate on the bifurcations at a fold caustic, and cusp caustic on its line of symmetry, i.e., the pitchfork bifurcation, as these are the most common real to complex bifurcations ($i = 1$, $\varrho = \varrho_1$). The normal forms $\mathscr{U}(\varrho, \Lambda)$ for these bifurcations are $\varrho^2 + \Lambda$ and $\varrho^3 + \varrho\Lambda$, respectively. For these cases $\mathscr{J}_1$ is expanded

[5] Our work is then easily adaptable to Golubitsky & Schaeffer [151].

[6] This allows for a substantial simplification in notation as opposed to Einstein notation.

[7] The operator E annihilates all vectors orthogonal to w_1.

as,

$$\mathscr{J}_1(\varrho,\Lambda) \approx \begin{cases} \frac{1}{2}\mathscr{J}_{1,\varrho\varrho}(0,0)\varrho^2 + \mathscr{J}_\Lambda\Lambda, & \text{Fold} \\ \frac{1}{6}\mathscr{J}_{1,\varrho\varrho\varrho}\varrho^3 + \frac{1}{2}\mathscr{J}_{1,\varrho\Lambda}\varrho\Lambda, & \text{Pitchfork.} \end{cases} \tag{4.21}$$

with recognition problems given by (see [151]),

$$\mathscr{J}_{1,\Lambda}(0,0) \neq 0, \mathscr{J}_{1,\varrho\varrho}(0,0) \neq 0, \quad \text{Fold} \tag{4.22}$$

$$\mathscr{J}_{1,\Lambda}(0,0) = 0, \mathscr{J}_{1,\varrho\varrho}(0,0) = 0, \mathscr{J}_{1,\Lambda\varrho}(0,0) \neq 0, \mathscr{J}_{1,\varrho\varrho\varrho}(0,0) \neq 0. \quad \text{Pitchfork} \tag{4.23}$$

Clearly, in both cases derivatives of $\mathscr{J}_1$ are required, and their calculation in this scenario is the most tedius aspect of the Liapunov-Schmidt method. In general for $\ell = 1$, the highest power of ϱ in the Taylor expansion, and hence the germ, is ϱ^{K+1} (for $K+1$ rays coalescing) necessitating a maximum of $K+1$ highest derivative in $\mathscr{J}_1$. Derivatives of $\mathscr{J}_i$ are automatically passed on to ϕ^{LS} and its arguments; consequently implicit differentiation typically leads to unwieldy formulae.

The full mechanics of the implicit differentiation are detailed in [151]. A few steps are highlighted (with no loss of generality) here starting with the use of the Gâteaux derivative,

$$(\mathrm{D}^k\mathbf{F})_{\boldsymbol{\varsigma},\Lambda}(v_1,\ldots,v_k) = \frac{\partial}{\partial\varrho_1}\cdots\frac{\partial}{\partial\varrho_k}\mathbf{F}\left(\boldsymbol{\varsigma} + \sum_{i=1}^{k}\varrho_i v_i, \Lambda\right)\Bigg|_{\varrho_1=\cdots=\varrho_k=0}. \tag{4.24}$$

For example for $k=2$, (4.24) can be written,

$$(\mathrm{D}^k\mathbf{F})_{\boldsymbol{\varsigma},\Lambda}(v_1,v_2) = \sum_{i,j=1}^{n}\frac{\partial^2\mathbf{F}}{\partial\varsigma_i\partial\varsigma_j}(\boldsymbol{\varsigma},\Lambda)v_{1_i}v_{2_j}. \tag{4.25}$$

For the case $\ell = 1$ it can then be shown that the first three derivatives of ϕ^{LS} evaluated at the caustic ($\varrho = \Lambda = 0$) are,

$$\begin{aligned} &\phi^{LS}_{\varrho}(0,0) = 0, \\ &\phi^{LS}_{\varrho\varrho}(0,0) = (I-E)(D^2\mathbf{F}(v_1,v_1)) \\ &\phi^{LS}_{\varrho\varrho\varrho}(0,0) = (I-E)(3D^2\mathbf{F}(v_1,W_{\varrho\varrho}(0,0)) + D^3\mathbf{F}(v_1,v_1,v_1)), \\ &\phi^{LS}_{\Lambda}(0,0) = (I-E)\mathbf{F}_\Lambda(0,0)), \\ &\phi^{LS}_{\Lambda\varrho}(0,0) = (I-E)(D\mathbf{F}_\Lambda(v_1) + D^2\mathbf{F}(v_1,W_\Lambda(0,0))), \end{aligned} \tag{4.26}$$

since it can be shown that $W_\varrho(0,0) = 0$. This gives the first three derivatives of $\mathscr{J}_1(0,0)$,

$$\begin{aligned}
\mathscr{J}_{1,\varrho}(0,0) &= 0,\\
\mathscr{J}_{1,\varrho\varrho}(0,0) &= \langle w_1^*, D^2\mathbf{F}(v_1,v_1)\rangle,\\
\mathscr{J}_{1,\varrho\varrho\varrho}(0,0) &= \langle w_1^*, D^3\mathbf{F}(v_1,v_1,v_1) - 3D^2\mathbf{F}(v_1,(EL)^{-1}ED^2\mathbf{F}(v_1,v_1))\rangle,\\
\mathscr{J}_{1,\Lambda}(0,0) &= \langle w_1^*, \mathbf{F}_\Lambda\rangle,\\
\mathscr{J}_{1,\Lambda\varrho}(0,0) &= \langle w_1^*, D\mathbf{F}_\Lambda(v_1) - D^2\mathbf{F}(v_1,(EL)^{-1}E\mathbf{F}_\Lambda)\rangle,
\end{aligned} \tag{4.27}$$

where $W_{\varrho\varrho}(0,0) = -(EL)^{-1}E\,D^2\mathbf{F}(v_1,v_1)$ has been determined.

Thus for the fold and pitckfork cases $\mathscr{J}_1(\varrho,\Lambda) = 0$ can be solved in terms of Λ:

$$\varsigma \approx \varsigma_C + \begin{cases} \begin{cases} \sqrt{\frac{-2\mathscr{J}_\Lambda(0,0)}{\mathscr{J}_{\varrho\varrho}(0,0)}}\Lambda^{1/2}v_1, \\ -\sqrt{\frac{-2\mathscr{J}_\Lambda(0,0)}{\mathscr{J}_{\varrho\varrho}(0,0)}}\Lambda^{1/2}v_1, \end{cases} & \text{Fold} \\ \begin{cases} \sqrt{\frac{3\mathscr{J}_{\varrho\Lambda}(0,0)}{\mathscr{J}_{\varrho\varrho\varrho}(0,0)}}\Lambda^{1/2}v_1, \\ 0, \\ -\sqrt{\frac{3\mathscr{J}_{\varrho\Lambda}(0,0)}{\mathscr{J}_{\varrho\varrho\varrho}(0,0)}}\Lambda^{1/2}v_1, \end{cases} & \text{Cusp} \end{cases} . \tag{4.28}$$

Equation (4.28) shows 2 and 3 distinct paths exist, sprouting from the fold and cusp caustics respectively as Λ is increased.[8] In each of these cases the complex paths ($v_1 \in \mathbb{R}^N$ for these cases) depend on the sign of $-2\mathscr{J}_\Lambda(0,0)/\mathscr{J}_{\varrho\varrho}(0,0)\Lambda$ and $3\mathscr{J}_{\varrho\Lambda}(0,0)/\mathscr{J}_{\varrho\varrho\varrho}(0,0)\Lambda$. When these quantities are negative this results in a complex path with tangent in imaginary space having the direction $\mathrm{i}v_1$ of the "rotated" real tangent.

Of course realistic computations mean that the algorithm will never be exactly at the caustic. Therefore standard routines for computing nullspaces will not return the correct number as the rank of these near-caustic matrices are likely to be maximal. The numerical method for approximating these spaces are shown in Appendix C for both corank cases. Additionally, numerical approximations must be provided for the Fréchet derivatives of $\mathbf{F}$ other than $D\mathbf{F}$: these are also shown in Appendix C.

The down side to the Liapunov-Schmidt method is significantly increased number of computations required to determine bifurcating branches. In order to determine the directions of the bifurcating branches it is necessary to know the number of coalescing rays *a priori* and this is not guaranteeable. However, in a large number of cases simpler

[8] Note that this expansion differs from that in Henderson [152] which is in terms of a small parameter, though expansions are the same if one sets that small parameter to one.

fold and cusp caustics prevail and it is not necessary to examine large numbers of coalescences. Nevertheless, there should be algorithms capable of tracking arbitrary numbers of coalescences, particularly as this number is used to solve the determinancy problem involved in the diagnosis of uniform functions.

4.3.4 Continuation at caustics: complex continuation

In the previous section the Liapunov-Schmidt method was used to find jump conditions at a caustic. The main problem with this method is the increasingly complicated bifurcation formulae required to make computations. In attempt to bypass this and create a simpler alternative algorithm that can be used with both the natural parameter and predictor-corrector continuation methods, this section examines a novel complex continuation method. Complex continuation itself is not novel in ray theory as it is widely used with WKB solutions (see Bender & Orszag [58]). In the context of ray-tracing complex continuation has been considered by both Chapman et al. [65] and Lustri [61], though both of these cases yield soluble ray trajectories that are often no more complicated than straight lines. In more complicated ray-tracing problems complex continuation was hinted at by Thomson [37] though this was mainly as argument for the importance of complex rays and to raise awareness of the consequent branch cuts coupling solutions together at caustics. However, Thomson does not see this continuation as a means for complex ray computation in general, and thus we consider a simple algorithm that is novel for generic numerically computed ray trajectories on the proviso that the caustic is stable. In the same way as the Liapunov-Schmidt expansions where based on canonical polynomials, the complex continuation also demands that the roots $\boldsymbol{\varsigma}$ each behave as the root of a canonical polynomial: however, this dependence is implicit.

The method proceeds by identifying all rays satisfying (4.1) that coalesce at the caustic point α_C in α-space. It is assumed that the caustic appears as a point in α-space, i.e $\boldsymbol{x}_R(\alpha)$ doesn't cut a caustic surface tangentially, and that other caustics aren't densely packed so that coalescences of bifurcation curves have some finite separation in α.

Starting at a point α_1 near the caustic, each coalescing ray solution can be analytically continued to the other side of the caustic α_2 by taking a path in complex α-space around α_C, so that $\boldsymbol{x}_R \in \mathbb{C}$ in (4.1). An example of two such paths is shown in Figure 4.1. The most straightforward paths are half-loops such as Path 1 and Path 2, although the exact path is arbitrary given sufficient distance from α_C.

The continuation method has the further advantage in that returning to the starting point α_1 (e.g, Path 1 followed by the reverse of Path 2 in Figure 4.1) $\boldsymbol{x}_R$ may have passed smoothly onto another branch of the ray solution that wasn't picked up in the

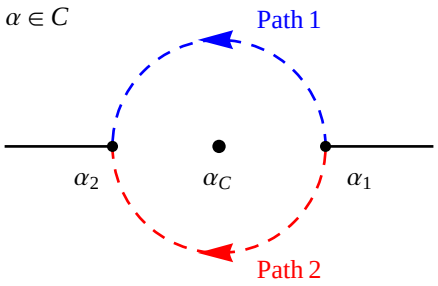

FIGURE 4.1: Continuation of rays from α_1 around the caustic α_C to α_2 demonstrating two equivalent paths. Where $\alpha_2 < \alpha_C < \alpha_1$.

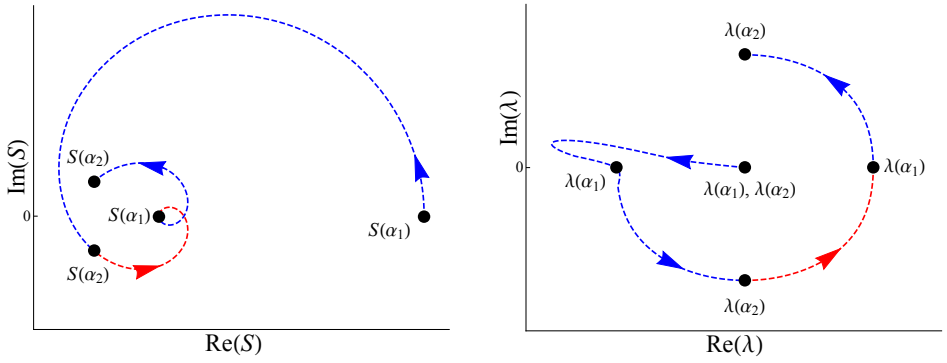

(a) $S(\alpha) \in \mathbb{C}$, $\alpha = \theta \in \mathbb{C}$ (b) $\lambda(\alpha) \in \mathbb{C}$, $\alpha = f(\theta, \Delta\varphi) \in \mathbb{C}$

FIGURE 4.2: Images of S and λ under the complex continuation of α about a caustic. Colouring and markers $\alpha_{1,2}$ correspond to that of Fig. 4.1. (a) Phase about the fold as the path wraps about α_C 1½ times, (b) λ about a pitchfork bif. with symmetry breaking perturbation in $\Delta\varphi \in \mathbb{R}$.

initial searches. In fact if a new solution is recorded then this branch should be continued around the caustic multiple times to generate the maximum number of new ray solutions at both α_1 and α_2. Doing so increases the chances of providing the appropriate local form to correct divergence at a caustic, since this relies upon identifying all coalescing ray contributions at α_C. This is a particular advantage compared to the Liapunov-Schmidt method. Furthermore, the natural parameter continuation for rays looping around the caustic is much smoother than a bifurcation analysis across the caustic and thus proves suitable for connecting to complex branches where only a small sign-independent imaginary perturbation is required when leaving α_1.

Examples of complex continuation are shown in Fig. 4.2 for two common cases. The first, Figure 4.2(a), shows the complex phase about the fold caustic as it wraps around θ_C 1½ times, smoothly transitioning to each complex branch. In this case we need only use $\alpha = \theta \in \mathbb{C}$ to transition between the two branches. In the pitchfork case it is not

possible to traverse all branches with loops in θ only. This is easy to see from (4.21) as one root, $\rho = 0$, is isolated from the others. The other two roots can be calculated from each other by rotating onto the other branch of $\Lambda^{1/2}$. Thus it is necessary to have a cut in the solution to pass smoothly from one branch to the other. In Figure 4.2(b) we have used a symmetry breaking perturbation in $\Delta\varphi$ in order to pass onto each branch.

We end this section discussing the property of structural stability known as the conservation rays. Put simply this means that whenever a caustic is crossed the number of bifurcation paths, or roots of the polynomial, leading into the caustic must equal those coming out, even if they are complex. Complex bifurcation curves, if they exist, must then have a conjugate path so that the disappearance of real ray solutions across the caustic will always be in multiples of 2.

4.4 Ray sums

While the continuation methods of the previous sections have allowed for the determination of as many ray contributions as possible, there is still the matter of summing the rays. In the following we shall use the computation of the Green's function component $\hat{g}_5$ of Chapter 3 (pertinent as it relates to acoustic pressure) as a specific example, though the method applies to other components in a similar manner.

The ray combination itself is trivial so long as the receiver is some distance away from any caustics. The ray solution is simply the superposition of all N physical rays (ignoring the role of Stokes multipliers for the mean time). For $\hat{g}_5$ this reads,

$$\hat{g}_5 = \sum_{n=1}^{N} A_0^{(n)} \mathrm{e}^{\mathrm{i}k_0 S^{(n)}}, \tag{4.29}$$

where any phase discontinuities that arise due to propagation through caustics are implicit in the amplitudes $A_0^{(n)}$. For real rays these discontinuities must equal $-\pi/2$, Berry [38], so that numerical codes calculating (4.29) must have the correct square-root chosen in (3.57).

The calculation of other Green's function components, for example $\hat{g}_{5i}$ which is used in (3.86) and related to $\hat{g}_5$ via the operator $\mathscr{A}_i$. Applying $\mathscr{A}_i$ to the ray sum in a component-wise manner,

$$\hat{g}_{5i} = \mathscr{A}_i \hat{g}_5 = \sum_{n=1}^{N} \mathscr{A}_i^{(n)} A_0^{(n)} \mathrm{e}^{\mathrm{i}k_0 S^{(n)}}, \tag{4.30}$$

which can be used to calculate the conjugate,

$$\hat{g}_{5i}^{*} = \mathscr{A}_i^{*}\hat{g}_5^{*} = \sum_{n=1}^{N} \mathscr{A}_i^{(n)*} A_0^{(n)*} \mathrm{e}^{-\mathrm{i}k_0 S^{(n)*}}. \tag{4.31}$$

The multiplication of the components $\hat{g}_{5i}^{*}\hat{g}_{5j}$ is also required in (3.86) and related integrals,

$$\hat{g}_{5i}^{*}\hat{g}_{5j} = \left(\sum_{n=1}^{N} \mathscr{A}_i^{(n)*} A_0^{(n)*} \mathrm{e}^{-\mathrm{i}k_0 S^{(n)*}}\right)\left(\sum_{n=1}^{N} \mathscr{A}_j^{(n)} A_0^{(n)} \mathrm{e}^{\mathrm{i}k_0 S^{(n)}}\right), \tag{4.32}$$

A simple component-wise multiplication of both brackets shows that the complex phase of each contributing ray is not redundant, neither does conjugacy lead to exponentially growing rays.

In this section we have assumed that a coherent sum is the correct way to combine rays. A coherent sum allows for the rays to interfere in a way that may not be possible in a turbulent medium, i.e., they may sum incoherently (absolute values), or perhaps multiplicities do not exist. However, we have reduced the jet noise problem into a mean-field Green's function and a source function where multiplicities do exist, consequently we must follow through with the mathematical programme devised so far and superpose the acoustic solutions as per (4.29).

4.5 Linear-layer example

As an example of the work developed so far in this chapter, a simple 2D linear-layer problem is considered. The linear-layer problem has been studied by several authors, e.g., Thomson [37], Kravstov [63], Amodei et al. [122] due to the solubility of its ray tracing equations, hence its inclusion here serves to demonstrate the algorithm so far and illicit ray properties in a simple setting.

The linear-layer is a no-flow problem in which the normalised sound speed varies according to $a^{-2}(\boldsymbol{x}) = l_1 - l_2 z,\ l_2 > 0$, where $x_1 \to x$ and $x_2 \to z$. This leads to eikonal and ray equations,

$$|\mathbf{p}|^2 - (l_1 - l_2 z)^2 = 0, \tag{4.33}$$

$$\frac{\mathrm{d}x}{\mathrm{d}\tau} = p_x,\ \frac{\mathrm{d}z}{\mathrm{d}\tau} = p_z,\ \frac{\mathrm{d}p_x}{\mathrm{d}\tau} = 0,\ \frac{\mathrm{d}p_z}{\mathrm{d}\tau} = -\frac{1}{2}l_2,\ \frac{\mathrm{d}S}{\mathrm{d}\tau} = l_1 - l_2 z, \tag{4.34}$$

with solutions for the path and slowness given by,

$$x(\tau) = x_s + a_s^{-1}\tau\cos\mu,\;\; z(\tau) = z_s + a_s^{-1}\tau\sin\mu - \frac{1}{4}l_2\tau^2, \tag{4.35}$$

$$p_x(\tau) = a_s^{-1}\cos\mu,\;\; p_z(\tau) = a_s^{-1}\sin\mu - \frac{1}{2}l_2\tau, \tag{4.36}$$

so that the geodesic and conjugate elements w.r.t μ are,

$$\frac{\partial x}{\partial\mu} = -a_s^{-1}\tau\sin\mu,\;\; \frac{\partial z}{\partial\mu} = a_s^{-1}\tau\cos\mu, \tag{4.37}$$

$$\frac{\partial p_x}{\partial\mu} = -a_s^{-1}\sin\mu,\;\; \frac{\partial p_z}{\partial\mu} = a_s^{-1}\cos\mu. \tag{4.38}$$

In this simple case it is possible to invert these equations so that for a given receiver position $\boldsymbol{x}_R = \{x_R, z_R\}$ the desired ray parameters can be found analytically, thus making it an ideal benchmark for the two-point boundary value problem. In this problem there are only two rays (both real or complex) that propagate to a point. In the case of real rays, these are labelled as direct (1) and indirect (2) - so called since a direct ray arrives at a receiver point without touching the caustic, while the indirect propagates through the caustic prior to arrival. In general this gives two propagation times $\tau_{1,2}$ and firing parameters $\mu_{1,2}$ per receiver point,

$$\tau_{1,2} = \frac{2}{l_2}\left(f_1^{1/2} \mp f_2^{1/2}\right),\;\; \sin\mu_{1,2} = \frac{x - x_s}{a_s^{-1}\tau_{1,2}}, \tag{4.39}$$

where $f_{1,2}$ are defined as,

$$f_{1,2} = \frac{1}{2}\left(2l_1 - l_2(z + z_s) \pm l_2 R\right), \quad R = \sqrt{(x - x_s)^2 + (z - z_s)^2}. \tag{4.40}$$

Using Eqs. (4.37) to (4.40), it can be shown that the phase and amplitude for each ray obey,

$$S^{(1,2)} = \frac{2}{3l_2}\left(f_1^{3/2} \mp f_2^{3/2}\right), \quad A_0^{(1)} = \frac{a_s^{-1/2}}{\tau_1^{1/2}(f_1 f_2)^{1/4}}, \quad A_0^{(2)} = \frac{-\mathrm{i}a_s^{-1/2}}{\tau_2^{1/2}(f_1 f_2)^{1/4}}. \tag{4.41}$$

Now defining the difference between the two phases as,

$$\chi_{\mathrm{sim}} = S^{(2)} - S^{(1)} = \frac{4}{3l_2}f_2^{3/2}, \tag{4.42}$$

which is proportional to a quantity known as the singulant and will be investigated further in the next chapter. At a caustic, the coalescence of two rays means that $\chi_{\mathrm{sim}} = 0$,

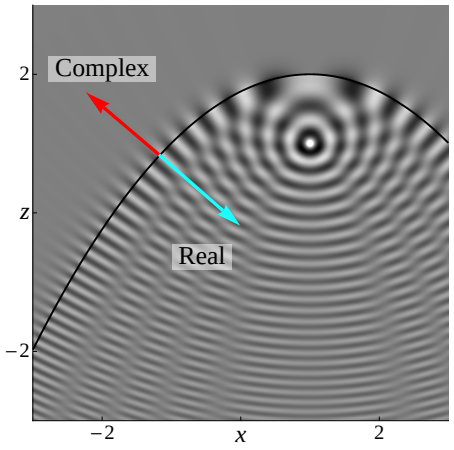

(a) Real part ray field.

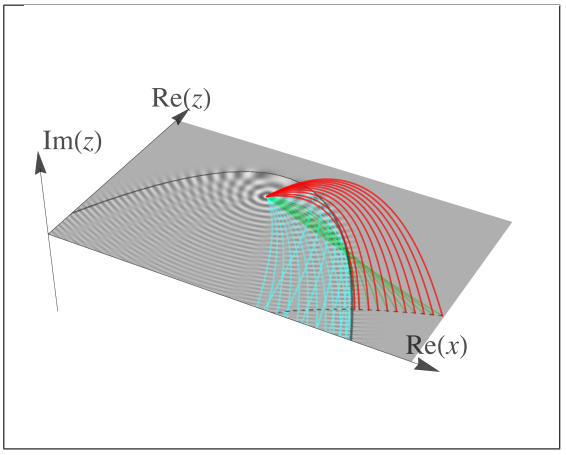

(b) Ray trajectories.

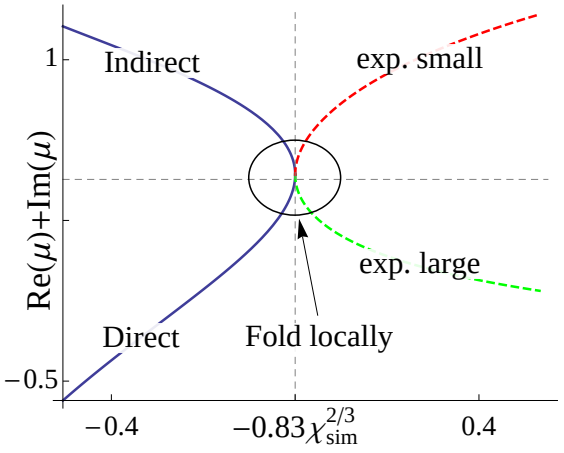

(c) μ-Bifurcation diagram.

FIGURE 4.3: Linear-layer computations for a point source at $\boldsymbol{x}_s = \{1, 1\}$ ($l_1 = 1$, $l_2 = 0.5$), (a) real part of ray field, caustic in black, (b) rays trajectories. Cyan, real; red, exp. small; green, exp. large; black-dashed, similarity curve, (c) μ-bifurcation diagram as a func. of χ_{sim}. Solid line, real solutions (correspond to cyan in (b)), dashed line complex (correspond as in (b)).

and unsurprisingly the amplitudes which diverge there, are also a function of χ_{sim}, e.g.,

$$A_0^{(1)} = \frac{a_s^{-1/2}}{\tau_1^{1/2}(f_1 f_2)^{1/4}} = \frac{a_s^{-1/2}}{\tau_1^{1/2} f_1^{1/4}(3l_2/4)^{1/6}\chi_{\text{sim}}^{1/6}}. \tag{4.43}$$

Setting the singulant equal to zero then gives the implicit caustic equation,

$$\chi_{\text{sim}} = 0 \implies 4a_s^2(l_1 - l_2 z) - l_2^2(x - x_s)^2 = 0, \tag{4.44}$$

which is the equation of a parabola. In fact, in this problem, setting $\chi_{\text{sim}} =$ constant defines a parabola in general, making it an ideal similarity parameter.

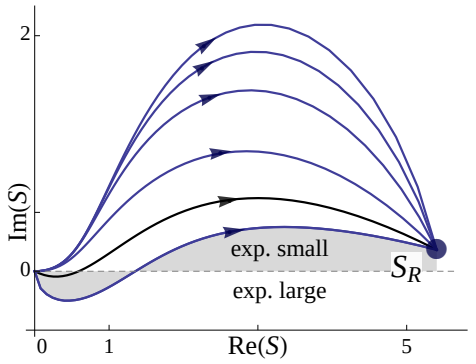

(a) Phase.

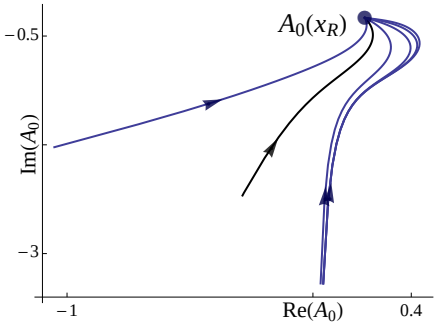

(b) Amplitude.

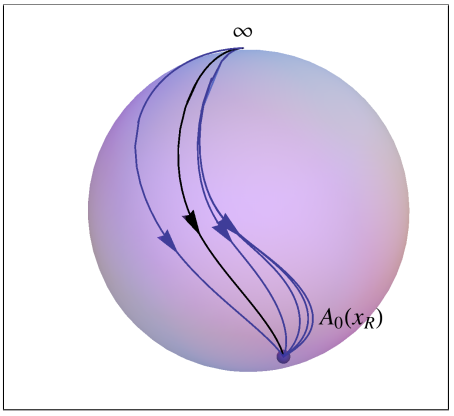

(c) Amplitude on $\mathbb{C} \cup \{\infty\}$ using a stereographic projection.

FIGURE 4.4: Variations of phase and amplitude along various τ-paths (arrows indicate increasing $|\tau|$) for an observer in the shadow zone. Black, standard path; blue, deviations. (a) invariance of complex phase at end points of τ-paths; (b) complex amplitudes converge to $A_0(\boldsymbol{x}_R)$ but do not make loops in $\mathbb{C}$; (c) amplitudes form closed loops in $\mathbb{C} \cup \{\infty\}$.

Given an implicit surface definition, e.g., χ_{sim} = constant then the equation of the normal (scaled) to this surface is,

$$\frac{\mathrm{d}\boldsymbol{x}}{\mathrm{d}n} = \partial_{\boldsymbol{x}}\chi_{\text{sim}}, \quad n \in \mathbb{R}, \text{ with } \boldsymbol{x}(0) : \chi_{\text{sim}}(\boldsymbol{x}) = 0, \tag{4.45}$$

which has closed form solution,

$$z - z(0) = \frac{2a_s^{-2}}{l_2} \ln \left| \frac{x - x_s}{x(0) - x_s} \right|. \tag{4.46}$$

The results for a point source located at $\boldsymbol{x}_s = \{1, 1\}$ are shown in Fig. 4.3. In the first of these, Fig. 4.3(a), the real part of the ray field shows the divergence in the field in the vicinity of the source, and the impact of the linear layer as waves are refracted away from the upper half plane forming a shadow zone. This zone is of course separated from the real ray zone by the caustic given by (4.44). In Fig. 4.3(b) the ray trajectories are

shown making contributions to the field, in which real rays bend away from the upper half-plane in a manner which is consistent with the increasing sound speed in that region. It can be seen with the complex rays - calculated on a similarity curve (4.46) - that we loose the intuitive feel that underlies the ability to explain the real ray refractive effects. Along the standard integration path the ray trajectories leave the real plane completely, and only return at the receiver points. The shape of the trajectory, albeit smooth, is not predictable to the same extent as real rays.

Using the same colour-coding as Fig. 4.3(b), the ray parameter μ is shown along the similarity curve. Importantly, the bifurcation of the ray parameter at $\chi_{\text{sim}} = 0$ - the caustic - behaves locally as the roots of quadratic, which is as expected. Away from the caustic the behaviour deviates from the quadratic, but complex solutions are *always* conjugate. This is the most the satisfactory aspect of the complex ray propagation: that *all* quantities involved in the propagation form a conjugate pair when complex.

The last part of this study is devoted to the invariance of the ray solution (keeping ray parameters fixed) at its end points $\tau = \{0, \tau_R\}$ though the connecting τ-path may vary. This property is important because it allows us to choose an arbitrary path, the straight line (the standard path) being the simplest, between the end points without changing the end result. A simple demonstration of this property considers the evaluation of any ray quantity on τ-paths that first loop from $\tau = 0$ to τ_R and then back again via another path. The result should be that the image of the ray quantity under these paths forms a closed loop in the complex plane. In Figure 4.4 we have plotted the complex phase and amplitude as functions of various τ-paths formed as perturbations from the standard path. It is clear from Fig. 4.4(a) that the complex phase behaves as expected; the amplitude, however, does not (see Fig. 4.4(b)). This is because the source point of the Green's function is singular, so different paths start off at different "complex infinities". Fortunately, as the ray integration reaches τ_R each amplitude converges to $A_0(\boldsymbol{x}_R)$. If one takes into account the singularity at source, then in the extended complex plane $\mathbb{C} \cup \{\infty\}$, Figure 4.4(c) shows that the amplitude paths are connected at ∞.

There is one last important feature that this invariance study shows, and this pertains to the complex phase. Depending on the path, the phase may leave the source either exponentially small or exponentially large, though the end result (as shown in Fig. 4.4(a)) is still exponentially small. This means that the ray evaluated along this path will have a confined region of growth that does not affect the physical contribution at the end point τ_R. Thus we must reinforce the notion that rays are selected at the receiver rather than at the source. Otherwise, this could lead to the neglect of potentially useful contributions.

4.6 Winding numbers

The winding number method (WNM) presented here is an extension of the two-point ray-tracing formulation. As a root finding algorithm it is much slower than a Newton method applied to the two-point formulation of (4.1), and so serves as a back-up tool for finding, or checking the existence of, solutions where two-point calculations are indecisive. One example where this method may have utility is the calculation of roots for which large jumps in the bifurcation paths occasionally coupled with the presence of easier-to-find real roots makes their determination difficult.

4.6.1 Single variable case

In a single complex variable the winding number computation is based on the logarithmic integral, Gamelin [153],

$$\mathrm{Res}_{f=0}\left(\frac{\mathrm{d}f}{f}\right) = \frac{1}{2\pi\mathrm{i}}\oint_{\gamma_{\mathscr{C}}}\frac{\mathrm{d}f}{f} = \frac{1}{2\pi\mathrm{i}}\oint_{\gamma_{\mathscr{C}}}\frac{f'(z)}{f(z)}\,\mathrm{d}z = N_z, \tag{4.47}$$

where $f(z)$ is a holomorphic function with a finite number of isolated zeros $\{z^\star\}$ within the complex contour $\gamma_{\mathscr{C}}$. If these zeros are of multiplicity 1, then N_z is equal to the number of zeros within the contour; otherwise it is the sum of the multiplicities of each zero, i.e., $N_z = \sum \mu_f(z^\star)$.

The winding number can be seen pictorially by considering the image of $\gamma_{\mathscr{C}}$ under $f(z)$. The number of zeros within $\gamma_{\mathscr{C}}$ is equal to the number of loops n_W the image makes around the origin,

$$n_W(f(\gamma_{\mathscr{C}}), 0) := \frac{1}{2\pi}\left[\arg f(z)\right]_{z\in\gamma_{\mathscr{C}}}. \tag{4.48}$$

An example of the image $f(\gamma_{\mathscr{C}})$ is shown in Fig. 4.5(b) for the function $f(z) = \mathrm{e}^{3z} + 20z\cos z - 1$ with contour $\gamma_{\mathscr{C}} = \{z \in \mathbb{C} : |z| = 2\}$, shown in Fig. 4.5(a). The test radius shows number of times contour passes around origin.

The main assumption using (4.47) is that $f(z)$ is indeed holomorphic and therefore contains no singularities. When this result is extended to rays, it is conceivable that one can find scenarios where the contour does encircle a singularity, for instance due to those found in the analytic continuation of the mean flow profiles.[9] The proof of (4.47) consists of expressing the function $f(z) = (z - z^\star)^{\mu_f} h(z)$ in local coordinates z, where $\mu_f \in \mathbb{N}^+$ is the multiplicity, $h(z)$ is analytic and non-zero at $z = z^\star$. It is trivial to show that the principal part of $f'(z)/f(z) = \mu_f/(z - z^\star)$ is a meromorphic function with

[9] The formulae here can be extended to meromorphic functions in this case. E.g., $\mathrm{Res}_{f=0}(\mathrm{d}f/f) = N_z - P_z$, $P_z = \#$ of poles enclosed.

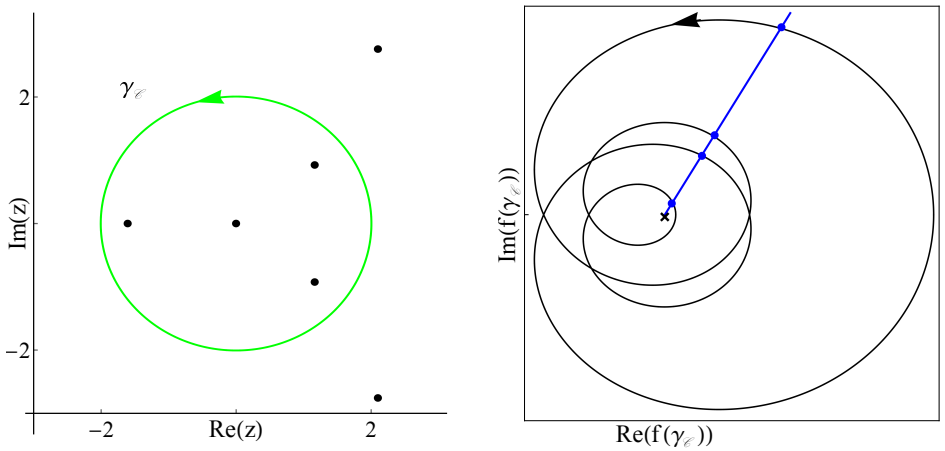

(a) $\gamma_{\mathscr{C}} = \{z \in \mathbb{C} : |z| = 2\}$ (b) $f(\gamma_{\mathscr{C}})$

FIGURE 4.5: Example of (a) $\gamma_{\mathscr{C}}$ encircling a finite of zeros of $f(z) = \mathrm{e}^{3z} + 20z\cos z - 1$ and (b) image $f(\gamma_{\mathscr{C}})$. In (b) the test radius drawn from the origin shows $n_W(f(\gamma_{\mathscr{C}}), 0)$.

μ_f the residue. This procedure can be applied to each zero of $f(z)$, generating a local residue, so that N_z may capture the number of zeros and their multiplicities.

In the following work the algorithm presented for calculating each $z^\star$ assumes that the multiplicity is equal to 1. As a consequence it is assumed that observers are not directly at the caustic whereby two solutions bifurcate and $\mu_f(z^\star) > 1$. The reason for doing so is to present the WNM in its simplest form and in a form where it is most useful (here at least). It should also be reinforced that the multiplicity of a zero μ_f is not the same as the multiplicity of rays, N, discussed in the first half of this chapter.

The following method of computing the zeros can be found in Kravanja & Barel [154]: however, this method has not been applied to two-point ray boundary value problems before and is worthwhile repeating. The contour integral applies to the two-point boundary problem in more than one way. First, there is the application to the components of (4.1), i.e., to each component F_i of the BVP $\mathbf{F} = \mathbf{0}$,

$$\begin{aligned} W_{ij}^{(1)} &= \frac{1}{2\pi\mathrm{i}} \oint_{\gamma_{\mathscr{C}}} \frac{\partial \mathrm{F}_i(\boldsymbol{\varsigma})/\partial \varsigma_j}{\mathrm{F}_i(\boldsymbol{\varsigma})} \,\mathrm{d}\varsigma_j \\ &= \frac{1}{2\pi\mathrm{i}} \oint_{\gamma_{\mathscr{C}}} \frac{\partial x_i(\boldsymbol{\varsigma})/\partial \varsigma_j}{\mathrm{F}_i(\boldsymbol{\varsigma})} \,\mathrm{d}\varsigma_j, \quad i,j = 1,\ldots,n. \end{aligned} \tag{4.49}$$

and then $\mathbf{F}\cdot\mathbf{F}$ the scalar equivalent of $\mathbf{F}$,

$$\begin{aligned} W_{j}^{(2)} &= \frac{1}{2\pi\mathrm{i}} \oint_{\gamma_{\mathscr{C}}} \frac{\partial(\mathbf{F}\cdot\mathbf{F})/\partial \varsigma_j}{\mathbf{F}\cdot\mathbf{F}} \,\mathrm{d}\varsigma_j \\ &= \frac{1}{\pi\mathrm{i}} \oint_{\gamma_{\mathscr{C}}} \frac{\mathbf{F}\cdot\partial\boldsymbol{x}/\partial \varsigma_j}{\mathbf{F}\cdot\mathbf{F}} \,\mathrm{d}\varsigma_j. \quad j = 1,\ldots,n. \end{aligned} \tag{4.50}$$

Note that an addition factor of 1/2 can be introduced into (4.50) due to dealing with a squared function (e.g., has the form $f^2(z) = (z - z_\star)^{2\mu_f} h^2(z)$ in (4.47)), i.e., one can allow for the appearance of simple root by now having a multiplicity equal to 2. For numerical reasons - and one of continuity - the integrals are kept as defined in (4.50).

Leaving the numerical computation of these integrals aside, it's possible to calculate the actual solutions in $\boldsymbol{\varsigma}^\star$ (desired ray firing parameters are now denoted by $\star$) for a specific observer ($\boldsymbol{x}_R$ has been suppressed above) by calculating the integrals,

$$\begin{aligned} W_{ij}^{(1,p)} &\equiv \frac{1}{2\pi \mathrm{i}} \oint_{\gamma_{\mathscr{C}}} \varsigma_j^p \frac{\partial x_i(\boldsymbol{\varsigma})/\partial \varsigma_j}{\mathrm{F}_i(\boldsymbol{\varsigma})} \, \mathrm{d}\varsigma_j, \\ &\equiv (\varsigma_{ij,1}^\star)^p + \ldots + (\varsigma_{ij,W_{ij}^{(1)}}^\star)^p, \end{aligned} \tag{4.51}$$

and likewise,

$$\begin{aligned} W_{j}^{(2,p)} &= \frac{1}{\pi \mathrm{i}} \oint_{\gamma_{\mathscr{C}}} \varsigma_j^p \frac{\mathbf{F} \cdot \partial \boldsymbol{x}/\partial \varsigma_j}{\mathbf{F} \cdot \mathbf{F}} \, \mathrm{d}\varsigma_j, \\ &= (\varsigma_{ij,1}^\star)^p + \ldots + (\varsigma_{ij,W_{ij}^{(2)}}^\star)^p. \end{aligned} \tag{4.52}$$

Where $(\varsigma_{ij,k}^\star)^p$ represents the k^{th} root $\varsigma_j^\star$ of F_i to the power $p \in \{1, \cdots, W_{ij}^{(O)}\}$, where $W_{ij}^{(O)}$ is shorthand for either $W_{ij}^{(1)}$ or $W_{j}^{(2)}$. Consequently a $W_{ij}^{(O)} \times W_{ij}^{(O)}$-size closed system of sums of powers in the roots can be formed. As it stands this is clearly more difficult to solve for each root with increasing number of roots within the contour. Of course in this case the contour $\gamma_{\mathscr{C}}$ can be subdivided into contours about smaller domains so that $W_{ij}^{(O)}$ is reduced in each case. The preferred method of calculating the roots is by using an associated polynomial [154] defined as,

$$P_{W_{ij}^{(O)}}(\varsigma) \equiv \prod_{n=1}^{W_{ij}^{(O)}} (\varsigma - \varsigma_{ij,n}^\star) = \varsigma^{W_{ij}^{(O)}} + \sigma_{ij,1} \varsigma^{W_{ij}^{(O)}-1} + \cdots + \sigma_{ij,W_{ij}^{(O)}}, \tag{4.53}$$

The connection between the coefficients $\sigma_{ij,k}$ of $P_{W_{ij}^{(O)}}$ and the sums of powers of roots is described by the Newton identities,

$$\begin{aligned} &W_{ij}^{(O,1)} + \sigma_{ij,1} = 0, \\ &W_{ij}^{(O,2)} + W_{ij}^{(O,1)} \sigma_{ij,1} + 2\sigma_{ij,2} = 0, \\ &\qquad\qquad \vdots \\ &W_{ij}^{(O,W_{ij}^{(O)})} + W_{ij}^{(O,W_{ij}^{(O)}-1)} \sigma_{ij,1} + \cdots + W_{ij}^{(O,1)} \sigma_{ij,W_{ij}^{(O)}-1} + W_{ij}^{(O)} \sigma_{ij,W_{ij}^{(O)}} = 0. \end{aligned} \tag{4.54}$$

In theory, the Newton identities are advantageous because the associated polynomial is much easier to solve for than the original system. The disadvantage is that the Newton

identities are potentially ill-conditioned for a large number of roots within the contour. Ill-conditioning also occurs when zeros are close together and exist in multiplicity (see for e.g., Wilkinson [155] & [156]). Usually the only solution to ill-conditioning is by using very high-precision arithmetic.

The main difficulty with the component-wise integration $W_{ij}^{(1)}$ is that each $W_{ij}^{(1)}$, for the same parameter i, but different component j, may have a different value. This is obvious if one does not use the same contour in each case, but there will exist solutions that are roots of one particular component and not another. Consequently, some effort must be made to syphon off spurious solutions. This is the most straightforward way of determining the correct solutions; however, it is possible to determine whether two components have a common root by using a *resultant*.

The resultant $R_{N,M}(P_{n,N}, P_{m,M})$ of two polynomials $P_{n,N}$ and $P_{m,M}$,

$$P_{n,N}(\varsigma) = \sigma_{n,0}\varsigma^N + \cdots + \sigma_{n,N-1}\varsigma + \sigma_{n,N},\ P_{m,M}(\varsigma) = \sigma_{m,0}\varsigma^M + \cdots + \sigma_{m,M-1}\varsigma + \sigma_{m,M}, \tag{4.55}$$

in a single variable ς (where in reference to (4.53): j is suppressed, n and m represent different components of the vector, $\sigma_{n,0} = \sigma_{m,0} = 1$ is left unchanged for a general result; N and M are $W_{nj}^{(1)}$ and $W_{mj}^{(1)}$, respectively) is defined as,

$$R_{N,M}(P_{n,N}, P_{m,M}) = \sigma_{n,0}^M \sigma_{m,0}^N \prod_{\ell_1,\ell_2} (\varsigma_{in,\ell_1}^\star - \varsigma_{im,\ell_2}^\star), \quad \ell_1 = 1,\ldots,N;\ \ell_2 = 1,\ldots,M. \tag{4.56}$$

The resultant can be computed using Sylvester's formula (Sturmfels [157]):

$$R_{N,M}(P_{n,N}, P_{m,M}) = \begin{vmatrix} \sigma_{n,N} & \sigma_{n,N-1} & & \cdots & \sigma_{n,0} & 0 & \cdots & & 0 \\ 0 & \sigma_{n,N} & \sigma_{n,N-1} & \cdots & \cdots & \sigma_{n,0} & 0 & \cdots & 0 \\ \vdots & & & & & & & & \\ 0 & 0 & \cdots & 0 & \sigma_{n,N} & \sigma_{n,N-1} & & \cdots & \sigma_{n,0} \\ \sigma_{m,M} & \sigma_{m,M-1} & \cdots & & \sigma_{m,1} & \sigma_{m,0} & 0 & \cdots & 0 \\ 0 & \sigma_{m,M} & \sigma_{m,M-1} & & \cdots & & \sigma_{m,0} & \cdots & 0 \\ \vdots & & & & & & & & \\ 0 & & \cdots & & 0 & \sigma_{m,M} & \sigma_{m,M-1} & \cdots & \sigma_{m,0} \end{vmatrix}. \tag{4.57}$$

It can be seen from (4.56) that $R_{N,M} = 0$ whenever any roots from either polynomial are equal. So a calculation of the resultant that is approximately zero means that a particular region enclosed by $\gamma_{\mathscr{C}}$ contains a root of at least two components. The resultant is most useful for determining whether to pursue a particular region for the location of

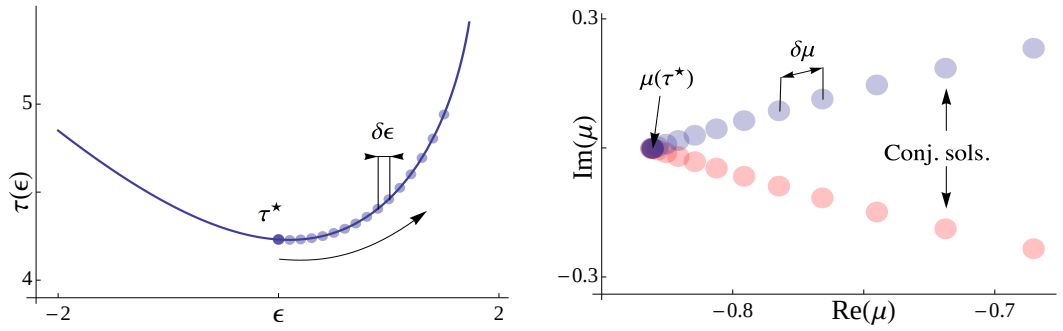

(a) $\tau(\epsilon)$ and $\tau^\star$ with test points.

(b) $\mu(\tau)$ and $\mu(\tau^\star)$ at test points.

FIGURE 4.6: Continuity of roots as $\tau(\epsilon)$ deviates from $\tau^\star$. In (a) τ_1 branch of the LLP problem generates a curve under epsilon with test points at $\delta\epsilon = 0.1$ intervals; (b) shows the intersection of those curves at $\mu(\tau^\star)$.

a root. The downside to the resultant is that, though it is generalisable to systems of polynomials in multiple variables, there is no trivial extension to systems of polynomials in one variable: such a case leads to resolvents (see for e.g., Gelfand et al. [158]) and a system of criteria.

4.6.1.1 Application to the linear-layer problem: Part I

As a demonstration of the winding number theory, the preceding theory can be applied to the linear-layer problem. The winding number integrals for the single ray firing variable cases are easily written down in closed form (using the expressions for geodesic elements from Eq. (3.61)). For example $W_{i1}^{(1)}$ where $j = 1$ signifies a search w.r.t. μ:

$$\begin{aligned} W_{11}^{(1)} &= -\frac{1}{2\pi \mathrm{i}} \oint_{\gamma_{\mathscr{C}}} \frac{\tau \sin\mu}{a_s(x_s - x_R) + \tau\cos\mu}\,\mathrm{d}\mu \\ W_{21}^{(1)} &= \frac{1}{2\pi \mathrm{i}} \oint_{\gamma_{\mathscr{C}}} \frac{\tau \cos\mu}{a_s(z_s - z_R) + \tau\sin\mu - 0.25 a_s b \tau^2}\,\mathrm{d}\mu, \end{aligned} \tag{4.58}$$

and $W_1^{(2)}$,

$$W_1^{(2)} = \frac{1}{2\pi \mathrm{i}} \oint_{\gamma_{\mathscr{C}}} \frac{-\tau\sin\mu + \frac{(a_s(z_s - z_R) + \tau\sin\mu - 0.25 a_s b\tau^2)\tau\cos\mu}{(a_s(x_s - x_R) + \tau\cos\mu)}}{(a_s(x_s - x_R) + \tau\cos\mu) + \frac{(a_s(z_s - z_R) + \tau\sin\mu - 0.25 a_s b\tau^2)^2}{(a_s(x_s - x_R) + \tau\cos\mu)}}\,\mathrm{d}\mu, \tag{4.59}$$

In the first case it can be seen that for an observer in the real ray region (such that $|\mu| < \pi/2$) that a contour $\gamma_{\mathscr{C}} = \{\mu \in \mathbb{C} : |\mu| = \pi/2\}$[10] for a particular $\tau^\star$ (or an estimate of) yields two roots in μ for $W_{11}^{(1)}$ and just one in $W_{21}^{(1)}$. Taking a Taylor expansion

[10] In order to keep $\gamma_{\mathscr{C}}$ at the origin, $-\pi < \mu \leq \pi$.

of $\sin\mu$ and $\cos\mu$ and solving for μ gives two approximations for the roots of $W_{11}^{(1)}$ as $\mu \approx \pm 2^{1/2}\sqrt{1 + a_s(x_s - x_R)(\tau^\star)^{-1}}$ and one of $W_{21}^{(1)}$ as $\mu \approx 0.25b\tau^\star/(z_s - z_R)$.

So far, not much has been said about the accuracy of $\tau^\star$ above or any of the estimates of $\boldsymbol{\varsigma}^\star\backslash\{\varsigma_j^\star\}$ implicit in the general single variable WNM. One might expect that $\tau^\star$ has to be exact in order to have $N_z \neq 0$. This would be a stringent requirement and one that wouldn't be met due to the numerical nature of this problem. However, the zeros of the components F_i *are not isolated* - a generic property of multiple variable problems - so that even a poor estimate of $\boldsymbol{\varsigma}^\star\backslash\{\varsigma_j^\star\}$ will yield some root $\varsigma_j^\star$.

The second application of the WNM to the scalar equivalent function $\mathbf{F}\cdot\mathbf{F}$ makes one improvement to the component case. That improvement is the elimination of roots that zero one component but not others. However, the non-isolated nature of these roots cannot be eliminated so estimates of $\boldsymbol{\varsigma}^\star\backslash\{\varsigma_j^\star\}$ can still lead to multiplicities in $\varsigma_j^\star$.

It was mentioned in the definition of $W_j^{(2)}$ that no special procedure would be introduced due to the squared nature of $\mathbf{F}\cdot\mathbf{F}$. Numerical analysis shown in Fig. 4.6 shows that if τ is perturbed from the exact value $\tau^\star$ root, then instead of a double root, two simple roots exist that are conjugate pairs. As the exact value is reached these pairs coalesce and coincide with the zero of $\mathbf{F}\cdot\partial\mathbf{F}/\partial\varsigma_j$ (the real part of these conj. roots) yielding a simple pole in the integral. If the squared definition is used (1/2 is factored in) then the solution is the real part of these roots: however, this is not satisfactory since this ignores the reality of two distinct simple poles in $W_j^{(2)}$.

It is natural to question whether these continued roots are indeed rays or pertain to some physical phenomenon that should be investigated. The answer is that they aren't, because the desired rays have the property,

$$\underbrace{\mathrm{F}_1}_{0} + \ldots + \underbrace{\mathrm{F}_n}_{0} = 0, \tag{4.60}$$

where as the extended roots only have the property,

$$\mathrm{F}_1^2 + \ldots + \mathrm{F}_n^2 = 0, \tag{4.61}$$

that is, all squared components of $\mathbf{F}$ conspire to yield a zero.

4.6.2 Multidimensional residue theorem

The main problem suffered by the single variable winding number algorithm is that it requires guesses for all other ray parameters $\boldsymbol{\varsigma}\backslash\{\varsigma_j\}$. Furthermore, the zeros of the components F_i are not isolated and one must determine the intersection of the zero sets

of each component to determine the overall root. One way of doing so was using the resultant and its generalisations. The utility of this method is really to track down one particular ray firing parameter whose bifurcation path may change rapidly while other paths $\Gamma^B_{\boldsymbol{\varsigma}\setminus\{\varsigma_j\}}$ behave smoothly.

What is preferable, and in some sense what we have been building up to, is a multi-dimensional residue theorem, or more precisely, a multidimensional logarithmic residue theorem. These exist but are more complicated, involving the integration of complex differential forms (see for e.g., Tsikh [159]). Typically the study of residue theory and its generalisations to higher dimensions should involve the theory of residue currents (Tsikh & Yger [160]). However, here the starting point is the Grothendieck residue integral (D'Angelo [161], Ajzenberg & Yuzhukov [162]),

$$\mathrm{Res}_{\boldsymbol{f}=\mathbf{0}}(\mathrm{d}\boldsymbol{f}/\boldsymbol{f}) = \frac{1}{(2\pi\mathrm{i})^{n_D}}\int_\Gamma \frac{\mathrm{d}f_1}{f_1}\wedge\frac{\mathrm{d}f_2}{f_2}\wedge\ldots\wedge\frac{\mathrm{d}f_{n_D}}{f_{n_D}} = \frac{1}{(2\pi\mathrm{i})^{n_D}}\int_\Gamma \frac{\mathrm{d}\boldsymbol{f}}{\boldsymbol{f}}, \tag{4.62}$$

where $\boldsymbol{f}$ is a tuple of holomorphic functions $\boldsymbol{f} = (f_1,\ldots,f_{n_D})$ such that $\boldsymbol{f}:(\mathbb{C}^{n_D},0)\to(\mathbb{C}^{n_D},0)$ and defines a complete intersection (i.e., a mapping of $\mathbb{C}^{n_D}$ to $\mathbb{C}^{n_D}$). Here $\Gamma=\Gamma_{\boldsymbol{f}}$ is a real n_D-dimensional cycle defined by the equations $|f_j|=\epsilon$ for sufficiently small positive ϵ, and is oriented so that,[11]

$$\mathrm{d}(\arg(f_1))\wedge\ldots\wedge\mathrm{d}(\arg(f_{n_D}))>0. \tag{4.63}$$

The Grothendieck residue is a natural generalisation of the one-variable residue integral (4.47) and can be generalised further by introducing local coordinates $\boldsymbol{\varsigma}=(\varsigma_1,\ldots,\varsigma_{n_D})$ with isolated common root $\boldsymbol{\varsigma}^\star$, and holomorphic function $h(\boldsymbol{\varsigma})$ and Jacobian $\det(\partial f_i/\partial\varsigma_j)$.

$$\mathrm{Res}_{\boldsymbol{\varsigma}^\star}\left(\frac{h(\boldsymbol{f})\det(\partial f_i/\partial\varsigma_j)\mathrm{d}\boldsymbol{\varsigma}}{\boldsymbol{f}}\right) = \frac{1}{(2\pi\mathrm{i})^{n_D}}\int_{\Gamma_{\boldsymbol{f}}}\frac{h(\boldsymbol{f})\det(\partial f_i/\partial\varsigma_j)\mathrm{d}\varsigma_1\wedge\ldots\wedge\mathrm{d}\varsigma_{n_D}}{f_1\ldots f_{n_D}} = \sum_i \mu_{\boldsymbol{f}}(\boldsymbol{\varsigma}_i^\star)h(\boldsymbol{\varsigma}_i^\star), \tag{4.64}$$

where the sum represents the possible case of multiple isolated zeros $\boldsymbol{\varsigma}_i^\star$ of $\boldsymbol{f}$ present within the cycles $\Gamma_{\boldsymbol{f}}$, and $\mu_{\boldsymbol{f}}(\boldsymbol{\varsigma}_i^\star)$ represents the multiplicity of the intersection of the zero sets of $\boldsymbol{f}$ at $\boldsymbol{\varsigma}_i^\star$.

The simplicity of the Cauchy kernel $(\mathrm{d}\boldsymbol{f}/\boldsymbol{f})$ in (4.62) makes it the natural candidate for studying residues in several variables. A further useful feature of this kernel is that it is universal: it does not depend on the domain. However this kernel involves the integration over a set of real dimension n_D and not over the whole $(2n_D-1)$-dimensional boundary of a domain. Rather than using the Cauchy kernel another integral representation can be used. This representation is known as the Bochner-Martinelli integral [162] and is

[11] Note that Eq. (4.62) is independent of ϵ.

a universal representation formula for holomorphic functions via integration over the whole boundary of a domain.

The Bochner-Martinelli kernel is defined in $\mathbb{C}^{n_D}$ as a differential form of bidegree (n_D, n_D-1) (compare with the Cauchy kernel which is an $(n_D, 0)$-form),

$$K_{\boldsymbol{f}} \equiv \frac{(-1)^{n_D(n_D-1)/2}(n_D-1)!}{(2\pi\mathrm{i})^{n_D}|\boldsymbol{f}|^{2n_D}} \sum_{i=1}^{n_D}(-)^{i-1}\bar{f}_i \,\mathrm{d}\boldsymbol{f}_{[i]}\wedge\mathrm{d}\boldsymbol{f} = \frac{(-1)^{n_D(n_D-1)/2}(n_D-1)!}{(2\pi\mathrm{i})^{n_D}|\boldsymbol{f}|^{2n_D}}\eta(\bar{\boldsymbol{f}})\wedge\mathrm{d}\boldsymbol{f}, \tag{4.65}$$

where,

$$\eta(\boldsymbol{f}) \equiv \sum_{i=1}^{n_D}(-)^{i-1} f_i \,\mathrm{d}\boldsymbol{f}_{[i]}, \tag{4.66}$$

is known as the *Leray form* and $\mathrm{d}\boldsymbol{f}_{[i]} = \mathrm{d}f_1\wedge\ldots\wedge\mathrm{d}f_{i-1}\wedge\mathrm{d}f_{i+1}\wedge\ldots\wedge\mathrm{d}f_{n_D}$. *Where an over bar denotes a complex conjugate and not a mean time derivative as in the remainder of the thesis.*[12]

A trivial example of the Bochner-Martinelli (BM) kernel is the reduction to the Cauchy kernel $\mathrm{d}f/2\pi\mathrm{i}f$ in one dimension when $n_D = 1$. Another important property of the BM kernel is that it is closed w.r.t. $\bar{\partial} \equiv \sum(\partial/\partial\bar{\varsigma}_i)\mathrm{d}\bar{\varsigma}_i$ (but not exact in the complement of the origin), so $\mathrm{d}K_{\boldsymbol{f}} = \bar{\partial}K_{\boldsymbol{f}} = 0$.

Now, integrating the BM kernel multiplied by a holomorphic function $h(\boldsymbol{\varsigma})$ (in local coordinates $\boldsymbol{\varsigma}$) over a $(2n_D-1)$ boundary ∂D of a polydisk $D \in \mathbb{C}^{n_D}$ defined by,

$$D = D_1 \times \cdots \times D_{n_D}, \tag{4.67}$$

containing the isolated common zeros of $\boldsymbol{f}$ (not lying on ∂D)

$$D_k = \{\varsigma \in \mathbb{C} : |\varsigma - C_k| < R_k\}, \quad k = 1, \ldots, n_D, \tag{4.68}$$

with $C_1, \ldots, C_{n_D} \in \mathbb{C}$ and $R_1, \ldots, R_{n_D} > 0$, gives,

$$\int_{\partial D} h(\boldsymbol{\varsigma})\det(\boldsymbol{f}(\boldsymbol{\varsigma}))K_{\boldsymbol{f}} = \sum_i \mu_{\boldsymbol{f}}(\boldsymbol{\varsigma}_i^\star)h(\boldsymbol{\varsigma}_i^\star). \tag{4.69}$$

Converting (4.69) to a problem relevant to the two-point problem is purely symbolic: it is sufficient to rewrite f_i as F_i ($\boldsymbol{f}$ by $\mathbf{F}$), $\mu_{\boldsymbol{f}}$ as $\mu_{\mathbf{F}}$ (distinguishing between the firing parameter μ and multiplicity of a root $\mu_{\mathbf{F}}$). The local coordinates are again chosen to be the ray firing parameters $\mathbf{s}$ so that the Jacobian of the transformation, J_T (we could use $\det(D\mathbf{F})$), is the determinant of the transpose of the ray Jacobian matrix, J_{mat}. Then

[12] This allows us to conform to a standard notation.

it can be shown [154] that $K_{\mathbf{F}}$ and $\eta(\mathbf{F})$ can be written,

$$K_{\mathbf{F}}(\boldsymbol{\varsigma}) = \frac{(-1)^{n_D(n_D-1)/2}(n_D-1)!}{(2\pi\mathrm{i})^{n_D}|\mathbf{F}|^{2n_D}}\eta(\overline{\mathbf{F}}) \wedge \mathrm{d}\boldsymbol{\varsigma}, \tag{4.70}$$

$$\eta(\mathbf{F}) = \sum_{i=1}^{n_D}\eta_i = \sum_{i=1}^{n_D}(-)^{i-1}J_{T_{[i]}}(\varsigma_1,\ldots,\varsigma_{n_D})\mathrm{d}\boldsymbol{\varsigma}_{[i]}, \tag{4.71}$$

where $J_{T_{[i]}}(\varsigma_1,\ldots,\varsigma_{n_D})$ is the Jacobian J_T with ith column replaced with $(\mathrm{F}_1,\ldots,\mathrm{F}_{n_D})^T$,

$$J_{T_{[i]}} \equiv \begin{vmatrix} \frac{\partial \mathrm{F}_1}{\partial \varsigma_1} & \cdots & \frac{\partial \mathrm{F}_1}{\partial \varsigma_{i-1}} & \mathrm{F}_1 & \frac{\partial \mathrm{F}_1}{\partial \varsigma_{i+1}} & \cdots & \frac{\partial \mathrm{F}_1}{\partial \varsigma_{n_D}} \\ \vdots & & \vdots & \vdots & \vdots & & \vdots \\ \frac{\partial \mathrm{F}_{n_D}}{\partial \varsigma_1} & \cdots & \frac{\partial \mathrm{F}_{n_D}}{\partial \varsigma_{i-1}} & \mathrm{F}_{n_D} & \frac{\partial \mathrm{F}_{n_D}}{\partial \varsigma_{i+1}} & \cdots & \frac{\partial \mathrm{F}_{n_D}}{\partial \varsigma_{n_D}} \end{vmatrix} = \begin{vmatrix} \frac{\partial x_1}{\partial \varsigma_1} & \cdots & \frac{\partial x_1}{\partial \varsigma_{i-1}} & \mathrm{F}_1 & \frac{\partial x_1}{\partial \varsigma_{i+1}} & \cdots & \frac{\partial x_1}{\partial \varsigma_{n_D}} \\ \vdots & & \vdots & \vdots & \vdots & & \vdots \\ \frac{\partial x_{n_D}}{\partial \varsigma_1} & \cdots & \frac{\partial x_{n_D}}{\partial \varsigma_{i-1}} & \mathrm{F}_{n_D} & \frac{\partial x_{n_D}}{\partial \varsigma_{i+1}} & \cdots & \frac{\partial x_{n_D}}{\partial \varsigma_{n_D}} \end{vmatrix}. \tag{4.72}$$

It can then be shown that,

$$\int_{\partial D} h(\boldsymbol{\varsigma})J_T(\boldsymbol{\varsigma})K_{\mathbf{F}}(\boldsymbol{\varsigma})\wedge\mathrm{d}\boldsymbol{\varsigma} = \frac{(-1)^{n_D(n_D-1)/2}(n_D-1)!}{(2\pi\mathrm{i})^{n_D}}\sum_{i=1}^{n_D}\int_{\partial D_{[i]}}\frac{1}{|\mathbf{F}|^{2n_D}}h(\boldsymbol{\varsigma})J_T(\boldsymbol{\varsigma})\eta_i(\overline{\mathbf{F}})\wedge\mathrm{d}\boldsymbol{\varsigma}, \tag{4.73}$$

where the boundary ∂D is given by,

$$\partial D = \partial D_{[1]} \cup \cdots \cup \partial D_{[n_D]}, \tag{4.74}$$

where,

$$\partial D_{[k]} \equiv D_1 \times \ldots \times D_{k-1} \times \partial D_k \times D_{k+1} \times \cdots \times D_{n_D}, \quad k = 1,\ldots,n_D. \tag{4.75}$$

The decomposition of the boundary ∂D into a sum of integrals over the boundaries $\partial D_{[k]}$ in (4.73) is permitted by Stokes theorem because an integral is closed when it does not contain a root, i.e., for $i \neq j$ then $\int_{\partial D_{[j]}} J_T(\boldsymbol{\varsigma})K_{\mathbf{F}}(\boldsymbol{\varsigma}) \wedge \mathrm{d}\boldsymbol{\varsigma}$ is closed. Equation (4.73) can be then treated as a sum of Riemann integrals by introducing polar coordinates as in [154]. A generic coordinate is represented as,

$$\varsigma_k = \varsigma_k(\theta_k) = C_k + R_k\mathrm{e}^{2\pi\mathrm{i}\theta_k}, \qquad \text{for the boundary of } \partial D_k \tag{4.76}$$

$$\varsigma_l = \varsigma_l(r_l,\theta_l) = C_k + r_l R_l\mathrm{e}^{2\pi\mathrm{i}\theta_l}, \quad \text{for the domain of } D_k \tag{4.77}$$

where $r_k, \theta_k \in [0,1]$. Thus the differential form $d\bar{\varsigma}_k \wedge \mathrm{d}\varsigma_k = 2(2\pi\mathrm{i})r_k R_k^2 \mathrm{d}r_k \wedge \mathrm{d}\theta_k$. Then it can be shown that,

$$\begin{aligned}\frac{(-1)^{n_D(n_D-1)/2}(n_D-1)!}{(2\pi\mathrm{i})^{n_D}} \int_{\partial D_{[k]}} \frac{1}{|\mathbf{F}|^{2n_D}} h(\boldsymbol{\varsigma}) J_T(\boldsymbol{\varsigma}) \eta_k(\overline{\mathbf{F}}) \wedge \mathrm{d}\boldsymbol{\varsigma} \\ = \rho_k \int_{[0,1]^{2n_D-1}} \frac{1}{|\mathbf{F}|^{2n_D}} h(\boldsymbol{\varsigma}) J_T(\boldsymbol{\varsigma}) \overline{J_{T_{[i]}}(\boldsymbol{\varsigma})} \\ \times \mathrm{e}^{2\pi\mathrm{i}\theta_k} r_1 \cdots r_{k-1} r_{k+1} \cdots r_{n_D} \mathrm{d}r_1 \ldots \mathrm{d}r_{k-1} \mathrm{d}r_{k+1} \ldots \mathrm{d}r_{n_D} \mathrm{d}\theta_1 \cdots \mathrm{d}\theta_{n_D},\end{aligned} \tag{4.78}$$

where $\rho_k = 2^{n_D-1}(n_D-1)! R_1^2 \cdots R_{k-1}^2 R_k R_{k+1}^2 \cdots R_{n_D}^2$, should not be confused with the density ρ and θ_k, R_k are distinct from the receiver polar angle θ and radius R, respectively.

4.6.2.1 Application to the linear-layer problem: Part II

We can write the multidimensional winding number for the linear-layer problem in closed form, where we set $n_D = 2$ in the preceding theory.

We need $J_{T_{[i]}}$ for $i = 1, 2$,

$$\begin{aligned}J_{T_{[1]}} = \begin{vmatrix} \mathrm{F}_1 & \partial_\tau x \\ \mathrm{F}_2 & \partial_\tau z \end{vmatrix} = \\ \Delta_x a_s^{-1} \cos\mu - \Delta_z a_s^{-1} \sin\mu - \frac{1}{2} l_2 \Delta_x \tau - \frac{1}{4} l_2 \tau^2 a_s^{-1} \sin\mu,\end{aligned} \tag{4.79}$$

and,

$$\begin{aligned}J_{T_{[2]}} = \begin{vmatrix} \partial_\mu x & \mathrm{F}_1 \\ \partial_\mu z & \mathrm{F}_2 \end{vmatrix} = \\ -a_s^{-1}\tau \sin\mu \Delta_z - 2a_s^{-2}\tau^2 \sin\mu\cos\mu + \frac{1}{4} l_2 \tau^3 a_s^{-1} \sin\mu - a_s^{-1}\tau\Delta_x \cos\mu,\end{aligned} \tag{4.80}$$

where $\Delta_x = x_s - x_R$ and $\Delta_z = z_s - z_R$.

$$\mathrm{F}_1^2 + \mathrm{F}_2^2 = R^2 + 2a_s^{-1}\tau\left(\Delta_x + \Delta_z\right)\cos\mu + a_s^{-2}\tau^2 - \frac{1}{2}\Delta_z l_2 \tau^2 - \frac{1}{2} l_2 \tau^3 a_s^{-1} \cos\mu + \frac{1}{16} l_2^2 \tau^4. \tag{4.81}$$

Substitution of these expressions into (4.78) allows the first numerical simulation to be carried out.

Before we proceed with a numerical calculation it should be mentioned that the multidimensional integrals are extremely tricky to evaluate and their efficient computation

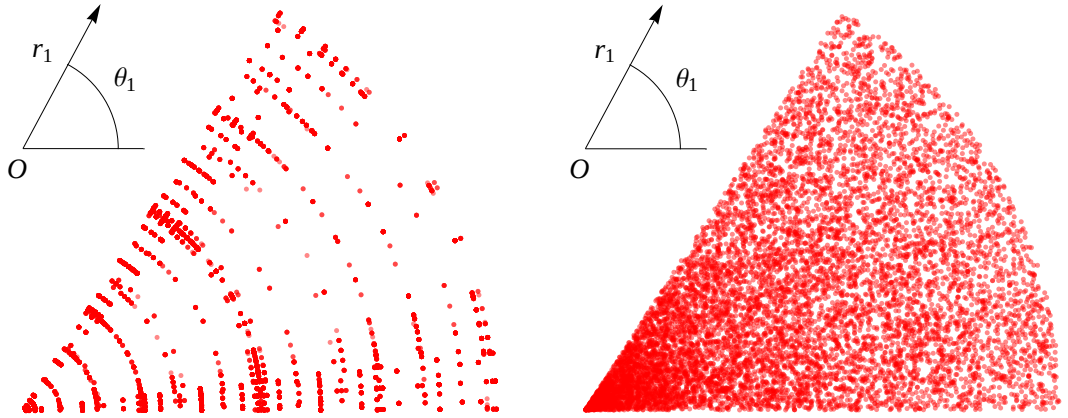

(a) Sparse grid (b) Monte-Carlo

FIGURE 4.7: Sparse grid and Monte-Carlo points in r_1 and θ_1 for the numerical integration of the LLP problem. These plots show $O(10^4)$ points contained within a wedge.

is still an open problem. There are several numerical approaches available for the computation of (4.78), which broadly speaking, can be placed in two categories based upon the sample points used: structured and unstructured/random grids. The purpose of this section is not to compare integration methods *ad nauseam* but to effect the first realisations of the WNM in the context of ray theory; for this reason we shall employ a Monte-Carlo method which fits into the latter of the aforementioned categories. Such a method has been shown to be a viable alternative to structured grid methods by Kalos & Whitlock [163] and Fishman [164].

The Monte-Carlo method is stochastic and estimates a given integral by averaging integrand values at uniformly distributed random points in the domain of integration. The density of these points is increased until precision or accuracy goals are satisfied. Monte-Carlo integration methods have advantages over other numerical integration methods in a space of many dimensions. Their efficiencies relative to other methods increase when the dimension of the problem increases. Monte Carlo integration remains almost unchanged for higher dimensions, whilst quadrature formula become increasingly complex. It is also suited for large structures and highly complex problems for which definite integral formulation is not obvious and standard analytical techniques are ineffective.

A demonstration of typical points used in the computation is shown in Fig. 4.7 for a wedge of the polar domain. Both of these point sets are for the r_1, θ_1 coordinates and are projected into that plane for various r_2 for the boundary integral with differential form $\mathrm{d}r_1\mathrm{d}\theta_1\mathrm{d}\theta_2$. The first of these, Fig. 4.7(a), shows a structured grid created using the

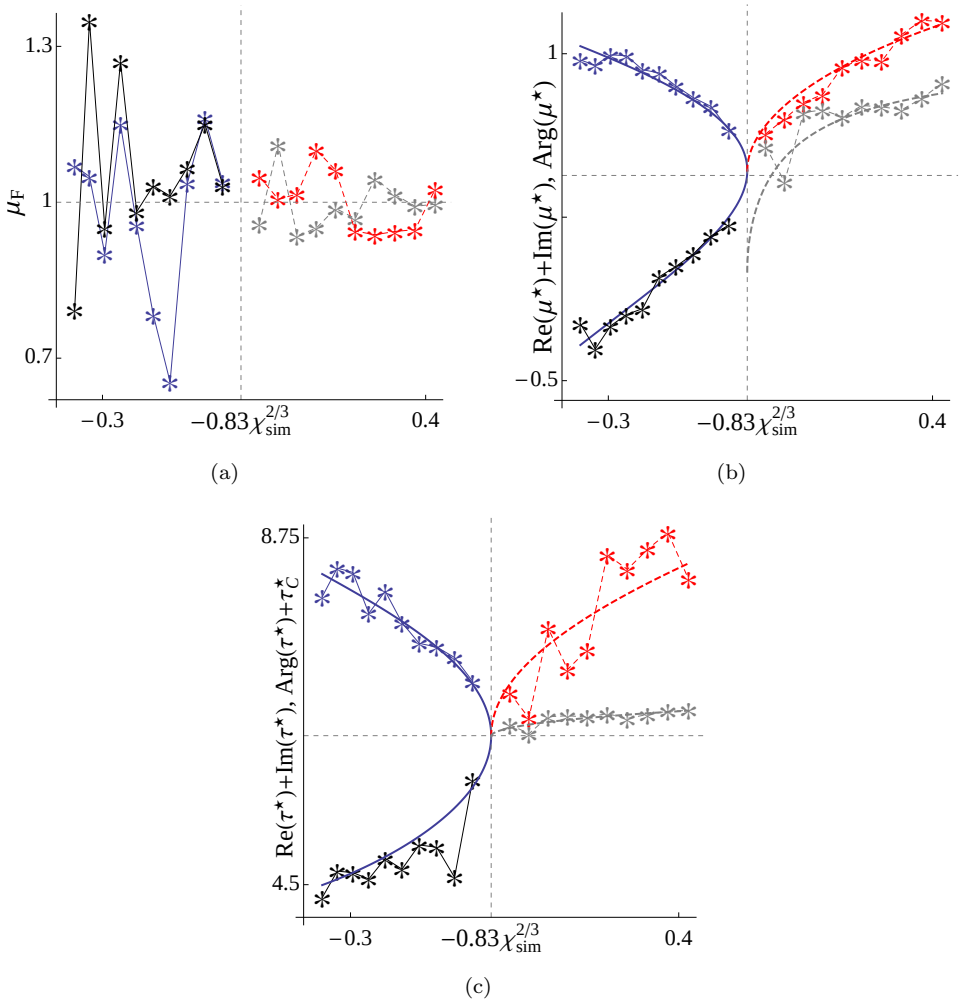

FIGURE 4.8: Calculation of ray parameters using multi-dim WNM. (a) $\mu_{\mathbf{F}}$, (b) $\mu^\star$, (c) $\tau^\star$. Solid (real) and dashed (complex) lines, exact. $*$, WNM calculations. All curves are $\mathrm{Re}(\mu_{\mathbf{F}}, \boldsymbol{\varsigma}^\star) + \mathrm{Im}(\mu_{\mathbf{F}}, \boldsymbol{\varsigma}^\star)$ except grey curves which are functions of $\mathrm{Arg}(\mu_{\mathbf{F}}, \boldsymbol{\varsigma}^\star)$ when $\mu_{\mathbf{F}}, \boldsymbol{\varsigma}^\star \in \mathbb{C}$.

sparse grid method. The grouping of points shown reveals that there is little deviation with changes in r_2. This contrasts significantly with the Monte-Carlo points that when projected into $r_1\theta_1$-space cover the wedge, albeit non-uniformly. Though the sparse grid is of course purposely sparse in its domain, other structured grids do not cover the domain to the extent of the Monte-Carlo method.

The point sets in Figure 4.7 do not tell the full story of the structured vs. random grid computation. Both subfigures show $O(10^4)$ sets of points, though in the case of the sparse grid this is only a fraction of $O(10^6)$ points used in a typical computation of the LLP. Consequently, the sparse grid method is more time consuming: another reason why it is not the main tool for winding number computation here.

The first computations of the multidimensional WNM for the LLP along the curve $-0.83\chi_{\text{sim}}^{2/3}$ (as in Fig. 4.3(c)) are shown in Fig. 4.8. This figure shows both the approximations to $\mu_{\mathbf{F}}$ and $\boldsymbol{\varsigma}^\star$ on both sides of the caustic. From Fig. 4.8(a) we see that the approximation to the multiplicity of $\mu_{\mathbf{F}} = 1$ for real branches is relatively poor with the complex multiplicities offering some improvement. Fortunately, this error appears not to propagate through into the $\boldsymbol{\varsigma}^\star$ calculation stage, where both real and complex solutions of $\boldsymbol{\varsigma}^\star$ match the exact solutions well.

Despite the success of these results, there are a several issues with the WNM. The first is identifiable from Fig. 4.8 and is specific to this computation. This concerns the caustic point at $\chi_{\text{sim}} = 0$ and the absence of a computation there. This is due to a large error that creeps into the result as the caustic is neared, rendering the method unintelligible. The second issue relates to the implementation of the algorithm in Appendix C.4 when $\mu_{\mathbf{F}}$ is not an integer. In this scenario the multiplicity is rounded to the closest integer $[\text{Re}(\mu_{\mathbf{F}})]$, where $[\cdot]$ is the nearest integer function. This means $W_{n_D}^{M,0}$ is interpreted as $[\text{Re}(N)]$ when considering the number of moments $h(\varsigma_{n_D}) = \varsigma_{n_D}^p$, otherwise $W_{n_D}^{M,0}$ is left as calculated by the winding number integrals, for instance when it is used in the matrix (C.29).

The final issue relates to the generality of the current algorithm. Unfortunately, the algorithm presented here is not readily available for the numerical problems that are found in jet noise, where the ray paths cannot be found in closed form. A big difference between the LLP and jet noise problems is that the LLP has no singularities in its analytic continuation whereas parallel shear flow problems typically contain singularities in complex space due to the exponential behaviour of the shear layer. The theory in this chapter doesn't allow for such singularities, though it is plausible that the differential forms used could be extended to allow for such cases.

4.7 Conclusion

In this chapter the problem of ray multiplicities has been addressed. This was achieved by introducing a two-point boundary value problem delimited by the ray ends at the source and receiver. Proceeding by firing a distribution of real test rays, an equivalent iterative system was used to locate all real rays that propagate to a desired receiver in a real ray illuminated region. The effectiveness of this algorithm can be enhanced by using a continuation method to generate bifurcation curves as the receiver curve varies. At caustics the continuation methods fail and so additional apparatus must be introduced: two distinct methods were considered. The first, based on a Liapunov-Schmidt reduction, provides jump conditions to continue through the caustic; the second,

a complex continuation method that draws from WKB theory, bypasses the caustic. The latter is favoured more in this thesis due to its ease of use and generality. The critical point of this chapter, and indeed this thesis, is that the caustics encountered are stable. Thus the ray parameters behave as roots of polynomials around, and through, the caustic. It will be shown that these polynomials - not explictly stated in full so far - are the derivatives of the catastrophe functions used in the next chapter.

In the final part of this chapter the two-point BVP was used to provide an extension of the root finding theory by tying together the ray and winding number theories. Though this method does not serve as a viable engineering method, i.e., it would not form the centrepiece of an AA solver, its presence here is not gratuitous. It is foreseeable that with more work, for example, extension to meromorphic functions, the method could be used as an investigative tool to provide the first approximations to, and proof of existence of, hard-to-find complex solutions.

Chapter 5

Uniform Functions and Catastrophe Theory

5.1 Introduction

In previous chapters ray solutions where developed according to a generic moving media framework providing a quick and efficient method of calculating both acoustic pressure, and correlation integrals and their Fourier transforms. However, ray solutions aren't a free lunch: several ray deficiencies exist that can sufficiently undermine the ray calculation. Fortunately, the number of deficiencies are reduced significantly when the solution is in free space, and aside from blow-ups near the source, the coalescence of multiple rays at a stable caustic remains the only cause for singularity. The appearance of stable caustics engenders a "live now, pay later" nature into the ray solver: in Chapter 4 the code was the beneficiary as the caustic was used as a stable springboard into the complex plane; now the singularity in amplitude cannot be ignored and must be corrected for realistic jet noise predictions.

The contents of this chapter are concerned with providing uniform solutions whilst still exploiting the $k_0 \to \infty$ limit of the field. The first section introduces catastrophe theory as a means of classifying the caustic using the corank and codimension of the singularity to determine the appropriate catastrophe germ. This is effected using elements of Chapter 4 where the connection between catastrophe and bifurcation theory is highlighted to elucidate the ray solvers recognition ability. The second section introduces the diffraction catastrophes which are the building blocks of the uniform method. In the third section the high-frequency field is expanded in terms of the diffraction catastrophes leading to a uniform asymptotic sequence valid across the relevant caustic. Methods of computing the mappings to diffraction catastrophes are discussed. In the final section we

use Dingle's singulant to identify and discuss the cross-over from ray to uniform fields. The singulant is also used to evaluate the catastrophe identification via bifurcation path method as the latter is restricted to the study of single parameter families.

5.2 Catastrophe theory

Catastrophe theory is a mathematical program that deals with the *local* behaviour of functions and how they change discontinuously under smooth changes in control variables. Catastrophe theory is far reaching and its use here is just one application of many. The aim of using catastrophe theory as opposed to other methods e.g., Maslov [88], Gaussian beams [94], coherent states [95], is that very simple computational algorithms can be effected once catastrophe theory is linked to the bifurcation analysis of Chapter 4.

5.2.1 Morse points and the Thom Splitting Lemma

Integral to the study of catastrophe is the study of critical points of function $f = f(x_1, x_2, \ldots, x_n)$, i.e., points at which $\partial_{x_i} f = \mathbf{0}$. The stability of a critical point depends on the Hessian matrix $\partial^2_{x_i x_j} f$; if $\det(\partial^2_{x_i x_j} f) \neq 0$ then Morse theory (Gilmore [111]) guarantees that the under a smooth change in variables (to y_i say) f can be written locally as a quadratic form (neglecting higher order terms),

$$f \approx \sum_{i=1}^{n} \lambda_i y_i^2, \tag{5.1}$$

or, absorbing the eigenvalues, as,

$$f \approx -y_1^2 - \cdots - y_i^2 + y_{i+1}^2 + \cdots + -y_n^2. \tag{5.2}$$

In this thesis interest is at points that are non-Morse critical points and cannot be written locally as (5.2). Non-morse points or degenerate points are those for which $\det(\partial^2_{x_i x_j} f) = 0$. Cases such as this may arise when the function f's eigenvalues, functions of control parameters $\xi = \{\xi_1, \ldots, \xi_k\}$, disappear at critical points. Catastrophe theory allows the study of these cases by using the Thom Splitting Lemma to split f into a non-Morse and Morse part:

$$f \approx f_{NM}(y_1(\xi), \ldots, y_\ell(\xi); \xi) + \sum_{j=\ell+1}^{n} \lambda_j(\xi) y_j^2(\boldsymbol{x}), \tag{5.3}$$

where ℓ is the number of degenerate eigenvalues and f_{NM} is the non-Morse part. The number of degenerate eignevalues ℓ is equal to the corank of the Hessian matrix $\partial^2_{x_i x_j} f$ so that corank (number of degenerate rows) in addition to rank (number of non-degenerate rows) equals n. The structural instability in f is thus confined to the "essential" variables $y_1, y_2, \ldots, y_\ell$, and the remaining "inessential" variables $y_{\ell+1}, \ldots, y_n$ may be ignored.

5.2.2 Stable forms and codimension

The Splitting Lemma in (5.3) makes no mention of the form f_{NM} takes. In order to provide a local form the Thom Theorem (Thom [98, 99]) can be used. This theorem guarantees the existence of a smooth change of variables so f can be written,

$$f \approx \mathrm{CG}(\ell) + \sum_{j=\ell+1}^{n} \lambda_j(\xi) y_j^2(\boldsymbol{x}), \tag{5.4}$$

where $\mathrm{CG}(\ell)$ is the catastrophe germ and is a multivariate polynomial. The germ depends on the number of essential variables, ℓ, as that decides the number of state variables in the germ. Thom proposed seven qualitatively different types of elementary catastrophe germ shown in Table 5.1,

The catastrophe germs are valid only at the non-Morse points and so are unstable in the presence of perturbations. Consequently, changes in the control variables promote discontinuities in the behaviour of f. For example, the number of non-zero eigenvalues may change with ξ leading to an unwrapping or unfolding of degeneracy into degenerate points of a simpler nature Therefore a perturbation term that describes the unfolding of the degeneracy, which may include other "lesser" degenerate points in ξ must be included. The addition of the perturbation $\mathrm{Pert}(\ell, K)$ (Table 5.1) to the catastrophe germ leads to the catastrophe function, $\mathrm{Cat}(\ell, K)$. The perturbation terms are also polynomials, though of a lesser degree than the germ. The control variables ξ are also expressed explicitly and simply as the coefficients of the polynomial. The number of these coefficients K is known as the codimension and are the minimum number of control variables that describe the unfolding of the singularity. In this thesis, the control variables are assumed to be smooth functions of the receiver coordinates when tracking the rays. We also assume that all cases $K \leq 4$ are sufficient to describe the phenomena found in this thesis.

The local behaviour of f is finally described by the stable approximation,

$$f \approx \mathrm{Cat}(\ell, K) + \sum_{j=\ell+1}^{n} \lambda_j(\xi) y_j^2(\boldsymbol{x}). \tag{5.5}$$

Corank ℓ	Codim. K	Catastrophe function, $\mathrm{Cat}(\ell, K)$		Name of catastrophe	
		$\mathrm{CG}(\ell)$	$\mathrm{Pert}(\ell, K)$	Symbol	Thom
1	1	t^3	$\xi_1 t$	Φ_1	fold
1	2	t^4	$\xi_2 t^2 + \xi_1 t$	Φ_2	cusp
1	3	t^5	$\xi_3 t^3 + \xi_2 t^2 + \xi_1 t$	Φ_3	swallowtail
1	4	t^6	$\xi_4 t^4 + \xi_3 t^3 + \xi_2 t^2 + \xi_1 t$	Φ_4	butterfly
2	3	$s^3 - 3st^2$	$\xi_{1,2}(s^2 + t^2) + \xi_{1,1} t + \xi_{2,1} s$	$\Phi^{(E)}$	elliptic
2	3	$s^3 + t^3$	$\xi_{1,2} st + \xi_{1,1} t + \xi_{2,1} s$	$\Phi^{(H)}$	hyperbolic
2	4	$t^2 s + s^4$	$\xi_{1,2} t^2 + \xi_{2,2} s^2 + \xi_{1,1} t + \xi_{2,1} s$	$\Phi^{(P)}$	parabolic

TABLE 5.1: Table of catastrophe functions with classifications in terms of corank and codimension.

The seven catastrophe functions along with moniker are shown in Table 5.1. A key point about (5.5) is that two functions f_1, f_2 both with the same expansion are *right-equivalent* as they can be related by,

$$f_1(s,t) = f_2(\mathrm{CG}(\ell)(s,t)) + \text{const.}, \tag{5.6}$$

which is critical for the existence integrals treated in §5.5. This compares to the contact equivalence shown in Equation (4.13) of Chapter 4 which has no constant.

5.3 Canonical functions and diffraction catastrophes

The canonical functions along with the closely related diffraction catastrophes are the building blocks of the uniform method. The canonical functions, Ψ, defined as in Berry [38] and Berry & Howls [113], are split into two families depending on the corank or number of state variables in the catastrophe function (from now on denoted by Φ as in Table 5.1). The first family is the cupsoids having one state variable, t;

$$\Psi_K(\xi) = \int_{-\infty}^{\infty} \mathrm{e}^{\mathrm{i}\Phi_K(t;\xi)}\,\mathrm{d}t, \quad 1 \le K \le 4. \tag{5.7}$$

The second family is the umbilics with two state variables t, s;

$$\Psi^{(E,H,P)}(\xi) = \int_{-\infty}^{\infty}\int_{-\infty}^{\infty} \mathrm{e}^{\mathrm{i}\Phi^{(E,H,P)}(s,t;\xi)}\,\mathrm{d}s\,\mathrm{d}t. \tag{5.8}$$

The diffraction catastrophes are then defined similarly. For the cuspoid diffraction catastrophes,

$$\tilde{\Psi}_K(\xi) = k_0^{1/2} \int_{-\infty}^{\infty} \mathrm{e}^{\mathrm{i}k_0\tilde{\Phi}_K(\xi)}\,\mathrm{d}t, \quad 1 \le K \le 4, \tag{5.9}$$

where $\tilde{\Phi}_K$ denotes a catastrophe function with germ $(K+2)^{-1}t^{K+2}$ replacing that given in Table 5.1.[1] The umbilics follow suit being defined as,

$$\tilde{\Psi}^{(E,H,P)} = k_0 \int_{-\infty}^{\infty}\int_{-\infty}^{\infty} \mathrm{e}^{\mathrm{i}k_0\Phi^{(E,H,P)}(s,t;\xi)}\,\mathrm{d}s\,\mathrm{d}t, \tag{5.10}$$

where $\Phi^{(E,H,P)}$ are unchanged from Table 5.1.

Fortunately, the diffraction catastrophes can be then expressed in terms of the canonical functions relatively painlessly. For example, the cuspoids all have the relationship,

$$\tilde{\Psi}_K(\xi) = k_0^{1/2}\left(\frac{k_0}{K+2}\right)^{-\frac{1}{K+2}}\Psi_K(\tilde{\xi}), \tag{5.11}$$

where $\tilde{\xi}_n = \xi_n k_0^{1-\frac{n}{K+2}}(K+2)^{\frac{1}{K+2}}, \quad n = 1,\ldots,K$. The umbilics on the other hand must be separated into two cases:

The elliptic and hyperbolic umbilics via,

$$\tilde{\Psi}^{(E,\,H)}(\xi) = k_0^{1/3}\int_{-\infty}^{\infty}\int_{-\infty}^{\infty} \mathrm{e}^{\mathrm{i}\Phi^{(E,\,H)}(s,t;\tilde{\xi})}\,\mathrm{d}s\,\mathrm{d}t, \tag{5.12}$$

where,

$$\tilde{\xi}_{1,2} = \xi_{1,2}k_0^{1/3}, \quad \tilde{\xi}_{i,1} = \xi_{i,1}k_0^{2/3}, \tag{5.13}$$

and the parabolic umbillic via,

$$\tilde{\Psi}^{(P)}(\xi) = k_0^{3/8}\int_{-\infty}^{\infty}\int_{-\infty}^{\infty} \mathrm{e}^{\mathrm{i}\Phi^{(P)}(s,t;\tilde{\xi})}\,\mathrm{d}s\,\mathrm{d}t, \tag{5.14}$$

where,

$$\tilde{\xi}_{1,1} = \xi_{1,1}k_0^{5/8}, \quad \tilde{\xi}_{1,2} = \xi_{1,2}k_0^{1/4}, \quad \tilde{\xi}_{2,1} = \xi_{2,1}k_0^{3/4}, \quad \tilde{\xi}_{2,2} = \xi_{2,2}k_0^{1/2}. \tag{5.15}$$

These relations are important because the mappings are best described in diffraction catastrophes, but the frequency independent basis, i.e., the canonical functions are those actually computed. As can be seen for both corank cases, the general form of the diffraction catastrophes in terms of canonical functions is through wavenumber scaling. The scalings of both the integrals and control variables have particular importance for understanding the physics of the catastrophes. The general form is,

$$\tilde{\Psi}(\xi) = k_0^{\beta^*}\Psi(k_0^{\sigma_j^*}\xi_j). \tag{5.16}$$

[1] This latter transformation is a convenience whose benefits will be apparent in the mapping process.

Here β^* is the singularity index and measures the increased intensity at a caustic. The scalings σ_j^* measure the fringe spacings of the diffraction catastrophe in each j^{th} control direction.

5.3.1 Computation, visualisation and singularity structures

The computation of the canonical functions is integral to the uniform method. There are two popular approaches to catastrophe computation: first, computation may be proceed directly from the integral, or, in the case of the cuspoids, from a system of partial differential equations. The pde method is due to Connor et al. [123] and is not pursued further here due to the large numerical error that often results when numerical errors excite exponentially large solutions thus polluting the results. The second method is from the integral itself: one can either choose a direct method e.g., a deformed contour or finite difference scheme, say, or otherwise a hybrid method can be used with a Taylor expansion of the function near its caustic structures matched with a steepest descents evaluation away from the caustic. This last approach may seem appealing, but Taylor expansions converge slowly and matching with a saddle expansion is cumbersome. The deformation of contour approach is preferred here. It is perhaps the most common method of computation and has already been used by several authors, for example Connor et al. [125], Kirk et al. [126]. For the cuspoids contour deformation is simple as integration is one dimensional and the regions of decay just off the real axis are determined by the catastrophe germ and are independent of control variables. The umbilics are best calculated by an alternate one dimensional integral representation, for example the following for the elliptic and hyperbolic umbilics is given by Berry & Howls [113],

$$\begin{aligned}
\Psi^{(E)}(\xi) &= 2\sqrt{\frac{\pi}{3}}\mathrm{e}^{\mathrm{i}(\frac{4}{27}\xi_{1,2}^3+\frac{1}{3}\xi_{2,1}\xi_{1,2}-\frac{\pi}{4})}\int_{\infty\mathrm{e}^{-7\pi\mathrm{i}/12}}^{\infty\mathrm{e}^{\pi\mathrm{i}/12}}\mathrm{e}^{(u^6+2\xi_{1,2}u^4+(\xi_{1,2}^2+\xi_{2,1})u^2+\frac{\xi_{1,1}^2}{12u^2})}\,\mathrm{d}u,\\
\Psi^{(H)}(\xi) &= 4\sqrt{\frac{\pi}{6}}\mathrm{e}^{\mathrm{i}(\frac{1}{27}\xi_{1,2}^3+\frac{1}{6}\xi_{1,2}(\xi_{1,1}+\xi_{2,1})+\frac{1}{4}\pi)}\int_{\infty\mathrm{e}^{5\pi\mathrm{i}/12}}^{\infty\mathrm{e}^{\pi\mathrm{i}/12}}\mathrm{e}^{\mathrm{i}(2u^6+2\xi_{1,2}u^4+(\frac{1}{2}\xi_{1,2}^2+\xi_{2,1}+\xi_{1,1})u^2-\frac{(\xi_{1,1}-\xi_{2,1})^2}{24u^2})}\,\mathrm{d}u,
\end{aligned} \tag{5.17}$$

where the contours link up the valleys at infinity avoiding the essential singularity at the origin.

Here we consider the computation of these integrals for real control variables. The integrals are meaningful for complex control variables, but for the problems consider here, real observer variables map only to real control variables. In terms of applying the results of the previous section, it is sufficient to compute each Ψ as a function of ξ, and then apply the mapping $\xi_j \to k_0^{\sigma_j^*}\xi_j$ to compute (5.16).

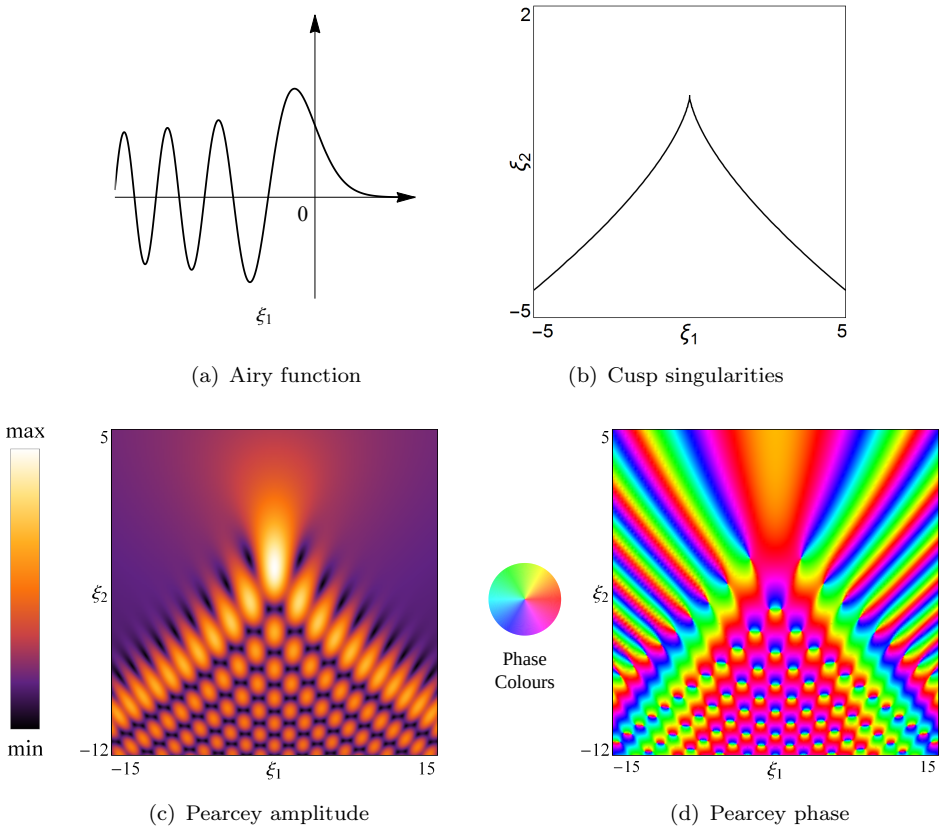

(a) Airy function (b) Cusp singularities

(c) Pearcey amplitude (d) Pearcey phase

FIGURE 5.1: Examples of corank 1 canonical functions and bifurcation sets: (a) Ψ_1 via the Airy function; (b)-(d) $\Psi_2 = \text{Pe}$.

In addition to the computations, it important to understand the role played by the singularity structure of each function. We know that the singularity structure is the locus of points for which the Hessian $\partial^2_{tt}\Phi\partial^2_{ss}\Phi - (\partial^2_{st}\Phi)^2$ is zero, and that this set increases in complexity with ℓ and K. These singularity sets are characterised by the coalescence of two or more roots of the catastrophe function's derivative(s). Each catastrophe function Φ contains the point $\xi = \mathbf{0}$ where all $K+1$ roots coalesce, formed by the union of lower order coalescences/singularities also belonging to Φ. The number of parameters needed to unfold the singularity completely is equal to the codimension K, and is thus the dimension of the singularity surface described by K equations. For the canonical functions considered in Table 5.1 unfolding decomposes the singularity into fold and cusp singularities only. Singularity sets are important to understand and visualise as they are coincident with the caustics present in high-frequency fields.

In order to demonstrate what can be expected from corank 1 canonical functions, Figure 5.1 shows the fold and cusp canonical functions with the singularity structure for the latter. Visualisations of these functions is arguably more important than others due to their prevalence in the unfolding of $K \geq 3$ singularities. The fold function which

is the simplest of all the canonical functions considered is shown in Fig. 5.1(a). It is has a singularity set consisting of just one point, $\xi_1 = 0$. It is expressible in terms of the Airy function and is therefore the easiest to compute as most computer language standards have routines for their computation.[2]

The cusp or Pearcey function, Pe,[3] is plotted in Figs. 5.1(c) (amplitude) and Figs. 5.1(d) (phase). It is more typical of canonical functions than the fold function as it is complex valued and not real. Its singularity structure is illustrated in Fig. 5.1(b) with cusp point at $\xi = \mathbf{0}$ which unfolds either side in the fold caustic. This singularity set is revisited in the next section.

To illustrate typical behaviour of corank 2 canonical functions, the hyperbolic umbilic $\Psi^{(H)}$ is shown in Fig. 5.2. Canonical functions of codimension greater than 2 must be visualised in terms of cross sections with one or more control variables are held constant. Figures 5.2(c), 5.2(e), 5.2(g) and 5.2(d), 5.2(f), 5.2(h) and show the amplitude and phase respectively, for constant values of $\xi_{1,2} = 0, 1, 3$. The corresponding singularity structure is shown in Fig. 5.2(a) formed by the union of a fold and cusp sheet. It should be pointed out that the cusp sheet decomposes into a fold away from rib $\xi_{2,1} = \xi_{1,1}$, so most of what can be seen will contain a fold. Cross-sections (constant $\xi_{1,2}$) of this structure are shown in Fig. 5.2(b), depicting the coalescence of the fold and cusp sheets. On $\xi_{1,2} = 0$ the bifurcation set consists of cusp *line* with 3 coalescences, while the point $\xi = \mathbf{0}$ has $K + 1 = 4$ coalescing roots.

A general feature that has become apparent is that the majority of the bifurcation set is controlled locally by a fold or a cusp. These diffraction patterns can be seen in $\Psi^{(H)}$ away from the surface $\xi_{1,2}$, for example compare Figs. 5.1(c) and 5.2(g). Even though only the hyperbolic umbilic has been visualised out of three possible corank 2 functions, it is possible to conclude that away from the highest order bifurcations that organise the complete structure, the bifurcation set is controlled by a lower order fold or cusp function.

[2]The relationship is in fact $\Psi_1(\xi_1) = (2\pi/3^{1/3})\mathrm{Ai}(\xi_1/3^{1/3})$.
[3]Equation (5.7) with $K = 2$ defines the Pearcey function, Pe.

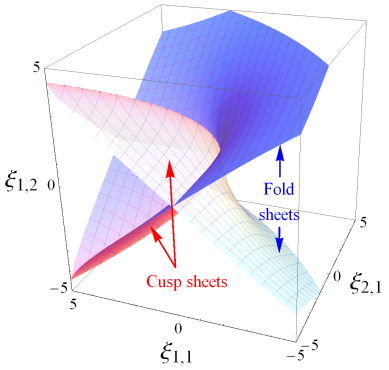

(a) Bifurcation sets

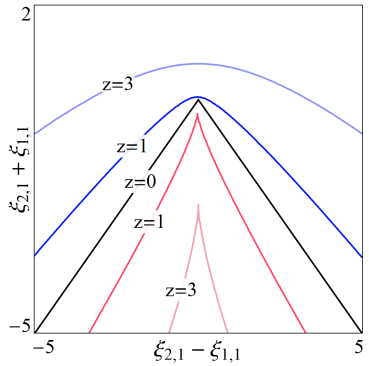

(b) Bif. sets for $\xi_{1,2} = 0, 1, 3$. Fold sheet blue shades, cusp sheet red shades, black line maximum coalescence

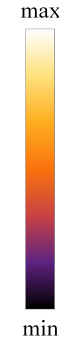

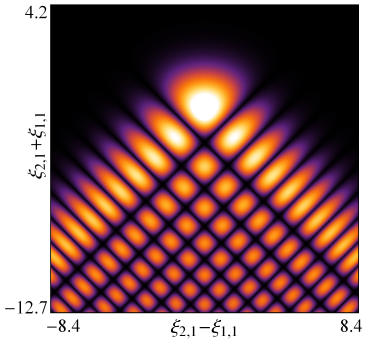

(c) $|\Psi^{(H)}(\xi_{1,1}, \xi_{2,1}, 0)|$

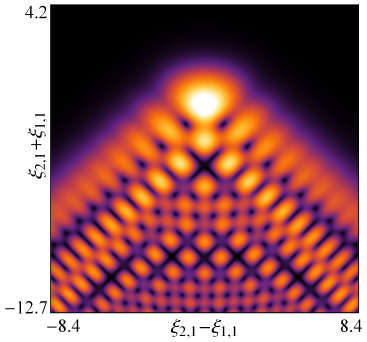

(e) $|\Psi^{(H)}(\xi_{1,1}, \xi_{2,1}, 1)|$

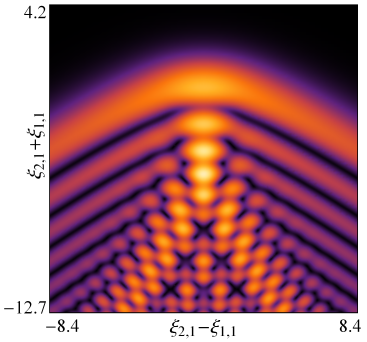

(g) $|\Psi^{(H)}(\xi_{1,1}, \xi_{2,1}, 3)|$

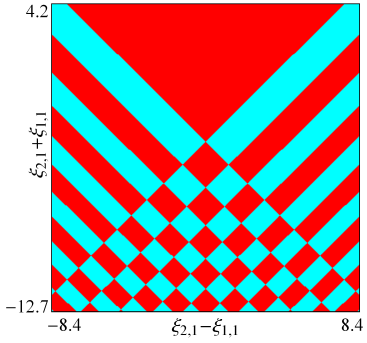

(d) $\arg\left(\Psi^{(H)}(\xi_{1,1}, \xi_{2,1}, 0)\right)$

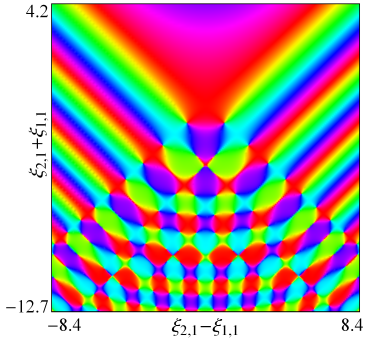

(f) $\arg\left(\Psi^{(H)}(\xi_{1,1}, \xi_{2,1}, 1)\right)$

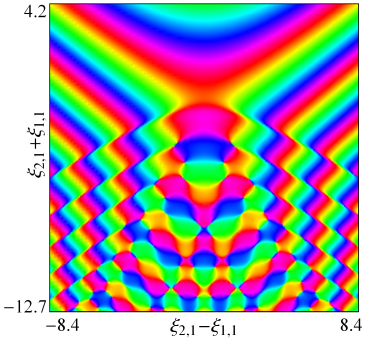

(h) $\arg\left(\Psi^{(H)}(\xi_{1,1}, \xi_{2,1}, 3)\right)$

FIGURE 5.2: Magnitude, phase and bifurcation sets of $\Psi^{(H)}(\xi)$. Figure (a) shows the bifurcation sets as union of fold and cusp sheets; (b) shows constant z cross sections of bifurcation sets as, coalescing at $z = 0$. Figures (c)-(h) $\xi_{1,2} = 0, 1, 3$ cross-sections: (c), (e), (f), magnitude; (d), (f), (h) phase. Use of the variables $\xi_{2,1} + \xi_{1,1}$ and $\xi_{2,1} - \xi_{1,1}$ is for symmetry purposes.

5.4 Catastrophe and bifurcation theory

The caustic classification problem is aided greatly by the relationship between bifurcation theory and catastrophe theory. Strictly speaking, one must distinguish between three theories: catastrophe theory, singularity theory, and bifurcation theory. While catastrophe theory considers the local structure of critical points of f, singularity theory studies the zeros of mappings $\mathscr{J} : \mathbb{R}^n \to \mathbb{R}^n$, whilst bifurcation theory studies the unfolding of these germs (and their roots) via distinguished parameters, i.e., $\mathscr{J} : \mathbb{R}^n \times \mathbb{R}^m \to \mathbb{R}^n$. As discussed in the previous section, the critical points of f are zeros of $\partial_{x_i} f$, hence the pictures generated by catastrophe theory are in the same singularity theory category. This is an important connection as initially the equivalence relations found in the two theories are different (see Eqs. (5.6) and (4.13)).

The connection between the two for the case of corank 1 bifurcations/catastrophes is highlighted via the path formulation [151]. This formulation aids us in the following way: it demonstrates the occurrence of bifurcations as one cuts the singularity surface of a cuspoid; justifies the focus on fold and pitchfork bifurcations as higher-order catastrophes decompose into such cases under path perturbations; raises awareness of classifying caustics using one parameter in the presence of a higher codimension caustic. We consider the expansion of the Liapunov-Schmidt (see Eq. (4.14), Chap. 4) reduced function with $k+1$-parameters $\Lambda = \{\Lambda_{\text{ctl}}, \Lambda_1, \ldots, \Lambda_k\}$ expanded up to the power t^{K+1} (we will use $\varrho \to t$ to switch notation from that of Chap. 4 to that of the §5.3),

$$\begin{aligned}&\mathscr{J}(t, \Lambda_{\text{ctl}}, \Lambda^c) = \\ &\mathscr{H}(t, \Lambda_{\text{ctl}}, \Lambda^c)(\mathscr{T}^{K+1}(t, \Lambda_{\text{ctl}}, \Lambda^c) + A_{K-1}(\Lambda_{\text{ctl}}, \Lambda^c)\mathscr{T}^{K-1}(t, \Lambda_{\text{ctl}}, \Lambda^c) + \ldots + A_0(\Lambda_{\text{ctl}}, \Lambda^c)),\end{aligned} \tag{5.18}$$

where Λ_{ctl} is variable and controls the bifurcation, and $\Lambda^c = \Lambda \backslash \{\Lambda_{\text{ctl}}\}$ are kept constant. The canonical form of the bifurcation is,

$$t^{K+1} + A_{K-1}(\Lambda_{\text{ctl}}, \Lambda^c)t^{K-1} + \ldots + A_0(\Lambda_{\text{ctl}}, \Lambda^c), \tag{5.19}$$

thus identifying a bifurcation problem with highest power $K+1$ and a path in K-dimensional parameter space of the universal unfolding of t^{K+1} given by,

$$\Lambda_{\text{ctl}} \to \{A_0(\Lambda_{\text{ctl}}, \Lambda^c), A_1(\Lambda_{\text{ctl}}, \Lambda^c), \ldots, A_{K-1}(\Lambda_{\text{ctl}}, \Lambda^c)\}. \tag{5.20}$$

In other words, the unfolding of any bifurcation problem with corank 1 may be identified with a parameterised family of paths through the universal unfolding of the cuspoid.

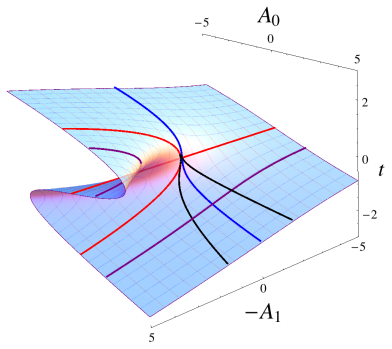

FIGURE 5.3: Path formulation showing bifurcations as paths on cusp surface: red, pitchfork; purple, perturbed pitchfork showing fold; blue, hysteresis, $\Lambda_1 = 0$; black, example of winged cusp, $\Lambda_1 = \Lambda_2 = 0, \Lambda_3 = 0.7$.

The difference between the path formulation and the canonical function coefficients ξ is that (5.20) may exhibit an explicit nonlinear relationship between the sets A and Λ; in the latter the coefficients are kept linear. Here the set A plays the role of ξ and though the codimension of (5.19) is K, this is not necessarily the codimension of the bifurcation as will be shown below.

The study of (5.20) is particularly apt as we are typically interested in collecting solutions along a receiver curve parameterized by one parameter, i.e., Λ_{ctl} which is a function of α (see Chap. 4). As an example of the path formulation bifurcations and their unfolding the cusp function is examined as in [151]. All the bifurcations found in this thesis can be explained from this example. Figure (5.3) shows four bifurcations found by traversing the cusp caustic. This example includes two bifurcations not discussed in Chap. 4 these are the hysteresis and winged cusp bifurcations that play a role in Chap. 6. These have unfolded normal forms,

$$\begin{aligned} \varrho^3 + \Lambda_{\text{ctl}} - \varrho\Lambda_1, \\ \varrho^3 + \Lambda_{\text{ctl}}^2 + (\Lambda_2 + \Lambda_3\Lambda_{\text{ctl}})\varrho + \Lambda_1, \end{aligned} \tag{5.21}$$

so that the path formulation gives,

$$\begin{aligned} A_0 = \Lambda_{\text{ctl}}, A_1 = -\Lambda_1; \quad \text{Hysteresis} \\ A_0 = \Lambda_{\text{ctl}}^2 + \Lambda_1, A_1 = \Lambda_2 + \Lambda_3\Lambda_{\text{ctl}}; \quad \text{Winged cusp.} \end{aligned} \tag{5.22}$$

A key point to note is that from a topological view, bifurcations only occur when the path cuts the singularity surface of the cuspoid. We shall see in the next chapter that bifurcations occur in $\Gamma_{\boldsymbol{\varsigma}}^B$ as a result of traversing a cuspoid surface: however, there will be *no* caustic in the solution. Furthermore $\text{Re}(\Gamma_{\boldsymbol{\varsigma}}^B)$ and $\text{Im}(\Gamma_{\boldsymbol{\varsigma}}^B)$ may behave according to two different bifurcations.

5.4.1 Classification

The classification of caustics is fairly simple given the equivalence discussed above. From the ray bifurcation problems in Chapter 3 the ray parameters each behaved as the roots of a polynomial under a a smooth change in the receiver variables. Though bifurcations arise from a path cutting a singularity surface, this does not necessarily indicate a caustic in the ray field. A necessary condition is that the ray Jacobian $J \to 0$ at these bifurcation points. The number of rays and their Jacobian matrices can be interrogated to determine the correct catastrophe.

The codimension is the easiest to calculate as the number of rays coalescing at the caustic is equal to $K + 1$. Given the continuation methods of Chapter 4 rely on determining K, this parameter is calculated without any additional difficulty. The corank is the most difficult of the pair since it relies on numerical approximations to compute the eigenvalues of the ray Jacobian. In theory the corank is the number of zeros eigenvalues of the Jacobian. These are likely never to be exactly zero at the caustic due to the difficulties of exact caustic location, so the corank is best determined by placing some tolerance on the magnitude of the eigenvalues, say $|\lambda| < a, a \ll 1$.

5.4.1.1 The case $K = 3$ and $\ell = 2$

The only case that does not determine a particular canonical function is $K = 3$ and $\ell = 2$. Table 5.1 shows that there are two possible catastrophes under this pairing: the hyperbolic and elliptic umbilics. In order to distinguish between the two, an extra criterion is required. The starting point for this is the classification of pdes. The monikers "hyperbolic", "elliptic", and "parabolic" in 2nd order p.d.e. classification all come from analogy with conic sections. It is for the same reason that these have been assigned to the catastrophes. The corank 2 catastrophe germs stem from a linear factor, $(a_1 x + b_1 y)$ multiplying a quadratic of the form $ax^2 + 2hxy + by^2$. It is the value of the discriminant, Δ, of this quadratic that leads to the hyperbolic, elliptic and parabolic cases. This means that at $\xi = \mathbf{0}$ the canonical functions satisfy either a hyperbolic, elliptic or parabolic pde For the cases of interest - the hyperbolic and elliptic umbilics - they satisfy [113],

$$\mathrm{i}\frac{\partial \Psi^{(E)}}{\partial \xi_{1,2}} = \frac{\partial^2 \Psi^{(E)}}{\partial \xi_{2,1}^2} + \frac{\partial^2 \Psi^{(E)}}{\partial \xi_{1,1}^2}, \quad \text{the paraxial wave equation,} \tag{5.23}$$

$$\mathrm{i}\frac{\partial \Psi^{(H)}}{\partial \xi_{1,2}} = \frac{\partial^2 \Psi^{(H)}}{\partial \xi_{2,1} \partial \xi_{1,1}}, \tag{5.24}$$

However as will be shown in the following sections, the high-frequency field is proportional to $c_{0,0}\mathrm{e}^{\mathrm{i}k_0 A}\Psi^{(H,E)}$ at leading order and not purely $\Psi^{(H,E)}$. So, one cannot simply replace $\Psi^{(H,E)}$ by the Green's function in (5.23) and (5.24). We can solve this problem by studying the Liapunov-Schmidt reduction of Chap. 4. To classify we need only study the germ of the catastrophe, i.e.,

$$\begin{aligned}\mathscr{J}_1(\{s,t\},0) &\approx \mathscr{J}_{1,tt}(\mathbf{0},0)t^2 + \mathscr{J}_{1,st}(\mathbf{0},0)st + \mathscr{J}_{1,ss}(\mathbf{0},0)s^2,\\ \mathscr{J}_2(\{s,t\},0) &\approx \mathscr{J}_{2,tt}(\mathbf{0},0)t^2 + \mathscr{J}_{2,st}(\mathbf{0},0)st + \mathscr{J}_{2,ss}(\mathbf{0},0)s^2,\end{aligned} \tag{5.25}$$

where we have used $\varrho_1 \to s$, $\varrho_2 \to t$ and $\ell = 2$ in (4.17)and (4.18) to update the notation of Chap. 4. Rather than dealing with two polynomials, it can be shown that (see [151] for proof) classification depends on the root structure of the polynomial,

$$\left|\frac{\partial(\mathscr{J}_1,\mathscr{J}_2)}{\partial(s,t)}\right| =$$
$$2(\mathscr{J}_{1,tt}\mathscr{J}_{2,st} - \mathscr{J}_{1,st}\mathscr{J}_{2,tt})t^2 + 4(\mathscr{J}_{1,tt}g_{2,ss} - \mathscr{J}_{1,ss}\mathscr{J}_{2,tt})st + 2(\mathscr{J}_{1,st}\mathscr{J}_{2,ss} - \mathscr{J}_{1,ss}\mathscr{J}_{2,st})s^2, \tag{5.26}$$

which in turn depends on the discriminant,

$$\Delta = 16[(\mathscr{J}_{1,tt}\mathscr{J}_{2,ss} - \mathscr{J}_{1,ss}\mathscr{J}_{2,tt})^2 - (\mathscr{J}_{1,tt}\mathscr{J}_{2,st} - \mathscr{J}_{1,st}\mathscr{J}_{2,tt})(\mathscr{J}_{1,st}\mathscr{J}_{2,ss} - \mathscr{J}_{1,ss}\mathscr{J}_{2,st})], \tag{5.27}$$

where the evaluation at $(\mathbf{0},0)$ has been suppressed.

The sign of the discriminant determines whether the canonical form is elliptic or hyperbolic. If $\Delta < 0$ then the appropriate form is elliptic as the roots are complex. If $\Delta > 0$ the appropriate form is then hyperbolic as the roots are real. If $\Delta = 0$ the this equation is degenerate, having repeated roots. In that case the canonical form is the parabolic umbilic, though we did not need to distinguish this case.

A subtlety that is not consider here is that the unfolding of the bifurcation does not take into account the asymptotic validity of unfolding the diffraction catastrophe into simpler catastrophe species. The validity of such unfolding from the diffraction catastrophe point of view is appraised in §5.6.

5.5 Mapping to the uniform field

In this chapter only the generic mapping process for corank 1 and 2 singularities are considered. In some instance there are closed form solutions to the mappings. These exist for the fold, cusp and swallowtail singularities as it is possible to find the roots of

2^{nd}, 3^{rd} and 4^{th} using Cardano's method (see for e.g., McNamee [165]). Later in this chapter the numerical methods of inverting the mappings are considered as this is the best way of tackling mappings in general. In later chapters an analytic solution of the fold singularity will be used to benchmark the mapping algorithm developed herein.

The uniform mapping starts by invoking the principle of superpostion. An integral of the Kirchhoff type is formed by integrating over waves that have a locally plane wave form. Thus it is conjectured that the coalescing ray contributions in the neighbourhood of the caustic can be written in terms of a uniformly valid integral expression (Hanyga [121], Berry [38]),

$$I \sim \left(\frac{k_0}{2\pi \mathrm{i}}\right)^{\ell} \int_{\mathscr{D}} a(\zeta; \boldsymbol{x}, k_0) \mathrm{e}^{\mathrm{i}k_0 \psi(\zeta;\boldsymbol{x})} \, \mathrm{d}^{\ell}\zeta, \quad \mathscr{D} \in \mathbb{R}^{\ell}, \tag{5.28}$$

where again ℓ is the corank of the singularity and ψ is a generating function. The integral of (5.28) is not unique due to its asymptotic nature, though this doesn't undermine the method since this is a means to an end. The integral is usually simplified by expanding the slow function $a(\zeta; \boldsymbol{x}, k_0) = \sum_{m=0}^{\infty} a_m(\zeta; \boldsymbol{x}) k_0^{-m}$ so that along with the frequency filter $(k_0/2\pi\mathrm{i})^{\ell}$ the mapping is independent of frequency.

The Kirchhoff integral allows the ray expansion Eq. (4.29) Chapter 4 as (for one caustic),

$$G_{\omega}(\boldsymbol{x}; k_0) \sim \underbrace{\left(\frac{k_0}{2\pi \mathrm{i}}\right)^{\ell} \int_{\mathscr{D}} a(\zeta; \boldsymbol{x}, k_0) \mathrm{e}^{\mathrm{i}k_0 \psi(\zeta;\boldsymbol{x})} \, \mathrm{d}^{\ell}\zeta}_{\sim\text{to rays that coalesce at caustic}} + \underbrace{\sum_{n=n_K+1}^{N} A^{(n)} \mathrm{e}^{\mathrm{i}k_0 S^{(n)}}}_{\text{rays not involved at caustics}} . \tag{5.29}$$

This partitions the rays contributions into two parts: contributions asymptotic to I and rays that do not coalesce; the latter do not need to be considered as part of the mapping. The mapping procedure is effectively the same for both coranks up to the expansion of the slow function $a(\cdot)$. The first step is to map ψ to the appropriate catastrophe function Φ; at this point Φ is assumed known. Mapping the old integration and observer variables to those of the diffraction integral, using $\mathbf{s} = \{s, t\} = \{T(\zeta, \boldsymbol{x}), S(\zeta, \boldsymbol{x})\}$ and $\xi = \boldsymbol{\Xi}(\boldsymbol{x})$, the phase is mapped to $\psi(\zeta; \boldsymbol{x}) = \Phi(\mathbf{s}; \xi) + A(\xi)$. Here A is just a constant that closes the mapping.

$$I \sim \left(\frac{k_0}{2\pi \mathrm{i}}\right)^{\ell} \mathrm{e}^{\mathrm{i}k_0 A} \int_{\mathscr{D}'} b(\zeta; \boldsymbol{\xi}) \mathrm{e}^{\mathrm{i}k_0 \Phi(\mathbf{s};\xi)} \, \mathrm{d}^{\ell}\mathbf{s}, \quad b = aJ(\mathbf{s}, \xi) \in \mathscr{C}^{\infty}, \tag{5.30}$$

with J the Jacobian of the map from ζ to state variables $\mathbf{s}$. The amplitude is then expanded using the Weierstrass-Malgrange preparatory lemma,

$$b = \begin{cases} \sum_{k=0}^{K} c_{k,0}(\xi) t^k + \frac{\mathrm{d}\Phi_K}{\mathrm{d}t} H_0(t;\,\xi), & \text{if } \ell = 1, \\ c_{0,0}(\xi) + \frac{\partial \Phi^{(E,H,P)}}{\partial \xi} \cdot \mathbf{c}_0(\xi) + H_{1,0}(\mathbf{s};\,\xi) \frac{\partial \Phi^{(E,H,P)}}{\partial s} + H_{2,0}(\mathbf{s};\,\xi) \frac{\partial \Phi^{(E,H,P)}}{\partial t}, & \text{if } \ell = 2, \end{cases} \tag{5.31}$$

where $\mathbf{c}_0 = \{c_{1,0}, \ldots, c_{K,0}\}$. For all cases the preparatory lemma is in the form of a (multivariate) polynomial plus a functions that disappears at the saddle points of Φ. The functions H are smooth functions and regular at the saddles, i.e., $H \in \mathscr{C}^\infty$.

Considering the $\ell = 1$ case first. The expansion for b is substituted into the integral I, then using derivatives of the catastrophe function w.r.t. the control variables ξ to generate the polynomial terms in the integrand, the integral can be expressed as a canonical function and a finite number of its derivatives with $O(1)$ remainder term R_0.

$$I \sim (k_0/2\pi\mathrm{i})^{1/2}\, \mathrm{e}^{\mathrm{i}k_0 A} \left[k_0^{-\frac{1}{K+2}} \left(c_{0,0} + \sum_{n=1}^{K} \frac{c_{k,0}}{\mathrm{i}k_0} \frac{\partial}{\partial \xi_k} \right) \Psi_K(\tilde{\boldsymbol{\xi}}) - \frac{1}{\mathrm{i}k_0} \underbrace{\int_{\mathscr{D}} \frac{\mathrm{d}H_0}{\mathrm{d}t} \mathrm{e}^{\mathrm{i}k_0 \psi_K} \mathrm{d}t}_{R_0} \right]. \tag{5.32}$$

This represents the beginnings of an ordered asymptotic sequence. To generate the full asymptotic sequence we define the following $\mathscr{C}^\infty$ smooth functions,

$$\mathrm{d}H_m(t;\boldsymbol{x})/\mathrm{d}t = \sum_{k=0}^{K} c_{k,m+1}(\boldsymbol{x}) t^k + (\mathrm{d}\psi_K/\mathrm{d}t) H_{m+1}(t;\boldsymbol{x}), \quad m \geq 0, \tag{5.33}$$

which, applied to the remainder integral R_0 and subsequent remainder integrals R_m,

$$R_m = \int_{\mathscr{D}} \frac{\mathrm{d}H_m}{\mathrm{d}t} \mathrm{e}^{\mathrm{i}k_0 \psi_K}\, \mathrm{d}t, \tag{5.34}$$

leads to the full ordered asymptotic expansion for the Kirchhoff integral,

$$I \sim (k_0/2\pi\mathrm{i})^{1/2} \mathrm{e}^{\mathrm{i}k_0 A} \left[\sum_{m=0}^{\infty} \mathrm{e}^{\mathrm{i}m\pi/2} k_0^{-(m+\frac{1}{K+2})} \left(c_{0,m} + \sum_{k=1}^{K} c_{k,m} \mathrm{e}^{-\mathrm{i}\pi/2} k_0^{-k/(K+2)} \frac{\partial}{\partial \tilde{\xi}_k} \right) \Psi_K(\tilde{\xi}) \right]. \tag{5.35}$$

The case $\ell = 2$ proceeds similarly, with a first expansion that leads to,

$$I \sim (k_0^{\beta^*}/2\pi\mathrm{i})\mathrm{e}^{\mathrm{i}k_0 A}\left[c_{0,0}\Psi^{(E,H,P)}(\tilde{\xi}) + \frac{1}{\mathrm{i}k_0}\mathbf{c}_0 \cdot \frac{\partial}{\partial \xi}\Psi^{(E,H,P)}(\tilde{\xi}) + \ldots \right.$$
$$\left. \ldots - \frac{1}{\mathrm{i}k_0}\underbrace{\int_{-\infty}^{\infty}\int_{-\infty}^{\infty}\left(\frac{\partial H_{1,0}}{\partial s} + \frac{\partial H_{2,0}}{\partial t}\right)\mathrm{e}^{\mathrm{i}k_0\Phi^{(E,H,P)}(s,t;\xi)}\,\mathrm{d}s\,\mathrm{d}t}_{R_0}\right]. \tag{5.36}$$

As with the $\ell = 1$ case, a complete asymptotic sequence can be generated by defining,

$$\frac{\partial H_{1,m}}{\partial s} + \frac{\partial H_{2,m}}{\partial t} = c_{0,m+1} + \frac{\partial \Phi^{(E,H,P)}}{\partial \xi}\cdot\mathbf{c}_{m+1} + H_{1,m+1}\frac{\partial \Phi^{(E,H,P)}}{\partial s} + H_{2,m+1}\frac{\partial \Phi^{(E,H,P)}}{\partial t}, \quad m \geq 0. \tag{5.37}$$

and repeatedly expanding the remainder integrals as before. The full asymptotic sequence is then given by,

$$I \sim \left(\frac{k_0^{\beta^*}}{2\pi\mathrm{i}}\right)\mathrm{e}^{\mathrm{i}k_0 A}\left[\sum_{m=0}^{\infty}\mathrm{e}^{\mathrm{i}m\pi/2}k_0^{-m}\left(c_{0,m}\Psi^{(E,H,P)}(\tilde{\xi}) + \sum_{j=1}^{K}\mathrm{e}^{-\mathrm{i}\pi/2}k_0^{-1+\sigma_j^*}c_{j,m}\frac{\partial}{\partial \tilde{\xi}_j}\Psi^{(E,H,P)}(\tilde{\xi})\right)\right]. \tag{5.38}$$

The asymptotic nature of (5.35) and (5.38) means that at most only the $m = 0$ layer is required to compute the acoustic field. In most cases the leading order term, that premultiplied by $c_{0,0}$, is sufficient to correct the non-uniformity at the caustic. The inclusion more terms in the series swells the range of validity of the uniform expansion; precisely why this is true will be shown in a later section.

5.5.1 Mapping

The expansions of Eqs. (5.35) and (5.38) describe how the acoustic field can be expressed in terms of uniform functions. This requires, in general, a hypothetical Kirchhoff integral to allow for instances in which the field is too complicated for a closed-form solution. However, although we can write this integral down, we do not have the means to compute it, so we must bypass the slow function b and generating function ψ in order to determine the coefficients c's and control variables $\{\xi, A\}$.

In order to make tangible evaluations of these variables the Kirchhoff integral can be compared with the coalescing ray contributions off-caustic. Expanding I in (5.30) about *all* $K+1$ coalescing stationary points, $t^\star$ or $\mathbf{s}^\star$, using the method of stationary phase, these asymptotic contributions are then identified and equated with the n_K physical coalescing contributions in addition to those excluded unphysical contributions that also coalesce (i.e., coalescing conjugate pairs). Though the correspondence between the

saddles and the rays is not yet fixed, symbolically the relation is,

$$\begin{aligned} b(t_n^\star;\xi)\left(\Phi_K''(t_n^\star;\xi)\right)^{-1/2}\mathrm{e}^{\mathrm{i}k_0(\Phi_K(t_n^\star;\xi)+A(\xi))} &= A_0^{(n)}\mathrm{e}^{\mathrm{i}k_0 S^{(n)}}, \quad \text{corank 1,} \\ b(\mathbf{s}_n^\star;\xi)\left(\det\Phi_{ij}^{(E,H,P)}(\mathbf{s}^\star;\xi)\right)^{-1/2}\mathrm{e}^{\mathrm{i}k_0(\Phi^{(E,H,P)}(\mathbf{s}^\star;\xi)+A(\xi))} &= A_0^{(n)}\mathrm{e}^{\mathrm{i}k_0 S^{(n)}}, \quad \text{corank 2,} \end{aligned} \tag{5.39}$$

from which it is deduced that,

$$\begin{aligned} b(t_n^\star;\xi)\left(\Phi_K''(t_n^\star;\xi)\right)^{-1/2} &= A_0^{(n)}, \text{ and, } \Phi_K(t_n^\star;\xi)+A(\xi)=S^{(n)} \quad \text{corank 1,} \\ b(\mathbf{s}_n^\star;\xi)\left(\det\Phi_{ij}^{(E,H,P)}(\mathbf{s}^\star;\xi)\right)^{-1/2} &= A_0^{(n)}, \text{ and, } \Phi^{(E,H,P)}(\mathbf{s}^\star;\xi)+A(\xi)=S^{(n)}, \quad \text{corank 2.} \end{aligned} \tag{5.40}$$

As we already know, the ray/stationary phase expansions are only valid as an approximation to the field off-caustic. Therefore it may seem paradoxical but in order to calculate the uniform expansions where they are required the most, the ray comparison (5.40) must be continued and relied upon in a region containing the caustic - exactly where rays fail! However, since both sides of the comparison are equivalent, then the ray failure (must) leads to an integrable singularity that occurs in the ratios,

$$\lim_{\Phi_K'',J\to 0}\frac{\Phi_K''(t_n^\star;\,\xi)}{J},\ \lim_{\det\Phi_{ij}^{(E,H,P)},J\to 0}\frac{\det\Phi_{ij}^{(E,H,P)}(\mathbf{s}^\star;\,\xi)}{J}, \tag{5.41}$$

as the caustic is approached (using the expression for A_0 in Eq. (3.59)) so that (5.40) remains meaningful. By this it is meant that $b = aJ$ contains no singularities and that the Jacobian of the map J between the generating function Ψ and canonical function Φ is conformal. It is worth mentioning - for future reference - that if a closed form integral expression for the field does exist, the integral singularity would be tackled using a limiting device such as l'Hospital's rule (see for e.g., Bleistein & Handelsman [134]).

Clearly, at this point the correspondence between the saddles and rays must be made concrete thus allowing for the solution of all control variables. Unfortunately, as K increases so does the degree of difficulty in inverting these nonlinear equations. In fact only for $K = 1, 2$, $\ell = 1$ are there well-known solutions to this mapping. In the generic cases we want to be able to look at we must recourse to a numerical iterative solution.

5.5.2 Numerical methods of inverting the mappings

Once the caustics have been classified according to §5.4.1, the appropriate uniform solution can be identified and a numerical scheme implemented as a means of inverting the maps in (5.40). Fortunately, there is little difference between the solution of the corank

1 and 2 maps. There are, however, additional tools that can be used to aid the former, so we still continue to distinguish between the two.

Before proceeding with the details of the inversion we should highlight two key points: first, that the numerical scheme is just one of several numerical techniques at inverting these maps. Other methods, such as that based on a Grobner basis (Connor & Curtis [123]), rely on symbolic algebraic manipulations that are believed to be too cumbersome for the purposes of this thesis. Second, the amplitude map aims only to provide the $m = 0$ layer of (5.35) and (5.38). The asymptoticness of these series means that this is more than sufficient for numerical accuracy. It will be shown that the full $m = 0$ layer results in an asymptotic solution of the same order as the ray solution when the uniform expansions re-order upon large parameter expansion.

The first part of the mapping relates to the phase and control set $\{\xi, A\}$. This is the most difficult aspect of the mapping, and once this has been achieved the calculation of the amplitude coefficients ($c_{k,0}$'s) is straightforward. The method is based on that of Amodei et al. [122], which is a derivative of the method due to Connor & Curtis [123]. The main workings are effectively the same as the former, though with additional tracking measures to ensure fast convergence and a generalisation to corank 2 cases.

The corank 1 algorithm starts by writing the ray phase comparison (5.40) explicitly with $\tilde{\Phi}_K$, as,

$$\frac{(t_i^\star)^{K+2}}{K+2} + \sum_{n=1}^{K} \xi_n (t_i^\star)^n + A = S^{(i)}, \tag{5.42}$$

where the saddle $t_i^\star$ satisfies the saddle condition,

$$\tilde{\Phi}'_K(t_i^\star) = (t_i^\star)^{K+1} + \sum_{n=1}^{K} \xi_n n (t_i^\star)^{n-1} = 0. \tag{5.43}$$

The iterative algorithm then rewrites (5.42) as,

$$\sum_{n=1}^{K} \delta\xi_{n,(r)} (t_{i,(r)}^\star)^n + \delta A_{(r)} = S^{(i)} - \frac{(t_{i,(r)}^\star)^{K+2}}{K+2} - \sum_{n=1}^{K} \xi_{n,(r)} (t_{i,(r)}^\star)^n - A_{(r)} = v_i \tag{5.44}$$

where subscript "(r)" denotes the r^{th} iteration ($r = 0 \Rightarrow$ initial guess) and δ denotes perturbation terms $\delta\xi_{n,(r)} = \xi_n - \xi_{n,(r)}$ and $\delta A_{(r)} = A - A_{(r)}$. This can be written in matrix form,

$$\mathbf{V} \begin{pmatrix} \delta A_{(r)} \\ \delta\xi_{(r)} \end{pmatrix} = \mathbf{v}, \tag{5.45}$$

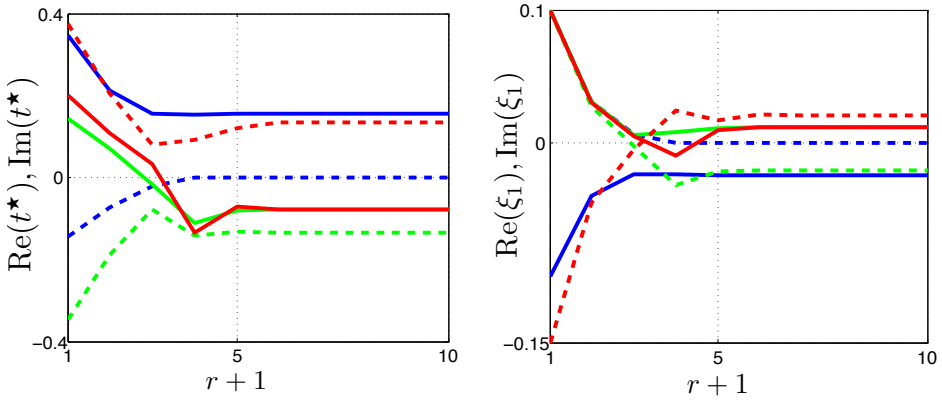

(a) Convergence of $t^\star_{i,(r)} \to t^\star$.

(b) Convergence of $\xi_{1,(r)} \to \xi_1$.

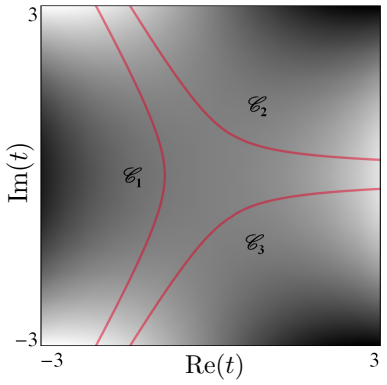

(c) Complex Airy/fold contours.

FIGURE 5.4: (a) and (b) examples of convergence to each of the three possible $t^\star$ and ξ_1 for the fold caustic, $K = 1$. Solid lines, $\mathrm{Re}\left(t^\star_{i,(r)}, \xi_{1,(r)}\right)$; dashed lines, $\mathrm{Im}\left(t^\star_{i,(r)}, \xi_{1,(r)}\right)$. Red lines, $\xi_{1,(0)} = 0.1 - 0.15\,\mathrm{i}$, green lines, $\xi_{1,(0)} = 0.1 + 0.1\,\mathrm{i}$, blue lines, $\xi_{1,(0)} = -0.1 + 0.1\,\mathrm{i}$. (c) shows the corresponding contours for the Airy/fold catastrophe in the complex plane. Each contour starts and ends in a valley at infinity.

where $\mathbf{V}$ is the Van der Monde matrix defined by $V_{\alpha,\beta} = (t^\star_\alpha)^{\beta-1}$. Once this matrix is inverted - using a pseudo-inverse - the perturbation term allows for a straightforward update upon the initial guess.

The algorithm steps are as follows:

1. Make an initial guess as to the coefficients $\{\xi_{n,(0)}, A_{(0)}\}$.
2. Solve for the roots of the polynomial $\tilde{\Phi}'_K(t^\star_{i,(0)}; \xi_{n,(0)}) = 0$.
3. Associate a saddle with a phase so $t^\star_{i,(0)}, \to S^{(i)}$.
4. Invert the matrix (5.45) in order to calculate perturbations.
5. Update the $\{\xi_{n,(0)}, A_{(0)}\}$ terms using the perturbations.
6. Repeat steps 1-5 until convergence is detected, i.e., $\delta\boldsymbol{\xi}_{(r)} \to \mathbf{0}, \delta A_{(r)} \to 0$.

In the above algorithm the iteration can be seen to be highly inefficient if the saddle associated with the ray phase changes significantly. For example, an update in the control variables may lead to a different set of saddles $t^\star$ that are picked out of the root solver in a different order (this is the easiest way of performing step 3 above). Ideally, one would like to make the association for the 0^{th} iteration determining changes to each root under the updated control variables, without calculating the roots from scratch. The following algorithm taken from Starer & Nehorai [166] allows exactly this. Expressing the coefficients of the saddle condition polynomial (5.43) as,

$$\boldsymbol{a} = \{a_1, a_2, \ldots, a_K\} = \{0, K\xi_K, \ldots, \xi_1\} \in \mathbb{C}^K, \quad a_0 = 1, \tag{5.46}$$

then the roots/saddles $\mathbf{t} = \{t_1^\star, \ldots, t_{K+1}^\star\} \in \mathbb{C}^K$ of (5.43) are related via,

$$\sum_{k=0}^{K+1} a_k t^{-k} = \prod_{k=1}^{K+1} (1 - t_k^\star t^{-1}). \tag{5.47}$$

Clearly, perturbations to the coefficient vector lead to perturbations in the root vector. Given the coefficients from one iteration (old) $\boldsymbol{a}[r]$ and the coefficients of the next iteration (new) $\boldsymbol{a}[r+1]$ the k^{th} root can be expressed as,[4]

$$t_k^\star[r+1] = t_k^\star[r] + \epsilon_k. \quad \text{where} \quad \boldsymbol{\epsilon} = \{\epsilon_1, \ldots, \epsilon_k\}, \tag{5.48}$$

Then a first order correction to find $\boldsymbol{\epsilon}$ is given by,

$$\boldsymbol{a}[r+1] - \boldsymbol{a}[r] = \boldsymbol{K}[r]\boldsymbol{\delta}, \tag{5.49}$$

where the k^{th} column of $\boldsymbol{K}[r]$, $\kappa_k[r]$ is a solution of,

$$\boldsymbol{\Lambda}_k[r]\kappa_k[r] = \boldsymbol{a}[r], \quad \boldsymbol{\Lambda}_k[r] = \begin{pmatrix} 1 & & & \mathbf{0} \\ -t_k^\star & 1 & & \\ & \ddots & \ddots & \\ \mathbf{0} & & -t_k^\star & 1 \end{pmatrix}. \tag{5.50}$$

It can be seen that this root-update algorithm is very simple to effect, and the first order nature of the approximation can be improved upon by iterating the update algorithm multiple times. This may seem to undermine the efficiency of the polynomial inversion algorithm but the increased ordering benefits are significant as oscillation due to switching in the association $t_{i,(r)}^\star \to S^{(i)}$ is virtually eliminated.

[4] The argument r is a counter variable.

Returning to the main inversion algorithm, it should be remembered that the mapping inversion is nonlinear and therefore admits multiple solutions. This means in addition to the multiple rays that coalesce, there is more than one possible set of coefficients for each caustic. These other solutions are not necessarily wrong, but only one set is consistent with a bounded uniform function for real control variables. As an example of the multiple inversion solutions for the fold mapping, Figure 5.4 shows three distinct convergences given three distinct starting values for the iterative method. Each of these three solutions corresponds to a different integral for the diffraction catastrophe, though the form of the canonical polynomial is the same. If one deforms the real line contours of the corank 1 singularities into valleys[5] in complex plane (either by pure deformation or combined with a change of variables) then the resulting contour will be one of $K+1$ possible valley-at-infinity deformations. Of course the correct contour is the only one that can be deformed back into the real line. For the fold case shown in Fig. 5.4(c) there are three contours possible, where $\mathscr{C}_1$ corresponds to the fold defined in (5.9). When using the analytic solutions of mappings, there is typically a large amount of work involved to calculate the correct branch of the mapping (see Appendix D).

The amplitude coefficients are then calculated by inverting the system given by the first of (5.40). From the Weierstrass-Malgrange preparatory lemma given in (5.31) then evaluating b at the saddles leads to a polynomial in the saddle, i.e.,

$$\sum_{k=0}^{K} c_{k,0}(\xi)(t_n^\star)^k = A_0^{(n)}(\Phi''_K(t_n^\star;\xi))^{1/2}. \tag{5.51}$$

which is a $K \times K$ size system since again all coalescing saddles are used. This is easily inverted numerically using a pseudo-inverse. Assuming the saddles have been matched with the correct amplitudes, then the right-hand-side of (5.51) should be real as the (possibly) complex phase provided by $\Phi''_K(t_n^\star;\xi)$ should be conjugate to that provided by the ray calculation of J.

As mentioned in the beginning of this section, the main inversion algorithm holds true for both corank 1 and 2 polynomials. The differences are only down to the apparatus available, which in the former case is appreciably larger. The iterative algorithm for the corank 2 cases can be written down concisely using modified notation from before for $\mathrm{Cat}(\ell, K)$ and $\mathrm{Pert}(\ell, K)$.

$$\mathrm{Pert}_{\ell,K}(\delta\xi_{(r)}, \mathbf{s}^\star_{i,(r)}) + \delta A_{(r)} = S^{(i)} - \mathrm{Cat}(\xi_{(r)}, \mathbf{s}^\star_{i,(r)}) - A_{(r)} = v_i, \tag{5.52}$$

where the saddle condition yields two equations $\partial_s\Phi$ and $\partial_t\Phi$ satisfied by $\mathbf{s}^\star$. The main difficulty with the corank 2 inversion is the availability of root solvers for polynomial

[5]Valleys are regions at infinity where the integrand decays exponentially; they are determined in the large by the catastrophe germ.

systems in multiple variables. Reliable solvers - giving the complete set of solutions for given coefficients do exist, for e.g., Mathematica's NSolve.

5.6 Engineering control variables: Singulants

The method described in this chapter so far uses the bifurcation paths (or more precisely the number of coalescing paths) of Chapter 3 to help categorise the caustic. Identification in this manner causes one problem that is not readily apparent. For example, if $K+1$ ($K>1$) rays are observed coalescing along an observer arc, then perturbations in the observer arc may see the paths break up so that the perturbed path sees a number less than $K+1$ coalescing. Thus in the vicinity of a higher order caustic a lower order diffraction catastrophe is applied according to the methods above. In fact this is not technically valid from a uniform asymptotics point of view as the accuracy of splitting the higher-order diffraction catastrophe into a lower order one doesn't depend upon the splitting of the bifurcation paths. The appropriate measure of "distance" is determined by a quantity known as the singulant. The singulant is defined as the quantity,

$$S_{nm} \equiv k_0(S^{(n)} - S^{(m)}), \tag{5.53}$$

and plays an important role in the resurgence of exponentially small rays across Stokes lines (see for e.g., Dingle [21]). The definition is extremely simple and straightforward to compute in practice as it is simple the difference of two phases multiplied by the wavenumber. Furthermore, $S_{nm} = -S_{mn}$. To see the importance of the singulant in terms of the ray solution consider the full (all terms in each ray series) ray field,

$$\hat{g}_5 \sim \sum_{n=1}^{N} \mathrm{e}^{\mathrm{i}k_0 S^{(n)}} \sum_{r=0}^{\infty} \frac{A_r^{(n)}}{(\mathrm{i}k_0)^{r+\gamma}}. \tag{5.54}$$

Then for a large class of systems the terms $A_r^{(n)}$ for large r, i.e., $r \gg 1$, known as late terms, have the factorial over power form (Berry [76, 81], Dingle [21], Howls [167]),

$$A_r^{(n)} \sim \sum_k \frac{B_{(n,k)}(\mathbf{x})\Gamma(r+\gamma_{(n,k)}(\mathbf{x}))}{S_{nk}^{r+\gamma_{(n,k)}(\mathbf{x})}}, \tag{5.55}$$

where B and γ are non-trivial functions of position, and $\Gamma(\cdot)$ is the gamma function. This assumption of late term behaviour has been found to be true for a number of complicated systems and this ubiquitous property is known as universality.

Now since an asymptotic series is one that initially converges and then diverges, the asymptotic form given by (5.55) can be used to find the smallest, or least, term in each ray expansion before the series begins to diverge. To calculate the r^{th} term at which

this occurs, the fact the rate of change of size of the coefficients slows down and two adjacent terms will become proportional in size, i.e.,

$$A_{(n,r)}/k_0^{r+\gamma} = O(A_{(n,r+1)}/k_0^{r+\gamma+1}), \tag{5.56}$$

which upon using (5.55) and replacing the order O by equality of magnitudes, can be used to calculate an explicit value for r. To proceed with the calculation the following result for quotients of Gamma functions with large argument (Paris [168]),

$$\frac{\Gamma(r+\gamma_{(n,k)}(\mathbf{x})+1)}{\Gamma(r+\gamma_{(n,k)}(\mathbf{x}))} \sim r, \quad r \to \infty. \tag{5.57}$$

Substitution into (5.56) gives a simple estimate for the least term,

$$r = \mathrm{Int}|S_{nk}|, \tag{5.58}$$

where "Int" denotes the integer part. This result implies that the least term is controlled by the singulant and that numerical evalulations of the singulant in a ray tracing problem can be used to judge the divergence away from the true field. The least terms itself is exponentially small as shown by an application of the Stirling formula for Gamma functions and (5.58). It has magnitude,

$$\sqrt{2\pi}\frac{|B_{(n,k)}(\mathbf{x})|\mathrm{e}^{-|S_{nk}|}\mathrm{e}^{-\arg(S_{nk})\Im(\gamma_{nk}(\mathbf{x}))}}{|S_{nk}|^{1/2}}. \tag{5.59}$$

For multiple rays (greater than 2) coalescing at a caustic there are multiple singulants tending to zero. In general these singulants will tend to zero at different rates. However, there is no dilemma as to which singulant to choose as the late term behaviour is governed by the singulant with the smallest value. This means (5.58) represents the smallest singulant available in (5.55).

The most important aspect of (5.58) is that it describes the approximate location of the least term. When the least term is $r = 1$ then the leading order behaviour itself is poor. So that (since it is the integer part) a singulant value of $r = 2$ describes the approximate location (in $\boldsymbol{x}$) that the ray solution begins to diverge away from the exact field. Additionally, this divergence is controlled simply by the wavenumber, meaning that the divergence becomes more localised with increasing k_0.

This has ramifications for the identification of diffraction catastrophes via bifurcation paths, as mentioned at the start of this section. Even if a bifurcation path splits away to form a set of simpler structures, it depends on the now non-coalescing singulants as to whether there is sufficient distance from the higher-order caustic for the lower-order diffraction catastrophes to be valid. Thus the ray solver, which currently has no

unfolding detection, may introduce an error - though not infinite - due to invalidity of a low order diffraction catastrophe in the presence of a higher order one.

As a precursor to the following example, it should be pointed out that a singulant is a necessary but not sufficient condition for two ray contributions tending to zero. This is why the ray solver uses the ray Jacobian and not the singulants as caustic identifiers.

The simplest example, shown in Fig. 5.5, deals with the unfolding of the cusp caustic into the fold caustic. The level sets of the two singulants corresponding to rays coalescing on the cusp are shown in red and blue. The position where the singulants are equal to 2 are emboldened. The red markers show the intersection of these particular level sets so that beyond this point in constant ξ_1, denoted by $\xi_1^{(S=2)}$, agreement of the fold function agrees well with the exact solution in the region of maximum divergence shown by the highlighted region in Fig. 5.5. This can be seen using the cross-section evaluations in Figs. 5.5(b)-5.5(e).

5.7 Conclusion

In this chapter catastrophe theory was used to supply uniformity to the high-frequency field. The starting point for the method is the classification of the caustic. This is a recognition problem and is, in all but one case, solved by determining the corank and codimension of the singularity. Due to the equivalence with the bifurcation theory of Chapter 4 the two-point ray tracing routine yields these parameters in a straightforward manner. The codimension is found by identifying the number of rays coalescing at the caustic and the corank by the number of zero eigenvalues at the caustic. This brought into question the classification-by-bifurcation question (still in progress), which uses Dingle's singulants to examine how far away from a caustic of higher order must an observer be in order to employ a canonical function of lower order.

Once classification is made the mechanics of re-expanding the field in the appropriate canonical function was detailed. Both the corank 1 and 2 cases are similar, but both require the existence of a hypothetical Kirchhoff integral in the locality of the caustic. The most computationally part of the expansion is the calculation of the control variables. As discussed, there are several possible solutions for each canonical function, and the incorrect one may lead to the erroneous substitution of unphysical waveforms into the field. Once the control variables are calculated it is simply a matter of inverting a matrix to calculate the amplitude coefficients. In the next chapter these mappings will be computationally realised allowing the numerical implications of the integrable singularity in the amplitude coefficients and impact of the higher terms in uniform expansion to be observed.

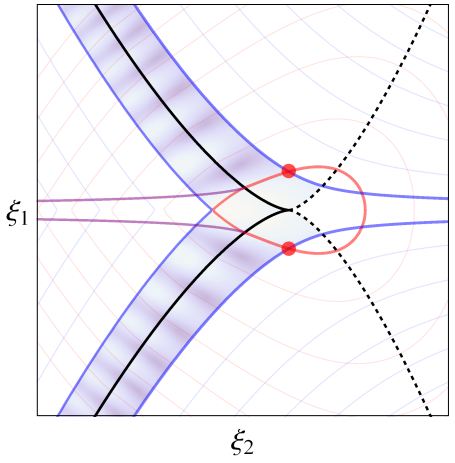

(a) Level sets of the singulant. Highlighted region showing field indicates maximum divergence

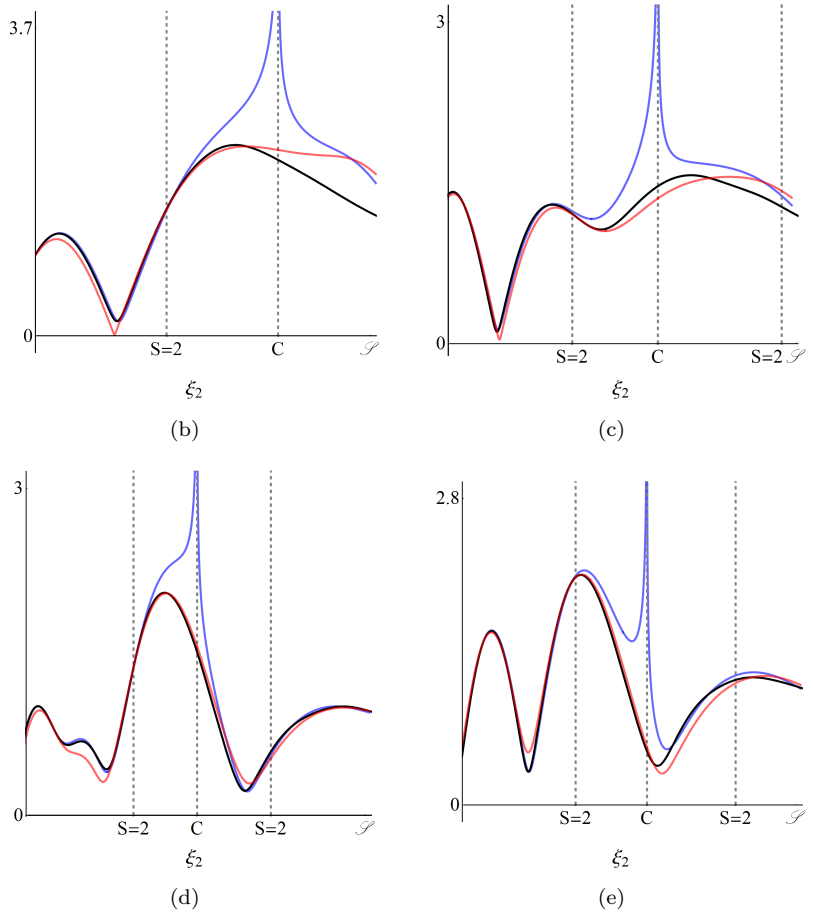

FIGURE 5.5: Singulant and unfolding cusp example: (a) Level sets of the Pearcey function's singulants, black, cusp caustic; black dashed, Stokes set; coloured lines, singulant level sets; red marker, intersection of singulants equal to 2. (b)-(e) cross sections of Pearcey at $\xi_1 = \text{const.}$; black, exact; blue, ray sol.; red, Airy uniform approx.: (b) $\xi_1^{(S=2)}/3$, (c) $2\xi_1^{(S=2)}/3$, (d) $4\xi_1^{(S=2)}/3$, (e) $\xi_1^{(S=2)}$.

Chapter 6

Application of the Ray Solver to a Parallel Shear Flow

6.1 Introduction

In this chapter the ray solver developed in Chapters 3-5 is applied to the isothermal parallel shear flow problem developed in §2 of Chapter 2. The first section of this chapter sees the ray equations reduce significantly for this particular case, where they are matched up with the far-field asymptotics of a modal rearrangement of the Wundrow and Khavaran solution [116] via Poisson summation. This work provides the benchmark for nearly all aspects of ray propagation and guides the generalisation to complex numbers. The remainder of this chapter is then split up into three sections: the first section examines the far-field ray solution, the caustic structures apparent in the point source field and their physical mechanisms; the second considers numerical evaluations of the ray tracing solution against the benchmark, comparing both the field and ray firing parameters, where in the case of the latter, near-to-farfield behaviour is examined; the third and final section undertakes a local analysis to decipher the mechanisms behind the anti-caustic: a novel singularity structure that delimits a section of the CoS.

6.2 Far-field ray solution

The isothermal parallel shear flow configuration input into the ray equations is exactly the same the same as Chap. 2, i.e., $a = 1$, $\overline{u}_i = \delta_{i1}\overline{u}_1 = \delta_{i1}\bar{c}_\infty M$.[1] Clearly, such a configuration reduces the severity of the ray equations (3.48)-(3.50). While we use the cartesian system to effect numerical computations of the parallel shear flow problem, the following cylindrical polar system (see for e.g., [22], [116]) is more convenient for

[1] Keeping $a \neq 1$ in the following work for generality until the results section.

analytical considerations and can be examined in the far-field:

$$\begin{aligned} \dot{x} &= p^{(x)} + M\Phi, \quad \dot{p^{(x)}} = 0, \\ (\dot{r})^2 &= \Phi^2 - \cos^2\theta - p^{(\phi)}, \quad r\dot{\varphi} = p^{(\varphi)}, \\ \dot{(rp^{(\varphi)})} &= \frac{1}{2}\partial(\Phi^2)/\partial\varphi = 0, \quad \dot{S}_\perp = rp^{(\varphi)}\dot{\varphi} + (\dot{r})^2 - \sin^2\theta, \end{aligned} \tag{6.1}$$

where $\perp$ denotes elements in the yz-plane and $\dot{()} \equiv \mathrm{d}/\mathrm{d}\tau$. This system has initial conditions,

$$x = x_s, \quad r = r_s, \quad \varphi = \varphi_s, \quad p^{(x)} = \cos\theta, \quad p^{(\varphi)} = \sigma_s \sin\mu \sin(\lambda - \varphi_s), \quad S_\perp = 0, \tag{6.2}$$

where the ray firing parameters μ and λ are as before, and $\sigma_s^{-2} = a_s^2 - M_s^2 \sin^2\mu$ from (3.51). It can be shown that in the far-field ($R \to \infty$),

$$\begin{aligned} \dot{r} &\sim \pm Q(r|\nu_\star), \quad r^2\dot{\varphi} = \nu_\star, \\ \dot{S}_\perp &\sim \nu_\star\dot{\varphi} + Q^2(r|\nu_\star) - \sin^2\theta, \end{aligned} \tag{6.3}$$

subject to,

$$r = r_s, \quad \varphi = \varphi_s, \quad S_\perp = 0, \tag{6.4}$$

where,

$$rQ(r|\nu_\star) = \sqrt{r^2q^2 - \nu_\star^2}, \quad \nu_\star \equiv r_s q_s \sin(\lambda - \varphi_s). \tag{6.5}$$

An interesting consequence of the initial conditions (6.2) is that,

$$\dot{r}_s = q_s \cos(\lambda - \varphi_s). \tag{6.6}$$

The sign of this equation indicates whether a ray is travelling towards the origin $r = 0$ initially. This leads to the monikers "direct" and "indirect" to distinguish between the two signs of (6.6) for real rays. Typically one could look at ray trajectories and class them according to these monikers based upon whether the ray bends back up toward the observer (indirect) or not (direct). This is not true as rays may be indirect and not have a bent path. However, this classification loses significance when dealing with complex rays as the aforementioned heuristic explanation is redundant.

Equations (6.3) can be solved (see for e.g., [22], [116]) to yield,

$$\Delta\varphi = \varphi - \varphi_s = \left(\int_{r_\delta}^{r} \mp \int_{r_\delta}^{r_s}\right) \frac{\nu_\star \,\mathrm{d}r'}{r'^2 Q(r'|\nu_\star)}, \tag{6.7}$$

$$S_\perp = \nu_\star\Delta\varphi + \zeta(r|\nu_\star) \mp \zeta(r_s|\nu_\star) - R\sin^2\theta, \tag{6.8}$$

where,

$$\zeta(r|\nu_\star) = \int_{r_\delta}^{r} Q(r'|\nu_\star)\,\mathrm{d}r', \quad Q^2(r_\delta|\nu_\star) = 0. \tag{6.9}$$

As per usual, the top sign of $\pm$ or $\mp$ indicates direct rays, while the bottom indicates the indirect branch.

In order to benchmark the ray solver it is necessary to match up at least one component with $\mathbb{G}_\omega$. This is done by rearranging (3.14)-(3.17), for a time harmonic source, into Lilley's equation for a parallel shear flow. It can be shown - using techniques in [9] - that the pressure component of the Green's function satisfies,

$$\begin{aligned}\overline{D}_\omega\left(\overline{D}_\omega^2 - \frac{\partial}{\partial x_j}\overline{c}^2\frac{\partial}{\partial x_j}\right)\hat{g}_{5\eta} + 2\overline{c}^2\frac{\partial\overline{u}_1}{\partial x_j}\frac{\partial^2}{\partial x_j\partial x_1}\hat{g}_{5\eta} = \\ \left(2\frac{\partial\overline{u}_1}{\partial x_i}\frac{\partial}{\partial x_1} - \overline{D}_\omega\frac{\partial}{\partial x_i}\overline{c}^2\right)\delta_{i\eta}\delta(\boldsymbol{x}-\boldsymbol{x}_s) + \overline{c}^2\overline{D}_\omega^2\delta_{4\eta}\delta(\boldsymbol{x}-\boldsymbol{x}_s).\end{aligned} \tag{6.10}$$

Now, given that $\hat{g}_{5\eta}$ satisfies (3.27), and G_ω satisfies (6.10) with right-hand-side of $\overline{c}_\infty^2\overline{D}_\omega$, then replacing $\hat{g}_{54}$ by $\overline{D}_\omega\hat{g}_5$ in (6.10) with $\eta = 4$, it can be seen that $\hat{g}_5/a_s^2$ matches up with G_ω. As a final check, the results of a generic ray contribution (3.57) with $n_D = 3$ can be calculated in the far-field and shown to match the steepest descents evaluation. Using the far-field result for the Jacobian given by [24] and [116], then,

$$J \sim R^2\sin\theta\,\frac{\partial(\theta,\varphi)}{\partial(\mu,\lambda)} = R^2\sin\theta\frac{\partial\theta}{\partial\mu}\frac{\partial\varphi}{\partial\lambda} = a_s^2\sigma_s^3R^2\sin\mu\frac{\partial\varphi}{\partial\lambda}, \quad R\to\infty, \tag{6.11}$$

since,

$$\frac{\partial\theta}{\partial\mu} = \frac{\mathrm{d}\theta}{\mathrm{d}\mu} = \frac{a_s^2\sigma_s^3\sin\mu}{\sin\theta}. \tag{6.12}$$

Then using the relation $\overline{\rho} = p_\infty\gamma_a/\overline{c}^2$,

$$\hat{g}_5/a_s^2 \sim \frac{(1-M_kp_k)}{a_sa(1-M_{s_k}p_{s_k})}\left(\frac{\partial\varphi}{\partial\lambda}\right)^{-1/2}\frac{\mathrm{e}^{\mathrm{i}k_0S}}{4\pi R} = \frac{1}{a_s(1-M_{s_k}p_{s_k})}\left(\frac{\partial\varphi}{\partial\lambda}\right)^{-1/2}\frac{\mathrm{e}^{\mathrm{i}k_0S}}{4\pi R}, \quad R\to\infty, \tag{6.13}$$

with,

$$S \sim S_\perp + R, \quad R\to\infty. \tag{6.14}$$

Further relations can be derived once the connection of the modal sum is made with ray solution in the far-field.

6.2.1 Poisson summation asymptotics

The connection between the modal summation and ray theory can be exploited using a Poisson summation. Techniques such as the Poisson sum and Watson transform are well known to yield ray theory solutions when evaluated asymptotically (see for e.g., Chapman et al. [65], Jones [169]). Both of these techniques have been used in acoustic

applications, for example Jones [169] in acoustic scattering problems and Abrahams et al. in aeroacoustic applications [26–28] (linear shear flows.) The solution here using a Poisson sum is due to Wundrow & Khavaran [116]. The Poisson recasts the modal sum via the identity,

$$\sum_{n=-\infty}^{\infty} f(n) \equiv \sum_{m=-\infty}^{\infty} \mathscr{F}(m), \tag{6.15}$$

where $f(n)$ is the modal term and $\mathscr{F}(m)$, in this instance, is the Fourier transform of $f(n)$ evaluated at integers m. In the limit $k_0 \to \infty$ the series of integrals $\mathscr{F}(m)$ can be evaluated using the method of steepest descent. These asymptotic contributions that are equivalent to ray contributions are used to guide the solution into the complex plane. This recasts (2.89) as,

$$\mathscr{R}_\omega \sim \sum_{m=-\infty}^{\infty} \int_{-\infty}^{\infty} \left(2k_0 \frac{\sqrt{-\eta(r_s|\nu)}}{r_s Q(r_s|\nu)} \right)^{1/2} \mathrm{Ai}\left(\eta(r_s|\nu)\right) \mathrm{e}^{\mathrm{i}k_0\left(\alpha_m \nu + \zeta(r|\nu) - R\sin^2\theta\right)} \,\mathrm{d}\nu, \tag{6.16}$$

where $\alpha_m = 2\pi m + \Delta\varphi$ and $\nu = n/k_0$. In order to express all fast components of the integrand in exponential form, the Airy function is expanded. The second order nature of the radial ode means that a two Riemann sheeted structure is expected, where $\pm$ denotes the indirect and direct ray branches as before. The branch cuts at $\pm r_s q_s$ are chosen to have orientation as in [116] and Chap. 2,

$$rQ(r|\nu) = \sqrt{|r^2q^2 - \nu^2|}\mathrm{e}^{\mathrm{i}[\arg(rq-\nu)+\arg(rq+\nu)]/2}, \quad \text{with} \quad -\frac{1}{2}\pi \le \arg(rq \pm \nu) < \frac{3}{2}\pi \tag{6.17}$$

so that mapping into the ν-plane reverses the $rq - \nu$ cut, since,

$$\begin{aligned} -\frac{1}{2}\pi \le \arg(rq-\nu) &= \pm\pi + \arg(\nu - rq) < 3\pi/2, \\ -\frac{3}{2}\pi \le \arg(\nu - rq) &< \frac{1}{2}\pi \quad \text{e.g., using } -\pi. \end{aligned} \tag{6.18}$$

The occurrence of only two cuts is due to assumption of a single turning-point problem in the $r \in \mathbb{C}$ plane. Cuts can arise due to both $Q(r_s|\nu)$ and $\zeta(r_s|\nu)$. However, the original contour passes through the cuts/turning points of $Q(r_s|\nu)$ so that a boundary-layer contribution occurs where the contour in (6.16) cannot be split up into the WKB branches, but must remain in the Airy function form. In fact the Airy function behaves analytically (i.e. no cut) and the prefactor,

$$\lim_{\nu^2 \to r_s^2 q_s^2} \frac{\sqrt{-\eta(r_s|\nu)}}{r_s Q(r_s|\nu)} = \left(k_0 \mathscr{P}(r_s)\right)^{1/3}, \tag{6.19}$$

remains bounded and blind to the branch cuts.

A further complication is that q_s is imaginary for some observer angles θ. This means we

expect the new contour definitions under this asymptotic expansion to change discontinuously as the branch cuts jump from the imaginary axis to the real line discontinuously. The integrals are then split up as follows,

$$\mathscr{R}_\omega \sim \begin{cases} \mathscr{R}_\omega^{(-)} - \mathrm{i}\mathscr{R}_\omega^{(+)} + \mathscr{R}_\omega^{(\times)}, & \text{for} \quad q_s^2 > 0, \\ \mathscr{R}_\omega^{(-)}, & \text{for} \quad q_s^2 < 0, \end{cases} \tag{6.20}$$

where the components of $\mathscr{R}_\omega$ in (6.20) are given by,

$$\mathscr{R}_\omega^{(\pm)} \equiv \sum_{m=-\infty}^{\infty} \int_{C^{(\pm)}} \left(\frac{\mathrm{i}k_0}{2\pi r_s Q(r_s|\nu)} \right)^{1/2} \mathrm{e}^{\mathrm{i}k_0(\alpha_m \nu + \zeta(r|\nu) \pm \zeta(r_s|\nu))} \, \mathrm{d}\nu, \tag{6.21}$$

and,

$$\mathscr{R}_\omega^{(\times)} \equiv \sum_{m=-\infty}^{\infty} \int_{C^{(\times)}} \left(2k_0 \frac{\sqrt{-\eta(r_s|\nu)}}{r_s Q(r_s|\nu)} \right)^{1/2} \mathrm{Ai}\left(\eta(r_s|\nu)\right) \mathrm{e}^{\mathrm{i}k_0\left(\alpha_m \nu + \zeta(r|\nu) - R\sin^2\theta\right)} \, \mathrm{d}\nu, \tag{6.22}$$

with the contours $C^{(\pm)}, C^{(\times)}$ yet to be defined.

In order to proceed with the steepest descent method, both contours and saddle points must be computed. While the saddles are interpreted as rays, their contribution is determined by the topology of the steepest contours in the complex plane. Here, computation of the saddles follows [116]. The integrand phase,

$$\Psi_{WK}(\nu) \equiv \alpha_m \nu + \zeta(r|\nu) \pm \zeta(r_s|\nu) - R\sin^2\theta, \tag{6.23}$$

is differentiated leading to the saddle point condition,

$$\frac{\partial \Psi_{WK}}{\partial \nu_\bigstar} = 0, \implies \alpha_{m_\bigstar} = \Delta\varphi + 2\pi m_\bigstar = \psi_{WK}(\nu_\bigstar) \equiv \left(\int_{r_\delta}^{\infty} \pm \int_{r_\delta}^{r_s} \right) \frac{\nu_\bigstar}{r^2 Q(r|\nu_\bigstar)} \, \mathrm{d}r, \tag{6.24}$$

where $\nu_\bigstar$ is the saddle and $\bigstar$ denotes the saddle condition. Here r_δ satisfies $r_\delta^2 q^2(r_\delta) - \nu_\bigstar^2$ (see defs. in (2.71)). To find the function ψ_{WK}, which is the derivative of $\zeta(r|\nu) \pm \zeta(r_s|\nu)$ w.r.t. ν the following were used,

$$\frac{\partial}{\partial \nu} Q(r|\nu) = -\frac{\nu}{r^2 Q(r|\nu)}, \quad \frac{\partial}{\partial r} rQ(r|\nu) = \frac{1}{2r^2 Q(r|\nu)\mathscr{P}(r)}, \quad \frac{\partial r_\delta}{\partial \nu_\bigstar} = 2\nu_\bigstar r_\delta \mathscr{P}(r_\delta), \tag{6.25}$$

$$\mathscr{P}(r) = \frac{1}{r(r^2 q^2)'}. \tag{6.26}$$

Computation of (6.24) is achieved numerically due to the lack of closed form solutions. One chooses an observer location $\{R, \theta, \varphi\}$ and index $m_\bigstar$, then starts a root finding process using an initial estimate of $\nu_\bigstar$, iterating until convergence. Due to the far-field

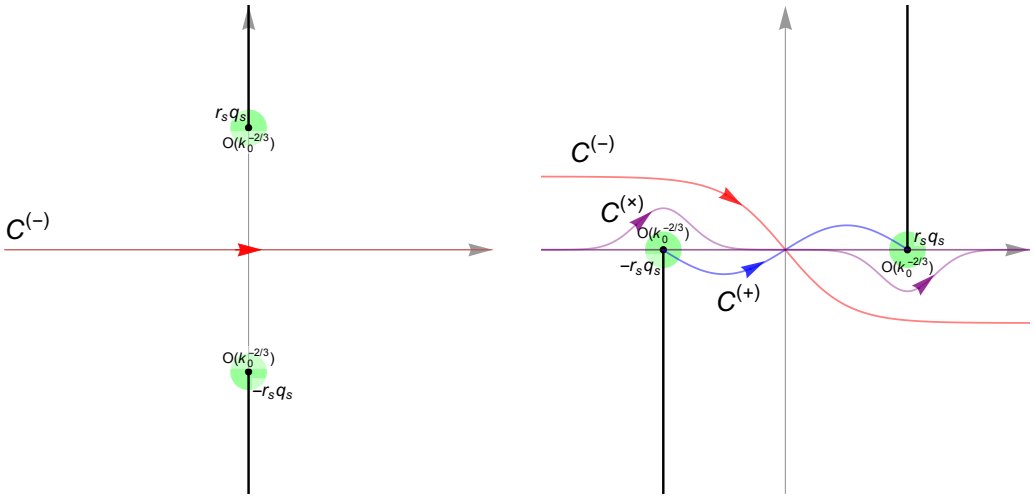

FIGURE 6.1: Definition of complex contours, $C^{(\pm)}$, $C^{(\times)}$. Solid black line, branch cuts; red, $C^{(-)}$; blue, $C^{(+)}$; purple, $C^{(\times)}$. (a) $C^{(-)}$ for $q_s^2 < 0$, (b) $C^{(\pm)}$, $C^{(\times)}$ for $q_s^2 > 0$. Green shaded region about points $\pm r_s q_s$ indicate boundary layer $O(k_0^{-2/3})$.

nature of this approximation, it is possible to evaluate the saddle condition (6.24) at $r = \infty$, since the derivatives of ζ w.r.t. ν do converge: this is distinct from the phase itself as integration of the phase (i.e., a regular wave field) to infinity will yield infinite results.

Once the saddles have been calculated the steepest descents evaluation of the integrals (6.21) are then given by,

$$\mathscr{R}_\omega^{(\pm)} \sim \sum_{\nu_\star} \left(r_s Q(r_s|\nu_\star) \left| \frac{\partial \psi_{WK}}{\partial \nu_\star} \right| \right)^{-1/2} \mathrm{e}^{\mathrm{i}(\mathrm{Ph}+\pi/4)} \mathrm{e}^{\mathrm{i}k_0 \left(\alpha_{m_\star} \nu_\star + \zeta(r|\nu_\star) \pm \zeta(r_s|\nu_\star) - R\sin^2\theta \right)}, \tag{6.27}$$

where as in [116],

$$-\frac{1}{2}\pi < \mathrm{Ph} \equiv -\arg\left((\mathrm{i}\partial\psi_{WK}/\partial\nu_\star)^{1/2} \right) \leq \frac{1}{2}\pi, \tag{6.28}$$

is used to provide analytic continuation to complex rays, and,

$$\frac{\partial \psi_{WK}}{\partial \nu_\star} = \left(\int_{r_\delta}^{\infty} \mp \int_{r_\delta}^{r_s} \right) \frac{1 + 2\nu_\star^2 r \mathscr{P}'(r)}{r^2 Q(r|\nu_\star)} \mathrm{d}r \pm \frac{2\nu_\star^2 \mathscr{P}(r_s)}{r_s Q(r_s|\nu_\star)}. \tag{6.29}$$

It should be noted that (6.27) makes no reference to Stokes multipliers and the orientation of the steepest descents path through the saddle (the orientation anomaly). These latter criteria can be provided using the steepest path topology. In the following we will determine the contours $C^{(\pm)}$ and plot them showing the relevant ray contributions.

The determination of the contours $C^{(\pm)}, C^{(\times)}$ is made trickier due to the fact the two-sheeted structure of the WKB solutions is not apparent for all values of ν. In a region of $O(k_0^{-2/3})$ the larger argument expansion of (6.16) must return to the uniform expansion. This generates two problems concerning the application of steepest descents to (6.16) that are not addressed in [116]: first, how to define the steepest descent contours for each sheet in terms of the original contour along the real ν axis; second how to account for the regions near the branch points. These problems can both be resolved using inner and outer expansions of the contour integral. To aid the following, the integration of the contour is visualised in Fig. 6.1 for angles in which $q_s^2 < 0$ - branch points $r_s q_s$ are imaginary; and $q_s^2 > 0$ - branch points $r_s q_s$ are real. The following method is essentially motivated by a similar (but simpler) problem due to Bleistein & Handelsman [170].

In Figure 6.1(a) we have imaginary branch points and only one contour $C^{(-)}$ equivalent to C of the original integral. The reason being is that the integrals must converge at infinity and an integral along the real line for $\mathscr{R}_\omega^{(+)}$ does not: furthermore another option - a truncated integral from $\pm r_s q_s$ with $q_s^2 < 0$ - yields exponentially large behaviour. In Figure 6.1(b), $\pm r_s q_s$ with $q_s^2 > 0$ and the branch points are real, and whilst they can be avoided via Cauchy's theorem in general, in order to split the integration path up we use these points to delimit the contours of $\mathscr{R}^{(+)}$. Thus we have inner integrals $C^{(\times)}$ rescaled when $\nu = O(k_0^{-2/3})$ starting and ending at infinity,[2] whose contribution via $\mathscr{R}^{(\times)}$ we will neglect as in [116]; outer integrals $C^{(\pm)}$ where $C^{(-)}$ is delimited by $\pm\infty$ as before, and $C^{(+)}$ a pseudo-endpoint problem which formally starts and ends at the points $\pm r_s q_s$. These contributions are distinct, so long as the saddles from the outer expansions don't move into the $O(k_0^{-2/3})$ neighbourhoods of the branch points. Due to the boundary layer nature of endpoints of $C^{(+)}$ there are no endpoint contributions to $\mathscr{R}_\omega^{(+)}$ as these are contained in $\mathscr{R}_\omega^{(\times)}$.

An example of saddle point computations is shown in Fig. 6.2 for $\Delta\varphi = \pi/3$ and $5^\circ \leq \theta \leq 150^\circ$ with Poisson index $m_\star = 0$.[3] We use the same isothermal shear flow as in Chap. 2, i.e., $a = 1,\ M(r) = M_J \mathrm{sech}^2(2r),\ M_J = 0.9$.

At low angles there are two complex saddles forming a conjugate pair. The saddle in the upper half plane, which yields an exponentially small contribution, belongs to the $(-)$ sheet, while the saddle in the lower half plane, which yields an exponentially large contribution, belongs to the $(+)$ sheet. Due to the conservation of rays the conjugate of a complex ray always exists (see Chap. 4), where we have explicitly added this contribution to Fig. 6.2 in order to emphasise this fact unlike [116] who neglect to add it to their diagram.

[2] In terms of an inner variable.

[3] It is convenient to keep $\Delta\varphi$ in its relative terms until ray computations are made and the source azimuth made explicit.

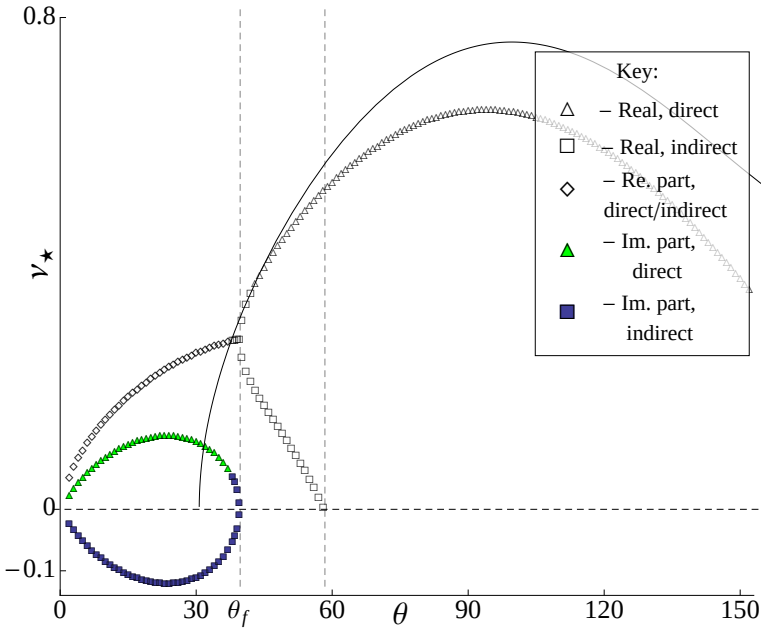

FIGURE 6.2: Saddles computations $\nu_\star$, $m_\star = 0$, for $\Delta\varphi = \pi/3$, $5° \leq \theta \leq 150°$. Key inset. θ_f, θ_d denote the fold caustic and disappearance point resp. Solid line, $\mathrm{Re}(r_s q_s)$.

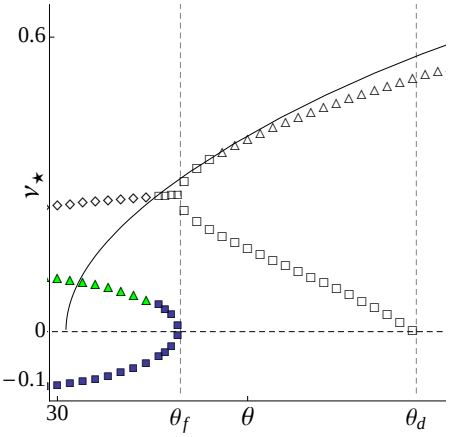

FIGURE 6.3: Close up of saddle coalescence and branch cut crossings for $\Delta\varphi = \pi/3$. Key is the same as Fig. 6.2.

As θ is increased the direct saddle crosses over the cut (as shown by the real part crossing the $\mathrm{Re}(r_s q_s)$) so that both complex rays are on the same sheet. Further increases see the saddles coalesce - implying a fold caustic - before they scatter off along the real axis. As both the saddles coalesce on the same sheet it can be seen from the $-\mathrm{i}\mathscr{R}_\omega^{(+)}$ definition that the real ray that reflects off of the caustic before reaching the observer point has no phase discontinuity in the amplitude given by (6.27); conversely the amplitude in (6.27) must provide "i" in order to cancel the factor premultiplying $\mathscr{R}_\omega^{(+)}$. One important feature of this saddle diagram is that the lower branch of real rays terminates at the origin and disappears from the calculation. This appears to contravene the conservation of rays. It will be shown that there is in fact a coalescence - of sorts - *without* a caustic that gives rise to another branch of rays that have not been found previously. In physical terms this related to the ability of the flow to refract rays upwards, see §6.3.

The steepest descent contours for the saddle computations in Fig. 6.2 are shown in Fig. 6.4. Steepest descent paths are isocontours defined by,

$$\begin{aligned} &\mathrm{Re}(\Psi_{WK}(\nu)) = \mathrm{Re}(\Psi_{WK}(\nu_\star)), \qquad \mathrm{Im}(\Psi_{WK}(\nu)) > 0, \quad \text{for saddles,} \\ &\mathrm{Re}(\Psi_{WK}(\nu)) = \mathrm{Re}(\Psi_{WK}(\pm r_s q_s)), \quad \mathrm{Im}(\Psi_{WK}(\nu)) > 0, \quad \text{for endpoints.} \end{aligned} \tag{6.30}$$

To continue the saddles across the cuts, the phase function of the adjacent sheet is evaluated at the saddle/endpoint whose contours are to be continued. For example, continuing the direct/indirect saddle contours means using isocontours of the indirect/direct phase function $\Psi_{WK}^{(\pm)}(\nu_\star^{(\mp)})$, where $\pm$, as usual, distinguishes between the direct and indirect phase functions.

The behaviour of the steepest paths are as follows. Starting with $\theta = 30°$ so that the branch points are complex and the only contour that exists is $C^{(-)}$, then it can be seen from Fig. 6.4(a) that the only way to pass through and collect the direct saddle is by incorporating the branch cut and engendering a lateral wave contribution (see for e.g., Brekhovskikh [171]). These contributions are new for the parallel shear flow problem and will be estimated in magnitude in the next section.

Increasing the angle to $\theta = 35°$ sees the branch points move to the real axis. Again in order to complete contours a branch cut contribution must be taken. As θ moves to 39° the direct saddle moves to the indirect sheet (which is now part of the def. of $\mathscr{R}_\omega$ since $\theta > 30.5°$). Figure 6.4(f) shows two features: first, the two saddles are connected via a steepest descent contour although only the exponentially small (upper half-plane) saddle is required; second, the branch contribution is turned off by the crossing of the cut. This second point shows that the lateral wave is turned off by the exponentially small ray. This contribution also is not required, as before there has been no way of returning to the direct sheet (see $\theta < 39°$ plots) and so a branch cut was necessitated; now, one can return to the sheet the saddle is on (now the indirect sheet) due to continuation of the integral endpoint contours. As the angle of 40° is reached the saddles have coalesced on the indirect sheet and moved away from each other on the real axis. It can be seen from Fig. 6.4(h) that in order to complete the contour both real saddles are needed. The steepest descent path behaviour is only considered up to 58° due to the non-canonical disappearance of one of these rays.

6.2.2 Branch cut contributions

Here we estimate the size of the branch cut contributions shown in Fig 6.4, so as to conclude whether we can proceed with saddles only. This is preferred as these can be equated with rays and no other considerations need to be made. Lateral rays with which branch cuts are typically associated are non-trivial to reproduce, for e.g., Doornbos [56].

The contribution of the branch cut here uses the method found in Miller [172]. The integral is written as,

$$\begin{aligned}\mathscr{R}_{\omega}^{(H)} &\equiv \int_{C^{(H)}} \left(\frac{\mathrm{i}k_0}{2\pi r_s Q(r_s|\nu)}\right)^{1/2} \mathrm{e}^{\mathrm{i}k_0\Psi_{WK}}\,\mathrm{d}\nu \\ &= \left(\frac{k_0}{2\pi}\right)^{1/2} \int_{C^{(H)}} \frac{1}{(\nu+r_sq_s)^{1/4}(\nu-r_sq_s)^{1/4}} \mathrm{e}^{\mathrm{i}k_0\Psi_{WK}}\,\mathrm{d}\nu,\end{aligned} \tag{6.31}$$

where superscript H allows us to distinguish the cut contribution, $C^{(H)}$ is a loop or Hankel contour around the branch point $\nu = r_sq_s$ in a locally clockwise manner, and the phase is integrated on the direct sheet. Since the integrand's singularity has a power $-1/4$ which is locally integrable it possible to write,

$$\mathscr{R}_{\omega}^{(H)} = (1-\mathrm{e}^{\mathrm{i}\pi/2}) \left(\frac{k_0}{2\pi}\right)^{1/2} \int_{C^{H'}} \frac{1}{(\nu+r_sq_s)^{1/4}(\nu-r_sq_s)^{1/4}} \mathrm{e}^{\mathrm{i}k_0\Psi_{WK}}\,\mathrm{d}\nu, \tag{6.32}$$

where $C^{H'}$ is a contour from the branch point to infinity along the branch cut on the $\nu > r_sq_s$ side of the cut. As $k_0 \to \infty$, a local expansion can be used, which since the branch cut contour travels through a valley of $\mathrm{i}\Psi_{WK}$, is approximated by the local steepest descent path direction.[4] This gives,

$$\mathscr{R}_{\omega}^{(H)} \sim \frac{\mathrm{e}^{-\mathrm{i}\pi/8}\pi^{-1/2}}{(2r_sq_s)^{1/4}} \mathrm{e}^{\mathrm{i}k_0\Psi_{WK}(r_sq_s)} \frac{\Gamma(3/4)}{\left(\partial\Psi_{WK}/\partial\nu|_{r_sq_s}\right)^{3/4} k_0^{1/4}}, \tag{6.33}$$

which shows that this contribution is $O(k_0^{-1/4})$. This lies outside the scope of the analysis undertaken in Chap. 3, and we do not have the means for calculating this ray. We will neglect this contribution on the grounds of its size and that other ray calculations [116] are successful without this contribution. This is also in-keeping with the idea of an asymptotic series and their components outlined in Chap. 1.

[4] The integrand's exponential decays along $C^{H'}$ so the steepest path approximation is not poor; there is no change in the k_0 magnitude estimation.

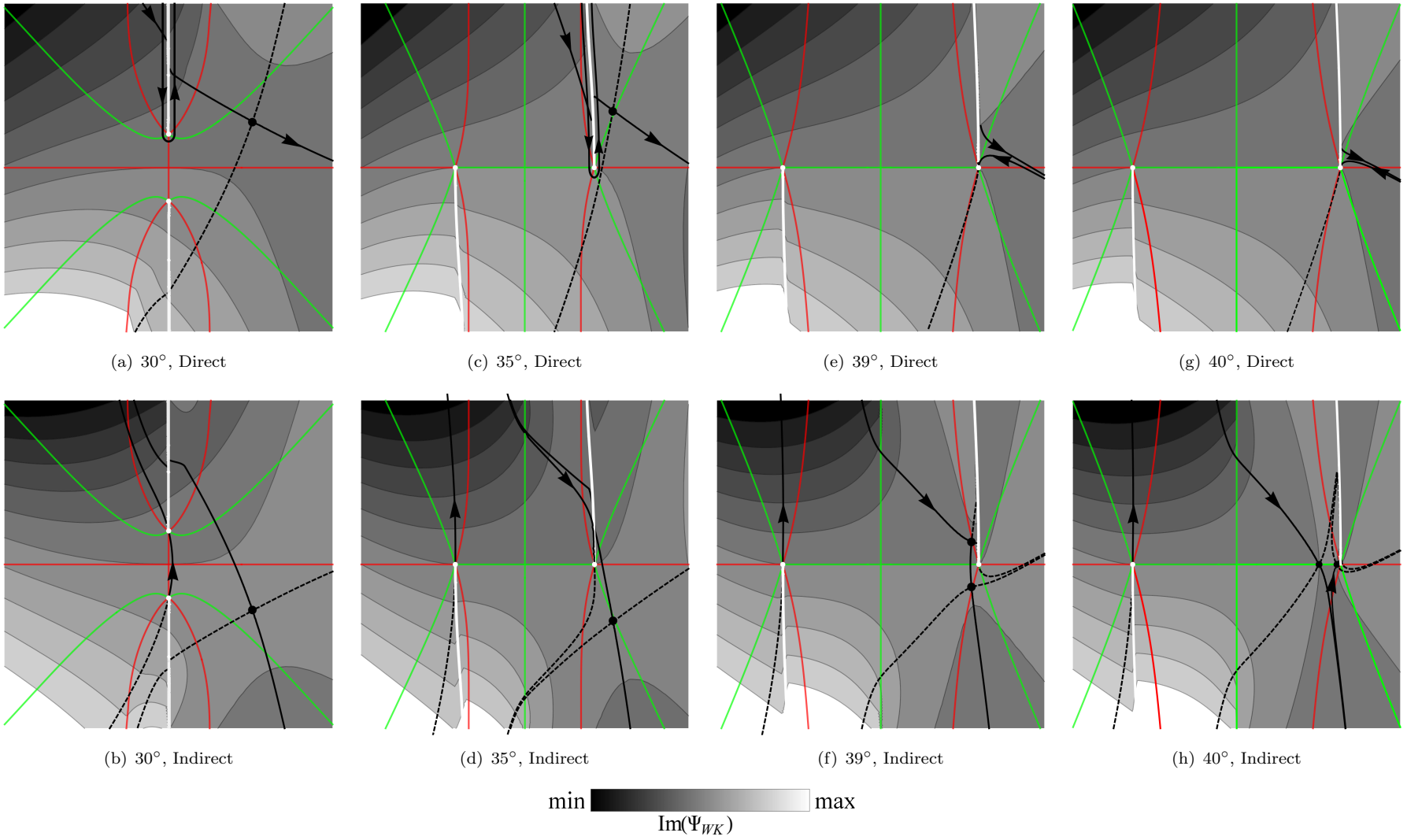

(a) 30°, Direct (c) 35°, Direct (e) 39°, Direct (g) 40°, Direct

(b) 30°, Indirect (d) 35°, Indirect (f) 39°, Indirect (h) 40°, Indirect

FIGURE 6.4: Steepest descents paths for $\Delta\varphi = \pi/3$. Black marker, saddles. Solid black line, steepest descent paths; white lines, branch cuts; green line, anti-Stokes mapping; red line, Stokes mapping.

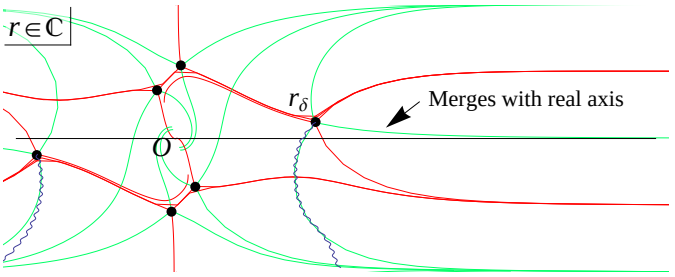

FIGURE 6.5: Stokes structure in the r-plane for $\nu_\star \in \mathbb{C}$. Key as in Fig. 2.5.

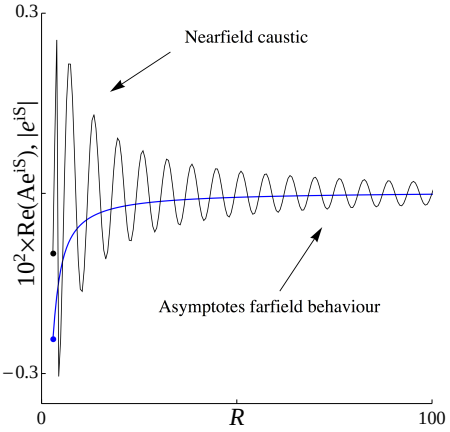

FIGURE 6.6: Near-to-farfield behaviour of a complex ray

6.2.3 Structure of a complex ray

In Chapter 2 two Stokes structures where shown for real modal indices. Both cases had single turning-points though of two different orders. The complex ray theory in the previous section has generalised and decoupled the modal index. The question is now, "What is the Stokes structure of $\int_{r_\delta} Q(r'|\nu_\star)\,\mathrm{d}r'$ given $\nu_\star \in \mathbb{C}$?"

The answer is simple if one considers a perturbation to the real mode case. As the turning-point is lifted into the complex plane the Stokes structure is pulled with it. This is shown in Fig. 6.5 where the primary turning-point is shown engendering a complex Stokes structure.[5] Notably, the anti-Stokes line emanating from r_δ merges back with the real line. This way only a finite amount of complex decay is obtained when integrating from r_s to r in the far-field. Such a phenomenon is known as "above-the-barrier" scattering in quantum mechanics (see for e.g., Boyd [173], Pokrovskii & Khalatnikov [174]), and the effect can be seen on a ray solution continued from the near-field to the far-field can be seen in Fig. 6.6. As the far-field is reached the behaviour asymptotes its far-field solution rapidly. Technically the far-field is the limit $R \to \infty$, however it is clear that close to the source we have already a good approximation of that behaviour.

[5] The Stokes diagram has been dressed-up somewhat with Stokes structures from other turning-points other than primary.

6.3 Ray tracing and benchmarking

It is clear from the results shown in Figs. 6.2 and 6.3 that the Poisson sum asymptotics are a suitable guide for the generalisation of the far-field system to complex numbers, namely through the variable $\nu_\star$, where $\nu_\star$ is equal to and generalises the ray initial condition (6.5). It is also clear that the azimuthal directivity factor (6.7) and the saddle condition (6.24) are equivalent, where in the latter $m_\star$ is an additional device facilitating multivalued branches of the analytic solution. So, not only can $\mathscr{R}_\omega$ be calculated using analytic complex ray theory, but through $\nu_\star$ other variables of the ray field can also be benchmarked. In fact the analytic solution provides a benchmark for quantities bar the integration times τ and geodesic/conjugate elements. In the case of the latter the Jacobian (6.11) can be used as an indirect check via,

$$J \sim \pm r_s a_s^2 \sigma_s^3 R^2 \sin\mu \, Q(r_s|\nu_\star) \frac{\partial\varphi}{\partial\nu_\star}, \tag{6.34}$$

where,

$$\frac{\partial\varphi}{\partial\lambda} = \frac{\partial\varphi}{\partial\nu_\star}\frac{\mathrm{d}\nu_\star}{\mathrm{d}\lambda}, \quad \text{with} \quad \frac{\mathrm{d}\nu_\star}{\mathrm{d}\lambda} = \pm r_s Q(r_s|\nu_\star), \tag{6.35}$$

from (6.5) and (6.7). However, the most interesting parameters to study are the ray firing parameters μ and λ. We can provide a benchmark by inverting the nonlinear - and hence multi-valued equations (3.51) and (6.5). For μ there are in fact two possible equations, the second results from an equation for $\mathrm{d}\theta/\mathrm{d}\mu$ in (6.12) and is more useful than (3.51) because the receiver variable θ appears explicitly, i.e.,

$$\sigma_s^{-2} = a_s^2 - M_s^2 \sin^2\mu, \quad \text{and} \quad \sigma_s^2 \sin^2\mu = \Phi_s^2 - \cos^2\theta. \tag{6.36}$$

In both cases of (6.36) $\sin\mu = \pm\sqrt{\ldots}$, so two branches of the solution exist. If we limit $\mu \in [0, \pi]$ for real solutions then we choose the positive branch. A consequence of the second equation of (6.36) is that for one observer θ there is only *one* solution branch of θ when $\mu \in \mathbb{R}$. This opposes the conclusions of Chap. 4, that when a caustic with multiple distinct branches is encountered, the ray firing parameters will also have the same number of distinct branches. We will resolve this problem in §6.3.1.

The firing parameter lambda λ ($\lambda \in [0, 2\pi]$, $\lambda \in \mathbb{R}$) can be obtained through $\nu_\star$ (once φ_s is made explicit) by inverting,

$$\sin(\lambda - \varphi_s) = \nu_\star / r_s q_s. \tag{6.37}$$

This may appear simple enough, however, q_s is known to jump - N.B. $r_s q_s$ are the branch points of the cuts in (6.18) - so at some point there will be ambiguity in the benchmark as $\nu_\star/r_s q_s$ jumps branches. The result is a discontinuity in λ for some ray solutions.

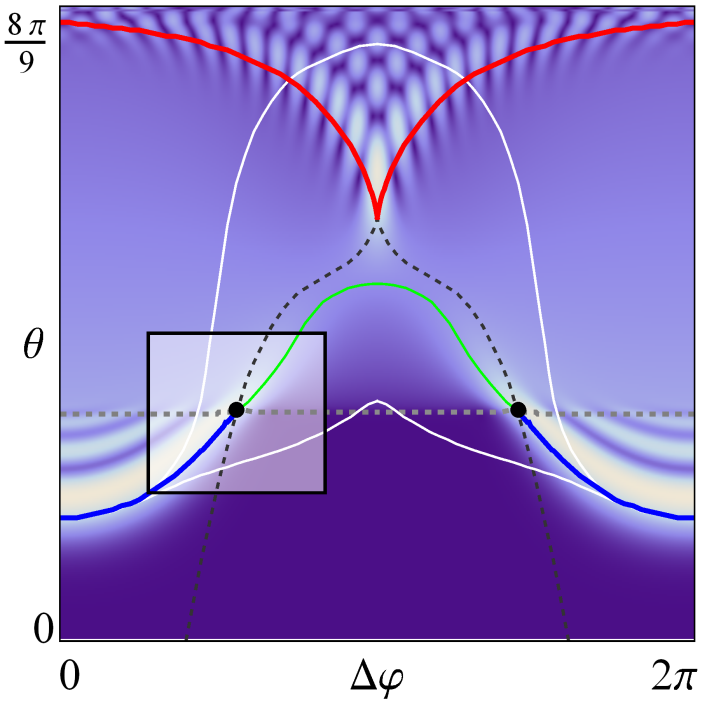

FIGURE 6.7: Green's function field $|\mathbb{G}_\omega/\mathscr{G}_\omega|$ with caustic and Stokes structures overlaid ($St = 5$ or $k_0 = 28.7$). Caustics structures: fold $\theta_f(\Delta\varphi)$, blue; cusp $\theta_c(\Delta\varphi)$, red. Stokes structures: Stokes, black dashed; anti-Stokes, green. Non-canonical/anti-caustic locus θ_d, grey dashed. CDPs, black marker . Ray species aid, white. Box for local analysis.

Now that we have a method for benchmarking both the accuracy of the ray method (both analytically (6.27) and numerically (2.89)), we can set up a ray tracing problem to benchmark. Using the theory of Chapter 2 the ray computations are made for an isothermal parallel shear flow using the same shear flow as for the saddles computations. Again, we place a source at $r_s = 0.75$, but now make $\varphi_s = \pi/2$ explicit. As the problem is translationally invariant in x, x_s is arbitrary so long as $x_s/R \ll 1$.

The first result of the ray tracing computations is perhaps the most important. These are the structural delineations of the field, such as caustics, Stokes structures and the CoS boundary; these are shown in Fig. 6.7 overlaying the modal solution of Chap. 2. Firstly, there are a wide variety of structures, some of which are familiar and others peculiar to this field. The more familiar features are the cusp and the fold caustic, with the Stokes structure emanating from the latter. The peculiar features are the caustic disappearance points (CDP), the non-canonical/anti-caustic line - a feature we discuss in more detail in §6.4, and the anti-Stokes structure. In the case of the latter, it is the presence of the anti-Stokes line emanating from the CDPs that is unfamiliar and not its action upon the dominancy of the ray solutions. Additionally, we note that only two of these structures have been encountered in the saddle-point analysis, and that these same structures are the only ones of those shown in Fig. 6.7 encountered in the high-frequency propagation from point sources in jets previously.

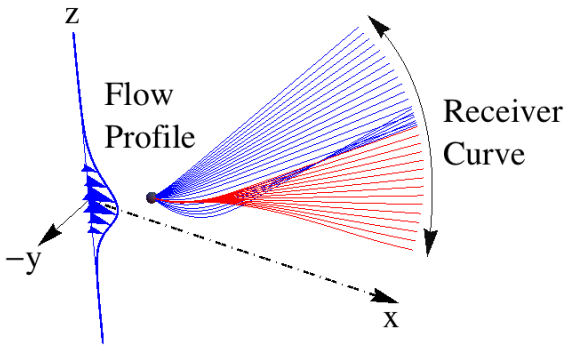

FIGURE 6.8: Near-field ray couple giving rise to a fold caustic θ_f. Real rays shown in blue; physical complex rays shown in red. Ray paths correspond to $\mathrm{Re}(\boldsymbol{x}(\boldsymbol{\varsigma}))$.

The familiar canonical structures in Fig. 6.7 can be easily understood by examining the ray paths as the observer cuts these structures. Starting with the fold caustic, it is understood that this should coincide with that found by [116] in the saddle-point study with $m_\star = 0$. Figure 6.8 shows the interfering couple that conspire to give the fold caustic. Though this figure is in the near-field[6] the caustic structures still persist and the physical mechanisms for the structures are invariant. It is clear from this figure that the fold caustic is created by two trajectories whose monikers where decided upon in the saddle-point analysis. There are those rays that propagate straight to the observer (direct), and those that propagate away initially (indirect) before being guided or "turned" back by the flow. Hence it is these indirect rays that have an explicit and observable turning-point (r_δ which otherwise can eliminated from the direct branch of the phase (6.23)). However, the ability of the flow to bend rays is not infinite; if one were to fire real rays downward recursively, only a small portion would be bent upwards, as shown by the relatively small interference pattern in Fig. 6.7 and multiplicity region. In other words, continuity of the ray firing parameters would see a discontinuity in the ray position, e.g., $\mu \geq \mu_{critical}$ hits the upper half-plane, $\mu < \mu_{critical}$ hits the lower half-plane. It is precisely this mechanism that leads to the disappearance of the saddle in Fig. 6.2 and the existence of θ_d in Fig. 6.7.

The Green's function field in Fig. 6.7 shows a second, previously undiscovered caustic (in this solution): the cusp caustic. Immediately, this singularity has implications for the noise content propagated against the flow as the location is clearly not in the forward arc. Though this is new, it is only really significant if the magnitude of the cusp is comparable to that of the fold. The rays culpable for this caustic are shown in Fig. 6.9 in the nearfield, off of the cusp's line of symmetry. The real triplet solutions are again

[6] All ray trajectories in this thesis are shown in the nearfield for illustrative purposes.

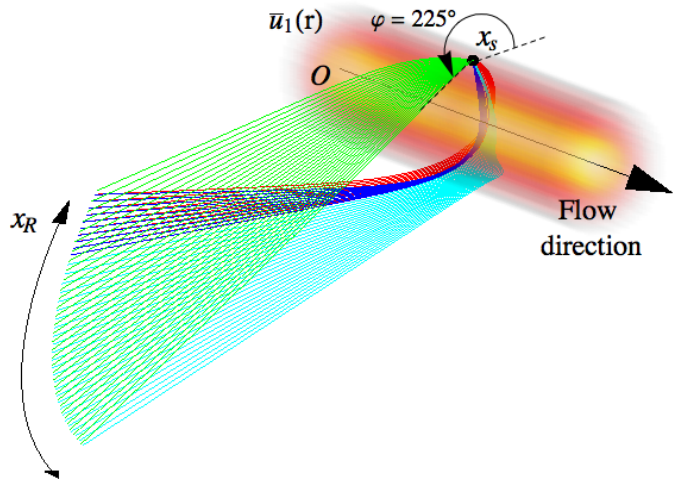

FIGURE 6.9: Interfering ray triplet forming cusp caustic (nearfield comp.) off symmetry line, $\varphi = 225°$. Real rays: red (sing.), green, blue (sing.). Complex ray, cyan. Ray paths correspond to $\mathrm{Re}(\boldsymbol{x}(\varsigma))$.

shown in Fig. 6.10 in the yz-plane with corresponding Poisson indices. From Fig. 6.9 we see that those solutions that blow up on the cusp favour the same path around the jet w.r.t. the origin, and that all these singular paths head to the rear arc. This former observation is corroborated by the bifurcation diagrams in Fig. 6.10, which also show that singular rays have the same Poisson index. On the symmetry line the interpretation of the Poisson indices is slightly more subtle. Here, one solution corresponds to $\nu_\star = 0, \forall\theta$, so the Poisson index is in fact arbitrary and may have solution $m_\star \in \mathbb{Z}$. This has implications for the sheet structure, as $\nu_\star = 0$ hangs around on the union of all the Poisson sheets.

Of the three rays that coalesce on the cusp, only one of these rays experiences the fold caustic in the forward arc. This same ray also experiences the anti-caustic located between the CDPs. This ray on the "dark" side of the cusp does not correspond to the same branches on the "light" side of the cusp as can be seen in Figs. 6.10, where the continuous branches off the line of symmetry, i.e., Figs. 6.10(d) and 6.10(f) do have the same Poisson index.

To conclude this study of the cusp it is worthwhile returning to the concept of upstream energy propagation. In particular we can consider the near-to-farfield behaviour of the cusp surface. This is shown in Fig. 6.11 where the cusp surface is detached from the source point $\boldsymbol{x}_R$ and is directed upstream in a conic/heartshape. The former observation is important for two reasons. First, the absence of the cusp caustic in the vicinity of the source allows the source to be locally Helmholtz so that §3.3.1, Chap. 3 remains valid. Secondly, it is possible that the caustic surface is a continuation of a caustic due to the tangency of trapped rays as they propagate upstream, as in this region the flow behaves

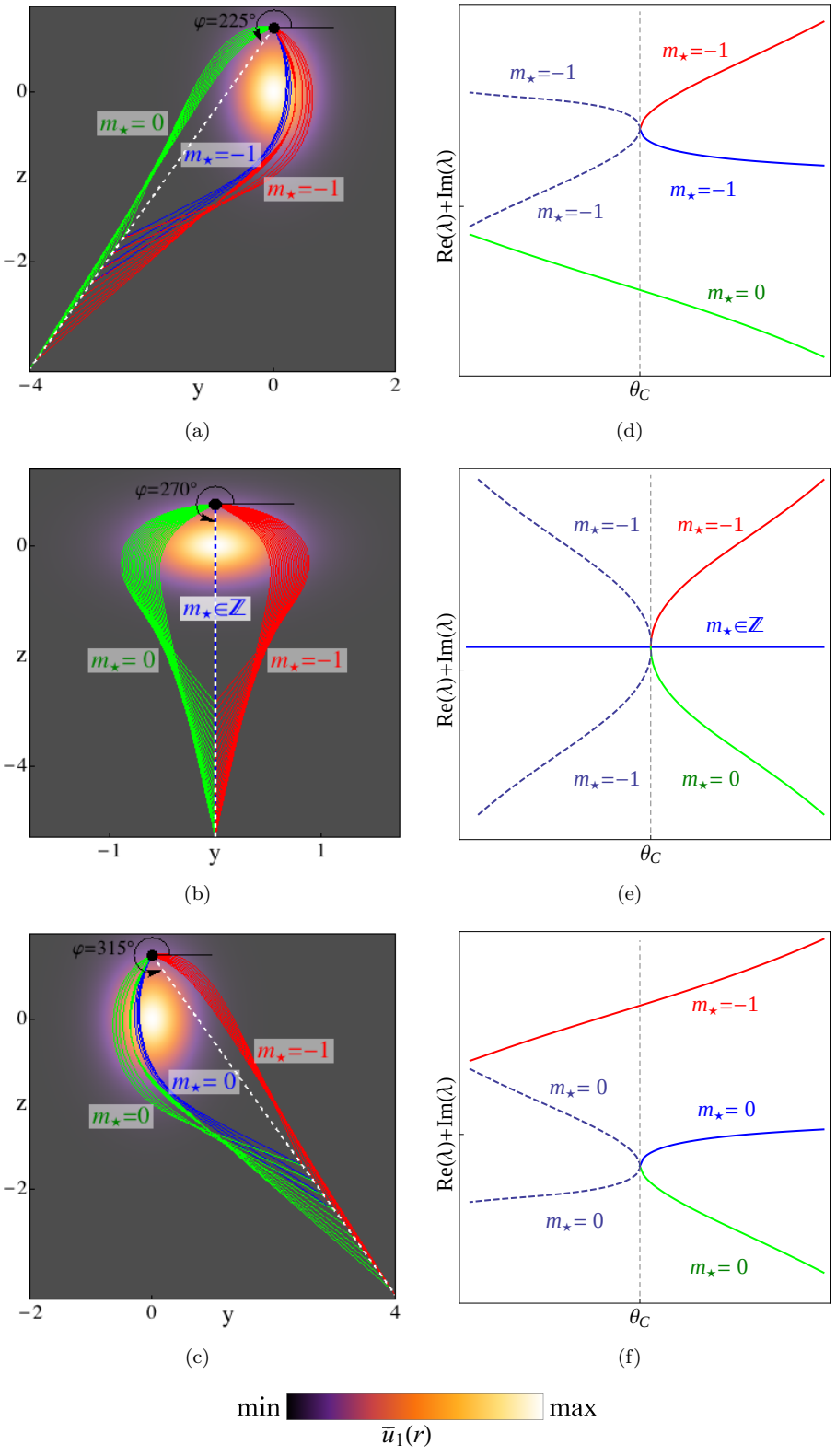

FIGURE 6.10: Cusp real ray paths in the yz-plane with corresponding λ bifurcation diagram and Poisson indices. Figures (a)-(c) ray paths for $\varphi = 225°, 270°, 315°$, resp. Jet flow cross-section in background. Figures (d)-(f) λ-bifurcation diagram in θ for $\varphi = 225°, 270°, 315°$, resp. Real branches solid line, complex branches dashed.

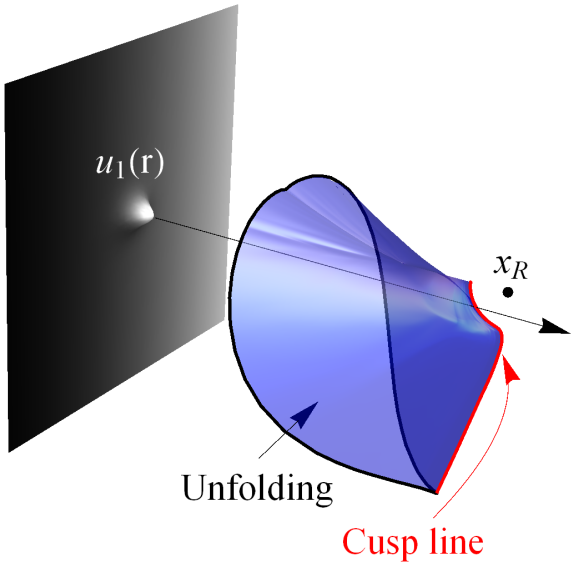

FIGURE 6.11: Near-to-farfield cusp surface. Figure shows unfolding of the cusp line (red) on $\Delta\varphi = 180°$ into a fold surface (blue). Flow profile $u_1(r)$ in background.

as a waveguide. These rays we have payed little attention to due to the likelihood that such rays do not contribute in the far-field, not to mention that they are much difficult to determine using the BVP as there are numerous solutions.

Though this surface is novel in the context of point source solutions in a free jet, such upstream beaming has been found before by Abrahams et al. [28] in shear flows bounded by elastic surfaces. Therein, a moving point source by a wall engenders both fold and cusp caustics, the latter of which beams upstream. The difference here is that reflections from the wall in 2D allow the field to have multiplicities, i.e., direct rays from the source and reflected rays from the wall, whereas the jet shear layer allows multiplicities by offering other routes to an observer in 3D. This work, more so than [28] shows the importance of upstream beaming when the refracting medium has a waveguide.

To conclude, we expect two distinct sets of singularities in the point source acoustic field, and these can be handled separately using the canonical functions machinery of Chap. 5. However, we have not yet described the effect on the magnitude of the field of the anti-caustic. It is readily seen that this structure limits the oscillation of the fold caustic and that it partially delimits the CoS. As the name may suggest the following computations show that it engenders unusual behaviour in the qualitative and quantitative behaviour of the ray firing parameters and acoustic field.

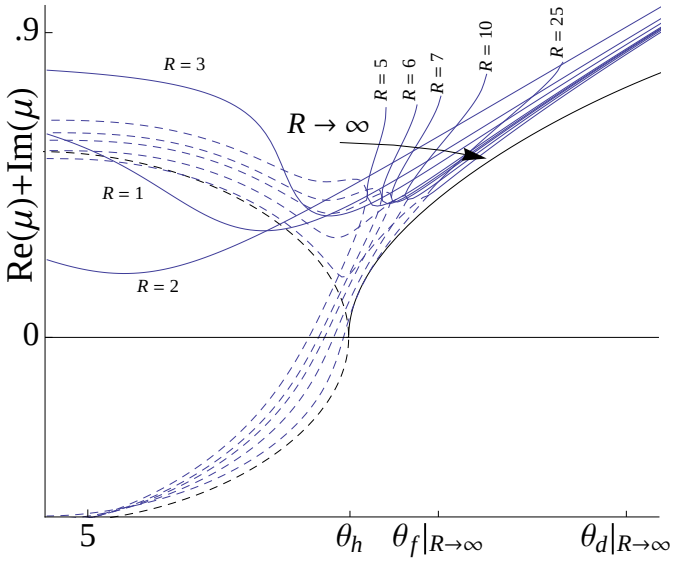

FIGURE 6.12: μ-firing parameter as a function of θ & R with $\Delta\varphi$ fixed. Black line, analytic sol. Blue lines, ray tracing sol. Solid, real; dashed, complex. θ_h, hysteresis/jump. θ_f, fold caustic. θ_d, disappearance point.

6.3.1 Ray parameters

The first check of the ray solver's accuracy is a comparison with the analytic ray firing parameters given by (6.36) and (6.37). To do this the behaviour of the ray parameters $\tilde{\mu} = \{\mu, \lambda\}$ is studied against θ for several different radii R about the source. As discussed before, the analytical WK solution is based at the origin in the far-field. This $\tilde{\mu}$-study based on the source should tend towards the WK result as $R \to \infty$ (which we effect with $R = 200$), i.e., $\Gamma^B_{\tilde{\mu}}\Big|_{R\to\infty} \sim \Gamma^{B,WK}_{\tilde{\mu}}$, as shown by (2.3). The first set of bifurcation curves to examine are those pertaining to μ, and are shown in Fig. 6.12. As usual rather than looking at Γ^B_μ we can look at $\mathrm{Re}(\Gamma^B_\mu) + \mathrm{Im}(\Gamma^B_\mu)$. From now on we will refer to these bifurcation paths by their ray parameter name.

Figure 6.12 shows several interesting features: however, the most important is that these ray bifurcation paths do indeed tend to the far-field solutions given by WK. We can see that of the two real branches one of the real branches disappears in the same way a branch of the saddles disappears, and that this is coincident with the anti-caustic θ_d. Though only the far-field θ_d is marked, Fig. 6.12 shows that the anti-caustic propagates into, and therefore exists, in the near-field. The real branches also show that they become less distinguished as $R \to \infty$, effectively collapsing onto one another. This resolves the issue of the analytic solution (6.36), as this only gives one real solution in the far-field. Additionally, the complex branches emanating out of the fold bifurcation

are also squashed together when R is large. Their imaginary part is vanishing as $R \to \infty$. Upon reaching a certain θ dependent on R, they spread out from each other rapidly as if they had experienced the fold bifurcation itself. As the WK solution is approached, this particular points tends to θ_h: the angle in θ invariant with φ that q_s goes complex. For the source and flow configuration shown Fig. 6.7 this line is $\theta \approx 31°$. This is also coincident with the branch points going complex in (6.20) and Figs. 6.1, 6.2, and 6.3. Hence the analytic solution as shown in Fig. 6.12 has an apparent real solution that stretches into the CoS in the far-field.

The final feature of note in Fig. 6.12 is the disappearance of the fold caustic as $R \to 0$. This phenomenon, appearing in all $\boldsymbol{\varsigma}$, is intimately related to θ_d. The general behaviour of this disappearance is that θ_f and θ_d eventually join up so that there is no bifurcation as $R \to 0$. Thus, for small R the real branches are continuous and there is no silent region. This is in fact an extremely important result, and one which is necessary in order for the near source matching of (3.34), Chap. 3. The assumption in this matching procedure is that under the variable ζ, the acoustic field is locally Helmholtz. It is clear that the anti-caustic θ_d is then a necessary requirement for locally Helmholtz fields in this solution as it kills off the fold.

The effects of θ_h and the anti-caustic are not limited to the μ-bifurcation set. This fact should be apparent for θ_d, but not necessarily θ_h. In fact the moniker θ_h for this phenomenon is derived from peculiar behaviour in λ not μ. Interestingly, the phenomenon associated with θ_h is restricted to just $\tilde{\mu}$ and not τ. For the jet under consideration τ behaves like $O(R)$ even for complex rays. This behaviour can be deduced from (6.1) and can be found in [116]. A physical explanation is that rays whether complex or real spend little time in the jet, so integration time is dominated by their propagation in a homogeneous field outside of the jet. Other than this, there is little noteworthy behaviour in τ except for the fold and cusp bifurcations expected.

The λ-bifurcation set is shown in Figs. 6.13 and 6.14, where in order to demonstrate the effect of θ_h the complex components of λ in the CoS have been split up into real and imaginary parts. In the first of these figures many of the features of the μ-diagram can be seen: namely, the fold caustic and disappearance of the real branch; the gradual engulfing of the fold and disappearance of complex rays by θ_d as $R \to 0$. Additional information about the exact point of the λ disappearance in the far-field is given by the saddle analysis which loses its second real branch when $\nu_\star = 0$. Inverting this using (6.37) yields $\lambda - \varphi_s = \pi$. However, approaching the near-field the second branch does not disappear at this point. This suggests that a near-field analysis does not provide the simple conditions afforded to the far-field.

The real ray behaviour is as expected, but it is the complex solutions that contain the contain the interesting and exotic features. The complex part of the analytical solution

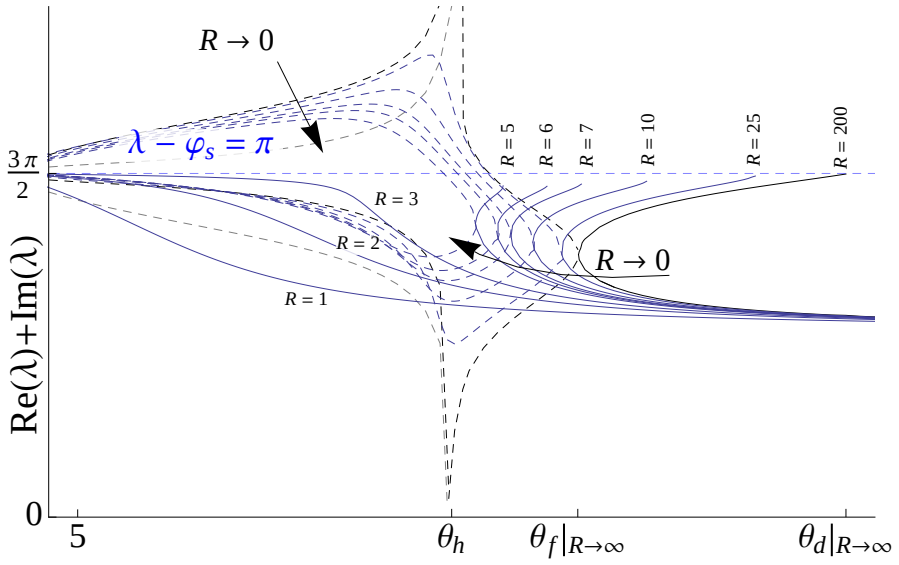

FIGURE 6.13: λ-firing parameter as a function of θ & R, φ fixed. Black line, analytic sol. Blue lines, ray tracing sol. Solid, real; dashed, complex. Grey dashed, same branch sol.

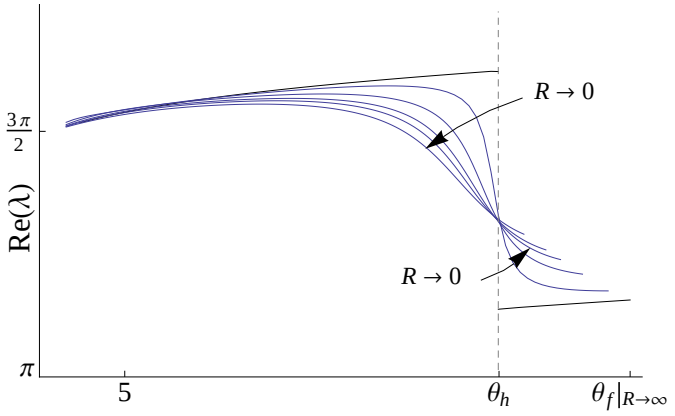

(a) $\mathrm{Re}(\lambda)$

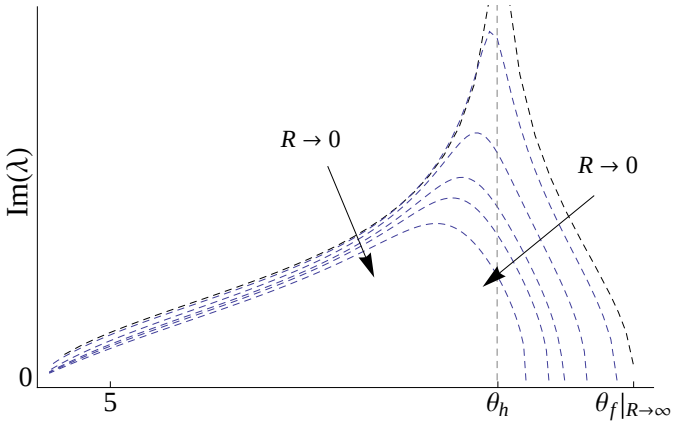

(b) $\mathrm{Im}(\lambda) > 0$

FIGURE 6.14: $\mathrm{Re}(\lambda)$ & $\mathrm{Im}(\lambda)$ components and the effect of θ_h as a function of R.

shows the discontinuity that we expected from q_s jumping into the complex plane as θ is decreased. Although the saddle $\nu_\star$ is continuous from (6.37), this can only be so if there is a discontinuity in λ to counter that in q_s. As R is decreased this discontinuity is softened though the change in ray parameters is still rapid for moderate values of R. The continuation of the solution across the discontinuity is not obvious from (6.37); thus only the tracing solution can provide the answer to this conundrum. In Fig. 6.13 we have also plotted the complex solution (grey dashed) obtained if one continues the solution using the same branch. This is clearly the wrong solution.

Though we have resolved the issue of calculating across the discontinuity, dressing up the complex solutions using $\mathrm{Re}(\lambda) + \mathrm{Im}(\lambda)$ covers up the true behaviour of the complex solutions. Examination of $\mathrm{Re}(\lambda)$ and $\mathrm{Im}(\lambda)$ can be undertaken by utilising the path formulation of Chap. 5. Figures 6.14(a) and 6.14(b) show these respective components for various $R \geq 5$. It is clear that both components do not share the same bifurcation and that a jump discontinuity is present in the real part; the imaginary part is continuous but appears non-differentiable in the far-field limit. The jump in the real part leads to the skewness of the complex solutions in Fig. 6.13 and is an artifact of the choice of branches when crossing the discontinuity. Other (incorrect) branches can lead to continuity in the real part and discontinuity in the imaginary part.

The path formulation allows us to consider the the bifurcations as resulting from curves on multi-valued surfaces. In particular in Chap. 5 it was claimed that paths on the cusp surface were all that were needed to describe the bifurcations that occurred in the parallel shear flow model. Already, it is clear that the fold and pitchfork bifurcations result from this (compare Fig. 6.10, with paths on Fig. 5.3). But it is not immediately clear what bifurcations $\mathrm{Re}(\lambda)$ and $\mathrm{Im}(\lambda)$ undergo. In the aforementioned cases the firing variable λ was treated as a variable on the cusp surface; allowing complex continuation led to complex rays. Now, though, the components $\mathrm{Re}(\lambda)$ and $\mathrm{Im}(\lambda)$ must be treated as variables on the cusp surface taking separate paths. This is where the hysteresis and winged cusp bifurcations of (5.21) and (5.22) come in. In general these bifurcations can cut the singularity structure of the cusp (at least in the case of the winged cusp) but in this instance the far-field solution only scrapes the cusp point $\xi = \mathbf{0}$.

If we take the path mapping in both of these cases, it is straightforward to observe that $\mathrm{Re}(\lambda)$ behaves according to a hysteresis bifurcation where the real part jumps to other real solutions discontinuously, namely because we do not allow it to have complex solutions. The problem with the hysteresis moniker here is that if one passes over the jump then and retraces ones steps, the same values across the jump should be found. The jump should also always be at θ_h, independent of which direction in θ one approaches.

To examine this behaviour we have plotted a hysteresis loop using the hysteresis bifurcation (5.21) in Fig. 6.15 and depicted the two jump conventions: the delay convention,

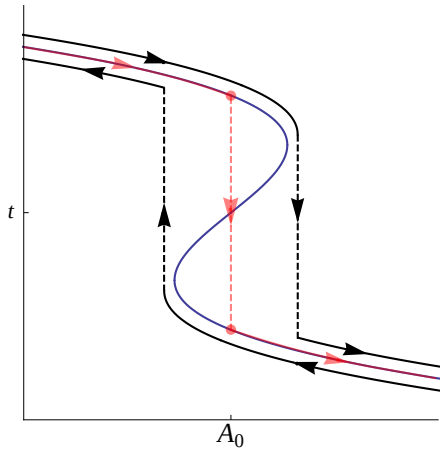

FIGURE 6.15: Hysteresis loop with delay and Maxwell conventions, $A_1 < 0$. Blue curve, hysteresis loop. Black line, delay convention. Red line, Maxwell convention.

and the Maxwell convention (see for e.g., Gilmore [111]). In the case of the first, the jumps are clearly at different points and the path is irreversible (this leads to the hysteresis phenomenon) by the fact that the path to the top solution is not the same as the inverse. In fact the bifurcation set/jumps are coincident with the cusp singularity sets. In the Maxwell convention the jump is on the symmetry line: it is also reversible. This latter convention will be adopted although further mathematics should be explored to justify this [111].

Examining Fig. 6.14(a) in the near-field we see that the jump in the solution is immediately smoothed for finite values of R, and that the smoothing is continual as R decreases. In terms of the universal form of the hysteresis this means the auxiliary parameters that are kept constant for a particular path are a function of R. The far-field limit $R \to \infty$ has $A_1 < 0$ in (5.21), but as soon as R takes on finite values the path jumps to $A_1 > 0$ where the hysteresis loop is smoothed out. Taking $R \to 0$ leads to $A_1 \to \infty$ giving the required smoothing.

The imaginary curve shown in Fig. 6.14(b) behaves according to a cross-section of values of the winged cusp. There maybe other bifurcations for which the behaviour in Fig. 6.14(b) can be mapped to. The winged cusp, however, illustrates an interesting aspect of the path formulation. It can be seen that this bifurcation is actually of codimension 3 (see [151]) whereas the cusp surface is only codim = 2. A suitable choice of auxiliary parameters for the far-field bifurcation is the control set $\Lambda^c = \mathbf{0}$, so that the farfield solution behaves as the germ of the bifurcation itself, i.e., $t^3 + \Lambda_{\text{ctl}}^2$, giving $t = -\Lambda_{\text{ctl}}^{2/3}$. As the near-field is approached the germ is perturbed. Here, we will not identify the exact mapping required, but will demonstrate that smoothing of the germ similar to Fig. 6.14(b) can be achieved using a positive linear perturbation in Λ^c. In Fig. 6.16 we have done this using $\Lambda^c = \{\Lambda_1, \Lambda_1, \Lambda_1\}$. Though this is a particular instance of

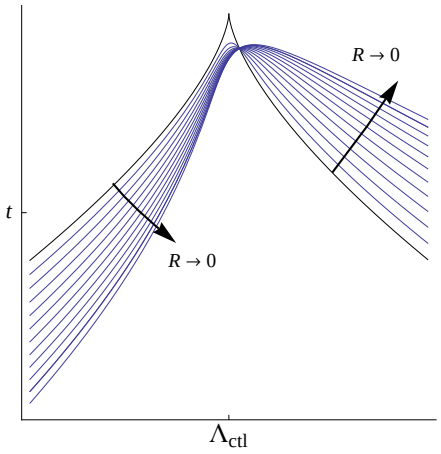

FIGURE 6.16: Smoothing a continuous but non-differentiable bifurcation using the winged cusp. Black line, $\Lambda^c = \mathbf{0}$. Blue lines, $\Lambda^c = \{\Lambda_1, \Lambda_1, \Lambda_1\}$.

the unfolding of the winged cusp, it is plausible that a more precise fix on the values of Λ^c could be achieved following through the LS methodology (i.e., solving another recognition problem).

6.3.2 Amplitude verification

In the previous section it was shown that we could match the analytic far-field ray firing parameter behaviour accurately and in the near-field limit some of the discontinuous behaviour found was smoothed. It was shown that for this flow & source configuration $R = 200$ is sufficiently large enough to match the analytic solution almost exactly. We only carried out this benchmark for the $m_\star = 0$ Poisson indices. The more interesting and telling demonstration of the solver is the amplitude verification in which all $m_\star$ are used that obey the selection conditions of Chap. 4. Unlike the previous section the solver will be based on the origin to provide the best match with the modal solution. Otherwise the solution is similar but slightly displaced due to phase discrepancies.

In Figure 6.17 constant φ cross-sections of the Green's function shown in Fig. 6.7 are judiciously chosen to illustrate all of the phenomena found therein. The calculations shown use the same parameters as before, i.e., $St = 5$, $M_J = 0.9$, $r_s = 0.75$. Considering the amplitude first, it is clear to see that a cross-section cutting a caustic leads to a singularity at that point with a marked divergence in a vicinity about that point. In all cross-sctions, encounters with a caustic are at a point only, though it is conceivable that a more general receiver curve could cut along a caustic. Notably, these same points do not engender a singularity, or divergence for that matter, in the phase of the solution. The worst case scenario for the phase is a small jump that occurs because the phase has an integrable singularity at a caustic (see Hayes [144]).

Aside from the divergences at the caustics - which is typical of these singularities - the field offers an excellent match. This is particularly notable in the CoS which is exclusive to complex solutions. In fact we will see that these solutions are even better once the field is amended for divergence. This is encouraging since the use of complex rays in this problem is novel and elsewhere in the problem complex rays add smoothing but do not dominate the field: thus checking the accuracy where quadrature of the ray tracing equations is more difficult, is important.

Additionally, the presence of Stokes lines emanating from the cusp leads to regions (see Fig. 6.7) where the cusp complex rays do not contribute. If these are included without knowledge of the Stokes structure, then this of course leads to a poor match. This also leads us to question the inclusion mechanisms behind the anti-Stokes crossing. As is well known the anti-Stokes changes the dominancy of two rays. It is unusual to have an anti-Stokes line cut into real observer space, however given that this is the case we must work out how to deal with it. Firstly, this phenomenon occurs to the two complex rays that coalesce at the fold caustic and they can be continued around the fold caustic outside of the cone of silence. The anti-Stokes line is a continuation of that experienced by the same rays if taken about the fold caustic in complex θ-space. The problem is resolved via backwards induction. The field contribution is best described by using the subdominant solution either side of the anti-Stokes line: thus we infer that a branch cut ordinarily used to continue solutions around folds analytically must be coincident with the anti-Stokes line. Knowing that these complex rays can be continued outside of the CoS in this manner is beneficial to resolving the disappearing branches.

There is one last structure to examine in the context of ray amplitudes: the anti-caustic or ray disappearance line. Across this line we lose one real solution, and at this point there is no continuation so the disappearance is discontinuous and appears to break ray conservation. When the observer curve cuts the fold caustic as in Figs. 6.17(a), 6.17(b), 6.17(c) and 6.17(d) the disappearance is minimal, with an abrupt change in the amplitude the significant defect. In the case of amplitude this is partly due to the high-frequency chosen: lower frequencies would show a larger disparity. In the two cases discussed, the disappearance is supported by a real ray contribution. In the two cases shown in Figs. 6.17(e), 6.17(f), 6.17(g) and 6.17(h) the disappearance line delimits the CoS and the background contribution is from complex rays that would otherwise have coalesced at the fold caustic. Thus, in these figures there is significant phase disparity due to the disappearance. The amplitude of the field across the disappearance line is small, this is part of why the future moniker anti-caustic is used.

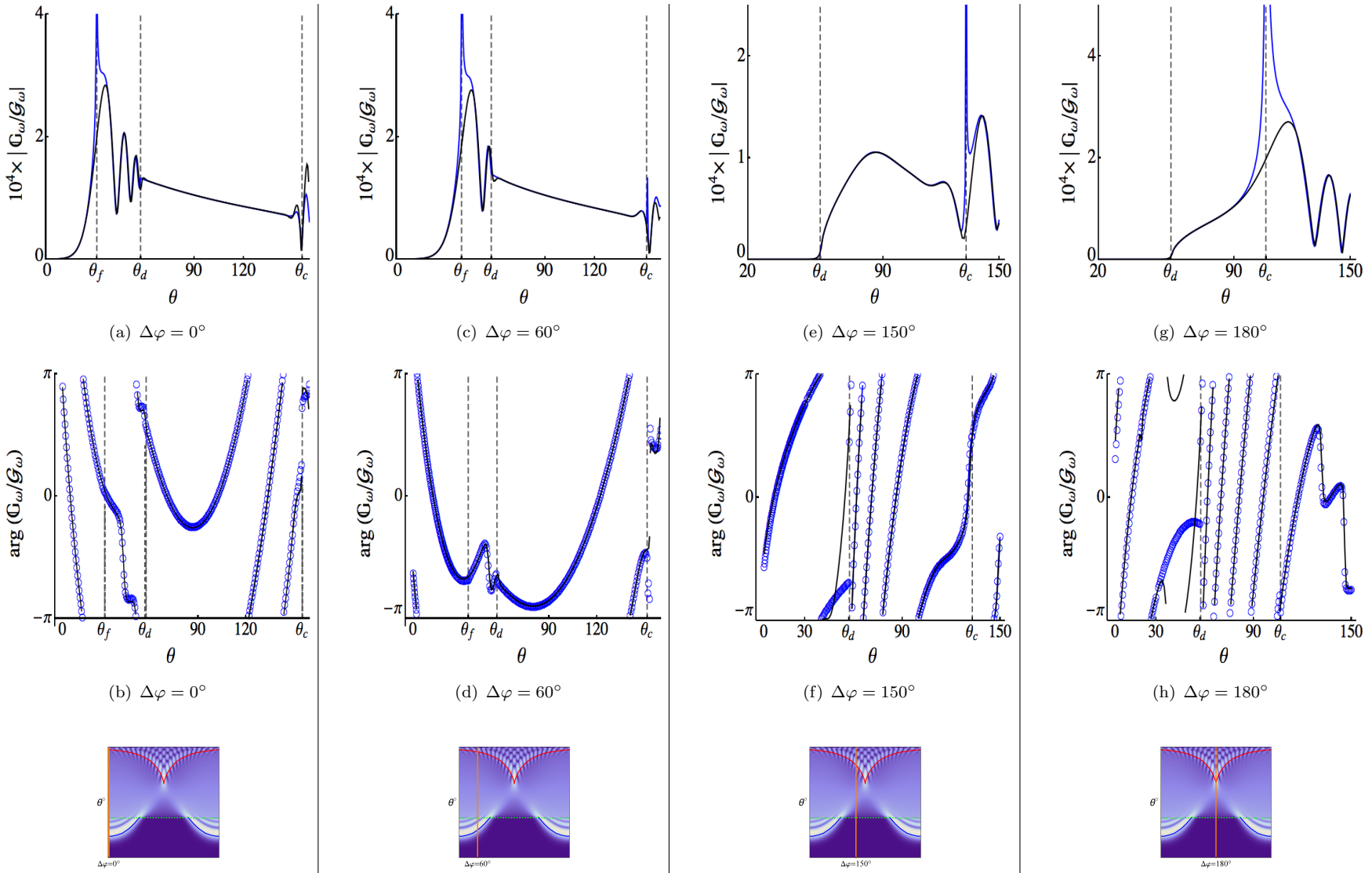

FIGURE 6.17: Ray calculations for $\mathbb{G}_\omega/\mathscr{G}_\omega$ for $\Delta\varphi = 0°, 60°, 150°$, and $180°$ with $r_s = 0.75$, $M_J = 0.9$, $k_0 = 28.7$. Figures (a, c, e, g) show $10^4 \times |\mathbb{G}_\omega/\mathscr{G}_\omega|$. Figures (b, d, f, h) show $\arg(\mathbb{G}_\omega/\mathscr{G}_\omega)$. Blue lines and symbols, ray calculation. Black line, high-frequency modal sol. θ_c and θ_f denote cusp and fold caustics.

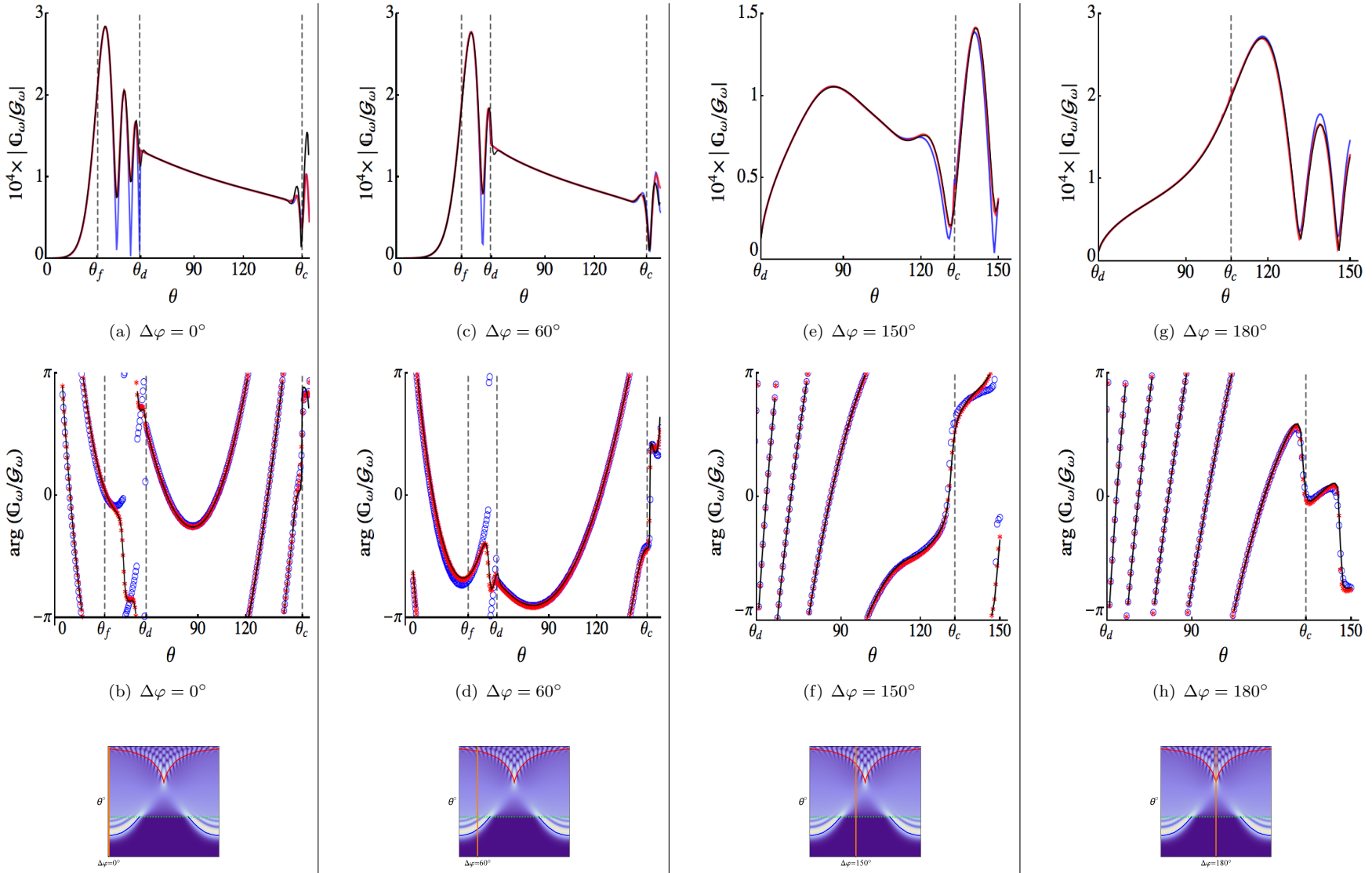

(a) $\Delta\varphi = 0°$ (c) $\Delta\varphi = 60°$ (e) $\Delta\varphi = 150°$ (g) $\Delta\varphi = 180°$

(b) $\Delta\varphi = 0°$ (d) $\Delta\varphi = 60°$ (f) $\Delta\varphi = 150°$ (h) $\Delta\varphi = 180°$

FIGURE 6.18: Uniform calculations for $\mathbb{G}_\omega/\mathcal{G}_\omega$ for $\Delta\varphi = 0°, 60°, 150°$, and $180°$ with $r_s = 0.75$, $M_J = 0.9$, $k_0 = 28.7$. Figures (a, c, e, g) show $10^4 \times |\mathbb{G}_\omega/\mathcal{G}_\omega|$. Figures (b, d, f, h) show $\arg(\mathbb{G}_\omega/\mathcal{G}_\omega)$. Blue lines and symbols, 1-term calculation. Red lines and symbols, 2-term calculation. Black line, high-frequency modal sol. θ_c and θ_f denote cusp and fold caustics.

Before we study the anti-caustic phenomenon in more detail, we consider the uniform amplitudes solutions under the same flow/source configuration. These are shown in Fig. 6.18 using the same cross-sections as before. Here two uniform solutions are plotted using either a leading order (one-term) expansion or a two-term uniform expansion in the catastrophes Ψ_1 and Ψ_2. This corresponds to the $m = 0$ layer in (5.35) and (5.38).[7] The cusp uniform asymptotics should strictly contain 3 terms: however, the second coefficient is zero on the cusp's line of symmetry and other intersections can be modelled using a fold expansion given that they are sufficiently distance from the cusp point; hence the one/terms monikers are appropriate.

The uniform results show that the singularity at the caustic along with the divergence in the immediate vicinity is corrected by both uniform expansions. The largest discrepancy occurs as the single term expansion is evaluated with increasing distance from the fold caustic. This term begins to oscillate predicting erroneous zeros in the field as it is proportional to the Airy function with negative argument. The zeros also lead to poor phase predictions, engendering a rapid change in phase not experienced by the Green's function field. The two-term expansions incorporate a derivative term in Ψ_1 and Ψ_2 and thus the explanation for their increased validity can be derived by expanding $\Psi_K(\tilde{\xi})$ and its derivatives to leading order about all of the n_K contributing saddles using the saddle-point technique. In the following this is done for the cuspoids, though the same principal applies to the umbilics. The expansion gives,

$$\Psi_K(\tilde{\boldsymbol{\xi}}) \sim \sum_{n=1}^{n_K} \left(\frac{2\pi \mathrm{i}}{k_0 \Phi_K''(t_n^\star)}\right)^{1/2} \mathrm{e}^{\mathrm{i}k_0 \Phi_K(t_n^\star)}, \; -\mathrm{i}k_0^{\frac{k+1}{K+2}} \frac{\partial \Psi_K(\tilde{\boldsymbol{\xi}})}{\partial \tilde{\xi}_k} \sim \sum_{n=1}^{n_K} \left(\frac{2\pi \mathrm{i}}{k_0 \Phi_K''(t_n^\star)}\right)^{1/2} (t_n^\star)^k \mathrm{e}^{\mathrm{i}k_0 \Phi_K(t_n^\star)}, \tag{6.38}$$

where $'' \equiv \mathrm{d}^2/\mathrm{d}t^2$. Substitution into (5.35), taking only the $m = 0$ layer, and collecting all $t_n^\star$ terms together gives,

$$I \sim \sum_{n=1}^{n_K} \underbrace{\sum_{k=0}^{K} c_{k,0} \left(\Phi_K''(t_n^\star)\right)\right)^{-1/2} (t_n^\star)^k \mathrm{e}^{\mathrm{i}k_0(\Phi_K(t_n^\star)+A)}}_{A_0^{(n)} \mathrm{e}^{\mathrm{i}k_0 S^{(n)}}}, \tag{6.39}$$

which is in fact just another statement of the matrix system given in (5.51). Equation (6.39) demonstrates that far off-caustic we need to incorporate more than just the $k = 0$ term (proportional to Ψ_K) to match up with the ray field. Only in the region close to the caustic will the $k = 0$ term make a good approximation on its own. As θ moves closer to the caustic the coalescing saddle points $t_n^\star$ tend to zero, since if the correct Ψ_K is chosen, then at a caustic they are roots of $\Phi_K'(t_n^\star; \mathbf{0})$. This allows $k > 0$ terms in (6.39) to be neglected without diminishing accuracy.

[7] This index should not be confused with the Poisson index.

One can also conclude from (6.39) that expanding the uniform expansions for layers $m > 0$ would lead to an amplitude matching with higher order terms in the ray expansion given by (4.29).

In the vicinity of the caustics we have improved the match of the high-frequency solution: however, we would ideally like to write the whole solution in terms of one catastrophe function, rather than in terms of dealing with the fold and cusp separately. In fact this is more realisable than is at first apparent. For example, the hyperbolic umbilic shown in Fig. 5.2 has a fold and cusp structure when unfolded, whereas the Green's function (6.7) contains both these species in a similar manner.[8] The fundamental difference between the two is the action of the disappearance line or anti-caustic. Not only does this change the types of rays contributing to the field but it limits the range in which we can apply the catastrophes. These rely on ray conservation fundamentally. Though we will show that ray conservation can be met in the next section, the non-canonical nature and the changing of types cannot be observed in the canonical catastrophes, therefore there is not one that can be relied upon to provide global uniformity. The impact upon Fig. 6.18 is that disparities due to the disappearance θ_d still persist.

As a final note on the efficiency of the uniform mappings it is useful to compare an analytical solution to the fold mapping with the numerical iterative method. Given the discussion of the iterative method in Chap. 5 and its rapid convergence, we can compare with the analytical solution of the fold mapping shown in Appendix D. The latter is cumbersome, longwinded, and hindered by the nature of phase integrals (i.e., no closed-form sols.). Such a method cannot be implemented into a ray solver in general, and even this is for the simplest case. The analytical solution can be used as a benchmark, and it has been observed that the accuracy is the same as the numerical solution in all aspects of the computation.

6.4 The anti-caustic

In the previous section a new feature, the non-canonical disappearance line, was discovered in the off-axis parallel shear flow Green's function. This had the impact of washing out the fold caustic diffraction pattern and delimiting the Cone of Silence without singularity thus leading to the new moniker of anti-caustic. The absence of singularity was peculiar as the real ray disappearing branch at the anti-caustic appears to form half of a standard fold caustic, i.e., two real rays bifurcating into two complex rays.

[8] Other corank 2 catastrophes contain the same two species as well. This example is a matter of choice.

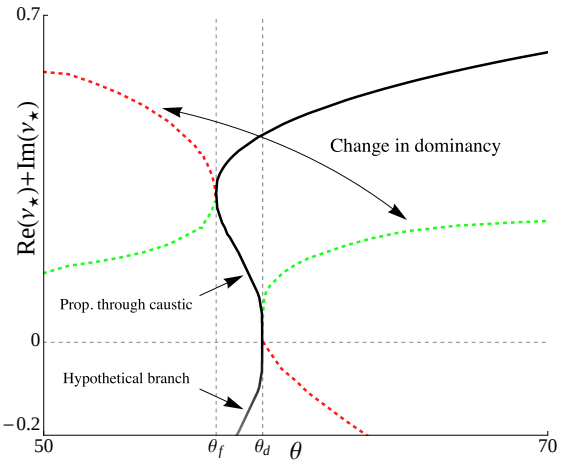

FIGURE 6.19: $\nu_\star$-bifurcation diagram at $\Delta\varphi = 8\pi/15$ with new complex branch. Green branches contribute. Hypothetical branch is mirror of calculated disappearing branch.

The current section investigates the disappearance further, first postulating the existence of the absent real ray and then locating the conjugate pair on the other side of the anti-caustic. The anti-caustic is then examined locally using the eucatastrophes derived in Appendix E.

6.4.1 Anti-caustics and non-canonical disappearances

When analysing the ray solutions of the parallel shear flow problem in §6.3.2 we saw a single non-canonical structure which we labelled as both a disappearance line and an anti-caustic. In the case of the former this was related to the discontinuities it engendered in the amplitude. In this section we shall resolve the issues of ray conservation across this line and describe why exactly this is an anti-caustic.

There are two critical steps in resolving the anti-caustic question. The first is a matter of ray conservation and its resolution is made possible by the continuation of complex rays outside of the CoS as discussed in §6.3.2. If these rays are continued out of the CoS across θ_d then they remain complex: no caustic is encountered. If these rays are continued back to θ_d for φ such that constant φ intersects the fold caustic then these rays appear to bifurcate from θ_d. We conclude that these form the complex branches of the missing rays. The reader may enquire as to why if this exponentially small solution is already known is the discontinuity in the ray results still apparent? The answer to this is that these solutions are notoriously difficult to continue far outside the CoS, though their existence is known.

To demonstrate the existence and contribution of these solutions, Figures 6.19 and 6.20 show the $\nu_\star$-bifurcation diagram and magnitude of the field for the $\Delta\varphi = 8\pi/15$ slice. This particular φ means the receiver curve is dangerously close to the CDP: however,

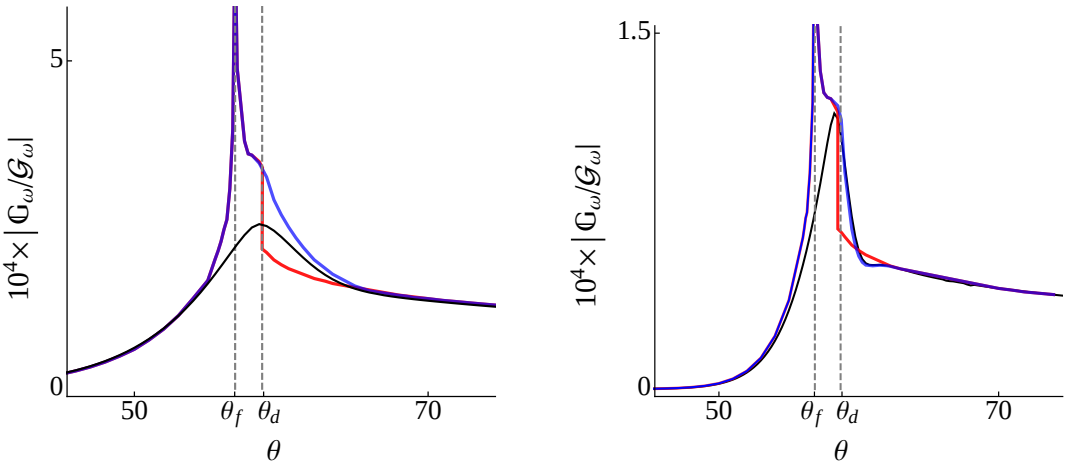

(a) $St = 5$, $k_0 = 28.7$ (b) $St = 15.9$, $k_0 = 90$

FIGURE 6.20: Comparison of new exponentially smooth field against discontinuous ray field. Black lines, modal solution. Red lines, discontinuous ray field. Blue lines, rays with exponential smoothing.

as mentioned above, this is perhaps one of the only regions we can currently calculate the rays. The bifurcation diagram shows the complex shedding that occurs at θ_d and illustrates the change in dominancy that results from the complex branch crossing the anti-Stokes line in Fig. 6.7. Figure 6.20 shows the effect of including the subdominant branch for two Strouhal numbers against the ray field without this branch. In the first of these, Fig. 6.20(a), the same wavenumber is used as in Fig. 6.17. Unfortunately, it is difficult to deduce whether this exponentially small wave is contributing because it is still experiencing divergence due to the close proximity of the fold caustic. Thus for large θ the exponential decay means both ray fields asymptote the modal field. However, from theory (see Chaps. 2 and 5) it is known that the singulant controls how localized the divergence is about the caustic: therefore we only need ramp up the frequency to witness a match as in Fig. 6.20(b). This shows that the "new" complex branch is indeed a contributor to the field.

Though it is satisfying to see the new branch contributes to the field and smooths the discontinuities seen in Fig. 6.17, there is still a missing ray contribution. Whereas before we where short of a ray for $\theta > \theta_d$, now we are short of a ray for $\theta < \theta_d$. Unfortunately, at this stage of the work with the Lilley equation we have not found this ray, though we believe it to exist possibly as an acausal branch (negative phase) or at least with $\nu_\star < 0$ as shown in Fig. 6.19, where it behaves locally as the negative reflection of the disappearing branch. We will include two of these rays to complete a local analysis of the CDP shown in Fig. 6.21. In other words, the coalescence of a real disappearing ray and a hypothetical ray is the putative mechanism to engender a complex conjugate pair. The reason we require two hypothetical rays about the CDP is due to the complex

shedding by different rays across θ_d either side of the CDP, i.e., at control points a_4 & a_8. Additionally, these rays are allowed to be complex and have their own caustic at the same control points as θ_f, though at this point the hypothetical rays are forced to cross back (on the crossover line) to the hypothetical sheet by the action of dot-dashed line (see control point a_{10}). This is supposedly before control point a_1 where both solutions begin to diverge as the caustic is approached on the rays' respective sheets.

Both occurrences of the complex shedding are without singularity, leading us to conclude that the mechanism for all θ_d sufficiently far from the CDP is the same. Though we have shown the existence and necessity of the branch crossing θ_d for $\Delta\varphi < \Delta\varphi_{\text{CDP}}$ we currently cannot do so for for $\Delta\varphi > \Delta\varphi_{\text{CDP}}$ as continuation of complex rays is not sufficient to create a bifurcation diagram. Thus the crossover line and the hypothetical caustic remain hypothetical until further progress is made with this solution. One explanation for the difficulty continuing rays is that there is also a singularity there meaning that θ_d is governed locally by a new form that differs from Thom's catastrophes.

A final note on the CDP diagram is that the Stokes line shown passing through the CDP is not integral to the local analysis as far as we know. However, its presence through the CDP may not be coincidence and may suggest that there *is* a global form that we can map the whole field to, though this form will not be in the catastrophe set.

6.4.2 Anti-caustics

The contribution of the new ray branches has been shown to improve the field by smoothing of the discontinuity at θ_d. However, the bifurcation is not typical of canonical functions. The ray behaviour across θ_d in Fig. 6.17(f) approaching from $\theta < \theta_d$ depicts a ray contribution whose amplitude dive-bombs into a vanishing value. This can be understood by studying the analytic ray solution, particularly the derivative of the saddle condition (6.29) when re-written as,

$$\frac{\partial\psi_{WK}}{\partial\nu_\star} = \frac{\psi_{WK}(\nu_\star)}{\nu_\star} + 2\nu_\star^2\left(\int_{r_\delta}^{\infty} \mp \int_{r_\delta}^{r_s}\right)\frac{\mathscr{P}'(r)}{rQ(r|\nu_\star)}\mathrm{d}r \pm \frac{2\nu_\star^2\mathscr{P}(r_s)}{r_sQ(r_s|\nu_\star)}. \tag{6.40}$$

In the far-field the anti-caustic is characterised by $\nu_\star = 0$ for any rays that disappear there. Clearly, the limit $\nu_\star \to 0$ in (6.40) is singular as $\partial\psi_{WK}/\partial\nu_\star \sim \alpha_{m_\star}/\nu_\star$, which is infinite as $\psi_{WK}(\nu_\star) = \alpha_{m_\star}$, the saddle condition, is still satisfied.

Whatever the mechanism, it is a relief to find there is no singularity in the amplitude. As we have not identified a bounded canonical form at this stage there would be no way to correct a singularity if it were present. Additionally, the agreement previously seen of the vanishing amplitude, suggests that whatever form governs θ_d, it is correct for it to vanish close to θ_d thus mirroring its ray expansion. This is contrary to the behaviour of catastrophes seen before.

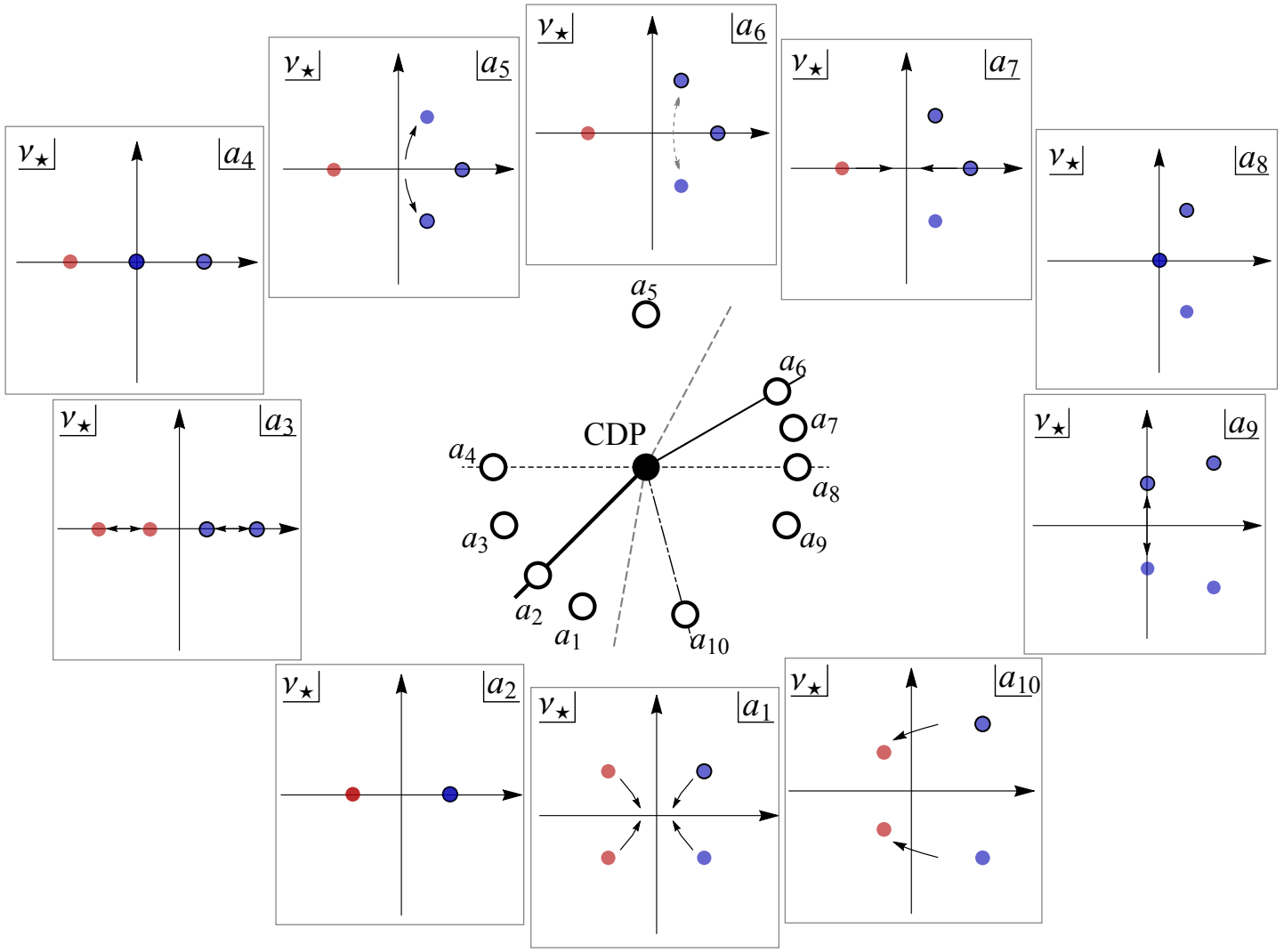

FIGURE 6.21: Local analysis about the CDP using rays that coalesce on θ_f and disappear on θ_d. a_n, local test points. Blue points, calculate rays. Red points, hypothetical rays. Encircled point, contributing ray. Solid thick line, fold caustic. Solid thin line, anti-Stokes line. Black dashed, θ_d. Grey dashed, Stokes line from cusp. Dot-dashed, putative crossover line.

Equation (6.40) shows that the ray amplitude vanishes as $\nu_\star \to 0$, and in fact all further derivatives of ψ_{WK} also vanish on this line, as higher derivatives of ψ_{WK} can be expressed as a mixture of lower derivatives and ψ_{WK} itself, for e.g., (D.28). Consequently, the *entire* ray expansion vanishes to all orders in k_0.

6.4.2.1 Local analysis of WKB solutions

In this section a local analysis is performed on the radial Green's function $v_1(r)$ and $v_2(r_s)$ of (2.70), Chap. 2 used to build the modal solution. The aim here is by doing this we can express the ray expansions in terms of the eucatastrophes $\mathscr{E}_K$. These functions are similar to the cuspoid diffraction catastrophes of Chap. 5 but differ by the addition of a logarithm to the potential, i.e., $\Phi_K^{\mathscr{E}}(\boldsymbol{\xi}) = \Phi_K(\boldsymbol{\xi}\backslash\{\xi_0\}) + \xi_0 \log \nu$. These functions are analysed in more detail in Appendix E, but the key points are that for the same K classification, the eucatastrophe has one more saddle than the corresponding catastrophe, given sufficient distance from the surface $\xi_0 = 0$; and that as this surface is approached at least one saddle behaves as $\nu_\star \to 0$. The special property of these $\nu_\star \to 0$ saddles is that they are accompanied by a vanishing ray amplitude.

To start the local analysis we shall only analyse $v_2(r_s)$ with r_s small, and then study the full Green's function $v_1(r)v_2(r_s)$ by partitioning the phase. The local analysis is also initially restricted by approaching the anti-caustic via $\theta < \theta_d$, i.e., $\theta \nearrow \theta_d$. We will show that the local analysis fits in closely with the behaviour shown by the eucatastrophes and then consider the ray expansion on the anti-caustic and see if this agrees with the putative mechanism given at the beginning of this chapter.

Starting with the equation (see (2.70) with $\nu_\star = n/k_0$),

$$v'' + k_0^2 \left(q^2 - \frac{\nu_\star^2}{r^2} \right) v = 0, \tag{6.41}$$

which has a WKB solution of the form (integrating up to r_s),

$$v_2(r_s) \sim \left(q^2 - \frac{\nu_\star^2}{r_s^2} \right)^{-1/4} \exp\left(\pm \mathrm{i} k_0 \int_{r_\delta}^{r_s} \left(q^2 - \frac{\nu_\star^2}{r'^2} \right)^{1/2} \mathrm{d}r' \right), \tag{6.42}$$

then for r_s, r_δ small, consider a Taylor expansion of $q^2 = T_{a_{(2)}}(\theta) r^2$ so v satisfies,[9]

$$v'' + k_0^2 \left(T_{a_{(2)}} r^2 - \frac{\nu_\star^2}{r^2} \right) v = 0, \tag{6.43}$$

which is the same local structure governed by the turning-point case shown in Chap. 2 §2.2.1.2. From that section we know that the solution can be found in terms of Bessel

[9]Note that q^2 has vanishing first term of its Taylor expansion at θ_d, i.e., $q^2(r,\theta) = \cancelto{\approx 0}{T_{a_{(1)}}(\theta)} + T_{a_{(2)}}(\theta) r^2 + O(r^4)$, since $T_{a_{(1)}}(\theta_d) = 0$.

functions,[10]

$$v_2(r_s) = C_1(\nu_\star, k_0) r_s^{1/2} J_{\frac{1}{4}\sqrt{1+4k_0^2\nu_\star^2}}\left(\frac{1}{2}k_0 r_s^2\sqrt{T_{a_{(2)}}}\right) + C_2(\nu_\star, k_0) r_s^{1/2} J_{-\frac{1}{4}\sqrt{1+4k_0^2\nu_\star^2}}\left(\frac{1}{2}k_0 r_s^2\sqrt{T_{a_{(2)}}}\right), \tag{6.44}$$

where the constants C_1 and C_2 are chosen to match with the WKB expansion. The constants chosen will depend on how we expand (6.44), i.e., with $k_0\nu_\star$ either small or large, as this affects the linear independence of the solutions in those limits. Dealing with the case that $\nu_\star$ is small but not zero and $k_0\nu_\star \gg 1$, then the WKB expansions of (6.43) are found to be,

$$v_2(r_s) \sim \frac{r_s^{1/2}}{\left(T_{a_{(2)}} r_s^4 - \nu_\star^2\right)^{1/4}} \exp\left\{\pm \mathrm{i} k_0 \left(\frac{1}{2}\sqrt{T_{a_{(2)}} r_s^4 - \nu_\star^2} + \frac{1}{2}\nu_\star \tan^{-1}\left(\frac{\nu_\star}{\sqrt{T_{a_{(2)}} r_s^4 - \nu_\star^2}}\right) - \nu_\star \frac{\pi}{4}\right)\right\}, \tag{6.45}$$

where,

$$\int_{r_\delta}^{r_s} \left(T_{a_{(2)}} r'^2 - \frac{\nu_\star^2}{r'^2}\right)^{1/2} \mathrm{d}r' = \frac{1}{2}\left(\sqrt{T_{a_{(2)}} r_s^4 - \nu_\star^2} + \nu_\star \tan^{-1}\left(\frac{\nu_\star}{\sqrt{T_{a_{(2)}} r_s^4 - \nu_\star^2}}\right)\right) - \nu_\star \frac{\pi}{4}, \tag{6.46}$$

has been used. Then using the relation,

$$\begin{aligned} \arccos\left(\frac{\nu_\star}{r_s^2\sqrt{A_2}}\right) &= \arctan\left(\frac{\sqrt{A_2 r_s^4 - \nu_\star^2}}{\nu_\star}\right) \\ &= \frac{\pi}{2} - \arctan\left(\frac{\nu_\star}{\sqrt{A_2 r_s^4 - \nu_\star^2}}\right), \end{aligned} \tag{6.47}$$

the phase (6.46) can be re-written with,

$$\begin{aligned} &\frac{1}{2}\left(\sqrt{T_{a_{(2)}} r_s^4 - \nu_\star^2} - \nu_\star \arctan\left(\frac{\sqrt{T_{a_{(2)}} r_s^4 - \nu_\star^2}}{\nu_\star}\right)\right) = \\ &\frac{1}{2}\left(\sqrt{T_{a_{(2)}} r_s^4 - \nu_\star^2} - \nu_\star \arccos\left(\frac{\nu_\star}{r_s^2\sqrt{T_{a_{(2)}}}}\right)\right). \end{aligned} \tag{6.48}$$

[10]The solution in that case could not be solved in terms of Bessel functions due to a bounded condition for zero argument.

Now if one uses the large k_0 expansion of the Bessel function from (6.44) where $\nu_\star < r_s^2\sqrt{T_{a_{(2)}}}$, then,

$$J_{\frac{1}{2}k_0\nu_\star}\left(\frac{1}{2}k_0r_s^2\sqrt{T_{a_{(2)}}}\right) \sim \sqrt{\frac{2}{\pi k_0}}\frac{\cos\left(k_0\sqrt{\frac{1}{4}r_s^4T_{a_{(2)}}-\frac{1}{4}\nu_\star^2}-k_0\frac{\nu_\star}{2}\arccos\left(\frac{\nu_\star}{r_s^2\sqrt{T_{a_{(2)}}}}\right)-\frac{\pi}{4}\right)}{(\frac{1}{4}r_s^4T_{a_{(2)}}-\frac{1}{4}\nu_\star^2)^{1/4}}, \tag{6.49}$$

since $\sqrt{1+4k_0^2\nu_\star^2} \sim 2k_0\nu_\star$ for $k_0\nu_\star \gg 1$. The expansion for $J_{-\frac{1}{2}k_0\nu_\star}\left(\frac{1}{2}k_0r_s^2\sqrt{T_{a_{(2)}}}\right)$ is exactly the same. Hence these two functions are not linearly independent under this approximation: immediately we set $C_2 = 0$. Then it is straightforward to show that $C_1 = \sqrt{\pi k_0}\mathrm{e}^{-\mathrm{i}\pi/4}$.

This solution gives us two branches as the Airy function before (see (2.79), Chap. 2): if one uses a uniform solution to $J_{\frac{1}{2}k_0\nu_\star}$ in terms of Airy functions, then this is the same as the Airy uniform solution to the WKB problem under the Taylor approximation in (6.43).

If $r_s^2\sqrt{T_{a_{(2)}}}$ becomes small such that $\nu_\star > r_s^2\sqrt{T_{a_{(2)}}}$, the expansion shown in Eq. (6.49) is not valid. The Bessel function begins to decay algebraically. If $\nu_\star \gg r_s^2\sqrt{T_{a_{(2)}}}$ the decaying behaviour is easy to witness,

$$J_{\frac{1}{2}k_0\nu_\star}\left(\frac{1}{2}k_0r_s^2\sqrt{T_{a_{(2)}}}\right) \sim \frac{1}{\sqrt{\pi k_0\nu_\star}}\left(\frac{1}{2}r_s^2\sqrt{T_{a_{(2)}}}\right)^{\frac{1}{2}k_0\nu_\star}\mathrm{e}^{\frac{1}{2}k_0(\nu_\star-\nu_\star\log(\nu_\star))}. \tag{6.50}$$

This explains the anti-caustic behaviour as the Bessel function has a zero that swells with increasing $k_0\nu_\star$, leading to a strong decay. Thus the small amplitude of the anti-caustic rays are due to strong algebraic decay as the order of the Bessel function is large but its argument is large but smaller. The exponential term of (6.50) is reminiscent of a eucatastrophe potential if one only considers the linear and logarithmic terms: the particular calculation would be $\{\xi_1, \xi_0\} \to \{-\xi_1, \xi_0\}$, then $\xi_1 = 1/2$ with $\xi_0 = \xi_1\nu_\star$. This also has amplitude proportional to $\sqrt{\nu_\star}$ if a Taylor expansion of $\left(\frac{1}{2}r_s^2\sqrt{T_{a_{(2)}}}\right)^{\frac{1}{2}k_0\nu_\star}$ is used, agreeing with the 2nd derivative of the exponent. Considering the peculiar case of $K = -1$ in the eucatastrophe set then this contains a single ray with vanishing amplitude.

When $k_0\nu_\star = O(1)$ or smaller then the approximation $\sqrt{1+4k_0^2\nu_\star^2} \sim 2k_0\nu_\star$ cannot be made. At the anti-caustic $\nu_\star = 0$, so substituting this value into (6.44) gives,

$$v_2(r_s) = C_1(\nu_\star, k_0)r_s^{1/2}J_{\frac{1}{4}}\left(\frac{1}{2}k_0r_s^2\sqrt{T_{a_{(2)}}}\right)+C_2(\nu_\star, k_0)r_s^{1/2}J_{-\frac{1}{4}}\left(\frac{1}{2}k_0r_s^2\sqrt{T_{a_{(2)}}}\right), \tag{6.51}$$

which gives two linearly independent solutions. For large argument the constants C_1 and C_2 can be determined again using the asymptotic expansions of the Bessel function

for large argument,

$$J_{\pm\frac{1}{4}}\left(\frac{1}{2}k_0 r_s^2\sqrt{T_{a_{(2)}}}\right) \sim \frac{2}{\sqrt{\pi}r_s T_{a_{(2)}}^{1/4}}\cos\left(\frac{1}{2}k_0 r_s^2\sqrt{T_{a_{(2)}}} - \pi/4\right), \tag{6.52}$$

and expressing the constants as $C_1 = -\mathrm{e}^{-\mathrm{i}\pi/8}\widetilde{C}_1$ and $C_2 = \mathrm{e}^{\mathrm{i}\pi/8}\widetilde{C}_2$, we can match with the single WKB branch given as,

$$v_2(r_s) \sim -\mathrm{i}r_s^{-1/2}T_{a_{(2)}}^{-1/4}\exp\left(+\mathrm{i}k_0\sqrt{T_{a_{(2)}}}r_s^2/2\right), \tag{6.53}$$

where we have remembered to include the $-\mathrm{i}$ factor due to this branch having been the reflected branch from the fold caustic.
Choosing the constants such that $\widetilde{C}_1 = \widetilde{C}_2$, it can then be shown that $\widetilde{C}_1 = \mathrm{e}^{-3\pi\mathrm{i}/4}\sqrt{\pi/2}$. Thus

$$v_2(r_s) \sim \sqrt{\frac{\pi}{2}}\mathrm{e}^{-3\pi\mathrm{i}/4}\left(\mathrm{e}^{\mathrm{i}\pi/8}r_s^{1/2}J_{-\frac{1}{4}}\left(\frac{1}{2}k_0 r_s^2\sqrt{T_{a_{(2)}}}\right) - \mathrm{e}^{-\mathrm{i}\pi/8}r_s^{1/2}J_{\frac{1}{4}}\left(\frac{1}{2}k_0 r_s^2\sqrt{T_{a_{(2)}}}\right)\right). \tag{6.54}$$

We can take this evaluation one step closer by identifying (6.54) as a special case of the catastrophe $\Psi_2(\xi_1, \xi_2)$, the Pearcey function. On its line of symmetry, $\xi_1 = 0$, the Pearcey function is soluble in terms of Bessel functions of the first kind, or a parabolic cylinder function. Both offer an interesting interpretation of the underlying mechanisms that occur at θ_d. Expressing (6.54) in terms of the Pearcey function leads to,

$$v_2(r_s) \sim \sqrt{\frac{2r_s}{\pi}}k_0^{-1/4}T_{a_{(2)}}^{-1/8}\mathrm{e}^{\mathrm{i}k_0 r_s^2\sqrt{T_{a_{(2)}}}/2}\mathrm{e}^{-3\pi\mathrm{i}/4}\Psi_2\left(0, \frac{1}{2}k_0 r_s^2\sqrt{T_{a_{(2)}}}\right). \tag{6.55}$$

Expressing (6.54) in terms of parabolic cylinder functions leads to,

$$v_2(r_s) \sim 2^{1/4}k_0^{1/4}T_{a_{(2)}}^{-1/8}\mathrm{e}^{-5\pi\mathrm{i}/8}D_{-1/2}\left(2^{1/2}\mathrm{e}^{-\pi\mathrm{i}/4}k_0^{1/2}r_s T_{a_{(2)}}^{1/4}\right). \tag{6.56}$$

Both of these solutions - which are equivalent - offer two different explanations to the behaviour on the anti-caustic. These are considered in the penultimate section of this chapter.

6.4.2.2 Partitioning of the phase

The analysis shown in this section can easily be generalised to incorporate the other element of the Green's function, $v_1(r)$. The local analysis above can be adapted to include $v_1(r)$ simply by considering the farfield WKB solution,

$$\begin{aligned} v_2(r_s)v_1(r) &\sim -\mathrm{i}Q^{-1/2}(r_s|\nu_\star)\exp\left(\mathrm{i}k_0\left(2\int_{r_\delta}^{r_s}Q(r'|\nu_\star)\,\mathrm{d}r' + \int_{r_s}^{r}Q(r'|\nu_\star)\,\mathrm{d}r'\right)\right) \\ &= \tilde{v}_2(r_s)\tilde{v}_1(r), \end{aligned} \tag{6.57}$$

where,

$$\tilde{v}_2(r_s) \sim -\mathrm{i}Q^{-1/2}(r_s|\nu_\star)\exp\left(2\mathrm{i}k_0\int_{r_\delta}^{r_s}Q(r'|\nu_\star)\,\mathrm{d}r'\right), \quad \tilde{v}_1(r) \sim \exp\left(\mathrm{i}k_0\int_{r_s}^{r}Q(r'|\nu_\star)\,\mathrm{d}r'\right). \tag{6.58}$$

This possible as the so-called phase-reference, r_δ in this case, is arbitrary and we can partition the phases anyway we like so long as we still integrate from r_s to r. The local solutions can be rewritten in both cases.

Approaching the anti-caustic, $\theta \nearrow \theta_d$,

$$\tilde{v}_2(r_s) \sim \begin{cases} -\frac{\mathrm{i}r_s^{1/2}}{(T_{a_{(2)}}r_s^4-\nu_\star^2)^{1/4}}\mathrm{e}^{\mathrm{i}k_0\left(\sqrt{T_{a_{(2)}}r_s^4-\nu_\star^2}+\nu_\star\tan^{-1}\left(\frac{\nu_\star}{\sqrt{T_{a_{(2)}}r_s^4-\nu_\star^2}}\right)-\nu_\star\frac{\pi}{2}\right)}, & \nu_\star > r_s^2\sqrt{T_{a_{(2)}}}, \\ \frac{\mathrm{e}^{-\mathrm{i}\pi/4}r_s^{1/2}}{\sqrt{2\nu_\star}}\left(\frac{r_s^2\sqrt{T_{a_{(2)}}}}{2}\right)^{k_0\nu_\star}\mathrm{e}^{k_0(\nu_\star-\nu_\star\log(\nu_\star))}, & \nu_\star < r_s^2\sqrt{T_{a_{(2)}}}, \end{cases} \tag{6.59}$$

At the anti-caustic, $\theta = \theta_d$,

$$\tilde{v}_2(r_s) \sim \sqrt{\frac{2^{3/2}r_s}{\pi}}k_0^{-1/4}T_{a_{(2)}}^{-1/8}\mathrm{e}^{\mathrm{i}k_0r_s^2\sqrt{T_{a_{(2)}}}}\mathrm{e}^{-3\pi\mathrm{i}/4}\Psi_2\left(0, k_0r_s^2\sqrt{T_{a_{(2)}}}\right), \tag{6.60}$$

or

$$\tilde{v}_2(r_s) \sim 2^{1/2}k_0^{1/4}T_{a_{(2)}}^{-1/8}\mathrm{e}^{-5\pi\mathrm{i}/8}D_{-1/2}\left(2\mathrm{e}^{-\pi\mathrm{i}/4}k_0^{1/2}r_sT_{a_{(2)}}^{1/4}\right), \tag{6.61}$$

which are simple re-scalings of (6.55) and (6.56) respectively.

6.4.2.3 Flow-factor

Once the radial Green's functions have been found it is a simple matter of determining the local ray field. Using the indirect flow-factor the $\tilde{v}_2$ Green's functions is treated as a slow function in the integrand. The indirect flow-factor is given as,

$$\mathscr{R}_{\omega}^{(+)} = \int_{C^{(+)}} \left(\frac{\mathrm{i}k_0}{2\pi r_s}\right)^{1/2} \tilde{v}_2(r_s)\tilde{v}_1(r)\mathrm{e}^{\mathrm{i}k_0\left(\Delta\varphi - R\sin^2\theta\right)}\,\mathrm{d}\nu, \tag{6.62}$$

where the constants $\gamma_{21}^{(2)}$ and $\gamma_{12}^{(2)} = \mathrm{e}^{\mathrm{i}\pi/4}\gamma_{12}^{(1)}$ from Eq. (2.72), Chap. 2 have been absorbed for the sake of simplicity.

Approaching the anti-caustic, $\theta \nearrow \theta_d$, using (6.59),

$$\mathscr{R}_{\omega}^{(+)} \sim \mathrm{i}\left(r_s\left|\frac{\partial\tilde{\psi}_{WK}}{\partial\nu_\star}\right|\right)^{-1/2} \mathrm{e}^{-\mathrm{i}\arg(\partial\tilde{\psi}_{WK}/\partial\nu_\star)/2}\mathrm{e}^{\mathrm{i}k_0\left(\nu_\star\Delta\varphi + \int_{r_s}^{r} Q(r'|\nu_\star)\,\mathrm{d}r' - R\sin^2\theta\right)} \times$$
$$\begin{cases} -\frac{\mathrm{i}r_s^{1/2}}{(T_{a_{(2)}}r_s^4 - \nu_\star^2)^{1/4}}\mathrm{e}^{\mathrm{i}k_0\left(\sqrt{T_{a_{(2)}}r_s^4-\nu_\star^2} + \nu_\star\tan^{-1}\left(\frac{\nu_\star}{\sqrt{T_{a_{(2)}}r_s^4-\nu_\star^2}}\right) - \nu_\star\frac{\pi}{2}\right)}, & \nu_\star > r_s^2\sqrt{T_{a_{(2)}}}, \\ \frac{\mathrm{e}^{-\mathrm{i}\pi/4}r_s^{1/2}}{\sqrt{2\nu_\star}}\left(\frac{r_s^2\sqrt{T_{a_{(2)}}}}{2}\right)^{k_0\nu_\star}\mathrm{e}^{k_0(\nu_\star - \nu_\star\log(\nu_\star))}, & \nu_\star < r_s^2\sqrt{T_{a_{(2)}}}. \end{cases} \tag{6.63}$$

At the anti-caustic, $\theta = \theta_d$, using (6.60) and (6.61),

$$\mathscr{R}_{\omega}^{(+)} \sim \mathrm{i}\sqrt{\frac{2^{3/2}r_s}{\pi}}k_0^{-1/4}T_{a_{(2)}}^{-1/8}\mathrm{e}^{\mathrm{i}k_0r_s^2\sqrt{T_{a_{(2)}}}}\mathrm{e}^{-3\pi\mathrm{i}/4}\Psi_2\left(0, k_0r_s^2\sqrt{T_{a_{(2)}}}\right) \times$$
$$\left(r_s\left|\frac{\partial\tilde{\psi}_{WK}}{\partial\nu_\star}\right|\right)^{-1/2} \mathrm{e}^{-\mathrm{i}\arg(\partial\tilde{\psi}_{WK}/\partial\nu_\star)/2}\mathrm{e}^{\mathrm{i}k_0\left(\nu_\star\Delta\varphi + \int_{r_s}^{r} Q(r'|\nu_\star)\,\mathrm{d}r' - R\sin^2\theta\right)}, \tag{6.64}$$

or,

$$\mathscr{R}_{\omega}^{(+)} \sim \mathrm{i}2^{1/2}k_0^{1/4}T_{a_{(2)}}^{-1/8}\mathrm{e}^{-5\pi\mathrm{i}/8}D_{-1/2}\left(2\mathrm{e}^{-\pi\mathrm{i}/4}k_0^{1/2}r_sT_{a_{(2)}}^{1/4}\right) \times$$
$$\left(r_s\left|\frac{\partial\tilde{\psi}_{WK}}{\partial\nu_\star}\right|\right)^{-1/2} \mathrm{e}^{-\mathrm{i}\arg(\partial\tilde{\psi}_{WK}/\partial\nu_\star)/2}\mathrm{e}^{\mathrm{i}k_0\left(\nu_\star\Delta\varphi + \int_{r_s}^{r} Q(r'|\nu_\star)\,\mathrm{d}r' - R\sin^2\theta\right)}, \tag{6.65}$$

where $\tilde{\psi}_{WK} \equiv \nu\int_{r_s}^{r}(r^2q^2(r) - \nu_\star^2)^{-1/2}/r^2\,\mathrm{d}r$, because we cannot use the same Taylor approximations in the evaluation of the $\tilde{v}_1$ phase. It is worth noting that we must remember to multiply $\tilde{v}_2$ by i in the above, as $-\mathrm{i}$ is already accounted for in the definition of $\mathscr{R}_{\omega}^{(+)}$.

From both cases shown above it is clear that the controlling behaviour of the odes persists into the ray evaluation, and this is obviously due to the treatment of $\tilde{v}_2$ as a slow function. As the anti-caustic is approached in (6.64) both flow-factor cases show that there is one ray contribution with the small amplitude case for the scenario $\nu_\star < r_s^2\sqrt{T_{a_{(2)}}}$. At the anti-caustic we see that the two equivalent expressions appear. The first of these - the Pearcey function - is evaluated on its line of symmetry and implies a three ray system on θ_d. In other words this means the local potential is quartic and Ψ_{WK} can be expanded this way if a local analysis is performed. The key point though is that the Pearcey function is evaluated on its line of symmetry away from its caustics, because we assume that $r_s^2\sqrt{T_{a_{(2)}}} > 0$. This line of symmetry is special in the sense that it is a Maxwell set which we have used before in Chap. 6 to describe the ray bifurcation in $\mathrm{Im}(\lambda)$. Maxwell sets do not describe caustics, i.e., saddle points do not coalesce: however, the saddle *values* - the phases evaluated at the saddle points do coalesce. This means the singulant goes to zero without a caustic. This is another good example of why we always demand the Jacobian accompanies the singulant as it goes to zero.

The Pearcey function throws up an interesting conundrum: the three ray system does not agree with putative mechanism seen at the beginning of this section, and if this corresponds to at least $\xi_0 = 0$, then it implies that the governing behaviour is (at least) controlled by $\mathscr{E}_2$. This makes matters worse in some sense as $\mathscr{E}_2$ is a four ray system - two more than the putative mechanism. One explanation is that we may indeed have a three ray system engendered by $\mathscr{E}_1$ perhaps, which of course could be mapped into the Pearcey function away from anti-caustic, then on the anti-caustic the loss of one ray is reflected by the Maxwell set.

The second expression of (6.65) in terms of parabolic cylinder functions is also enlightening. This is the outgoing solution found in quantum mechanics for the scattering of waves off the peak of a potential barrier [58]. This differs from the solution given in Chap. 2 as we required two branches of the WKB solution. This was due to the modal solution having a modal index n that was the same for both branches; now the variable $\nu_\star$ in the ray solution has uncoupled the branches so that only one is required. This description is more in-keeping with the putative mechanism discussed before, as it is a two-ray system: the difficulty is the Parabolic cylinder does not fit in so easily with the eucatastrophe framework.

In this section we have considered the local analysis of the anti-caustic for small r_s. The analysis shown in here is not complete and should be read as a stimulus for future investigation. There are several obvious immediate steps to continue this work. First, there is the allowance of $T_{a_{(1)}} \neq 0$ in the Taylor expansion that would see the solution in terms of confluent hypergeometric functions, and secondly r_s, should be allowed to take on $O(1)$ values. The next steps after this would then be an assault on the CDP

itself. Of course this is difficult without more detailed information on the exact number of rays and their contributions.

6.5 Conclusion

In this chapter the ray solver developed in Chapters 3-5 was applied to an isothermal parallel shear flow problem. Using the high-frequency asymptotics of a Poisson summation to generalise the theoretical ray solution to complex numbers, the ray tracing solution was benchmarked in both its field evaluation - using the modal solution - and its ray parameters. The evaluations of the ray solver against the modal solution yielded excellent results in all regions except the divergence of the amplitude at caustics. These divergences were corrected using the appropriate diffraction catastrophes, where multiple-term corrections provided a near perfect match.

In the context of noise control we have seen two cuspoids: a fold and - for the first time in free jet flows - a cusp caustic. Significantly, they are both of the same order of magnitude, though both in distinct regions of the jet, i.e., the fold in the forward arc, the cusp in the rear arc. We may expect then that the aggregate effects of sources may influenced greatly by these singularities. This will be investigated further in the next chapter.

Perhaps the most interesting feature of this chapter has been the non-canonical disappearance of rays at what we have deemed to be an anti-caustic. This anti-caustic clashes with and is the likely cause of the fold caustic's disappearance at the CDP whilst inhibiting the application of the diffraction catastrophes. Though the underlying physical principle is simple, the mathematical explanation is non-trivial. We attempted to provide the latter undertaking a local analysis near θ_d and explaining our results in terms of eucatastrophes: local forms that generalise the diffraction catastrophes.

Chapter 7

Caustics in ring source models

7.1 Caustics in the ring source models

In this chapter we consider the effect of multiple off-axis sources in the jet, and how they interact with each other. Interest lies in estimating the impact of the fold and cusp caustics of Chapter 6 on the resulting acoustic field. A conclusion can then be reached concerning the significance of these caustics for noise control purposes.

The first part of this chapter considers the effect of a finite number of point sources placed in the shear layer of a parallel shear flow. This is representative of current AA methods (see for e.g., Ilário [11]) whereby an interpolation scheme is applied to a large number of points sources distributed about a mean jet flow to create a global flow factor. The second part of this chapter considers a continuum of sources, namely derivatives of the ring-source model from Chap. 2. These are in the form of a weighted and perturbed ring source mode. In both the discrete and continuum cases, the easiest route is to construct the solution using the modal solution. This is particularly useful for the latter as the ray solution would have to reworked for a ring source.

7.1.1 Multiple point sources

The effect of multiple point sources on the field can be examined easily if they lie on the same source radius due to the separable nature of the Green's function (2.89). A sum of Green's functions with the same source weighting is given by,

$$\frac{1}{\mathscr{G}_\omega^{(3)}} \sum_{m=1}^{N_s} \mathbb{G}_\omega(\varphi|\varphi_{s_m}) = \frac{\mathrm{i}}{\overline{c}_\infty k_0 (1 - M(r_s)\cos\theta)^2} \sum_{n=-\infty}^{\infty} \left(\frac{2}{k_0} \frac{\sqrt{-\eta_n(r_s)}}{r_s Q_n(r_s)} \right)^{1/2} \mathrm{Ai}\left(\eta_n(r_s)\right) \mathrm{e}^{\mathrm{i}k_0(\zeta_n - R\sin^2\theta)} \times \mathrm{e}^{\mathrm{i}n\Delta\varphi} \left[1 + \mathrm{e}^{\mathrm{i}k_0\Delta\varphi_{12}} + \ldots + \mathrm{e}^{\mathrm{i}k_0\Delta\varphi_{1N_s}} \right], \tag{7.1}$$

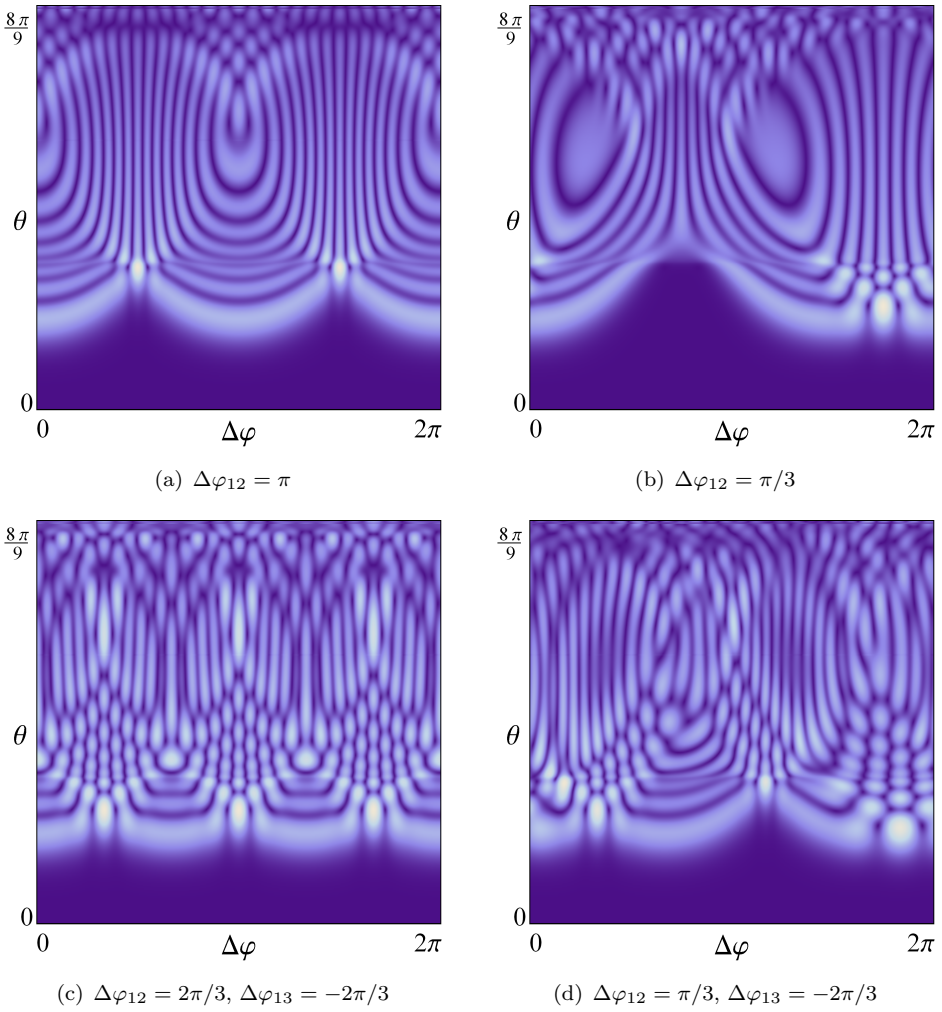

(a) $\Delta\varphi_{12} = \pi$

(b) $\Delta\varphi_{12} = \pi/3$

(c) $\Delta\varphi_{12} = 2\pi/3$, $\Delta\varphi_{13} = -2\pi/3$

(d) $\Delta\varphi_{12} = \pi/3$, $\Delta\varphi_{13} = -2\pi/3$

FIGURE 7.1: Examples of the magnitude of Eq. (7.1). (a, b) Two sources, (c, d) three sources. (a, c) Symmetric fields, (b, d) asymmetric fields.

where in this instance $\Delta\varphi = \varphi - \varphi_1$ and $\Delta\varphi_{1N_s} = \varphi_1 - \varphi_{N_s}$ (see Fig. 7.2(b) for $N_s = 2$). The fields of two and three point sources at a source radius of 0.75 are shown in Fig. 7.1. In the cases where these sources are symmetrically placed, i.e., Figs. 7.3(a) and 7.3(c) the cone of silence begins to become symmetric in $\Delta\varphi$ having a periodic boundary, whereas asymmetric source positioning (Figs. 7.3(b) and 7.1(d)) leads to an asymmetric boundary though not to the degree of the single point source cases. In each case the field is complicated by the overlapping interference patterns, distributing the interference across the whole range in $\Delta\varphi$. The distribution appears to reduce the intensity of the cusp diffraction patterns particularly in the two source cases. If one were to add sources with the same weight and radius at different azimuthal angles indefinitely then this would approach a ring source. This limiting case would conclude the impact of repeated overlapping of each interference pattern.

7.1.2 Ring sources

Ring sources are frequently used in aeroacoustics as a model simplification. We argued in Chapter 2 that round single stream and coaxial jets are assumed to have little azimuthal variation and therefore a coherent averaging process can be used to eliminate this coordinate both from the source model and the Green's function in an acoustic analogy. In Chapter 3 we then developed a directivity factor that can extend the ring source of Chap. 2 to the vector Green's function case. In this section two instances of high-frequency ring source are examined. The first instance appears in a convolution integral for the acoustic pressure, while the latter appears in a two-point correlation integral for the power-spectral-density.

7.1.2.1 Effects of a simple ring source

The simple ring source model is a convolution of the 3D Green's function given by (2.89), with a delta function in the radial coordinate only. A delta function in the streamwise coordinate, x, is not necessary because there is no dependency on this coordinate in the far-field. The first ring source directivity factor is given by,

$$\begin{aligned}\mathscr{D}_{\omega}^{(r,0)} &\sim \frac{1}{\mathscr{G}_{\omega}} \int_{-\pi}^{\pi}\int_{0}^{\infty} \mathbb{G}_{\omega}(\boldsymbol{x}|\boldsymbol{x}')\frac{\delta(r'-r_s)}{r'}\, r'\mathrm{d}r'\mathrm{d}\varphi' \\ &= \frac{\mathrm{i}}{\bar{c}_{\infty}k_0(1-M(r_s)\cos\theta)^2}\int_{-\pi}^{\pi}\mathscr{R}_{\omega}(\boldsymbol{x}|\boldsymbol{x}')\,\mathrm{d}\varphi' \\ &= \frac{2\pi\mathrm{i}}{\bar{c}_{\infty}k_0(1-M(r_s)\cos\theta)^2}\left(\frac{2}{k_0}\frac{\sqrt{-\eta_0(r_s)}}{r_sQ_0(r_s)}\right)^{1/2}\mathrm{Ai}\left(\eta_0(r_s)\right)\mathrm{e}^{\mathrm{i}k_0(\zeta_0-R\sin^2\theta)},\end{aligned} \tag{7.2}$$

since $\int_{-\pi}^{\pi}\mathrm{e}^{-\mathrm{i}n\varphi'}\,\mathrm{d}\varphi' = 2\pi\delta_{n0}$ sifts out the zeroth mode only.
An expansion of the Airy mode for large argument would show that this result is proportional to the Flow-Factor used in the MGB method [175]. Thus if the flow is azimuthally symmetric then a Flow-Factor of this form is appropriate. If, however, the flow is not symmetric then one cannot use the zeroth mode only.

7.1.2.2 Ring-source directivity factor

The ring-source directivity is the extension of (7.2) to two-point correlations. In the introduction to this thesis, it was stressed that correlation integrals are those used in

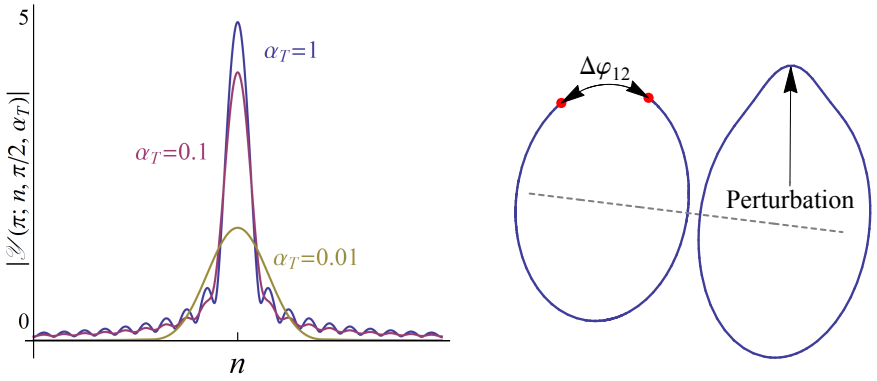

(a) $|\mathscr{Y}| : \alpha_T \in \{0.01, 0.1, 1\}$ (b)

FIGURE 7.2: (a) Examples of $|\mathscr{Y}|$ as a function of n. (b) Example of $\Delta\varphi_{12}$, ring source, and exponential perturbation to ring source.

making tangible calculations.

$$\begin{aligned}\mathscr{D}_\omega^{(c,0)} &\sim \frac{1}{|\mathscr{G}_\omega|^2}\int_{-\pi}^{\pi}\int_0^\infty \mathbb{G}_\omega^*(\boldsymbol{x}|\boldsymbol{x}')\mathbb{G}_\omega(\boldsymbol{x}|\boldsymbol{x}')\frac{\delta(r'-r_s)}{r'}\,r'\mathrm{d}r'\mathrm{d}\varphi' \\ &= \frac{1}{\bar{c}_\infty^2 k_0^2(1-M(r_s)\cos\theta)^4}\int_{-\pi}^{\pi}\mathscr{R}_\omega^*(\boldsymbol{x}|\boldsymbol{x}')\mathscr{R}_\omega(\boldsymbol{x}|\boldsymbol{x}')\,\mathrm{d}\varphi' \\ &= \frac{4\pi}{\bar{c}_\infty^2 k_0^2(1-M(r_s)\cos\theta)^4}\sum_{n=-\infty}^{\infty}\left(\frac{1}{k_0}\frac{\sqrt{-\eta_n(r_s)}}{r_s Q_n(r_s)}\right)\mathrm{Ai}^2\left(\eta_n(r_s)\right),\end{aligned} \tag{7.3}$$

since $\int_{-\pi}^{\pi}\mathrm{e}^{\mathrm{i}(m-n)\varphi'}\,\mathrm{d}\varphi' = 2\pi\delta_{nm}$.

This same function is defined in Wundrow & Khavaran [116] and Khavaran et al. [176]. If one uses the zeroth mode as an approximation to the sum as in the previous section, then the result is the same as the Flow-Factor given by Self [148].

7.1.2.3 Weighted ring source

It is possible to examine cases where one might apply a parallel shear flow Green's function with an azimuthally varying source. In the case of azimuthally weighted ring of sources the convolutions of (7.2) and (7.3) are more complicated. For $\mathscr{D}_\omega^{(r,0)}$, this

becomes,

$$\begin{aligned}\mathscr{D}_{\omega}^{(r,0)} &\sim \frac{1}{\mathscr{G}_{\omega}}\int_{-\pi}^{\pi}\int_{0}^{\infty}\mathbb{G}_{\omega}(\boldsymbol{x}|\boldsymbol{x}')h(\varphi';\alpha_T)\frac{\delta(r'-r_s)}{r'}\,r'\mathrm{d}r'\mathrm{d}\varphi' \\ &= \frac{\mathrm{i}}{\bar{c}_{\infty}k_0(1-M(r_s)\cos\theta)^2}\int_{-\pi}^{\pi}\mathscr{R}_{\omega}(\boldsymbol{x}|\boldsymbol{x}')h(\varphi';\varphi_P,\alpha_T)\,\mathrm{d}\varphi' \\ &= \frac{\mathrm{i}}{\bar{c}_{\infty}k_0(1-M(r_s)\cos\theta)^2}\sum_{n=-\infty}^{\infty}\left(\frac{2}{k_0}\frac{\sqrt{-\eta_n(r_s)}}{r_sQ_n(r_s)}\right)^{1/2}\mathrm{Ai}\left(\eta_n(r_s)\right)\mathrm{e}^{\mathrm{i}k_0(\zeta_n-R\sin^2\theta)}\mathscr{Y}(\varphi;n,\varphi_P,\alpha_T),\end{aligned} \tag{7.4}$$

where,

$$\mathscr{Y}(\varphi;n,\varphi_P,\alpha_T)=\int_{-\pi}^{\pi}\mathrm{e}^{\mathrm{i}n(\varphi-\varphi')}h(\varphi';\varphi_P,\alpha_T)\,\mathrm{d}\varphi', \tag{7.5}$$

which can be "solved" in terms of error functions if a Gaussian is used for $h(\varphi';\varphi_P,\alpha_T)$,

$$\begin{aligned}&\mathscr{Y}(\varphi;n,\varphi_P,\alpha_T)=\int_{-\pi}^{\pi}\mathrm{e}^{\mathrm{i}n(\varphi-\varphi')-\alpha_T(\varphi'-\varphi_P)^2}\,\mathrm{d}\varphi'= \\ &\frac{\sqrt{\pi}}{2\sqrt{\alpha_T}}\mathrm{e}^{-\frac{n(n-4\mathrm{i}\alpha_T(\pi-\varphi_P))}{4\alpha_T}}\left[\mathrm{erf}\left(\frac{2\alpha_T(\pi-\varphi_P)+\mathrm{i}n}{2\sqrt{\alpha_T}}\right)-\mathrm{erf}\left(\frac{-2\alpha_T(\varphi-\varphi_P)+\mathrm{i}n}{2\sqrt{\alpha_T}}\right)\right].\end{aligned} \tag{7.6}$$

Here α_T measures the decay of the source distribution strength, and φ_P the azimuthal point at which the distribution is highest. An example of $|\mathscr{Y}|$ as a function of n is shown in Fig. 7.2(a). While the magnitude remains similar for the angular variables φ,φ_P, it is the phase that provides the azimuthal asymmetry. As α_T decreases (symmetry increases) $\mathscr{Y}$ behaves more and more like a scaled delta function that sifts out only the zeroth mode as in (7.3).

Likewise an expression for $\mathscr{D}_{\omega}^{(c,0)}$ can be derived using the Gaussian weighting.

$$\begin{aligned}\mathscr{D}_{\omega}^{(c,0)} &= \frac{1}{|\mathscr{G}_{\omega}|^2}\int_{-\pi}^{\pi}\int_{0}^{\infty}\mathbb{G}_{\omega}^{*}(\boldsymbol{x}|\boldsymbol{x}')\mathbb{G}_{\omega}(\boldsymbol{x}|\boldsymbol{x}')h^{*}(\varphi';\varphi_P,\alpha_T)h(\varphi';\varphi_P,\alpha_T)\frac{\delta(r'-r_s)}{r'}\,r'\mathrm{d}r'\mathrm{d}\varphi' \\ &= \frac{1}{|\mathscr{G}_{\omega}|^2}\int_{-\pi}^{\pi}\mathbb{G}_{\omega}^{*}(\boldsymbol{x}|\varphi')\mathbb{G}_{\omega}(\boldsymbol{x}|\varphi')h^{*}(\varphi';\varphi_P,\alpha_T)h(\varphi';\varphi_P,\alpha_T)\,\mathrm{d}\varphi'.\end{aligned} \tag{7.7}$$

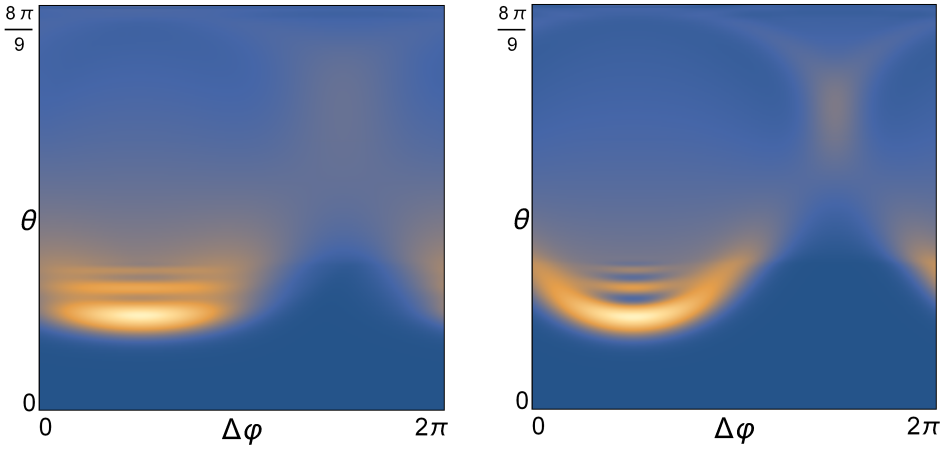

(a) $\varphi_P = \pi/2$, $\alpha_T = 1$ (b) $\varphi_P = \pi/2$, $\alpha_T = 5$

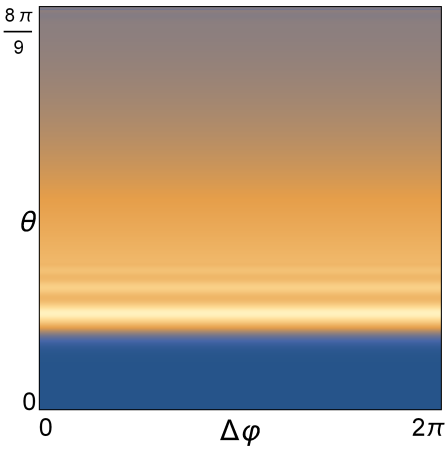

(c) Unweighted ring source

FIGURE 7.3: Magnitude of ring source and weighted ring source solutions, $\mathscr{D}_\omega^{(c,0)}$. (a,b) weighted ring source solutions. (c) unweighted ring source solution given by Eq. (7.3).

It is straightforward to show that,

$$\mathscr{D}_\omega^{(c,0)} \sim \frac{2}{\overline{c}_\infty^2 k_0^3 (1 - M(r_s)\cos\theta)^4} \times \sum_{n=-\infty}^{\infty} \sum_{m=-\infty}^{\infty} \left(\frac{\sqrt{-\eta_n(r_s)}}{r_s Q_n(r_s)} \right)^{1/2*} \left(\frac{\sqrt{-\eta_m(r_s)}}{r_s Q_m(r_s)} \right)^{1/2} \mathrm{Ai}\left(\eta_n(r_s)\right) \mathrm{Ai}\left(\eta_m(r_s)\right) \times \mathrm{e}^{\mathrm{i}k_0(\zeta_m - \zeta_n)} \mathscr{Y}(\varphi; m-n, \varphi_P, \alpha_T), \tag{7.8}$$

where the square due to $h^*(\varphi'; \varphi_P, \alpha_T) h(\varphi'; \varphi_P, \alpha_T)$ is absorbed into α_T for simplicity. Equation (7.8) is computed for $\varphi_P = \pi/2$ and $\alpha_T = 1, 2$ in Figs. 7.3(a) and 7.3(b). The values of $\alpha_T = 1, 2$ are in fact large deviations from the symmetric field and this can be

seen in comparison with symmetric field of (7.3). The noticeable feature of increasing α_T is that a smoothed cusp diffraction pattern begins to appear in the large θ ranges. This is a feature purely of asymmetry as the cusp diffraction pattern is completely absent from the unweighted ring source.

Of course the work in this section can easily be generalised to contain multiple peaks. In this case,

$$h^*h(\varphi';\varphi_P,\alpha_T) = 1 + \exp\left(-\alpha_{T_1}(\varphi'-\varphi_{P_1})^2\right) + \exp\left(-\alpha_{T_2}(\varphi'-\varphi_{P_2})^2\right) + \ldots \\ \cdots + \exp\left(-\alpha_{T_N}(\varphi'-\varphi_{P_N})^2\right). \tag{7.9}$$

The introduction of a constant is aimed at providing approximate continuity in the source (as φ varies) when a symmetry in φ_P is present. Integration of $h * h(\varphi';\varphi_P,\alpha_T)$ with $\exp(\mathrm{i}(m-n)(\varphi-\varphi'))$ gives,

$$2\pi\delta_{nm} + \mathscr{Y}(\varphi;m-n,\varphi_{P_1},\alpha_{T_1}) + \mathscr{Y}(\varphi;m-n,\varphi_{P_2},\alpha_{T_2}) + \ldots + \mathscr{Y}(\varphi;m-n,\varphi_{P_N},\alpha_{T_N}), \tag{7.10}$$

so that $\mathscr{D}_\omega^{(c,0)}$ is a combination of (7.3) and (7.8),

$$\begin{aligned}\mathscr{D}_\omega^{(c,0)} \sim\ & \\ & \frac{4\pi}{\overline{c}_\infty^2 k_0^3(1-M(r_s)\cos\theta)^4}\sum_{n=-\infty}^{\infty}\left(\frac{\sqrt{-\eta_n(r_s)}}{r_s Q_n(r_s)}\right)\mathrm{Ai}^2\left(\eta_n(r_s)\right) + \ldots \\ & \ldots + \frac{2}{\overline{c}_\infty^2 k_0^3(1-M(r_s)\cos\theta)^4}\times \\ & \sum_{n=-\infty}^{\infty}\sum_{m=-\infty}^{\infty}\left(\frac{\sqrt{-\eta_n(r_s)}}{r_s Q_n(r_s)}\right)^{1/2*}\left(\frac{\sqrt{-\eta_m(r_s)}}{r_s Q_m(r_s)}\right)^{1/2}\mathrm{Ai}\left(\eta_n(r_s)\right)\mathrm{Ai}\left(\eta_m(r_s)\right)\times \\ & \mathrm{e}^{\mathrm{i}k_0(\zeta_m-\zeta_n)}\left[\mathscr{Y}(\varphi;m-n,\varphi_{P_1},\alpha_{T_1}) + \mathscr{Y}(\varphi;m-n,\varphi_{P_2},\alpha_{T_2}) + \ldots + \mathscr{Y}(\varphi;m-n,\varphi_{P_N},\alpha_{T_N})\right].\end{aligned} \tag{7.11}$$

7.1.2.4 Perturbed ring source

In the case of an asymmetric source position the argument of the delta function can be adapted. The resulting integrals, though, are even more cumbersome than before. The purpose of these sections is to illustrate the effects of asymmetry and so some progress can be made if a perturbed ring source is considered. This allows a perturbation expansion to be constructed in the small parameter $\epsilon \ll 1$ say. An illustration of perturbation in position to the ring source is shown in Fig. 7.2(b).

Formally the expansion is based on the Taylor expansion of a function ϵ, for example,

$$f(x;\epsilon) = f(x;0) + \epsilon\left.\frac{\partial}{\partial\epsilon}f(x;\epsilon)\right|_{\epsilon=0} + O(\epsilon^2), \quad \epsilon \ll 1, \tag{7.12}$$

which can either be applied to the delta function in the convolution integral,

$$\delta(r - g(\varphi; r_s, \varphi_P, \epsilon)) = \delta(r - g(\varphi; r_s, \varphi_P, 0)) + \epsilon \left.\frac{\partial \delta}{\partial g}\frac{\partial g}{\partial \epsilon}\right|_{\epsilon=0} + O(\epsilon^2), \tag{7.13}$$

using the chain rule, or to the Green's function post sifting with the delta function: the latter is pursued here.

Green's function convolved with perturbed ring source $\delta(r' - g(\varphi, r_s, \varphi_s, \epsilon))/r'$, where $g(\varphi, r_s, \varphi_s, 0) = r_s$, is,

$$\int_{-\pi}^{\pi}\int_{0}^{\infty} \mathbb{G}_\omega(\boldsymbol{x}|\boldsymbol{x}')\frac{\delta(r' - g(\varphi'; r_s, \varphi_P, \epsilon))}{r'}\, r'\mathrm{d}r'\mathrm{d}\varphi' = \int_{-\pi}^{\pi} \mathbb{G}_\omega(\boldsymbol{x}|g(\varphi'; r_s, \varphi_P, \epsilon), \varphi')\,\mathrm{d}\varphi', \tag{7.14}$$

which expanded to $O(\epsilon)$,

$$\begin{aligned}\mathscr{D}_\omega = &\int_{-\pi}^{\pi} \mathbb{G}_\omega(\boldsymbol{x}|\, g(\varphi'; r_s, \varphi_P, \epsilon), \varphi')\,\mathrm{d}\varphi' = \\ &\int_{-\pi}^{\pi} \mathbb{G}_\omega(\boldsymbol{x}|\, g(\varphi'; r_s, \varphi_P, 0), \varphi')\,\mathrm{d}\varphi' + \epsilon\int_{-\pi}^{\pi} \left.\frac{\partial g}{\partial \epsilon}\frac{\partial}{\partial g}\mathbb{G}_\omega(\boldsymbol{x}|\, g(\varphi'; r_s, \varphi_P, \epsilon), \varphi')\right|_{\epsilon=0}\mathrm{d}\varphi' + O(\epsilon^2).\end{aligned} \tag{7.15}$$

The perturbed ring source solution can be written in terms of $\mathscr{D}_\omega^{(r,0)}$,

$$\mathscr{D}_\omega^{(r)} \sim \mathscr{D}_\omega^0 + \epsilon\mathscr{D}_\omega^\epsilon. \tag{7.16}$$

Using the expression for $\mathbb{G}_\omega$, $\mathscr{D}_\omega^\epsilon$ can be written as,

$$\mathscr{D}_\omega^\epsilon = \frac{\mathrm{i}}{\bar{c}_\infty k_0}\left[\frac{2M'(r_s)\cos\theta}{(1 - M(r_s)\cos\theta)^3}\int_{-\pi}^{\pi}\left.\frac{\partial g}{\partial \epsilon}\mathscr{R}_\omega\right|_{\epsilon=0}\mathrm{d}\varphi' + \frac{1}{(1 - M(r_s)\cos\theta)^2}\int_{-\pi}^{\pi}\left.\frac{\partial g}{\partial \epsilon}\frac{\partial \mathscr{R}_\omega}{\partial g}\right|_{\epsilon=0}\mathrm{d}\varphi'\right]. \tag{7.17}$$

The expression for $\mathscr{R}_\omega$ is given by (2.89). It has derivative with respect to the source,

$$\frac{\partial}{\partial r_s}\mathscr{R}_\omega \sim -\sum_{n=-\infty}^{\infty}\left(\frac{2k_0 Q_n(r_s)}{r_s\sqrt{-\eta_n(r_s)}}\right)^{1/2}\mathrm{Ai}'\left(\eta_n(r_s)\right)\mathrm{e}^{\mathrm{i}n\Delta\varphi + \mathrm{i}k_0(\zeta_n - R\sin^2\theta)}. \tag{7.18}$$

so $\mathscr{D}_\omega^\epsilon$ is formed from,

$$\int_{-\pi}^{\pi}\left.\frac{\partial g}{\partial \epsilon}\mathscr{R}_\omega\right|_{\epsilon=0}\mathrm{d}\varphi' = \sum_{n=-\infty}^{\infty}\left(\frac{2}{k_0}\frac{\sqrt{-\eta_n(r_s)}}{r_s Q_n(r_s)}\right)^{1/2}\mathrm{Ai}\left(\eta_n(r_s)\right)\mathrm{e}^{\mathrm{i}k_0(\zeta_n - R\sin^2\theta)}\mathscr{Y}(\varphi; \varphi_P, \alpha_T), \tag{7.19}$$

and,

$$\int_{-\pi}^{\pi} \frac{\partial g}{\partial \epsilon}\frac{\partial \mathscr{R}_\omega}{\partial g}\bigg|_{\epsilon=0} \mathrm{d}\varphi' = -\sum_{n=-\infty}^{\infty}\left(\frac{2k_0 Q_n(r_s)}{r_s\sqrt{-\eta_n(r_s)}}\right)^{1/2} \mathrm{Ai}'\left(\eta_n(r_s)\right)\mathrm{e}^{\mathrm{i}k_0(\zeta_n - R\sin^2\theta)}\mathscr{Y}(\varphi; n, \varphi_P, \alpha_T). \tag{7.20}$$

where,

$$\mathscr{Y}(\varphi; n, \varphi_P, \alpha_T) = \int_{-\pi}^{\pi} \frac{\partial g}{\partial \epsilon}\bigg|_{\epsilon=0} \mathrm{e}^{\mathrm{i}n(\varphi-\varphi')}\,\mathrm{d}\varphi', \tag{7.21}$$

The smooth perturbation applied here is in the form of a Gaussian function, i.e.,

$$g(\varphi'; r_s, \varphi_P, \epsilon) = r_s + \epsilon\exp(-\alpha_T(\varphi' - \varphi_P)^2), \tag{7.22}$$

with,

$$\frac{\partial}{\partial \epsilon} g(\varphi'; r_s, \varphi_P, \epsilon) = \exp(-\alpha_T(\varphi' - \varphi_P)^2). \tag{7.23}$$

so that the integrals can be "solved" in terms of error functions as before.

The perturbation method can be applied to the correlation integral in a similar manner. It is straightforward to show that this results in,

$$\mathscr{D}_\omega^{(c)} \sim \mathscr{D}_\omega^{(c,0)} + \epsilon\mathscr{D}_\omega^{(c,\epsilon)}, \tag{7.24}$$

where $\mathscr{D}_\omega^{(c,0)}$ is given by (7.3). The perturbed term is the sum of the following two functions,

$$\frac{1}{|\mathscr{G}_\omega|^2}\int_{-\pi}^{\pi} \mathbb{G}_\omega^*(\boldsymbol{x}|r_s, \varphi')\,\frac{\partial g}{\partial \epsilon}\frac{\partial}{\partial g}\mathbb{G}_\omega(\boldsymbol{x}|g(\varphi'; r_s, \varphi_P, \epsilon), \varphi')\bigg|_{\epsilon=0}\mathrm{d}\varphi' =$$
$$\frac{-\mathrm{i}}{\overline{c}_\infty k_0(1 - M(r_s)\cos\theta)^2}\sum_{n=-\infty}^{\infty}\left(\frac{2}{k_0}\frac{\sqrt{-\eta_n(r_s)}}{r_s Q_n(r_s)}\right)^{1/2*}\mathrm{Ai}\left(\eta_n(r_s)\right)\mathrm{e}^{-\mathrm{i}k_0\zeta_n}\sum_{m=-\infty}^{\infty}\mathscr{M}_m\mathscr{Y}(\varphi; m-n, \varphi_P, \alpha_T), \tag{7.25}$$

and,

$$\frac{1}{|\mathscr{G}_\omega|^2}\int_{-\pi}^{\pi} \mathbb{G}_\omega(\boldsymbol{x}|r_s, \varphi')\,\frac{\partial g}{\partial \epsilon}\frac{\partial}{\partial g}\mathbb{G}_\omega^*(\boldsymbol{x}|g(\varphi'; r_s, \varphi_P, \epsilon), \varphi')\bigg|_{\epsilon=0}\mathrm{d}\varphi' =$$
$$\frac{\mathrm{i}}{\overline{c}_\infty k_0(1 - M(r_s)\cos\theta)^2}\sum_{n=-\infty}^{\infty}\left(\frac{2}{k_0}\frac{\sqrt{-\eta_n(r_s)}}{r_s Q_n(r_s)}\right)^{1/2}\mathrm{Ai}\left(\eta_n(r_s)\right)\mathrm{e}^{\mathrm{i}k_0\zeta_n}\sum_{m=-\infty}^{\infty}\mathscr{M}_m^*\mathscr{Y}(\varphi; n-m, \varphi_P, \alpha_T), \tag{7.26}$$

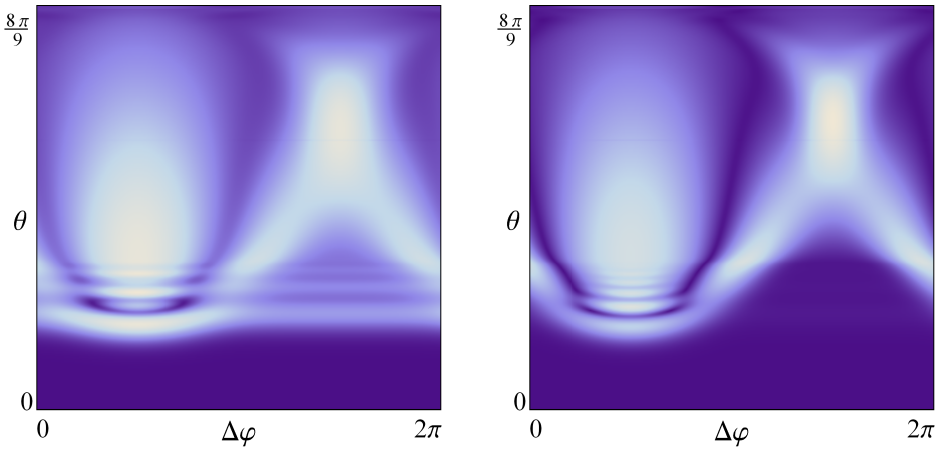

(a) $\varphi_P = \pi/2$, $\alpha_T = 2.5$, $\epsilon = 0.01$ (b) $\varphi_P = \pi/2$, $\alpha_T = 5$, $\epsilon = 0.25$

FIGURE 7.4: Magnitude of perturbed ring source solutions, $\mathscr{D}_\omega^{(c,0)}$.

where,

$$\mathscr{M}_m = \frac{\mathrm{i}}{\overline{c}_\infty k_0 (1 - M(r_s)\cos\theta)^2} \times \left[\sum_{m=-\infty}^{\infty} \left(\frac{2M'(r_s)\cos\theta}{(1 - M(r_s)\cos\theta)} \left(\frac{2}{k_0} \frac{\sqrt{-\eta_m(r_s)}}{r_s Q_m(r_s)} \right)^{1/2} \mathrm{Ai}\left(\eta_m(r_s)\right) + \ldots - \left(\frac{2k_0 Q_m(r_s)}{r_s \sqrt{-\eta_m(r_s)}} \right)^{1/2} \mathrm{Ai}'\left(\eta_m(r_s)\right) \right) \mathrm{e}^{\mathrm{i}k_0\zeta_m} \right]. \tag{7.27}$$

The addition of these two functions is simply,

$$2\,\mathrm{Re}\left[\frac{-\mathrm{i}}{\overline{c}_\infty k_0 (1 - M(r_s)\cos\theta)^2} \sum_{n=-\infty}^{\infty} \left(\frac{2}{k_0} \frac{\sqrt{-\eta_n(r_s)}}{r_s Q_n(r_s)} \right)^{1/2*} \mathrm{Ai}\left(\eta_n(r_s)\right) \mathrm{e}^{-\mathrm{i}k_0\zeta_n} \times \sum_{m=-\infty}^{\infty} \mathscr{M}_m \mathscr{Y}(\varphi; m-n, \varphi_P, \alpha_T) \right], \tag{7.28}$$

since,

$$\mathscr{Y}(\varphi; -m, \varphi_P, \alpha_T) = \mathscr{Y}^*(\varphi; m, \varphi_P, \alpha_T), \tag{7.29}$$

meaning the two functions are conjugates.

The effect of the perturbations on the ring source (shown in Fig. 7.3(c)) are shown in Fig. 7.4. These figures show even for small changes in the symmetry of the source there are significant changes in the symmetry of the field. The cusp pattern is immediately recognisable as soon as the field is perturbed, which is contrast with the weighted fields where the cusp pattern is not too distinguishable. Furthermore, the cusp pattern is of a similar magnitude to the diffraction patterns delimiting the cone of silence.

As with the weighted ring source, the perturbation method can be generalised to include multiple perturbations to the source position. The source distribution is altered to,

$$g(\varphi';r_s,\varphi_{\mathbf{P}},\alpha_{\mathbf{T}},\epsilon) = r_s + \exp\left(-\alpha_{T_1}(\varphi'-\varphi_{P_1})^2\right) + \exp\left(-\alpha_{T_2}(\varphi'-\varphi_{P_2})^2\right) + \ldots \\ \ldots + \exp\left(-\alpha_{T_N}(\varphi'-\varphi_{P_N})^2\right), \tag{7.30}$$

so that $\mathscr{D}_{\omega}^{(c,\epsilon)}$ in (7.24),

$$2\Re\left[\frac{-\mathrm{i}}{\overline{c}_{\infty}k_0(1-M(r_s)\cos\theta)^2}\sum_{n=-\infty}^{\infty}\left(\frac{2}{k_0}\frac{\sqrt{-\eta_n(r_s)}}{r_sQ_n(r_s)}\right)^{1/2*}\mathrm{Ai}\left(\eta_n(r_s)\right)\mathrm{e}^{-\mathrm{i}k_0\zeta_n}\times\right.$$

$$\left.\sum_{m=-\infty}^{\infty}\mathscr{M}_m\left[\mathscr{Y}(\varphi;m-n,\varphi_{P_1},\alpha_{T_1})+\mathscr{Y}(\varphi;m-n,\varphi_{P_2},\alpha_{T_2})+\ldots+\mathscr{Y}(\varphi;m-n,\varphi_{P_N},\alpha_{T_N})\right]\right] \tag{7.31}$$

It is clear from this work that caustics found in the off-axis single point source field do contribute to the field when the source model is asymmetric. This is particularly important to the cusp caustic discovered earlier on in this chapter. This seems to contradict the Gaussian source model shown in Fig. 3.3 which suggests otherwise, as for large angles the source model is exponentially small. Further work is thus required to determine the subtleties of the ring source in this case.

7.2 Conclusion

In this chapter we have investigated the presence of caustics in both discrete and continuous source models. In particular, we were interested in the effect of the cusp caustic discovered in the asymmetric solution of Chapter 6. In the discrete cases, which composed of multiple point sources on the same radius with varying azimuthal positions, the solutions showed the interference between the fold and cusp caustics as the CoS boundary flattened with increasing source numbers. The extreme case of this - the ring source - was the first continuous model examined. The perfect symmetry of this model saw the cusp solutions completely washed out of the field. However, as asymmetry was introduced through perturbations, the cusp becomes more and more important. This is critical for two reasons: first, that the cusp is important because it has the same order of magnitude as the fold; and second, the cusp is a rear-arc or forward beaming phenomenon that has previously not been discovered and may have implications for nozzle interaction.

Chapter 8

Conclusions and future work

In this thesis a CRT solver has been developed to tackle three ray deficiencies: multiplicities, complex rays, and caustics, in an arbitrary inhomogeneous moving medium using a vector Green's function. The aim was to present a viable method for the computation of Green's functions for use with an AA. The utility of this ray solver is greatly enhanced due to the inherent connection between ray bifurcation paths and stable caustics. Caustic stability is an important feature of this thesis as it allows the determination of complex rays through local analysis, thus solving the complex ray deficiency.

The final part of this thesis serves as a proof of principle with the CRT method applied to Lilley's equation in the high-frequency limit. There were several aspects of the solver to benchmark, for instance, the ray parameters, the amplitude and the phase. In the case of the former, the ray solver was used to resolve several ambiguities in the ray parameter bifurcation paths, many of which were explained using the path formulation in bifurcation theory. In the case of the ray amplitude and phase, the ray solver was shown to work well, providing high accuracy. In addition to the exotic behaviour shown by the ray parameters, the amplitude divergences tested the uniform theory by presenting two cuspoid caustics of the same order of magnitude: a fold, and a cusp. While the former is fairly well known, the latter is a new discovery in parallel flows and one that implies that a significant proportion of energy is propagated against the flow.

While the caustics represent the stand out features of the off-axis solution, the use of complex ray tracing for the first time in aeroacoustics would be easy to overlook. These solutions were used mainly to propagate into the cone of silence, a shadow region whose modelling we spent a significant amount of time arguing for. These solutions were straightforward to propagate once the equivalent two-point BVP was posed.

The equivalent BVP also illustrates features in this thesis that we couldn't have predicted at the outset. The identification of the BVP as an optimisation problem allowed us to try other optimisation or root finding methods that were not gratuitous, but shed light on the minimum requirements and limitations of each method. Both the GA and winding

number method were presented in a new setting in the context of ray theory. The former gave a derivative-free route to ray determination, while the WNM was developed to try and provide a method to track down hard-to-find complex solutions. Even though this latter method is still in its infancy, further work could make it a useful addition to the ray menagerie. Another unexpected feature found is the anti-caustic which delimits a section of the CoS. This structure has all the hallmarks of a stable caustic, i.e., the coalescence of ray solutions: however, the singularity was absent and the converse - a vanishing amplitude - is predicted by the rays. We used a new branch of local forms to investigate this, and though the analysis is somewhat limited, it appears that these forms are the correct ones to pursue for further work.

When we consider the larger picture of how the ray solver can be incorporated into a jet-engine noise calculator, we note that noise sources modelled by the Green's function developed in this thesis need not be jet noise sources. The work here could be used to propagate any high-frequency disturbance, for e.g., any of the monopole, dipole or quadrupole sources involved in the modelling of noise generated by solid or permeable boundaries thus potentially extending the Ffowsc Williams-Hawkings [15] acoustic analogies (see also Curle [177]). It is also foreseeable that the solver could propagate modes emitted from the lip of a duct. Modal solutions in ducts with parallel shear but no swirl use the Lilley propagator (known as the Pridmore-Brown [178] operator in this context), see for e.g., Lloyd & Peake [179], and can be described in terms of ray theory. Of course in both cases this would mean the inclusion of solid or permeable boundaries, the possibility of which we discuss in the next section.

A whole-engine prediction tool would also permit further investigation of the effect of the cusp structure discovered in this thesis. The cusp structure has two major implications. The first, that the singularity structure is directed upstream towards the nozzle, could be investigated if the field is allowed to scatter from the nozzle. Even though real flows do spread, the flow near the exit of a round nozzle is essentially parallel shear which lends credibility to such a study. The second implication of the cusp - and the fold for that matter - was noted by (Abrahams et al [28]). Caustics are regions of high intensity and one might expect that these may affect the compressibility of the flow in a non-linear interaction. Of course the acoustic analogy neglects interaction as the regime is purely linear. The present tool being an extension of an analogy is currently incapable of this.

If one were to incorporate the above then the potential is enormous. A generalised framework for doing this would be utilised for the same reasons as the jet: to interrogate novel nozzle geometries. Returning to the work completed in this thesis, it is believed that the ability of the ray solver to provide accurate results particularly in the CoS should prove critical in future jet calculations and that further applications to more complicated and fully asymmetric flow regimes should show similar accuracy.

8.1 Future work

There are several strands of work that can be improved upon or followed up in this thesis. The most important are listed below. They are motivated from all parts of this thesis, and range from general improvements to the ray method to the derivation of new asymptotic methods.

8.1.1 Improvements to the code

This first section outlines some obvious improvements to the ray code, though these are non-trivial.

8.1.1.1 Unfolding singularities in 2D

The first extension is to improve the determination and unfolding of singularities in 2D coordinates. The current method parameterises the receiver curve in one scalar parameter, so the Green's function is calculated in cross-sections. This is not the most efficient method of determining singularities and uniform asymptotics. Each cross-section is currently isolated from its neighbour as the algorithm currently goes. The distance of a caustic point experienced along the receiver curve from a caustic point of higher degeneracy is measured by the singulant Chap. 5. This can be avoided if the most degenerate point on a caustic surface is identified and thus a nearby cross-section of the same caustic can be identified as part of this larger structure.

8.1.1.2 Inclusion of boundaries

An obvious improvement to this code is the effect of boundaries. Boundaries are well known to exhibit peculiarities not found in free space problems (see for e.g., Keller's GTD [40]). Some work that may be of use is Hanyga's use of two-point ray tracing for plane layers, Hanyga [50]. This introduces Snell's law constraints as well as that of the receiver position. This could be used to apply constraints at the surface of a boundary with the final ray segment passing through the observer. Of course boundaries in CRT are analytically continued which introduces interesting problems concering the analytic continuation of non-closed form boundaries that must be expressed by fitting curves.

8.1.1.3 Complex rays without CRT

A question that may arise is, "How do we approximate the field in the CoS without using complex ray tracing?" This motivation for this may be to reduce the computational burden introduced when the ray tracing system doubles in size, or perhaps to stick with an IVP for real rays outside of the CoS. One possible way of doing this is to use

the two-point ray tracing within the fold region near the CoSB delimited by the fold caustic. The field near the caustic is larger than that near the CoSB delimited by the anti-caustic. The two-point bifurcation paths of the fold-coalescing rays are collected and then reflected into the CoS about the fold caustic. The uniform solution to the fold has an analytic solution to its coefficients, these are then calculated using the reflected phase and amplitude. The main issue here would be that this method only works in a region limited to the CoS delimited by the fold (in the φ sense) and there may be phase discrepancies.

8.1.1.4 CRT in an industrial setting

Using the suggestions in this first section on improvements to the CRT code, we can outline a plan for the implementation of CRT in an industrial setting. Despite CRT ticking the requisite boxes of speed, efficiency and accuracy; it is possible that the added complexity of CRT/complex-space setting may be off-putting for industrial software engineers. In large scale computations, there may be the temptation to bypass some of the security mechanisms that increase the likelihood of convergence to ray solutions in aid of computation time (e.g., predictor-corrector). This is understandable, but complex solutions that fail (i.e., diverge) will typically cause the failure of code as whole. Whereas it is advised to use a BVP as the primary calculation stage for the ray solution, the previous section offers a means of bypassing complex ray computation (as opposed to real solutions). One can use symmetry arguments for *all* catastrophe functions to compute their shadow zones; the most important being the fold delimiting the CoS discussed above. Failure from divergence is then cut out of the algorithm and, though spurious convergence of real rays may occur, even the minimum BVP requirements should guarantee physical branches are found.

The CoS problem is one that appears in a variety of jet flows: however, the majority of the apparatus for dealing with complex rays in this thesis is limited by requirements of analytic continuation (i.e., complexification of jet profiles). Industrial solvers typically use RANS whereby mean flow quantities are specified at grid points with an interpolation scheme to fill in the gaps. Although, interpolation schemes can be used to provide analytic continuation, finding a complex global function is expensive. This is where symmetry methods come into the fore. Symmetry methods eliminate any analytic continuation requirements.

A suggested industrial algorithm would be as follows:

1. Fire off a real ray distribution (according to IVP) and calculate intersections with observer sphere.
2. Determine and classify caustics using caustic condition (Jacobian of rays at intersection points to zero) and catastrophe theory, resp.

3. Apply BVP to calculate real multiplicities using caustic classification. Calculate uniform theory coefficients and then apply symmetry methods to calculate complex rays.

For CoS particularly:

1. Proceed with real ray distribution as above.
2. CoS is region for small angles void of real rays. Determine boundary of CoS.
3. Calculate caustic rays along boundary. Assume caustic is fold.
4. Apply BVP in multiplicity region near fold. Calculate real uniform theory coefficients.
5. Use symmetry to propagate into the CoS.
6. Method calculates the dominant near-fold CoS field.

8.1.2 Complex ray methods and expansions

There are several mathematical methods that could be developed to help tricky problems similar to this in the future.

8.1.2.1 Generalised method of Steepest Descents

The first deals with the method of steepest descents used in Chapter 6 to determine the saddle contributions. In specifying the $\mathscr{C}^{(+)}$ contour end-points we have not been rigorous but introduced a heuristic argument for these points. It seems that there is some arbitrariness in specifying the contour, though it is believed the endpoints used in this thesis are correct (this is supported by the contributions matching the field).

The motivation for the paths was the work by Bleistein [170] on a generalisation of the method of steepest descents. The problem therein is much simpler than that in this thesis, as here we deal with nested asymptotic solutions due to the approximations in the integrand. However, the use of the Stokes structure of the integrand is used as in [170] to guide the selection of the paths. Future work would involve the further generalisation of Bleistein's method thus developing a recipe for tackling complicated scattering problems that appear in integral form.

8.1.2.2 Incomplete Erdélyi-Kober expansions

As a subset of the work above a useful technique to have at our disposal is the asymptotic expansion of incomplete Erdélyi-Kober (EK) integrals (Samko et al. [180]). These expansions would allow for a more in-depth study of the phase of the WKB solutions in the ν-plane, particularly in the limit $\nu \to 0$ which is of interest at the anti-caustic. The connection between the phase integral and the EK integrals can be seen as follows.

Taking the phase,

$$I = \int_{r_\delta}^{\gamma} \frac{(r^2 q^2(r) - \nu^2)^{1/2}}{r}\,\mathrm{d}r, \tag{8.1}$$

where γ is a makeshift parameter to illustrate both the incomplete ($\gamma < \infty$) and complete ($\gamma = \infty$) cases. Now make the substitution $u = rq(r)$, so that the phase becomes,

$$I = \int_{\nu}^{u_\gamma} (u^2 - \nu^2)^{1/2} F(u)\,\mathrm{d}u, \tag{8.2}$$

where $F(rq(r)) = 1/r(rq(r))'$. This can be compared to the incomplete left-hand sided EK integral,

$$\left[K^{\tau,\alpha}_{\beta,u_\gamma} f\right](\nu) = \frac{\beta}{\Gamma(\alpha)} \nu^{\beta\tau} \int_{\nu}^{u_\gamma} (u^\beta - \nu^\beta)^{\alpha-1} u^{-\beta(\tau+\alpha-1)-1} f(u)\,\mathrm{d}u, \quad \alpha, \beta > 0 \tag{8.3}$$

so that,

$$I = \frac{\Gamma(\alpha)}{\beta} \nu^{-\beta\tau} \left[K^{\tau,\alpha}_{\beta,u_\gamma} u^{\beta(\tau+\alpha-1)+1} F\right](\nu) = \int_{\nu}^{u_\gamma} (u^\beta - \nu^\beta)^{\alpha-1} F(u)\,\mathrm{d}u, \tag{8.4}$$

with $\alpha = 3/2, \beta = 1/2$.

The reason for requiring incompleteness is simple: the integration of regular phases to the far-field $u_\gamma = \infty$ will lead to a divergent result. The integrals must be truncated and expansions may contain information pertinent to both limits of the integral. If the integrals did converge with $u_\gamma = \infty$ then one possible starting point for asymptotic analysis would be the Mellin-Barnes technique (Bleistein & Handelsman [134]) which can handle $\nu \to 0$ and $\nu \to \infty$.

8.1.2.3 CDP and Eucatastrophes

The work in this thesis concerning the CDP and eucatastrophes is incomplete. The eucatastrophes were introduced to analyse the anti-caustic away from the CDP. Further work is required to finish this analysis which would involve: an indepth study of the eucatastrophes' singularity structures, particularly their degenerate points for which the logarithmic term is zero, and a determination of appropriate contours to fix the definition; complete the analysis of the anti-caustic away from the CDP (as suggest in the main text) to fix the correct $\mathscr{E}_K$; finally, undertake a local analysis near CDP to determine if this can be explained in terms of a higher-order $\mathscr{E}_K$.

This should allow the clock diagram of Chapter 6 to be completed with certainty whereas at the moment the hypothetical ray explanation is speculative. Furthermore, this may lead to a global expression of the field once all rays of the field are included.

8.1.2.4 Adapt winding number calculation to forms with poles and cases of non-soluble two-point ray tracing

The winding number method developed in Chapter 4 has some serious shortcomings. The obvious issue is the limitation to analytic profiles without poles. The first amendment would to develop theory for the case where the analytic continuation of the ray trajectories contains poles: such cases occur in the jet where the exponential decay of the shear layer engenders poles in the complex plane.

The second amendment would be to extend the method to cases where the two-point function is not soluble in closed form as in the LLP case. This means a numerical procedure for sampling the two-point function to compute the winding number integrals.

8.1.2.5 Trapezoidal rule for amplitude coefficients

One reason we might pursue the catastrophe theory based uniform approximations is due to recent developments in the computation of the uniform amplitude coefficients. From (5.31) and (5.33), Chapter 5, for corank 1 potentials then,

$$G_r(t) = \sum_{k=0}^{K} c_{k,r}(\boldsymbol{\xi}) t^k + \frac{\mathrm{d}\Phi_K}{\mathrm{d}t} H_r(t;\boldsymbol{\xi}) = \frac{\mathrm{d}H_{r-1}}{\mathrm{d}t}, \tag{8.5}$$

then $G_0(t)$ can be trivially expressed as,

$$G_0(t) = \frac{1}{2\pi \mathrm{i}} \oint_\gamma G_0(t') R_0(t,t')\,\mathrm{d}t', \quad R_0(t,t') = \frac{1}{t'-t}, \tag{8.6}$$

where γ is a circular contour that encompasses the origin and any saddles $t^\star$. This can be shown to extend to any level r (Berry & Howls [81]) as,

$$G_r(t) = \frac{1}{2\pi \mathrm{i}} \oint_\gamma G_0(t') R_r(t,t')\,\mathrm{d}t', \quad R_r(t,t') = \left(-\frac{1}{\mathrm{d}\Phi_K/\mathrm{d}t}\frac{\partial}{\partial t'}\right)^r \frac{1}{t'-t}. \tag{8.7}$$

This allows any level of coefficients $c_{k,r}$ to be calculated (further details in [81]). Surprisingly, this is not the further development alluded to: this is in how we calculate the contour integrals to find $G_r(t)$. The development of a exponentially convergent trapezoidal rule due to Trefethen & Weideman [181] allows the contour integrals to be evaluated to a high-degree of accuracy by evaluating the integrand on the unit circle at a discrete number of points (e.g., $2N$), for example,

$$\begin{aligned} G_r(t) = \frac{1}{2\pi \mathrm{i}} \oint_\gamma G_0(t') R_r(t,t')\,\mathrm{d}t' \approx \\ \frac{1}{2N} \sum_{k=1}^{2N} \rho_\gamma \omega_k G_0(\rho_\gamma \omega_k) R_r(t, \rho_\gamma \omega_k), \end{aligned} \tag{8.8}$$

where here $\omega_k = \mathrm{e}^{\pi \mathrm{i}/N}$ is the $2N^{th}$ root of unity and ρ_γ is the radius of the circular contour γ. This approximation converges exponentially fast if the integrand is analytic in an annulus supporting the contour γ.

This provides an alternative method to calculating the coefficients that otherwise are tackled by an iterative method. An interesting study would be to compare these methods both in the accuracy of the uniform field and speed of computation as integral approximations such as this have not be carried out using ray tracing methods before. It is also plausible that this method could be applied to the single variable winding number theory mentioned in the previous section.

Appendix A

Second Order Quadrupole Tensor

In this appendix a second order quadrupole tensor is derived that is valid in arbitrary orthogonal coordinates. Commonly this tensor is only required in Cartesian coordinates, but for the purposes of the main text a general expression is derived, which is then specialised to cylindrical polar coordinates. The notation in this appendix is self-contained. The operator required is the double divergence applied to the source distribution F_{ij}. Using the economy of index notation this is typically written,

$$\frac{\partial^2 F_{ij}}{\partial \xi_i \partial \xi_j}. \tag{A.1}$$

It is well known that the derivative of a tensor is not a tensor, so the derivatives must be corrected for the spurious effects in coordinate curvature. What is really meant by (A.1) is $F_{ij,ij}$, where F_{ij} are the ordinary components of a second order tensor and $,ij$ denotes a double derivative.

First, the ordinary components of a tensor are converted to contravariant components (denoted by lowercase and upstairs indices) using the following,

$$\begin{aligned} \text{First order (vector)}, \quad \boldsymbol{F} &= a_n F_n = a_n h_n \left(\frac{F_n}{h_n} \right) = a_n h_n f^n, \\ \text{Second order}, \quad \boldsymbol{F} &= a_n a_m F_{nm} = a_n a_n h_n h_m \left(\frac{F_{nm}}{h_n h_m} \right) = a_n a_m h_n h_m f^{nm}, \end{aligned} \tag{A.2}$$

where the a_i's are basis vectors and h_i's are the stretch factors of vector calculus.

From Morse & Feshbach [57], the derivatives and divergence (respectively) of contravariant tensors are:

First order,

$$f^i{}_{,j} = \frac{\partial f^i}{\partial \xi_j} + f^m \left\{ \begin{matrix} i \\ m\, j \end{matrix} \right\}, \tag{A.3}$$

and

$$f^{n}{}_{,n} = \frac{1}{h_1 h_2 h_3}\frac{\partial}{\partial \xi_n}\left(f^n h_1 h_2 h_3\right). \tag{A.4}$$

Second order,

$$f^{ij}{}_{,k} = \left(\frac{\partial f^{ij}}{\partial \xi_k}\right) + f^{im}\left\{ \begin{matrix} j \\ m\,k \end{matrix} \right\} + f^{nj}\left\{ \begin{matrix} i \\ n\,k \end{matrix} \right\}. \tag{A.5}$$

Where the terms in braces are Christoffel symbols and are defined as,

$$\left\{ \begin{matrix} i \\ i\,i \end{matrix} \right\} = \frac{1}{h_i}\frac{\partial h_i}{\partial \xi_i}, \quad \left\{ \begin{matrix} i \\ i\,j \end{matrix} \right\} = \left\{ \begin{matrix} i \\ j\,i \end{matrix} \right\} = \frac{1}{h_i}\frac{\partial h_i}{\partial \xi_j}, \quad \left\{ \begin{matrix} j \\ i\,i \end{matrix} \right\} = -\frac{h_i}{h_j^2}\frac{\partial h_i}{\partial \xi_j}, \quad \left\{ \begin{matrix} i \\ j\,k \end{matrix} \right\} = 0, \tag{A.6}$$

with the last term true if all indices are different.

For the quadrupole tensor, equations (A.4) and (A.5) are applied in series. Firstly, to calculate $F_{ij,ij}$, one of the indices of $f^{ij}{}_{,k}$ is contracted, j say,[1]

$$f^{ij}{}_{,j} = \left(\frac{\partial f^{ij}}{\partial \xi_j}\right) + f^{im}\left\{ \begin{matrix} j \\ m\,j \end{matrix} \right\} + f^{nj}\left\{ \begin{matrix} i \\ n\,j \end{matrix} \right\}. \tag{A.7}$$

The divergence is then taken on the last remaining free index, i, using the following notation $f^{ij}{}_{,ji} = \left(f^{ij}{}_{,j}\right)_{,i} = \tilde{f}^{i}{}_{,i}$. The divergence $\tilde{f}^{i}{}_{,i}$ can be used to write the expression out in full,

$$\begin{aligned} \tilde{f}^{i}{}_{,i} &= \frac{1}{h_1 h_2 h_3}\frac{\partial}{\partial \xi_i}\left(\tilde{f}^i h_1 h_2 h_3\right), \\ &= \frac{1}{h_1 h_2 h_3}\frac{\partial}{\partial \xi_i}\left(\left[\left(\frac{\partial f^{ij}}{\partial \xi_j}\right) + f^{im}\left\{ \begin{matrix} j \\ m\,j \end{matrix} \right\} + f^{nj}\left\{ \begin{matrix} i \\ n\,j \end{matrix} \right\}\right] h_1 h_2 h_3\right). \end{aligned} \tag{A.8}$$

Finally, converting back to ordinary components F_{ij},

$$F_{ij,ij} = \frac{1}{h_1 h_2 h_3}\frac{\partial}{\partial \xi_i}\left(\left[\frac{\partial}{\partial \xi_j}\left(\frac{F_{ij}}{h_i h_j}\right) + \frac{F_{im}}{h_i h_m}\left\{ \begin{matrix} j \\ m\,j \end{matrix} \right\} + \frac{F_{nj}}{h_n h_j}\left\{ \begin{matrix} i \\ n\,j \end{matrix} \right\}\right] h_1 h_2 h_3\right). \tag{A.9}$$

A.0.1 Cylindrical polar example

In cylindrical polar coordinates $\{\xi_1, \xi_2, \xi_3\} = \{x, r, \varphi\}$ the stretch factors are as follows $\{h_1, h_2, h_3\} = \{1, 1, r\}$. The Christoffel matrices are,

$$\left\{ \begin{matrix} 1 \\ i\,j \end{matrix} \right\} = \begin{pmatrix} 0 & 0 & 0 \\ 0 & 0 & 0 \\ 0 & 0 & 0 \end{pmatrix}, \quad \left\{ \begin{matrix} 2 \\ i\,j \end{matrix} \right\} = \begin{pmatrix} 0 & 0 & 0 \\ 0 & 0 & 0 \\ 0 & 0 & -r \end{pmatrix}, \quad \left\{ \begin{matrix} 3 \\ i\,j \end{matrix} \right\} = \begin{pmatrix} 0 & 0 & 0 \\ 0 & 0 & r^{-1} \\ 0 & r^{-1} & 0 \end{pmatrix}. \tag{A.10}$$

[1] The end result is independent of contraction order.

The full tensor sum in (i,j) is then,[2]

$$\begin{aligned}
&\underbrace{\frac{\partial^2 f^{11}}{\partial x^2}}_{(1,1)} + \underbrace{\frac{\partial^2 f^{12}}{\partial x \partial r}}_{(1,2)} + \underbrace{\frac{\partial^2 f^{13}}{\partial x \partial \varphi} + \frac{1}{r}\frac{\partial f^{12}}{\partial x}}_{(1,3)} + \underbrace{\frac{1}{r}\frac{\partial^2}{\partial x \partial r} r f^{21}}_{(2,1)} + \underbrace{\frac{1}{r}\frac{\partial}{\partial r} r \frac{\partial f^{22}}{\partial r}}_{(2,2)} + \dots \\
\dots + &\underbrace{\frac{1}{r}\frac{\partial^2}{\partial \varphi \partial r} r f^{23} + \frac{1}{r}\frac{\partial f^{22}}{\partial r} - \frac{1}{r}\frac{\partial}{\partial r} r^2 f^{33}}_{(2,3)} + \underbrace{\frac{\partial^2 f^{31}}{\partial x \partial \varphi}}_{(3,1)} + \underbrace{\frac{\partial^2 f^{32}}{\partial \varphi \partial r} + \frac{1}{r}\frac{\partial f^{32}}{\partial \varphi}}_{(3,2)} + \dots \\
&\dots + \underbrace{\frac{\partial^2 f^{33}}{\partial \varphi^2} + \frac{1}{r}\frac{\partial f^{23}}{\partial \varphi} + \frac{1}{r}\frac{\partial f^{32}}{\partial \varphi}}_{(3,3)}.
\end{aligned} \tag{A.11}$$

Converting back to ordinary tensor components,

$$\begin{aligned}
&\underbrace{\frac{\partial^2 F_{11}}{\partial x^2}}_{(1,1)} + \underbrace{\frac{\partial^2 F_{12}}{\partial x \partial r}}_{(1,2)} + \frac{1}{r}\underbrace{\frac{\partial^2 F_{13}}{\partial x \partial \varphi} + \frac{1}{r}\frac{\partial F_{12}}{\partial x}}_{(1,3)} + \underbrace{\frac{1}{r}\frac{\partial^2}{\partial x \partial r} r F_{21}}_{(2,1)} + \underbrace{\frac{1}{r}\frac{\partial}{\partial r} r \frac{\partial F_{22}}{\partial r}}_{(2,2)} + \dots \\
\dots + &\underbrace{\frac{1}{r}\frac{\partial^2}{\partial \varphi \partial r} F_{23} + \frac{1}{r}\frac{\partial F_{22}}{\partial r} - \frac{1}{r}\frac{\partial}{\partial r} F_{33}}_{(2,3)} + \underbrace{\frac{1}{r}\frac{\partial^2 F_{31}}{\partial x \partial \varphi}}_{(3,1)} + \underbrace{\frac{\partial^2}{\partial \varphi \partial r}\frac{F_{32}}{r} + \frac{1}{r^2}\frac{\partial F_{32}}{\partial \varphi}}_{(3,2)} + \dots \\
&\dots + \underbrace{\frac{1}{r^2}\frac{\partial^2 F_{33}}{\partial \varphi^2} + \frac{1}{r^2}\frac{\partial F_{23}}{\partial \varphi} + \frac{1}{r^2}\frac{\partial F_{32}}{\partial \varphi}}_{(3,3)},
\end{aligned} \tag{A.12}$$

If the operators are rearranged according to which component F_{ij} they operate on (simplifying some of the operators) then it is clear the divergence can be written as the contraction of a symmetric quadrupole operator, M_{ij}, with the component tensor F_{ij}. M_{ij} is given as,

$$M_{ij} = \begin{pmatrix} \frac{\partial^2}{\partial x^2} & \frac{1}{r}\frac{\partial^2}{\partial x \partial r} r & \frac{1}{r}\frac{\partial^2}{\partial x \partial \varphi} \\ \frac{1}{r}\frac{\partial^2}{\partial x \partial r} r & \frac{1}{r}\frac{\partial^2}{\partial r^2} r & \frac{1}{r^2}\frac{\partial^2}{\partial r \partial \varphi} r \\ \frac{1}{r}\frac{\partial^2}{\partial x \partial \varphi} & \frac{1}{r^2}\frac{\partial^2}{\partial r \partial \varphi} r & \frac{1}{r^2}\frac{\partial^2}{\partial \varphi^2} - \frac{1}{r}\frac{\partial}{\partial r} \end{pmatrix}. \tag{A.13}$$

This final expression can be found in Tester & Morfey [29], however the general expression (A.9) is not readily available in books on tensor analysis. A final check can be made on this operator by taking the trace of M_{ij} and comparing with the Laplacian operator in cylindrical polars: the two must be equal.

[2] Contributions from the term (i,j) are not equal to those of (j,i) in general.

Appendix B

Delta Function Properties

Rather than having to compute a new solution for each component of the Green's function, it is convenient to express each component in terms of one solution to which a variety of derivatives and scalar multiplications can be applied (in the source variable) to generate other components. In the main text this technique is also used when convolution algebra is used to transfer source derivatives to the Green's function.

A good example is the general expression for the solutions to Lilley's equation. These are in the form,

$$\mathscr{L}_\omega g_i = \mathscr{A}_i(\delta(\boldsymbol{x} - \boldsymbol{x}_s)\delta(t - t_s)), \tag{B.1}$$

where $\mathscr{A}_{\boldsymbol{x}_i}$ is shorthand for linear derivative operations and multiplications by scalar functions. The properties of the delta function allows $\mathscr{A}_{\boldsymbol{x}_i}$ to be replaced by its adjoint $\mathscr{A}^*_{\boldsymbol{x}_{s_i}}$ operating on the source coordinates. So if g is a solution to (B.1) with $\mathscr{A}_i = 1$ then $g_i = \mathscr{A}^*_{\boldsymbol{x}_{s_i}} g$.

The following sections look at the adjoint for the most common components of $\mathscr{A}$ and how these can be applied to the ray theory solution.

B.1 Scalars and derivatives

B.1.1 Multiplication by scalars

Multiplication by a scalar function is simple using the properties of delta functions,

$$f(\boldsymbol{x})\delta(\boldsymbol{x} - \boldsymbol{x}_s) = f(\boldsymbol{x}_s)\delta(\boldsymbol{x} - \boldsymbol{x}_s), \tag{B.2}$$

B.1.2 Action of derivatives on the delta function

The action of the observer and time derivatives can be transferred to source function as follows,

$$\int_{-\infty}^{\infty}\left(\frac{\partial}{\partial x}\delta(x-x_s)\right)\varphi(x)\,\mathrm{d}x=-\int_{-\infty}^{\infty}\left(\frac{\partial}{\partial x_s}\delta(x-x_s)\right)\varphi(x)\,\mathrm{d}x,\quad \varphi\in\mathbb{C}^{\infty},\tag{B.3}$$

so,

$$\frac{\partial}{\partial x}\delta(x-x_s)=-\frac{\partial}{\partial x_s}\delta(x-x_s).\tag{B.4}$$

Using this result the following operator relation holds,

$$\frac{\overline{D}}{Dt}\delta(x-x_s)\delta(t-t_s)=-\frac{\overline{D}}{Dt_s}\delta(x-x_s)\delta(t-t_s),\tag{B.5}$$

where,

$$\frac{\overline{D}}{Dt_s}=\frac{\partial}{\partial t_s}+\bar{u}_1(x_s)\frac{\partial}{\partial x_s}.\tag{B.6}$$

For multidimensional delta functions,

$$\frac{\partial^{n_1+\cdots+n_k}}{\partial x_1^{n_1}\cdots\partial x_k^{n_k}}\delta(\boldsymbol{x}-\boldsymbol{x}_s)=(-)^{n_1+\cdots+n_k}\frac{\partial^{n_1+\cdots+n_k}}{\partial x_{s_1}^{n_1}\cdots\partial x_{s_k}^{n_k}}\delta(\boldsymbol{x}-\boldsymbol{x}_s),\tag{B.7}$$

and,

$$\frac{\partial^{n}}{\partial x_1\cdots\partial x_n}f(\boldsymbol{x})\delta(\boldsymbol{x}-\boldsymbol{x}_s)=\sum_{S}(-)^{L_s}\frac{\partial^{|S|}\delta(\boldsymbol{x}-\boldsymbol{x}_s)}{\Pi_{i\in S}\partial x_{s_i}}\frac{\partial^{n-|S|}f(\boldsymbol{x}_s)}{\Pi_{i\notin S}\partial x_i},\tag{B.8}$$

where S ranges from 0 to n and indexes the 2^n subsets of $\{1,...,n\}$ (i.e. the power set of S), and L_s is the cardinality of the subset of $i\in S$. This can be used to generalise (B.7) either by applying (B.8) and then collapsing some of the indices (i.e. $n=n_1+\cdots+n_k$), or by applying the following,

$$\frac{\partial^{n_1+\cdots+n_k}}{\partial x_1^{n_1}\cdots\partial x_k^{n_k}}f(\boldsymbol{x})\delta(\boldsymbol{x}-\boldsymbol{x}_s)=\sum_{\ell_1=0}^{n_1}\cdots\sum_{\ell_k=0}^{n_k}\binom{n_1}{\ell_1}\cdots\binom{n_k}{\ell_k}(-)^{\ell_1+\cdots+\ell_k}\frac{\partial^{\ell_1+\cdots+\ell_k}\delta(\boldsymbol{x}-\boldsymbol{x}_s)}{\partial x_{s_1}^{\ell_1}\cdots\partial x_{s_k}^{\ell_k}}\frac{\partial^{n_1-\ell_1+\cdots+n_k-\ell_k}f(\boldsymbol{x}_s)}{\partial x_1^{n_1-\ell_1}\cdots\partial x_k^{n_k-\ell_k}},\tag{B.9}$$

B.2 Application to ray solution

When applying the adjoint operator to the ray solution it is only the derivatives w.r.t. the source that are of concern. Using (B.10) the source derivatives are applied to the

pressure ray ansatz (for e.g., see Chap. 3, §3.3.2),

$$\frac{\partial^{n_1+\cdots+n_k}}{\partial x_{s1}^{n_1}\cdots\partial x_{s_k}^{n_k}}\mathrm{e}^{\mathrm{i}k_0 S}\sum_{m=0}^{\infty}\frac{A_m}{(\mathrm{i}k_0)^m} = \sum_{m=0}^{\infty}\frac{1}{(\mathrm{i}k_0)^m}\sum_{\ell_1=0}^{n_1}\cdots\sum_{\ell_k=0}^{n_k}\binom{n_1}{\ell_1}\cdots\binom{n_k}{\ell_k}\frac{\partial^{\ell_1+\cdots+\ell_k}\mathrm{e}^{\mathrm{i}k_0 S}}{\partial x_{s1}^{\ell_1}\cdots\partial x_{s_k}^{\ell_k}}\frac{\partial^{n_1-\ell_1+\cdots+n_k-\ell_k}A_m}{\partial x_{s1}^{n_1-\ell_1}\cdots\partial x_{s_k}^{n_k-\ell_k}}. \tag{B.10}$$

It is the differentiation of the $\mathrm{e}^{\mathrm{i}k_0 S}$ term that generates new powers of k_0 so that asymptotically only the term multiplied by the largest power is required. The exponential part of the sum has leading order,

$$\frac{\partial^{\ell_1+\cdots+\ell_k}\mathrm{e}^{\mathrm{i}k_0 S}}{\partial x_{s1}^{\ell_1}\cdots\partial x_{s_k}^{\ell_k}} \sim (\mathrm{i}k_0)^{\ell_1+\cdots+\ell_k}\Pi_{i=1}^{k}\left(\frac{\partial S}{\partial x_{s_i}}\right)^{\ell_i}\mathrm{e}^{\mathrm{i}k_0 S} \quad k_0\to\infty. \tag{B.11}$$

Given this, it is clear that the dominant term in (B.10) occurs when $\ell_1+\cdots+\ell_k = n$, so under this evaluation (B.10) is asymptotic to (B.11) multiplied by the leading order ray amplitude term A_0.

As an example with $n = 2$, a quadrupole operator $\partial^2/\partial x_i\partial x_j$ will give leading order solution,

$$\frac{\partial^2\mathrm{e}^{\mathrm{i}k_0 S}}{\partial x_i\partial x_j} \sim -k_0^2 p_{s_i}p_{s_j}\mathrm{e}^{\mathrm{i}k_0 S}, \tag{B.12}$$

since,

$$\frac{\partial S}{\partial x_{s_i}} = -p_{s_i}. \tag{B.13}$$

Appendix C

Numerical methods for continuation

This appendix contains the machinery for realising the continuation theory of Chapter 4 numerically. The first part of this appendix is devoted to computing the tangent vector to $D_Z\mathbf{F}$ at regular points using the QR decomposition. The second part concentrates on calculating the null spaces of $D_Z\mathbf{F}$ using Langrangian multipliers, where $D_Z\mathbf{F}$ is preferred to $D_z\mathbf{F}$ as the former is the more general case. The third part of this appendix is devoted to the numerical calculation of the Fréchet derivatives required in the Liapunov-Schmidt reduction.

C.1 QR decomposition to calculate tangent vectors

The QR decomposition is the most straightforward way of calculating the tangent $\mathbf{t}$ induced by the matrix $D_Z\mathbf{F}$. The QR decomposition factors a matrix $A \in \mathbb{R}^{n\times k}$ with rank r, into the product of a square orthogonal $Q \in \mathbb{R}^{n\times n}$, and upper triangular $R \in \mathbb{R}^{n\times k}$ with its bottom $(n-r)\times k$ block zero. If the matrix is singular, that is $r < n$, then the QR decomposition exists, but it is not unique.

Since the tangent satisfies $D_Z\mathbf{F}\cdot\mathbf{t} = 0$, which implies $\mathbf{t}^* D_Z\mathbf{F}^* = \mathbf{0}$ (the RHS is a vector when matrix isn't square), then,

$$D_Z\mathbf{F}^* = Q\begin{pmatrix}\widetilde{R}\\ \mathbf{0}^T\end{pmatrix}. \tag{C.1}$$

Here the standard notation of QR is changed slightly and the zero bottom row elicited due to a result on skinny matrices ($n > k$). Now taking the last column of Q, Q_{N+1},

and calculating $Q_{N+1}^{*} D_Z \mathbf{F}^{*}$ then due to the orthogonality of Q,

$$Q_{N+1}^{*} \begin{pmatrix} & & \\ Q_1, Q_2, \ldots, Q_{N+1} & & \\ & & \end{pmatrix} \begin{pmatrix} \widetilde{R}_1 \\ \widetilde{R}_2 \\ \vdots \\ \widetilde{R}_N \\ \mathbf{0}^T \end{pmatrix} = \mathbf{0}, \tag{C.2}$$

where $\widetilde{R}_i$ denotes a row of $\widetilde{R}$. Clearly Q_{N+1} is the desired vector that can then be normalised to find $\mathbf{t}$.

C.2 Calculating null spaces using Lagrangian multipliers

The method of Lagrangian multipliers is a strategy for finding the local maxima and minima of a function subject to constraints. The method yields necessary, but not sufficient, conditions for optimality in constrained problems. Consider the optimisation problem,

$$\begin{aligned} &\text{maximize} \quad f(\boldsymbol{x}), \\ &\text{subject to} \quad g(\boldsymbol{x}) = c, \quad c \in \mathbb{R}. \end{aligned}$$

Then one looks to form the Lagrangian $\mathscr{K}$, with Lagrangian multipler k,

$$\mathscr{K}(\boldsymbol{x}) = f(\boldsymbol{x}) + k\left(g(\boldsymbol{x}) - c\right), \tag{C.3}$$

finding all the stationary points $\{\boldsymbol{x}^{\star}, k^{\star}\}$ for which $\partial_{x_i} \mathscr{K} = \mathbf{0}$. The gradient condition means that the level sets of f and g are parallel at optimum or stationary points. However, not all the stationary points will satisfy the constraints so another simultaneous equation $g(\boldsymbol{x}^{\star}) = c$ is added.

C.2.1 Application to the nonlinear map $\mathbf{F}(\mathbf{Z}) = \mathbf{0}$

As a first application, it is possible to show that calculating the tangent to bifurcation paths using (C.1) minimizes the error in the estimate $\widetilde{\mathbf{Z}}$ of $\mathbf{Z}$. As an optimisation problem this is stated as finding the minimal $||\mathbf{Z} - \widetilde{\mathbf{Z}}||$ with the constraint $\mathbf{F}(\mathbf{Z}) = \mathbf{0}$, i.e., $\min_{\mathbf{Z}}\{||\mathbf{Z} - \widetilde{\mathbf{Z}}|| : \mathbf{F}(\mathbf{Z}) = \mathbf{0}\}$. As there are a vector of constraints, a multiple constraint generalisation of the Lagrangian (C.3) can be formed,

$$||\mathbf{Z} - \widetilde{\mathbf{Z}}||^2 - \mathbf{F}^{*} k = 0, \quad k \in \mathbb{C}^{n_D}, \quad n_D = \dim(\mathbf{F}), \tag{C.4}$$

leading to the simultaneous equations,

$$\mathbf{F} = \mathbf{0}, \qquad n_D \text{ equations}, \tag{C.5}$$

$$\mathbf{Z} - \widetilde{\mathbf{Z}} = D_Z\mathbf{F}^* k, \quad n_D \text{ equations}. \tag{C.6}$$

Equation (C.6) can be improved upon by eliminating the multipliers at the expense of computing the tangent. Since the tangent is orthogonal to $D_Z\mathbf{F}$, dot both sides with $\mathbf{t}$,

$$\mathbf{t}^* \left(\mathbf{Z} - \widetilde{\mathbf{Z}}\right) = \mathbf{t}^* D_Z\mathbf{F}^* k = 0. \tag{C.7}$$

This is just a statement that the predicted point (from an Euler step) subtracted (vectorially) from the true point creates a vector perpendicular to the curve at the true point.

C.2.2 Application to tangent computation at a caustic

At bifurcation points the Liapunov-Schmidt decomposition requires all left-null and null vectors. Dealing with approximations means a minimisation problem needs to be formed in order to get a close approximation to these vectors. One of the null vectors is already found using the QR decomposition (still a valid at the caustic) from the previous section, so it is a matter of computing the other members. For a corank 1 problem, the matrix $D_Z\mathbf{F}$ has one left-null vector and two null space vectors; for corank 2, the matrix $D_Z\mathbf{F}$ has two left-null vectors and three null vectors.

Consider the vector v_1 as the null vector that has already been computed from the QR decomposition. Then the other members of the null space v_i can be computed using the minimisation problem [55]:

$$\min_{v_i}\{||D_Z\mathbf{F}\, v_i||^2 + (v_1^* v_i)^2 : ||v_i|| = 1\}. \tag{C.8}$$

Define the matrix A as,

$$A \equiv \begin{pmatrix} D_Z\mathbf{F} \\ v_1^* \end{pmatrix}, \tag{C.9}$$

then the minimisation problem is

$$\min_{v_i}\{v_i^* A^* A\, v_i : ||v_i|| = 1\}. \tag{C.10}$$

Now forming the Lagrangian,

$$\mathscr{K} = \frac{1}{2}\left(v_i^* A^* A\, v_i - k\left(||v_i||^2 - 1\right)\right), \tag{C.11}$$

and then differentiating (the matrix A is known at the bifurcation point and is constant),

$$\frac{\partial \mathscr{K}}{\partial v_i} = v_i^* A A^* - k v_i^*, \tag{C.12}$$

equating to zero to find the stationary points and taking the conjugate transpose leads to the eigenvalue equation,

$$A^* A v_i = k v_i, \tag{C.13}$$

where k is the eigenvalue and v_i is the eigenvector. Substituting $v_i^* A^* A v_i = k v_i^* v_i$ back into the minimisation problem then,

$$\min_{v_i} \{k v_i^* v_i : ||v_i|| = 1\}. \tag{C.14}$$

which, with clearly non-trivial v_i, must mean that the smallest eigenvalue(s) k is required along with corresponding eigenvector(s) v_i to be the solutions.

For the left-null vector w a similar approach is taken by forming the minimisation problem,

$$\min_{w} \{||D_Z \mathbf{F}^* w_i|| : ||w_i|| = 1\}. \tag{C.15}$$

which again has an eigenvalue - eigenvector solution if the Lagrangian approach is utilised.

The QR decomposition for $D_Z \mathbf{F}^*$ (see Eq. (C.1)) allows the problem to be reduced to calculating the smallest eigenvalues and corresponding eigenvectors of the matrices $\widetilde{R}\widetilde{R}^*$ and $\widetilde{R}^*\widetilde{R}$ for the null vector and left-null vectors respectively.

C.2.3 Numerical examples of null spaces

To illustrate how well the above algorithm works for computing each null space, it is applied to a perturbation of the following matrix which suffers from a corank 1 degeneracy,

$$A = \begin{pmatrix} 1 & 2 & 1 & 2 \\ 1 & 2 & 1 & 3 \\ 3 & 6 & 3 & 7 \end{pmatrix}. \tag{C.16}$$

It is straightforward to show that A has nullspace spanned by $v_1 = (-2, 1, 0, 0)^T$ and $v_2 = (0, 0, 0, 1)^T$ and left-nullspace spanned by $w_1 = (-2, -1, 1)^T$. However at the approximate bifurcation point the matrix A will contain some numerical error so the algorithm is applied to,

$$A_p = \begin{pmatrix} 1 & 2 & 1 & 2 \\ 1 & 2 & 1 & 3 \\ 3 & 6.001 & 3 & 7.001 \end{pmatrix}. \tag{C.17}$$

The small perturbation to A means it has full rank, empty left-null set, and one null vector $(0.7071, 0, -0.7071, 0)^T$. As an approximation to the spaces of A this is not complete.

The calculation of the null spaces is greatly facilitated by the following transformation,

$$v_2 = Q \begin{pmatrix} e \\ 0 \end{pmatrix}, \tag{C.18}$$

where e is the eigenvector of $\widetilde{R}\widetilde{R}^*$. Then the QR decomposition of A_p^* is,

$$Q = \begin{pmatrix} 0.3162 & -0.2582 & -0.5774 & 0.7071 \\ 0.6325 & -0.5164 & 0.5774 & 0 \\ 0.3162 & -0.2582 & -0.5774 & -0.7071 \\ 0.6325 & 0.7746 & 0 & 0 \end{pmatrix}, \quad R = \begin{pmatrix} 3.1623 & 3.7947 & 10.1206 \\ 0 & 0.7746 & 0.7749 \\ 0 & 0 & 0.0006 \\ 0 & 0 & 0 \end{pmatrix}, \tag{C.19}$$

so we can form $\widetilde{R}^*\widetilde{R}$ and $\widetilde{R}\widetilde{R}^*$,

$$\widetilde{R}^*\widetilde{R} = \begin{pmatrix} 10.0001 & 12.0000 & 32.0044 \\ 12.0000 & 14.9998 & 39.0049 \\ 32.0044 & 39.0049 & 103.0270 \end{pmatrix}, \quad \widetilde{R}\widetilde{R}^* = \begin{pmatrix} 126.8264 & 10.7818 & 0.0061 \\ 10.7818 & 1.2005 & 0.0005 \\ 0.0061 & 0.0005 & 0.0000 \end{pmatrix}. \tag{C.20}$$

and then calculate the eigenvalues and eigenvectors for each matrix:

For $\widetilde{R}^*\widetilde{R}$,

$$k = \{0, 0.2818, 127.75\}, \quad e = \begin{pmatrix} 0.8164 \\ 0.4084 \\ -0.4082 \end{pmatrix}, \begin{pmatrix} 0.5057 \\ -0.8470 \\ 0.1640 \end{pmatrix}, \begin{pmatrix} 0.2788 \\ 0.3403 \\ 0.8980 \end{pmatrix} \tag{C.21}$$

For $\widetilde{R}\widetilde{R}^*$,

$$k = \{0, 0.2818, 127.7451\}, \quad e = \begin{pmatrix} -0.0001 \\ 0.0002 \\ 1.0000 \end{pmatrix}, \begin{pmatrix} 0.0849 \\ -0.9964 \\ 0.0002 \end{pmatrix}, \begin{pmatrix} 0.9964 \\ 0.0849 \\ 0 \end{pmatrix}. \tag{C.22}$$

The left-null and null vectors can be calculated thus,

$$w_1 = \begin{pmatrix} 0.8164 \\ 0.4084 \\ -0.4082 \end{pmatrix}, \quad v_2 = Q \begin{pmatrix} -0.0001 \\ 0.0002 \\ 1.0000 \\ 0.0000 \end{pmatrix} = \begin{pmatrix} -0.5774 \\ 0.5772 \\ -0.5774 \\ 0 \end{pmatrix}. \tag{C.23}$$

Finally, we can check that the candidate vectors do indeed belong in their respective subspaces:

$$A_p^* w_1 = 10^{-3} \begin{pmatrix} 0.2000 \\ -0.0082 \\ 0.2000 \\ 0.1918 \end{pmatrix}, \quad A_p v_2 = -10^{-3} \begin{pmatrix} 0.4000 \\ 0.4000 \\ 0.6228 \end{pmatrix}. \tag{C.24}$$

One can check that these results, which are subject to normalisation, can be expressed in terms of the exact results at the beginning of the section.

C.3 Numerical approximation of LS derivatives

There are two ways of approximating the derivatives used in Chapter 4, §4.3.3: first, the function $\mathscr{J}_i$ may have its derivatives approximated directly; second, the Fréchet derivatives in $\mathbf{s}$ and Λ may be computed by finite differences if progress cannot be made analytically, e.g. $D\mathbf{F}$ can be computed via the ray Jacobian. Here the former is preferred. Standard finite difference schemes applied to $\mathscr{J}_i$ (see for e.g. Kincaid & Cheney [150]) give the following approximations to its derivatives,

$$\begin{aligned}
\mathscr{J}_{i,\varrho_1\varrho_1}(\mathbf{0},0) &\approx \epsilon^{-2}\left(\mathscr{J}_i(\{\epsilon,0\},0) - 2\,\mathscr{J}_i(\mathbf{0},0) + \mathscr{J}_i(\{-\epsilon,0\},0)\right) + O(\epsilon^2),\\
\mathscr{J}_{i,,\varrho_1\varrho_2}(\mathbf{0},0) &\approx \frac{1}{4}\epsilon^{-2}\left(\mathscr{J}_i(\{\epsilon,\epsilon\},0) + \mathscr{J}_i(\{-\epsilon,-\epsilon\},0) - \mathscr{J}_i(\{\epsilon,-\epsilon\},0) - \mathscr{J}_i(\{-\epsilon,\epsilon\},0)\right) + O(\epsilon^2),\\
\mathscr{J}_{i,\varrho_1\Lambda}(\mathbf{0},0) &\approx \frac{1}{4}\epsilon^{-2}\left(\mathscr{J}_i(\{\epsilon,0\},\epsilon) + \mathscr{J}_i(\{-\epsilon,0\},-\epsilon) - \mathscr{J}_i(\{\epsilon,0\},-\epsilon) - \mathscr{J}_i(\{-\epsilon,0\},\epsilon)\right) + O(\epsilon^2),\\
\mathscr{J}_{i,\varrho_1\varrho_1\varrho_1}(\mathbf{0},0) &\approx \epsilon^{-3}\left(-\frac{1}{2}\mathscr{J}_i(\{-2\epsilon,0\},0) + \mathscr{J}_i(\{-\epsilon,0\},0) - \mathscr{J}_i(\{\epsilon,0\},0) + \frac{1}{2}\mathscr{J}_i(\{2\epsilon,0\},0)\right) + O(\epsilon^2),
\end{aligned} \tag{C.25}$$

where $\epsilon \ll 1$, and we have listed selected derivatives (only in two variables) that are required for the demonstrations of fold and pitchfork in Chap. 4 and for the classification problem in Chap. 5, §5.4.1.1.

To spell out the mechanics of these finite differences in the context of the ray problem, the perturbations to g_i are shown explicitly in terms of $\boldsymbol{x}(\boldsymbol{\varsigma})$ and $\boldsymbol{x}_R(\alpha)$, where $\Lambda = \alpha - \alpha_C$.

So we have,

$$\mathscr{J}_i(\{\epsilon,\epsilon\},\epsilon) = \langle w_i^*, \boldsymbol{x}(\boldsymbol{\varsigma}_C + \epsilon v_1 + \epsilon v_2) - \boldsymbol{x}_R(\alpha_C + \epsilon)\rangle, \tag{C.26}$$

where we neglect W in the approximation because its Taylor expansion near the caustic yields powers $O(\epsilon^n), n > 1$. The value of ϵ used in (C.26) is real, so $\mathbf{F}$ is non-trivial and real in the cases of fold and pitchfork caustic.

C.4 Multidimensional winding number calculation

The algorithm for computing the solutions to the multidimensional WNM of Chap. 4, §4.6.2 is consider here for completeness. It is similar to the algorithm for the single WNM found in §4.6 of the same chapter, albeit slightly more involved due to the allowance of multiplicity of roots other than one. The algorithm with proof can be found in Kravanja & Barel [154] p. 97 *et seq.* In the following the dimension of the problem is kept general and equal to n_D.

In brief, the strategy is to first solve for the last component of every root vector i.e. the set $\{\varsigma^\star_{n_D,i}\}$, where again n_D is the last component of a root vector, and i book-keeps the root number. The reason for a component-wise calculation is due to the fact that $h(\varsigma)$ is a scalar and not a vector (see Eq. (4.64)).

We set $h(\boldsymbol{\varsigma}) = h(\varsigma_{n_D}) = \varsigma^p_{n_D}$ to generate a system of polynomials similar to the single variable WNM. Using this form of h, (4.69) is used to define,

$$W^{M,p}_{n_D} \equiv \sum_i \mu_F(\boldsymbol{\varsigma}^\star_i)(\varsigma^\star_{n_D,i})^p, \tag{C.27}$$

whereas usual $W^{M,0}_{n_D} = W^{M,0} = W^M = N$ is the sum of the multiplicities (equal to the number of roots if $\mu_F = 1, \forall \boldsymbol{\varsigma}^\star$). The algorithm proceeds by working with the arithmetic mean (denoted by $\acute{}$) of the desired roots, for e.g.,

$$\acute{\varsigma}^\star_{n_D} \equiv \frac{\sum_i \mu_F(\boldsymbol{\varsigma}^\star_i)\varsigma^\star_{n_D,i}}{\sum_i \mu_F(\boldsymbol{\varsigma}^\star_i)} = \frac{W^{M,1}_{n_D}}{W^M}, \tag{C.28}$$

in order to reduce the ill-conditioning of the matrices in the following. Thus, rather than computing $h(\varsigma_{n_D})$ we will use a shifted version, i.e., $h(\varsigma_{n_D} - \acute{\varsigma}_{n_D})$. Corresponding values are denoted with an accent, e.g., $\acute{W}^{M,p}_{n_D}$.

ALGORITHM:

1. $N \leftarrow W^{M,0}$
2. $\acute{\varsigma}^\star_{n_D} \leftarrow W^{M,1}_{n_D}/W^M$
3. $\acute{W}^{M,0}_{n_D} \leftarrow N; \quad \acute{W}^{M,0}_{n_D} \leftarrow 0; \quad \acute{W}^{M,p}_{n_D} \leftarrow h(\varsigma_{n_D} - \acute{\varsigma}^\star_{n_D}) = (\varsigma_{n_D} - \acute{\varsigma}^\star_{n_D})^p,$ for $p = 2, \ldots, 2N-1$

4. Calculate the eigenvalues, $\pounds_1, \ldots, \pounds_N$, of the pencil,

$$\left[\acute{W}_{n_D}^{M,r+q+1}\right]_{r,q=0}^{N-1} - \pounds \left[\acute{W}_{n_D}^{M,r+q}\right]_{r,q=0}^{N-1} \tag{C.29}$$

where,

$$\left[\acute{W}_{n_D}^{M,r+q}\right]_{r,q=0}^{\alpha,\beta} = \begin{pmatrix} \acute{W}_{n_D}^{M,0} & \acute{W}_{n_D}^{M,1} & \ldots & \acute{W}_{n_D}^{M,\beta} \\ \acute{W}_{n_D}^{M,1} & \acute{W}_{n_D}^{M,2} & \ldots & \acute{W}_{n_D}^{M,\beta+1} \\ \vdots & \vdots & & \vdots \\ \acute{W}_{n_D}^{M,\alpha} & \acute{W}_{n_D}^{M,\alpha+1} & \ldots & \acute{W}_{n_D}^{M,\alpha+\beta} \end{pmatrix} \tag{C.30}$$

5. $\varsigma_{n_D,i}^{\star} \leftarrow \pounds_i + \acute{\varsigma}_{n_D,i}^{\star}$, for $i = 1, \ldots, N$

6. Solve the Vandermode system

$$\begin{pmatrix} 1 & 1 & \ldots & 1 \\ \pounds_1 & \pounds_2 & \ldots & \pounds_N \\ \vdots & \vdots & & \vdots \\ \pounds_1^{N-1} & \pounds_2^{N-1} & \ldots & \pounds_N^{N-1} \end{pmatrix} \begin{pmatrix} \mu_F(\boldsymbol{\varsigma}_1^{\star}) \\ \mu_F(\boldsymbol{\varsigma}_2^{\star}) \\ \vdots \\ \mu_F(\boldsymbol{\varsigma}_N^{\star}) \end{pmatrix} = \begin{pmatrix} \acute{W}_{n_D}^{M,0} \\ \acute{W}_{n_D}^{M,1} \\ \vdots \\ \acute{W}_{n_D}^{M,N-1} \end{pmatrix}, \tag{C.31}$$

7. $\acute{t}_{k,p} \leftarrow h = \varsigma_k(\varsigma_{n_D} - \acute{\varsigma}_{n_D}^{\star})^p$, for $k = 1, \ldots, n_D - 1$ and $p = 0, \ldots, N-1$

8. Solve the Vandermonde system

$$\begin{pmatrix} 1 & 1 & \ldots & 1 \\ \pounds_1 & \pounds_2 & \ldots & \pounds_N \\ \vdots & \vdots & & \vdots \\ \pounds_1^{N-1} & \pounds_2^{N-1} & \ldots & \pounds_N^{N-1} \end{pmatrix} \begin{pmatrix} \mathring{\varsigma}_{1,1} & \ldots & \mathring{\varsigma}_{n_D-1,1} \\ \mathring{\varsigma}_{1,2} & \ldots & \mathring{\varsigma}_{n_D-1,2} \\ \vdots & & \vdots \\ \mathring{\varsigma}_{1,N} & \ldots & \mathring{\varsigma}_{n_D-1,N} \end{pmatrix} = \begin{pmatrix} \acute{t}_{1,0} & \ldots & \acute{t}_{n_D-1,0} \\ \acute{t}_{1,1} & \ldots & \acute{t}_{n_D-1,1} \\ \vdots & & \vdots \\ \acute{t}_{1,N-1} & \ldots & \acute{t}_{n_D-1,N-1} \end{pmatrix} \tag{C.32}$$

$\varsigma_{k,i}^{\star} \leftarrow \mathring{\varsigma}_{k,i}/\mu_F(\boldsymbol{\varsigma}_i^{\star})$ for $k = 1, \ldots, n_D - 1$ and $i = 1, \ldots, N$

9. $\varsigma_{n_D,i}^{\star},\ \mu_F(\boldsymbol{\varsigma}_i^{\star}) \leftarrow \{\varsigma_{n_D,i}^{\star}\} \backslash \{\varsigma_{n_D,i}^{\star} \,|\, \mu_F(\boldsymbol{\varsigma}_i^{\star}) = 0\},\ \{\mu_F(\boldsymbol{\varsigma}_i^{\star})\} \backslash \{\mu_F(\boldsymbol{\varsigma}_i^{\star} \,|\, \mu_F(\boldsymbol{\varsigma}_i^{\star}) = 0\}$

In the above, the last step is used to discard all spurious solutions with multiplicity equal to 0. Due to the numerical nature of the problem, the discard criterion $\mu_F(\boldsymbol{\varsigma}_i^{\star}) = 0$, can be replaced by $\mu_F(\boldsymbol{\varsigma}_i^{\star}) \approx 0$.

Appendix D

Uniform solution to the fold caustic using Bleistein's method

D.1 Mapping

When there is an integral representation of the field it is possible to calculate the mapping discussed in Chapter 5 without resorting to numerical inversions of the canonical function mappings. However, only in the simplest cases, e.g., $K = 0, 1, 2$, does a closed form solution of the mapping exist, and even then the difficulty of rigorously defining the mapping is a function of the original integrand. In this section the closed form solution given in Chapter 6 is used to calculate the uniform solution at the CoS boundary (CoSB) $\theta_C \approx 39.5°$ for $\Delta\varphi = \pi/3$. This can be used across the CoSB that is delimited by a fold caustic only.

It has already been seen that the complex solutions of the integral are already quite challenging due to the Riemann sheet structures introduced to allow for multiplicities. At the caustic special measures must be taken in order to ensure that the map remains conformal and this requires higher-derivatives of the phase function Ψ_{WK}. At a fold, the limiting process requires its third derivative. From a novelty point of view, this is the first proper use of an analytic mapping applied to the Lilley problem. The uniform method used by Wundrow & Khavaran [116] was based on an "at-caustic" expansion mixed with a polynomial interpolation scheme.

Since the behaviour of the saddles has been studied, it is known that they coalesce on the indirect sheet, so it is $\mathscr{R}_\omega^{(+)}$ that is of interest. A reminder of the closed form integral,

$$\mathscr{R}_\omega^{(+)} = \int_{C^{(+)}} \left[\frac{\mathrm{i}k_0}{2\pi r_s Q(r_s|\nu)}\right]^{1/2} \mathrm{e}^{\mathrm{i}k_0\left[\Delta\varphi\,\nu+\zeta(r|\nu)+\zeta(r_s|\nu)-R\sin^2\theta\right]}\mathrm{d}\nu = \int_{C^{(+)}} \hat{a}(\nu)\mathrm{e}^{\mathrm{i}k_0\Psi_{WK}(\nu)}\,\mathrm{d}\nu. \tag{D.1}$$

The flow factor is expressed in terms of $\mathscr{R}_\omega^{(+)}$ solely,

$$\frac{\mathbb{G}_\omega}{\mathscr{G}_\omega} \sim \frac{\mathscr{R}_\omega^{(+)}}{\omega(1 - M_s \cos\theta)^2}\,. \tag{D.2}$$

This has interesting ramifications when the saddles move across to the $\mathscr{R}_\omega^{(-)}$ sheet.

The following mapping for the fold caustic is slightly different from that in the main text, with the full details given in Bleistein and Handelsman [134]. Here the canonical function,

$$\hat{\Psi}_2(\gamma) = \int_C \mathrm{e}^{\hat{\psi}_2(t;\gamma)}\mathrm{d}t = \int_C \mathrm{e}^{-\left(\frac{t^3}{3} - \gamma^2 t\right)}\mathrm{d}t, \tag{D.3}$$

where the complex contour starts and ends in the valleys $\infty\mathrm{e}^{-2\pi\mathrm{i}/3}, \infty\mathrm{e}^{2\pi\mathrm{i}/3}$ respectively. There are two reasons why this form is preferred over the fold used in Chapter 5. The first is that the unfolding of the saddle point structure away from the caustic requires complex rays and therefore a contour deformation anyway; secondly, the mapping of the canonical polynomial is multi-valued and choosing the correct branch is greatly facilitated by a complex contour.

The following changes are made for convenience in comparsion to Chap. 5: $(k_0/2\pi\mathrm{i})^{1/2}b = \hat{b}$; $\mathrm{i}\Phi_2 = \hat{\psi}_2$; $\mathrm{i}A = \hat{A}$; $\mathrm{d}\nu/\mathrm{d}t = J$ (see Eq. (5.30)). For clarity $\hat{b}$ is rewritten in terms of coefficients $\hat{c}$ because, even though $\hat{\Psi}_2$ is easily expressible in terms an Airy function, the change in canonical polynomial does affect the value of the uniform amplitude coefficients.

$$\hat{b}(t_i) = \sum_{k=0}^{2} \hat{c}_k(\boldsymbol{x}) t_i^k, \quad \frac{\partial}{\partial t}\hat{\psi}_2(t_i;\gamma) = 0,\ i = 1, 2. \tag{D.4}$$

The uniform form is given by [134],

$$\mathscr{R}_\omega^{(+)} \sim 2\pi\mathrm{i}\exp^{k_0\hat{A}}\left[\frac{\mathrm{Ai}(k_0^{2/3}\gamma^2)}{k_0^{1/3}}\hat{c}_0 + \frac{\mathrm{Ai}'(k_0^{2/3}\gamma^2)}{k_0^{2/3}}\hat{c}_1\right]. \tag{D.5}$$

In the following a plus or minus attached to the saddle $\nu_\star^\pm$ does not denote the Riemann sheet it is on: this is still denoted by superscript $(\pm)$ on $\mathscr{R}_\omega$. Also, the Schwartz reflection principle is used in the locality of the caustic for functions that have real values on the real line. Put simply the following conjugate property holds $F(\bar{\nu}) = \overline{F(\nu)}$. This aids the calculation of the mapping since the phase has this property and can be used to make sure the following mappings are consistent.

The fold caustic has closed form solutions to the mapping $\mathrm{i}\Phi_2 = \hat{\psi}_2 + A$ and the system in (D.4). These are detailed in [134] and are given by,

$$\frac{4\gamma^3}{3} = \mathrm{i}\left\{\Delta\varphi\,\nu_\star^+ + \zeta(r|\nu_\star^+) + \zeta(r_s|\nu_\star^+) - \Delta\varphi\,\nu_\star^- - \zeta(r|\nu_\star^-) - \zeta(r_s|\nu_\star^-)\right\}, \tag{D.6}$$

$$\hat{A} = \frac{\mathrm{i}}{2}\left\{\Delta\varphi\,\nu_\star^+ + \zeta(r|\nu_\star^+) + \zeta(r_s|\nu_\star^+) + \Delta\varphi\,\nu_\star^- + \zeta(r|\nu_\star^-) + \zeta(r_s|\nu_\star^-)\right\} - \mathrm{i}R\sin^2\theta \quad \text{(D.7)}$$

$$\hat{c}_0 = \frac{1}{2}\left[\left(\frac{\mathrm{i}k_0}{2\pi r_s Q(r_s|\nu_\star^+)}\right)^{1/2}\left.\frac{\mathrm{d}\nu}{\mathrm{d}t}\right|_{\nu_\star^+} + \left(\frac{\mathrm{i}k_0}{2\pi r_s Q(r_s|\nu_\star^-)}\right)^{1/2}\left.\frac{\mathrm{d}\nu}{\mathrm{d}t}\right|_{\nu_\star^-}\right] \quad \text{(D.8)}$$

$$\hat{c}_1 = \frac{1}{2\gamma}\left[\left(\frac{\mathrm{i}k_0}{2\pi r_s Q(r_s|\nu_\star^+)}\right)^{1/2}\left.\frac{\mathrm{d}\nu}{\mathrm{d}t}\right|_{\nu_\star^+} - \left(\frac{\mathrm{i}k_0}{2\pi r_s Q(r_s|\nu_\star^-)}\right)^{1/2}\left.\frac{\mathrm{d}\nu}{\mathrm{d}t}\right|_{\nu_\star^-}\right] \quad \text{(D.9)}$$

The Jacobians $\mathrm{d}\nu/\mathrm{d}t$ must be defined uniquely by fixing the cube root of γ in (D.6). The cube root can be calculated using the local method found in [134],

$$\frac{1}{2}\arg\Delta\nu+\frac{1}{2}\arg(\mathrm{i}(\Delta\varphi-\psi_{WK}(\bar{\nu})))-\frac{2\pi}{3} < \arg(\gamma) < \frac{1}{2}\arg\Delta\nu+\frac{1}{2}\arg(\mathrm{i}(\Delta\varphi-\psi_{WK}(\bar{\nu})))-\frac{\pi}{3}, \mod\pi \quad \text{(D.10)}$$

where $\bar{\nu}$ is the point of coalesence and the increment $\Delta\nu$ is in the direction of the original complex contour from the point of coalescence. Here $\mathrm{e}^{\mathrm{i}\pi/2}$ is used as the exponential part as prior to coalescence ($\theta < \theta_f$) the complex contour given in Fig. 6.4(f) is at an angle of $\pi/2$ w.r.t. the coalescence point. This fixes γ as follows,

$$\theta < \theta_f: \quad \arg(\mathrm{i}(\Delta\varphi - \psi_{WK}(\bar{\nu}))) = \frac{\pi}{2}, \quad -\frac{\pi}{6} < \arg\gamma < \frac{\pi}{6}. \quad \text{(D.11)}$$

$$\theta > \theta_f: \quad \arg(\mathrm{i}(\Delta\varphi - \psi_{WK}(\bar{\nu}))) = -\frac{\pi}{2}, \quad -\frac{2\pi}{3} < \arg\gamma < -\frac{\pi}{3}. \quad \text{(D.12)}$$

where a separate determination of γ is used either side of the caustic.

This allows the root on $\mathrm{d}\nu/\mathrm{d}t$ to be fixed when evaluating at the saddles. Using another local method from [134],

$$\dot{\nu}|_{t=\pm\gamma} \approx \frac{\nu_\star^+ - \nu_\star^-}{2\gamma}, \quad \arg(\dot{\nu})|_{t=\pm\gamma} \approx \arg(\nu_\star^+ - \nu_\star^-) - \arg(\gamma), \quad \text{(D.13)}$$

which requires that all functions are evaluated near $\theta = \theta_c$.

$$\theta < \theta_f: \quad \arg(\dot{\nu})|_{t=\pm\gamma} \approx -\frac{\pi}{2} \quad \text{(D.14)}$$

$$\theta > \theta_f: \quad \arg(\dot{\nu})|_{t=\pm\gamma} \approx -\frac{\pi}{2} \quad \text{(D.15)}$$

The derivatives of the mapping are determined to be

$$\begin{aligned}
&\theta < \theta_f: \quad \dot{\nu}|_{t=\pm\gamma} = -\mathrm{e}^{\mp\mathrm{i}\pi/4}(2|\gamma|)^{1/2}\mathrm{e}^{\mathrm{i}\arg(\gamma)/2}\mathrm{e}^{-\mathrm{i}\arg(\partial\psi_{WK}/\partial\nu_\star^\pm)/2}/|\partial\psi_{WK}/\partial\nu_\star^\pm|^{1/2}, \quad \mathrm{Im}(\nu_\star^+) > \mathrm{Im}(\nu_\star^-).\\
&\theta > \theta_f: \quad \dot{\nu}|_{t=\pm\gamma} = \mathrm{e}^{\mp\mathrm{i}\pi/4}(2|\gamma|)^{1/2}\mathrm{e}^{\mathrm{i}\arg(\gamma)/2}\mathrm{e}^{-\mathrm{i}\arg(\partial\psi_{WK}/\partial\nu_\star^\pm)/2}/|\partial\psi_{WK}/\partial\nu_\star^\pm|^{1/2}, \quad \nu_\star^- > \nu_\star^+.
\end{aligned} \quad \text{(D.16)}$$

D.1.1 Coalesced saddle

When the two saddles coalesce a cube root needs to be determined. The best way of determining the root is by comparing directly with a saddle point expansion about the coalescence.

Considering an integral of the form,

$$I(k_0) = \int_{C^{(+)}} \hat{a}(\nu) \exp\left(\mathrm{i}k_0 \Psi_{WK}(\nu)\right) \, \mathrm{d}\nu, \quad k_0 \to +\infty, \tag{D.17}$$

then the contribution from a saddle ν_0 of order m is given to leading order as,

$$I(k_0) \sim \frac{\hat{a}(\nu_0)}{m} \left(\frac{m!}{k_0 \left| \Psi_{WK}^{(m)}(\nu_0) \right|} \right)^{\beta/m} \Gamma\left(\tfrac{\beta}{m}\right) \exp\left[\mathrm{i}k_0 \Psi_{WK}(\nu_0) - \mathrm{i}\beta\frac{\alpha}{m}\right] \sum_{p=0}^{m-1} \gamma_p \exp\left[\mathrm{i}\beta(2p+1)\pi/m\right]. \tag{D.18}$$

Where $\beta = 1$ for $\hat{a}$ regular, $\alpha = \arg(\mathrm{i}\Psi_{WK})$, and γ_p is an orientation anomaly that depends on the direction of the path through the saddle(s). For a contour that passes through a critical point once, only two terms of the sum are non-zero: one for entering the critical point, the other leaving.

At the fold caustic $m = 3$ and applying Eqs. (D.18)-(D.1), denoting the coalesced values by $\bar{\ }$, we have,

$$\begin{aligned} \overline{\mathscr{R}}_{\omega}^{(+)} \sim \frac{1}{3} \hat{a}(\bar{\nu}) \left(\frac{3!}{k_0 \left| -\mathrm{i}\partial^2 \psi_{WK}/\partial \bar{\nu}^2 \right|} \right)^{1/3} \mathrm{e}^{-\frac{\mathrm{i}}{3}\arg(-\mathrm{i}\,\partial^2 \psi_{WK}/\partial \bar{\nu}^2)} \times \\ \Gamma\left(\tfrac{1}{3}\right) \mathrm{e}^{\mathrm{i}k_0\left[\Delta\varphi\bar{\nu} + \zeta(r|\bar{\nu}) + \zeta(r_s|\bar{\nu}) - R\sin^2\theta\right]} 2\mathrm{e}^{\frac{\mathrm{i}\pi}{6}} \cos(\tfrac{\pi}{6}), \end{aligned} \tag{D.19}$$

with,

$$\hat{a}(\bar{\nu}) \sim \left[\frac{\mathrm{i}k_0}{2\pi r_s Q(r_s|\bar{\nu})} \right]^{1/2}, \tag{D.20}$$

and the orientation anomalies have been set to $\gamma_1 = 1$, $\gamma_2 = -1$, and $\gamma_3 = 0$.

A direct comparison is made by evaluating the leading order term of (D.5) with (D.19), using the following: $\mathrm{Ai}(0) = 3^{-2/3}/\Gamma\left(\frac{2}{3}\right)$ and $\Gamma(z)\Gamma(1-z) = \pi/\sin(\pi z)$.

$$\begin{aligned} \mathscr{R}_{\omega}^{(+)} \sim -2^{4/3}\pi\mathrm{i}\omega_{\mathrm{root}} \hat{a}(\bar{\nu}) \left(k_0 \left| -\mathrm{i}\frac{\partial^2 \psi_{WK}}{\partial \bar{\nu}^2} \right| \right)^{-1/3} \times \\ \mathrm{e}^{-\frac{\mathrm{i}}{3}\arg(-\mathrm{i}\,\partial^2 \psi_{WK}/\partial \bar{\nu}^2)} \mathrm{Ai}(0) \mathrm{e}^{\mathrm{i}k_0\left[\Delta\varphi\bar{\nu} + \zeta(r|\bar{\nu}) + \zeta(r_s|\bar{\nu}) - R\sin^2\theta\right]}, \end{aligned} \tag{D.21}$$

where ω_{root} is the cube root of one, to be determined. Upon applying the reflection formula to the Airy zero ($\Gamma(1/3)\Gamma(2/3) = 2\pi/\sqrt{3}$), we can see that the solutions match iff $\omega_{\mathrm{root}} \equiv \mathrm{e}^{2\pi\mathrm{i}/3}$.

D.1.2 Calculation of derivatives

In addition to the first derivative of ψ_{WK} a second derivative w.r.t ν is required. As in Chap. 6 this is achieved by differentiating under the integral sign and then syphoning off any singularities introduced by the turning-point.

Reintroducing,

$$\frac{\partial Q(r|\nu)}{\partial \nu} = -\frac{\nu}{r^2 Q(r|\nu)}, \quad \frac{\partial}{\partial r}\, rQ(r|\nu) = \frac{1}{2r^2 Q(r|\nu)\mathscr{P}(r)}, \quad \frac{\partial r_\delta}{\partial \nu_\star} = 2\nu_\star r_\delta \mathscr{P}(r_\delta), \tag{D.22}$$

where,

$$\mathscr{P}(r) = \frac{1}{r(r^2 q^2)'}. \tag{D.23}$$

The general form of $\partial\psi_{WK}/\partial\nu_\star$ (where $\pm$ references the $(\pm)$ Riemann sheets)

$$\frac{\partial \psi_{WK}}{\partial \nu_\star} = \left(\int_{r_\delta}^{\infty} \mp \int_{r_\delta}^{r_s}\right) \frac{1 + 2\nu_\star^2 r\mathscr{P}'(r)}{r^2 Q(r|\nu_\star)} \mathrm{d}r \pm \frac{2\nu_\star^2 \mathscr{P}(r_s)}{r_s Q(r_s|\nu_\star)}, \tag{D.24}$$

and the second derivative is found by expressing the singularity producing part of this integrand as,

$$\frac{\partial}{\partial \nu}\left[\frac{2\nu^2\mathscr{P}'(r)}{rQ(r|\nu)}\right] = \frac{4\nu}{rQ(r|\nu)}\left[\mathscr{P}'(r) + \nu^2\mathscr{P}(r)\mathscr{P}'(r) + r\nu^2\left(\mathscr{P}'^2(r) + \mathscr{P}(r)\mathscr{P}''(r)\right)\right] + \cdots$$
$$\cdots - \frac{\partial}{\partial r}\left[\frac{4\nu^3\mathscr{P}(r)\mathscr{P}'(r)}{Q(r|\nu)}\right]. \tag{D.25}$$

and integrating the result to give,

$$\frac{\partial^2 \psi_{WK}}{\partial \nu^2} = \frac{1}{\nu}\frac{\partial \psi_{WK}}{\partial \nu} - \frac{\psi_{WK}}{\nu^2} + \cdots$$
$$\cdots + \left(\int_{r_\delta}^{\infty} \mp \int_{r_\delta}^{r_s}\right) \frac{4\nu}{rQ(r|\nu)}\left[\mathscr{P}'(r) + \nu^2\mathscr{P}(r)\mathscr{P}'(r) + r\nu^2\left(\mathscr{P}'^2(r) + \mathscr{P}(r)\mathscr{P}''(r)\right)\right] \mathrm{d}r + \ldots$$
$$\cdots \pm \frac{4\nu^3\mathscr{P}(r_s)\mathscr{P}'(r_s)}{Q(r_s|\nu)} \pm \frac{\partial}{\partial \nu}\left[\frac{2\nu^2\mathscr{P}(r_s)}{r_s Q(r_s|\nu)}\right], \tag{D.26}$$

whereupon the use of,

$$\frac{\partial}{\partial \nu}\left[\frac{2\nu^2\mathscr{P}(r_s)}{r_s Q(r_s|\nu)}\right] = \frac{4\nu\mathscr{P}(r_s)}{r_s Q(r_s|\nu)} + \frac{2\nu^3\mathscr{P}(r_s)}{r_s^3 Q^3(r_s|\nu)}, \tag{D.27}$$

and simplification due to $\partial^2\psi_{WK}/\partial\nu^2$ containing $\partial\psi_{WK}/\partial\nu$ and ψ_{WK} gives the final form,

$$\frac{\partial^2\psi_{WK}}{\partial\nu^2} = \frac{3}{\nu}\frac{\partial\psi_{WK}}{\partial\nu} - \frac{3\psi_{WK}}{\nu^2} + \dots$$
$$\dots + \left(\int_{r_\delta}^{\infty} \mp \int_{r_\delta}^{r_s}\right) \frac{4\nu^3}{rQ(r|\nu)}\left[\mathscr{P}(r)\mathscr{P}'(r) + r\left(\mathscr{P}'^2(r) + \mathscr{P}(r)\mathscr{P}''(r)\right)\right]\,\mathrm{d}r + \dots$$
$$\dots \pm \left[\frac{4\nu^3\mathscr{P}(r_s)\mathscr{P}'(r_s)}{Q(r_s|\nu)} + \frac{2\nu^3\mathscr{P}(r_s)}{r_s^3Q^3(r_s|\nu)}\right]. \tag{D.28}$$

D.1.3 Continuation when the integrand is not regular

An analytical mapping may prove limited when the integrand contains multivalued functions. The above mapping actually applies to a fairly small range of control variable in its current form. One of the rays changes sheets (on both sides of the caustic), and so it is interesting to see how the uniform mapping can account for this even though the assumption the integrand is regular and one-to-one in the domain of interest has been made. However, as long as the ray doesn't go too near the branch point then some amendments should be possible particularly as the ray numbers are still conserved and branch cut orientations are arbitrary.

The necessary amendments are found by tracking the multivalued factor,

$$\left[\frac{\mathrm{i}k_0}{r_sQ(r_s|\nu)}\right]^{1/2}. \tag{D.29}$$

The $-\mathrm{i}$ factor that comes out of this when crossing Riemann sheets is the Stokes multiplier from before. This is the correction factor that needs to be applied to components of the $\hat{c}_0$ and $\hat{c}_1$ already given. For example $\hat{c}_0$ is corrected to,

$$\hat{c}_0 = \begin{cases} \frac{1}{2}\left[-\mathrm{i}\left(\frac{\mathrm{i}k_0}{2\pi r_sQ(r_s|\nu^+)}\right)^{1/2}\frac{\mathrm{d}\nu}{\mathrm{d}t}\big|_{\nu^+} + \left(\frac{\mathrm{i}k_0}{2\pi r_sQ(r_s|\nu^-)}\right)^{1/2}\frac{\mathrm{d}\nu}{\mathrm{d}t}\big|_{\nu^-}\right], & \theta < \theta_f \\ \frac{1}{2}\left[\left(\frac{\mathrm{i}k_0}{2\pi r_sQ(r_s|\nu^+)}\right)^{1/2}\frac{\mathrm{d}\nu}{\mathrm{d}t}\big|_{\nu^+} - \mathrm{i}\left(\frac{\mathrm{i}k_0}{2\pi r_sQ(r_s|\nu^-)}\right)^{1/2}\frac{\mathrm{d}\nu}{\mathrm{d}t}\big|_{\nu^-}\right], & \theta > \theta_f. \end{cases} \tag{D.30}$$

Even though the mapping derivatives are multi-valued, they aren't of a sufficiently simple form that a $\pm$ factor can be drawn out. The continuation allows the asymptotic calculation of the field over a large range of angles since the saddles are mostly on the direct sheet, $\mathscr{R}_\omega^{(-)}$. Although the steepest descent paths of the integrals $\mathscr{R}_\omega^{(\pm)}$ were complicated, the local mappings in Eqs. (D.6)-(D.16) mean that all the steepest path information is contained within the uniform solution.

Appendix E

Eucatastrophes

In this appendix we introduce the eucatastrophes utilised in the main text in order to aid the discussion of the behaviour in the region containing the anti-caustic. These functions are scaled versions of the functions used by Bleistein [182] to model the coalesence of stationary points with algebraic singularities. The eucatastrophe moniker is simply meant to reflect that these forms have similarities with catastrophes but without the singularity at the control variables origin $\boldsymbol{\xi} = \mathbf{0}$, hence eu-catastrophe.[1] Bleistein's paper considers functions of the form (see (3.1), p. 541 of [182]),

$$I(k_0, \boldsymbol{\alpha}, \boldsymbol{\beta}, \boldsymbol{r}) = \int_{\mathscr{C}} \prod_{\mu=1}^{q} (t - \beta_\mu)^{r_\mu} g(t) \mathrm{e}^{-k_0 f(t;\boldsymbol{\alpha})} \, \mathrm{d}t; \qquad \boldsymbol{\beta} = \{\beta_1, \ldots, \beta_1\}, \quad \boldsymbol{r} = \{r_1, \ldots, r_q\}. \tag{E.1}$$

Here the quantities of interest are the set of algebraic singularity points $\boldsymbol{\beta}$, their powers $\boldsymbol{r}$ - possibly fractional - and the control variables $\boldsymbol{\alpha}$. It is the addition of these algebraic singularities that perturbs these forms from the usual catastrophes. We will take this one step further by allowing the power (we will only consider one algebraic singularity, i.e., $q = 1$ in (E.1)) to be a function of a control variable, whilst also scaling by the wavenumber k_0 so as to include it in exponent of the exponential. Indeed, we could also allow the algebraic singularity position to be a function of another control variable, but we don't consider that case here. The eucatastrophes are defined as,

$$\mathscr{E}_K(\boldsymbol{\xi}) \equiv \int_{\mathscr{C}} \mathrm{e}^{-k_0 \Phi_K^{\mathscr{E}}(\nu;\boldsymbol{\xi})} \, \mathrm{d}\nu = \int_{\mathscr{C}} \exp\left[-k_0 \left(\nu^{K+2} + \sum_{n=1}^{K} \xi_n \nu^n + \xi_0 \log \nu\right)\right] \mathrm{d}\nu, \quad 0 \leq K \leq 4, \tag{E.2}$$

where $\Phi_K^{\mathscr{E}}$ is the eucatastrophe potential.

[1] In fact eucatastrophe is in fact a Tolkeinism for happy accident in the spirit of "deus ex machina". In our scenario the accident pertains to coalescence, the happiness due to absence of singularity.

Modulo the wavenumber scaling and imaginary factor in the exponent, the eucatastrophes are symbolically the same as the diffraction catastrophes (see (5.9)) when the logarithmic term is turned off via $\xi_0 = 0$, as the potentials of both theories are related via $\Phi^{\mathscr{E}}_K(\nu;\boldsymbol{\xi}) = \Phi_K(\nu;\boldsymbol{\xi}\backslash\{\xi_0\}) + \xi_0 \log\nu$. We have also allowed for $K = 0$, though this case is not forbidden in the study of uniform asymptotics (see for e.g., [81]). In this work no contour $\mathscr{C}$ is made explicit which limits the study of these functions: however, we require that $\mathscr{E}_K(\mathbf{0}) \neq 0$ and that the function remains physical for $\xi_n \in \mathbb{R}$. The reason for introducing these functions is purely to study the behaviour of the saddles and further derivatives of the exponent, and the effect of the logarithmic term.

Though the similarities between diffraction catastrophes and eucatastrophes are clear, there is one significant difference pertaining to the number of saddle points. The presence of the logarithm in the exponent allows the eucatastrophe $\mathscr{E}_K$ to have $K + 2$ saddles in general, which compares to the $K + 1$ of the diffraction catastrophe Ψ_K. In the former, this is true for all regions bar $\xi_0 = 0$ (the anti-caustic structure), where the number of saddles reduces to $K + 1$, as the logarithm is turned off. Consequently, we expect a change of *form* in $\mathscr{E}_K$ not found in Ψ_K. As we shall see, this has implications for the caustic structure of $\mathscr{E}_K$.

Additionally the eucatastrophe potential has an infinite number of derivatives with pole at $\nu = 0$. An interesting case then arises when $\boldsymbol{\xi} = \{0, \ldots, 0, -\xi_0\}$, this has $K + 2$ saddles at a position proportional to $\xi_0^{1/K+2}$. As $\xi_0 \to 0$ the derivatives of $\Phi^{\mathscr{E}}_K$ will become infinite as the saddles coalesce, thus giving a ray field which vanishes. This can be seen from the general expression,

$$\frac{\partial^m \Phi^{\mathscr{E}}_K}{\partial \nu^m} = \frac{\Gamma(K+3)}{\Gamma(K+3-m)}\nu^{K+2-m} + \sum_{n=1}^{K} \xi_n \frac{\Gamma(n+1)}{\Gamma(n+1-m)}\nu^{n-m} + \frac{(-)^{m+1}\xi_0}{\nu^m} \sim \frac{(-)^{m+1}\xi_0}{\nu^m}, \quad \nu \to 0, \tag{E.3}$$

which is independent of K. However, just like the diffraction catastrophes are bounded at a caustic despite their ray expansions diverging, the eucatastrophes are also bounded despite their ray expansions vanishing. This can be seen by setting $\xi_0 = 0$ in $\mathscr{E}_K$, which yields a finite value for the integral by definition. We can guarantee this is true by analogy with the diffraction catastrophes for both $\xi_0 = 0$ and $\boldsymbol{\xi} = \mathbf{0}$ without specifying $\mathscr{C}$. Therefore the eucatastrophe exhibits a clash of limits and sheds light on the eucatastrophic moniker as the coalescence does not diverge but the converse occurs where the rays predict a diminishing field as the anti-caustic is approached.

E.1 Other eucatastrophes

In the previous section we described the corank 1 eucatastrophes. These were essentially chosen due to their vanishing ray contributions near the anti-caustic structures. It is worth bearing in mind that the eucatastrophes $\mathscr{E}_K$ motivate further forms which have similar properties. These are based upon the derivative of $\Phi_K^{\mathscr{E}}$ shown in (E.3), so that,

$$\mathscr{E}_K^m(\boldsymbol{\xi}) \equiv \int_{\mathscr{C}} \mathrm{e}^{-k_0\Phi_K^{\mathscr{E},m}(\nu;\boldsymbol{\xi})}\,\mathrm{d}\nu = \int_{\mathscr{C}} \exp\left[-k_0\left(\nu^{K+2-m} + \sum_{n=1}^{K}\xi_n\nu^{n-m} + \frac{\xi_0}{\nu^m}\right)\right]\mathrm{d}\nu, \qquad 0 \leq K \leq 4,\ m \leq K+1, \tag{E.4}$$

where the restriction upon m means that $\mathscr{E}_K^m$ always has saddles.

While $\mathscr{E}_K^m(\boldsymbol{\xi})$ contains eucatastrophic structures there is a notable difference compared with $\mathscr{E}_K(\boldsymbol{\xi})$. While the latter contains a logarithmic singularity the former contains an algebraic singularity in its potential: the integrand thus has an essential singularity. Though the focus of this chapter is concerned with $\mathscr{E}_K$, $\mathscr{E}_K^m(\boldsymbol{\xi})$ are interesting themselves and are indeed reminiscent of the corank 2 catastrophes shown in (5.17) and Berry & Howls [132].

E.2 Caustics of the eucatastrophes

The eucatastrophes may stand out from other local forms used in this thesis by containing anti-caustics: however, as the potentials of these functions are a linear combination of catastrophe polynomials and a logarithm, the eucatastrophes also contain caustics. Clearly on the surface $\xi_0 = 0$ these caustics coincide with those of Φ_K. In this section we consider the effect of the logarithm upon the caustic structures of $\mathscr{E}_K$.

Caustics are found the same way as in previous chapters, i.e., the solution in $\boldsymbol{\xi}$ to the equations,

$$\begin{aligned}\frac{\partial\Phi_K^{\mathscr{E}}}{\partial\nu} &= \frac{(K+2)\nu^{K+2} + \sum_{n=1}^{K}\xi_n n\nu^n + \xi_0}{\nu} = 0,\\ \frac{\partial^2\Phi_K^{\mathscr{E}}}{\partial\nu^2} &= \frac{(K+2)(K+1)\nu^{K+2} + \sum_{n=1}^{K}\xi_n n(n-1)\nu^n - \xi_0}{\nu^2} = 0,\end{aligned} \tag{E.5}$$

where the polynomials in the numerator of each are of the same power.

A straightforward example of a caustic in a eucatastrophe can be shown by $\Phi_1^{\mathscr{E}}$. The relevant equations are,

$$\begin{aligned}3\nu^3 + \xi_1\nu + \xi_0 &= 0,\\ 6\nu^3 - \xi_0 &= 0.\end{aligned} \tag{E.6}$$

The solution to this is in the form $\xi_1^3 = const.\xi_0^2$. Notably this is the same as the Pearcey function with $\xi_0 = 0$ its line of symmetry. This means $\mathscr{E}_1$ has two folds meeting at a cusp-like point. Also $\boldsymbol{\xi} = \mathbf{0}$ is the caustic point of Pearcey but the full anti-caustic of $\mathscr{E}_1$ controlled by the Airy function. Clearly this is because $\mathscr{E}_1(\mathbf{0}) \neq \Psi_2(\mathbf{0})$.

E.2.1 Derivatives of catastrophes

The eucatastrophes have an interesting relationship with the diffraction catastrophes of Chap. 5. This can be seen by taking derivatives w.r.t. the control variable ξ_1 of a diffraction catastrophe, for example,

$$\left(\frac{\partial}{\partial\xi_1}\right)^{\xi_0}\Psi_K = (\mathrm{i}k_0)^{\xi_0}\int_{\mathscr{C}'}\nu^{\xi_0}\mathrm{e}^{\mathrm{i}k_0\Phi_K(\nu;\boldsymbol{\xi}\backslash\{\xi_0\})}\,\mathrm{d}\nu = \int_{\mathscr{C}'}\mathrm{e}^{\mathrm{i}k_0\Phi_K(\nu;\boldsymbol{\xi}\backslash\{\xi_0\})+\mathrm{i}k_0\xi_0\log(\nu)}\,\mathrm{d}\nu. \tag{E.7}$$

What (E.7) says about the eucatastrophes is that - bar a scaling by $\mathrm{i}k_0$ - the eucatastrophes result from the diffraction catastrophes by a generalisation of the derivative formula to real values rather than just real integers. More surprising is that while $\mathscr{E}_K$ has $K+2$ rays away from $\xi_0 = 0$ it is expressible in terms of diffraction catastrophes and derivatives that have $K+1$ rays. This can lead to peculiar alternative descriptions of local behaviour in terms of both $K+1$ and $K+2$ ray systems at the same time (see §6.4.2.3, Chap. 6).

Bibliography

[1] J. Böttcher. Aircraft Noise Certification: Annex 16, Volume I and equivalent procedures, October 2004. URL `http://www.icao.int/Meetings/EnvironmentalWorkshops/Documents/NoiseCertificationWorkshop-2004/BIP_2_2_jb.pdf`.

[2] N. Dickson. ICAO Noise Standards, May 2013. URL `http://www.icao.int/Meetings/Green/Documents/day%201pdf/session%202/2-Dickson.pdf`.

[3] M. Van Dyke. *An album of fluid motion*. Parabolic Press Stanford, 1982.

[4] M. J. Lighthill. On sound generated aerodynamically. I. General theory. *Proceedings of the Royal Society of London. Series A. Mathematical and Physical Sciences*, 211(1107):564–587, 1952.

[5] M. J. Lighthill. On sound generated aerodynamically. II. Turbulence as a source of sound. *Proceedings of the Royal Society of London. Series A. Mathematical and Physical Sciences*, 222(1148):1–32, 1954.

[6] P. J. Morris and F. Farassat. Acoustic analogy and alternative theories for jet noise prediction. *AIAA journal*, 40(4):671–680, 2002.

[7] C. K. W. Tam and L. Auriault. Jet mixing noise from fine-scale turbulence. *AIAA journal*, 37(2):145–153, 1999.

[8] P. A. Lush. Measurements of subsonic jet noise and comparison with theory. *Journal of Fluid Mechanics*, 46(03):477–500, 1971.

[9] M. E. Goldstein. Aeroacoustics. *New York, McGraw-Hill International Book Co., 1976. 305 p.*, 1, 1976.

[10] S. Engelberg. *Random signals and noise: a mathematical introduction*. CRC Press, 2006.

[11] C. R. Ilário. *Development of a novel RANS-based method for the computational aeroacoustics of high speed jets*. PhD thesis, Universidade de São Paulo Escola Politécnica, 2011.

[12] O. M. Phillips. On the generation of sound by supersonic turbulent shear layers. *Journal of Fluid Mechanics*, 9(01):1–28, 1960.

[13] G. M. Lilley. *On the noise from air jets.* Aeronautical Research Council, Noise Research Committee, 1958.

[14] G. M. Lilley. On the noise from jets. *Agard cp-131*, pages 13–1, 1974.

[15] J. E. Ffowcs Williams and D. L. Hawkings. Sound generation by turbulence and surfaces in arbitrary motion. *Philosophical Transactions of the Royal Society of London. Series A, Mathematical and Physical Sciences*, 264(1151):321–342, 1969.

[16] H. S. Ribner. The generation of sound by turbulent jets. *Advances in Applied Mechanics*, 8(103-182):10, 1964.

[17] M. E. Goldstein and B. Rosenbaum. Effect of anisotropic turbulence on aerodynamic noise. *The Journal of the Acoustical Society of America*, 54(3):630–645, 1973.

[18] M. E. Goldstein. An exact form of Lilley's equation with a velocity quadrupole/temperature dipole source term. *Journal of Fluid Mechanics*, 443: 231–236, 2001.

[19] A. Samanta, J. B. Freund, M. Wei, and S. K. Lele. Robustness of acoustic analogies for predicting mixing-layer noise. *AIAA journal*, 44(11):2780–2786, 2006.

[20] J. B. Freund and T. G. Fleischman. Ray traces through unsteady jet turbulence. *International Journal of Aeroacoustics*, 1(1):83–96, 2002.

[21] R.B. Dingle. *Asymptotic Expansions: Their Derivation and Interpretation.* Academic Press, New York, 1973.

[22] M. E. Goldstein. High frequency sound emission from moving point multipole sources embedded in arbitrary transversely sheared mean flows. *Journal of Sound and Vibration*, 80(4):499–522, 1982.

[23] S. M. Candel. Numerical solution of conservation equations arising in linear wave theory: application to aeroacoustics. *Journal of Fluid Mechanics*, 83:465–493, 1977.

[24] P. A. Durbin. High frequency Green function for aerodynamic noise moving media, Part I: general theory. *Journal of Sound and Vibration*, 91:519–525, 1983.

[25] T. Colonius, S. K. Lele, and P. Moin. The scattering of sound waves by a vortex: numerical simulations and analytical solutions. *Journal of Fluid Mechanics*, 260: 271–298, 1994.

[26] I. D. Abrahams, G. A. Kriegsmann, and E. L. Reiss. On the development of caustics in shear flows over rigid walls. *SIAM Journal on Applied Mathematics*, 49(6):1652–1664, 1989.

[27] I. D. Abrahams, G. A. Kriegsmann, and E. L. Reiss. On the development and control of caustics in shear flows over elastic surfaces. *The Journal of the Acoustical Society of America*, 92(1):428–434, 1992.

[28] I. D. Abrahams, G. A. Kriegsmann, and E. L. Reiss. Sound radiation and caustic formation from a point source in a wall shear layer. *AIAA journal*, 32(6):1135–1144, 1994.

[29] B. J. Tester and C. L. Morfey. Developments in jet noise modelling—theoretical predictions and comparisons with measured data. *Journal of Sound and Vibration*, 46(1):79–103, 1976.

[30] M. V. Berry. Evanescent and real waves in quantum billiards and Gaussian beams. *Journal of Physics A: Mathematical and General*, 27(11):L391, 1994.

[31] B. W. T. Kelvin. *Popular lectures and addresses*, volume 3. Macmillan and Company, 1891.

[32] B. W. T. Kelvin. Deep water ship-waves. *Proceedings of the Royal Society of Edinburgh, XXV (1903-05)*, 565, 1905.

[33] F. Ursell. On Kelvin's ship-wave pattern. *Journal of fluid mechanics*, 8(03):418–431, 1960.

[34] F. Ursell. *Ship Hydrodynamics, Water Waves, and Asymptotics: Collected Papers of F. Ursell, 1946-1992*, volume 1. World Scientific, 1994.

[35] V. Červenỳ, I. A. Molotkov, and I. Pšenčík. *Ray method in seismology*. Univerzita Karlova, 1977.

[36] V. Červenỳ. *Seismic ray theory*. Cambridge University Press, 2005.

[37] C. J. Thomson. Complex rays and wave packets for decaying signals in inhomogeneous, anisotropic and anelastic media. *Studia Geophysica et Geodaetica*, 41(4): 345–381, 1997.

[38] M. V. Berry and C. Upstill. Catastrophe optics: morphologies of caustics and their diffraction patterns. *Prog. Opt*, 18:257–346, 1980.

[39] R. A. Egorchenkov and Y. A. Kravtsov. Complex ray-tracing algorithms with application to optical problems. *JOSA A*, 18(3):650–656, 2001.

[40] J. B. Keller. Geometrical theory of diffraction. *JOSA*, 52(2):116–130, 1962.

[41] I. N. Sneddon. *Elements of partial differential equations*. Courier Dover Publications, 2006.

[42] M. S. Sambridge and B. L. N. Kennett. Boundary value ray tracing in a heterogeneous medium: a simple and versatile algorithm. *International Journal of Geophysics*, 101:157–168, 1990.

[43] R. L. Wesson. *Seismic ray computation in laterally inhomogeneous crustal models*. PhD thesis, Department of Geophysics, Stanford University, 1970.

[44] R. L. Wesson. Travel-time inversion for laterally inhomogeneous crustal velocity models. *Bulletin of the Seismological Society of America*, 61(3):729–746, 1971.

[45] B. R. Julian and D. B. Gubbins. Three-dimensional seismic ray tracing. *J. Geophys*, 43(1):95–114, 1977.

[46] V. W. H. K. Pereyra, W. H. K. Lee, and H. B. Keller. Solving two-point seismic-ray tracing problems in a heterogeneous medium Part 1. A general adaptive finite difference method. *Bulletin of the Seismological Society of America*, 70(1):79–99, 1980.

[47] A. Hanyga and H. B. Helle. Synthetic seismograms from generalized ray tracing. *Geophysical prospecting*, 43(1):51–75, 1995.

[48] H. B. Keller and D. J. Perozzi. Fast seismic ray tracing. *SIAM Journal on Applied Mathematics*, 43(4):981–992, 1983.

[49] V. Farra. Ray tracing in complex media. *Journal of Applied Geophysics*, 30(1): 55–73, 1993.

[50] A. Hanyga. Point-to-curve ray tracing. *Pure and Applied Geophysics*, 148(3-4): 387–420, 1996.

[51] H. B. Keller. Lectures on numerical methods in bifurcation problems. *Applied Mathematics*, 217:50, 1987.

[52] M. E. Henderson and H. B Keller. Complex bifurcation from real paths. *Society for Industrial and Applied Mathematics*, 50(2):460–482, 1990.

[53] H. B. Keller. *Numerical methods for two-point boundary-value problems*. Dover Publications New York, NY, 1992.

[54] E. Doedel, H. B. Keller, and J. P. Kernevez. Numerical analysis and control of bifurcation problems (I): Bifurcation in finite dimensions. *International Journal of Bifurcation and Chaos*, 1(03):493–520, 1991.

[55] E. L. Allgower and K. Georg. *Numerical continuation methods*, volume 13. Springer-Verlag Berlin, 1990.

[56] D. J. Doornbos. *Seismological algorithms: computational methods and computer programs*. Academic Pr, 1988.

[57] P. M. Morse and H. Feshbach. Methods of theoretical physics. *International Series in Pure and Applied Physics, New York: McGraw-Hill*, 1, 1953.

[58] C. M. Bender and S. A. Orszag. *Advanced mathematical methods for scientists and engineers I: Asymptotics methods and perturbation theory*, volume 1. Springer, 1999.

[59] J. Heading. *An introduction to phase-integral methods*. Courier Dover Publications, 2013.

[60] J. B. Keller. The ray theory of ship waves and the class of streamlined ships. *Journal of Fluid Mechanics*, 91(03):465–488, 1979.

[61] C. J. Lustri, S. W. McCue, and S. J. Chapman. Exponential asymptotics of free surface flow due to a line source. *IMA Journal of Applied Mathematics*, 78(4): 697–713, 2013.

[62] A. Hanyga and M. Seredyńska. Diffraction of pulses in the vicinity of simple caustics and caustic cusps. *Wave Motion*, 14(2):101–121, 1991.

[63] Y. A. Kravtsov. Complex rays and complex caustics. *Radiophysics and Quantum Electronics*, 10(9):719–730, 1967.

[64] A. D. Pierce et al. *Acoustics: an introduction to its physical principles and applications*. McGraw-Hill New York, 1981.

[65] S. J. Chapman, J. M. H. Lawry, J. R. Ockendon, and R. H. Tew. On the theory of complex rays. *SIAM review*, pages 417–509, 1999.

[66] G. A. Deschamps. Gaussian beam as a bundle of complex rays. *Electronics letters*, 7(23):684–685, 1971.

[67] L. B. Felsen. Geometrical theory of diffraction, evanescent waves, complex rays and Gaussian beams. *Geophysical Journal International*, 79(1):77–88, 1984.

[68] J. Arnaud. Representation of Gaussian beams by complex rays. *Applied optics*, 24(4):538–543, 1985.

[69] A. N. Norris. Complex point-source representation of real point sources and the Gaussian beam summation method. *JOSA A*, 3(12):2005–2010, 1986.

[70] B. D. Seckler and J. B. Keller. Geometrical theory of diffraction in inhomogeneous media. *The Journal of the Acoustical Society of America*, 31(2):192–205, 1959.

[71] B. D. Seckler and J. B. Keller. Asymptotic theory of diffraction in inhomogeneous media. *The Journal of the Acoustical Society of America*, 31(2):206–216, 1959.

[72] P. A. Durbin. High frequency Green function for aerodynamic noise moving media, Part II: noise from a spreading jet. *Journal of Sound and Vibration*, 91:527–538, 1983.

[73] H. H. Hubbard. Aeroacoustics of flight vehicles: Theory and practice. Volume 1. Noise sources. Technical report, DTIC Document, 1991.

[74] M. V. Berry. Stokes' phenomenon; smoothing a Victorian discontinuity. *Publications Mathématiques de l'Institut des Hautes Études Scientifiques*, 68(1):211–221, 1988.

[75] M. V. Berry. Uniform asymptotic smoothing of Stokes' discontinuities. *Proceedings of the Royal Society of London. A. Mathematical and Physical Sciences*, 422(1862): 7–21, 1989.

[76] M. V. Berry and C. J. Howls. Overlapping Stokes smoothings: survival of the error function and canonical catastrophe integrals. *Proceedings of the Royal Society of London. Series A: Mathematical and Physical Sciences*, 444(1920):201–216, 1994.

[77] J. Heading. Phase-integral methods I. *The Quarterly Journal of Mechanics and Applied Mathematics*, 15(2):215–244, 1962.

[78] J. Heading. Global phase-integral methods. *The Quarterly Journal of Mechanics and Applied Mathematics*, 30(3):281–302, 1977.

[79] M. V. Berry. Asymptotics, superasymptotics, hyperasymptotics... In *Asymptotics beyond all orders*, pages 1–14. Springer, 1991.

[80] M. V. Berry and C. J. Howls. Hyperasymptotics for integrals with saddles. *Proceedings of the Royal Society of London. Series A: Mathematical and Physical Sciences*, 434(1892):657–675, 1991.

[81] M. V. Berry and C. J. Howls. Unfolding the high orders of asymptotic expansions with coalescing saddles: singularity theory, crossover and duality. *Proceedings of the Royal Society of London. Series A: Mathematical and Physical Sciences*, 443 (1917):107–126, 1993.

[82] SJ Chapman, JMH Lawry, JR Ockendon, and VH Saward. Edge diffraction of complex rays. *Wave motion*, 33(1):41–49, 2001.

[83] C. J. Lustri. *Exponential asymptotics in unsteady and three-dimensional flows.* PhD thesis, Brasenose College, University of Cambridge, 2012.

[84] M. V. Berry. Caustics, catastrophes and quantum chaos. *Nexus News*, pages 4–5, February 1997.

[85] L. B. Felsen. Novel ways for tracking rays. *JOSA A*, 2(6):954–963, 1985.

[86] R. Mazar and L. B. Felsen. Stochastic geometrical theory of diffraction. *The Journal of the Acoustical Society of America*, 86(6):2292–2308, 1989.

[87] V. M. Babich, N. Buldyrev, and I. A. Molotkov. Space-time ray methods. *Linear and Non-Linear Waves*, 1985.

[88] V. Červenỳ, M. M. Popov, and I. Pšenčík. Computation of wave fields in inhomogeneous media—Gaussian beam approach. *Geophysical Journal International*, 70 (1):109–128, 1982.

[89] J. R. Klauder. Global, uniform, asymptotic wave-equation solutions for large wavenumbers. *Annals of Physics*, 180(1):108–151, 1987.

[90] C. J. Thomson. Seismic coherent states and ray geometrical spreading. *Geophysical Journal International*, 144(2):320–342, 2001.

[91] V. P. Maslov. *Perturbation theory and asymptotic methods.* Moscow State University Publications, 1965.

[92] V. P. Maslov. *The WKB method in many dimensions. Supplement to the book of G. Heading: Introduction to the Method Phase Integrals.* Mir, 1965.

[93] V. P. Maslov and M. V. Fedoriuk. *Semi-classical approximation in quantum mechanics*, volume 7. Springer, 2001.

[94] C. J. Thomson and C. H. Chapman. An introduction to Maslov's asymptotic method. *Geophysical Journal International*, 83(1):143–168, 1985.

[95] J. M. Kendall and C. J. Thomson. Maslov ray summation, pseudo-caustics, Lagrangian equivalence and transient seismic waveforms. *Geophysical Journal International*, 113(1):186–214, 1993.

[96] R. W. Ziolkowski and G. A. Deschamps. Asymptotic evaluation of high-frequency fields near a caustic: An introduction to Maslov's method. *Radio Science*, 19(4): 1001–1025, 1984.

[97] V. I. Arnol'd. Singularities of smooth mappings. *Russian Mathematical Surveys*, 23(1):1–43, 1968.

[98] R. Thom. Structural stability, catastrophe theory, and applied mathematics. *SIAM review*, 19(2):189–201, 1977.

[99] R. Thom. Structural stability and morphogenesis. 1989.

[100] V. I. Arnol'd. Catastrophe theory. *Berlin: Springer-Verlag. Fraser-Smith, AC, Bernardi, A., McGill, PR, Ladd, ME, Helliwell, RA, Villard, OG, Jr. Low-frequency magnetic field measurements near the epicenter of the Ms*, 7:1465–1468, 1992.

[101] E. C. Zeeman. *Catastrophe theory: Selected papers, 1972–1977.* Addison-Wesley, 1977.

[102] V. I. Arnol'd. *Singularities of caustics and wave fronts*, volume 62. Springer, 1990.

[103] E. Arnol'd, S. M. Gusein-Zade, and A. N. Varchenko. *Singularities of Differentiable Maps, Volume 2: Monodromy and Asymptotics of Integrals*, volume 2. Springer, 2012.

[104] J. J. Duistermaat. Applications of Fourier integral operators. In *Proceedings of the International Congress of Mathematicians (Vancouver, BC, 1974), Vol. 2*, pages 263–268, 1975.

[105] M. V. Berry. *The diffraction of light by ultrasound.* Academic Press, 1966.

[106] M. V. Berry, J. F. Nye, and F. J. Wright. The elliptic umbilic diffraction catastrophe. *Philosophical Transactions for the Royal Society of London. Series A, Mathematical and Physical Sciences*, pages 453–484, 1979.

[107] J. F. Nye. The catastrophe optics of liquid drop lenses. *Proceedings of the Royal Society of London. A. Mathematical and Physical Sciences*, 403(1824):1–26, 1986.

[108] J. F. Nye. *Natural focusing and fine structure of light: caustics and wave dislocations.* CRC Press, 1999.

[109] F. J. Wright. Wavefront dislocations and their analysis using catastrophe theory. In *Structural Stability in Physics*, pages 141–156. Springer, 1979.

[110] F. J. Wright. Singularities of plane curves which occur as singular sections of the bifurcation sets of the cuspoid catastrophes. *Journal of Physics A: Mathematical and General*, 14(7):1587, 1981.

[111] R. Gilmore. *Catastrophe theory for scientists and engineers.* Courier Dover Publications, 1993.

[112] M. Abramowitz and I. A. Stegun. Handbook of mathematical functions with formulas, graphs, and mathematical tables. In *Conference on XYZ*. Dover, 2006.

[113] M. V. Berry and C. J. Howls. Integrals with coalescing saddles. *Digital Library of Mathematical Functions, http://dlmf.nist.gov*, 2006.

[114] D. Ludwig. Uniform asymptotic expansions at a caustic. *Communications on Pure and Applied Mathematics*, 19(2):215–250, 1966.

[115] Y. A. Kravtsov. A modification of the geometrical optics method. *Izv. Vysshikh Uchebn. Zavedenii, Radiofiz.*, 7, 1964.

[116] D. W. Wundrow and A. Khavaran. On the applicability of high-frequency approximations to Lilley's equation. *Journal of sound and vibration*, 272(3):793–830, 2004.

[117] T. Pearcey. The structure of an electromagnetic field in the neighbourhood of a cusp of a caustic. *The London, Edinburgh, and Dublin Philosophical Magazine and Journal of Science*, 37(268):311–317, 1946.

[118] F. Coulouvrat. Focusing of weak acoustic shock waves at a caustic cusp. *Wave Motion*, 32(3):233–245, 2000.

[119] W. D. Hayes. Sonic boom. *Annual Review of Fluid Mechanics*, 3(1):269–290, 1971.

[120] J. K. Hunter and J. B. Keller. Caustics of nonlinear waves. *Wave motion*, 9(5): 429–443, 1987.

[121] A. Hanyga. Canonical functions of asymptotic diffraction theory associated with symplectic singularities. *Banach Center Publications*, 39:57–71, 1997.

[122] D. Amodei, H. Keers, D. Vasco, and L. Johnson. Computation of uniform wave forms using complex rays. *Physical Review E*, 73(3), 2006.

[123] J. N. L. Connor and P. R. Curtis. Differential equations for the cuspoid canonical integrals. *Journal of Mathematical Physics*, 25(10):2895–2902, 1984.

[124] J. J. Stamnes and B. Spjelkavik. Evaluation of the field near a cusp of a caustic. *Journal of Modern Optics*, 30(9):1331–1358, 1983.

[125] J. N. L. Connor, P. R. Curtis, and D. Farrelly. The uniform asymptotic swallowtail approximation: Practical methods for oscillating integrals with four coalescing saddle points. *Journal of Physics A: Mathematical and General*, 17(2):283, 1984.

[126] N. P. Kirk, J. N. L. Connor, and C. A. Hobbs. An adaptive contour code for the numerical evaluation of the oscillatory cuspoid canonical integrals and their derivatives. *Computer physics communications*, 132(1):142–165, 2000.

[127] J. J. Stamnes. Hybrid integration technique for efficient and accurate computation of diffraction integrals. *JOSA A*, 6(9):1330–1342, 1989.

[128] J. F. Nye. Dislocation lines in the hyperbolic umbilic diffraction catastrophe. In *Proceedings of the Royal Society of London A: Mathematical, Physical and Engineering Sciences*, volume 462, pages 2299–2313. The Royal Society, 2006.

[129] R. Borghi. Evaluation of diffraction catastrophes by using Weniger transformation. *Optics letters*, 32(3):226–228, 2007.

[130] R. Borghi. On the numerical evaluation of umbilic diffraction catastrophes. *JOSA A*, 27(7):1661–1670, 2010.

[131] F. J. Wright. The Stokes set of the cusp diffraction catastrophe. *Journal of Physics A: Mathematical and General*, 13(9):2913, 1980.

[132] M. V. Berry and C. J. Howls. Stokes surfaces of diffraction catastrophes with codimension three. *Nonlinearity*, 3(2):281, 1990.

[133] D. G. Duffy. *Green's functions with applications*. CRC Press, 2010.

[134] N. Bleistein and R. A. Handelsman. *Asymptotic Expansions of Integrals*. Dover, 1986.

[135] A. Erdélyi. *Asymptotic expansions*. Number 3. Courier Dover Publications, 1956.

[136] M. F. Kewin. Deriving a far-field solution for the Lilley equation, for two-dimensional and axisymmetric flows. Technical report, ISVR, University of Southampton, April 2009.

[137] P. M. Morse and K. Ingard. *Theoretical acoustics*. Princeton University Press, 1986.

[138] H. Schlichting and K. Gersten. *Boundary-layer theory*. Springer, 2000.

[139] F. W. J. Olver. *Asymtotics and special functions*. Academic Press, New York, 1974.

[140] J. T. Stone, R. H. Self, and Howls C. J. A complex ray-tracing tool for high-frequency mean-field flow interaction effects in jets. *AIAA paper*, June 2014. URL `http://dx.doi.org/10.2514/6.2014-2757`.

[141] R. E. Langer. On the connection formulas and the solutions of the wave equation. *Physical Review*, 51(8):669, 1937.

[142] N. Bleistein. *Mathematical methods for wave phenomena*. Academic Press, 1984.

[143] D. S. Jones. The mathematical theory of noise shielding. *Progress in Aerospace Sciences*, 17:149–229, 1976.

[144] W. D. Hayes. Kinematic wave theory. *Proceedings of the Royal Society of London. A. Mathematical and Physical Sciences*, 320(1541):209–226, 1970.

[145] A. Hatcher. *Algebraic topology.* , 2002.

[146] M. E. Goldstein and S. J. Leib. The role of instability waves in predicting jet noise. *Journal of Fluid Mechanics*, 525:37–72, 2005.

[147] G. K. Batchelor. *The Theory of Homogeneous Turbulence.* Cambridge University Press, 1953.

[148] R. H. Self. A RANS CFD coupled model for predicting coaxial jet noise. Technical Report 304, ISVR, University of Southampton, January 2005.

[149] L. Davis et al. *Handbook of genetic algorithms*, volume 115. Van Nostrand Reinhold New York, 1991.

[150] E. Cheney and D. Kincaid. *Numerical mathematics and computing.* Cengage Learning, 2012.

[151] M. Golubitsky and D. G. Schaeffer. *Singularities and groups in bifurcation theory*, volume 1. Springer New York, 1985.

[152] M. E. Henderson. *Complex bifurcation.* PhD thesis, California Institute of Technology, 1985.

[153] T. W. Gamelin. *Complex analysis.* Springer, 2001.

[154] P. Kravanja and M. Van Barel. *Computing the zeros of analytic functions.* Number 1727. Springer, 2000.

[155] J. H. Wilkinson. The evaluation of the zeros of ill-conditioned polynomials. Part I. *Numerische Mathematik*, 1(1):150–166, 1959.

[156] J. H. Wilkinson. The evaluation of the zeros of ill-conditioned polynomials. Part II. *Numerische Mathematik*, 1(1):167–180, 1959.

[157] B. Sturmfels. *Solving systems of polynomial equations*, volume 97. American Mathematical Soc., 2002.

[158] I. M. Gelfand, M. Kapranov, and A. Zelevinsky. *Discriminants, resultants, and multidimensional determinants.* Springer Science & Business Media, 2008.

[159] A. K. Tsikh. *Multidimensional residues and their applications*. American Mathematical Soc., 1992.

[160] A. Tsikh and A. Yger. Residue currents. *Journal of Mathematical Sciences*, 120 (6):1916–1971, 2004.

[161] J. P. D'Angelo. *Several complex variables and the geometry of real hypersurfaces*, volume 8. CRC Press, 1993.

[162] L. A. Ajzenberg and A. P. Yuzhakov. *Integral representations and residues in multidimensional complex analysis*, volume 58. American Mathematical Soc., 1983.

[163] M. H. Kalos and P. A. Whitlock. *Monte Carlo methods*. John Wiley & Sons, 2008.

[164] G. Fishman. *Monte Carlo: concepts, algorithms, and applications*. Springer Science & Business Media, 2013.

[165] J. M. McNamee. A bibliography on roots of polynomials. *Journal of Computational and Applied Mathematics*, 47(3):391–394, 1993.

[166] D. Starer and A. Nehorai. High-order polynomial root tracking algorithm. In *Acoustics, Speech, and Signal Processing, 1992. ICASSP-92., 1992 IEEE International Conference on*, volume 4, pages 465–468. IEEE, 1992.

[167] C. J. Howls. An introduction to hyperasymptotics using Borel-Laplace transforms (algebraic analysis of singular perturbations). , 968:31–48, 1996.

[168] R. B. Paris and D. Kaminski. *Asymptotics and Mellin-Barnes Integrals*, volume 85. Cambdrige University Press, 2001.

[169] D. S. Jones. Acoustic and electromagnetic waves. *Oxford/New York, Clarendon Press/Oxford University Press, 1986, 764 p.*, 1, 1986.

[170] N. Bleistein and R. A. Handelsman. A generalization of the method of steepest descent. *IMA Journal of Applied Mathematics*, 10(2):211–230, 1972.

[171] L. Brekhovskikh. *Waves in Layered Media 2*, volume 16. Elsevier, 2012.

[172] P. D. Miller. *Applied asymptotic analysis*, volume 75. American Mathematical Soc., 2006.

[173] J. P. Boyd. The devil's invention: asymptotic, superasymptotic and hyperasymptotic series. *Acta Applicandae Mathematica*, 56(1):1–98, 1999.

[174] V. L. Pokrovskii and I. M. Khalatnikov. On the problem of above-barrier reflection of high-energy particles. *Soviet Phys. JETP*, 13:1207–1210, 1961.

[175] R. Mani, P. R. Gliebe, and T. F. Balsa. High velocity jet noise source location and reduction. *Task 2, Federal Aviation Administration Report, FAA-RD-76-II*, 1978.

[176] A. Khavaran, N. J. Georgiadis, J. Bridges, and V. F. Dippold. Effect of free jet on refraction and noise. *AIAA Paper*, 2941, 2005.

[177] N. Curle. The influence of solid boundaries upon aerodynamic sound. In *Proceedings of the Royal Society of London A: Mathematical, Physical and Engineering Sciences*, volume 231, pages 505–514. The Royal Society, 1955.

[178] D. Pridmore-Brown. Sound propagation in a fluid flowing through an attenuating duct. *Journal of Fluid Mechanics*, 4:393–406, 1958.

[179] A.E.D. Lloyd and N. Peake. The propagation of acoustic waves in a slowly varying duct with radially sheared axial mean flow. *Journal of Sound and Vibration*, 332 (17):3937–3946, August 2013.

[180] S. G. Samko, A. A. Kilbas, and O. I. Marichev. Fractional integrals and derivatives. *Theory and Applications, Gordon and Breach, Yverdon*, 1993, 1993.

[181] L. N. Trefethen and J. A. C. Weideman. The exponentially convergent trapezoidal rule. *SIAM Review*, 56(3):385–458, 2014.

[182] N. Bleistein. Uniform asymptotic expansions of integrals with many nearby stationary points of algebraic singularities. *Journal of Mathematics and Mechanics*, 17(6):533–559, 1967.